TESI DOCTORAL / 2016

Finite element simulation of the healthy and degenerated lumbar spine

Interplay between muscle activity and intervertebral disc multiphysics

Themis Toumanidou

Universitat Politècnica de Catalunya | 2016

Finite element simulation of the healthy and degenerated lumbar spine

Interplay between muscle activity and intervertebral disc multiphysics

Themis Toumanidou

Tesi presentada per obtenir el títol de Doctora amb menció
Internacional per la Universitat Politècnica de Catalunya

Institut de Bioenginyeria de Catalunya - Universitat Politècnica de Catalunya
septembre 2016

About the cover
Serpens is an anatomical collage of the artist Travis Bedel (aka Bedelgeuse). The image has no licensing restrictions but the written agreement of the artist was requested anyway. <*bedelgeuse.tumblr.com*> 15 Sept. 2016.

This research was carried out at the Biomechanics and Mechanobiology group at the Institute for Bioengineering of Catalonia (IBEC). Financial support was provided by the European Union Seventh Framework Programme (FP7) under grant agreement Nr 269909, My SPINE project (ICT 2009.5.3 Virtual Physiological Human).

Director:
Dr. Jérôme Noailly | Departament de Tecnologies de la Informació i les Comunicacions, UPF

Ponent:
Dr. Josep Maria Font Llagunes | Departament d'Enginyeria Mecànica, UPC

Programa de Doctorat:
Enginyeria Mecànica, Fluids i Aeronàutica, Departament d'Enginyeria Mecànica, Escola Tècnica Superior d'Enginyeria Industrial de Barcelona, UPC

Everything should be made as simple as possible, but not simpler.

Albert Einstein

Abstract | Resum

Abstract - The human spine acts as a scaffold for the entire body by providing mechanical support and mobility of the torso while protecting the spinal cord and nerves from the external loads transferred during daily activities. Such loads are largely controlled by the stabilizing action of spine muscles and influence the biophysical regulation of the intervertebral discs (IVD) through complex biomechanical interactions. Numerical models have been important tools for the translation of the external forces into specific distributions of internal loads that otherwise cannot be easily measured directly in the lumbar spine. This PhD thesis used the predictive ability of constitutive equations to reflect the basic mechanical properties of the lumbar IVD and muscles in order to explore the interplay between disc multiphysics and muscle activity on the healthy and degenerated spine.

At first, an extensive review of the existing experimental and numerical studies reported for the estimation of lumbar spinal loads was performed focusing on the representation of muscle role. The three-element Hill approximation that takes into account the internal constitution of the tissue, i.e. active and passive components, to model skeletal muscle mechanics was detailed, and the poro-hyperelastic formulations used for IVD modeling were also discussed. A new constitutive equation assembly was proposed for the description of back muscle contraction involving one active parameter that was controlled via strain-based criteria and four passive parameters. For the latters, literature-driven values were initially defined, while a parametric study was designed for the active parameter by proposing activation thresholds related to the stretch level. As a next step, an optimization scheme was developed to define a full set of calibrated parameter values for each muscle fascicle using force estimations from the analysis of a reported lumbar spine (LS) rigid body (RB) model based on the measured kinematics of the vertebra.

To test the robustness of the constitutive muscle model proposed, a L3-S1 finite element (FE) model was developed with a generic geometry that included 46 back muscle fascicles and all passive tissues. Simulation of forward trunk bending (10° flexion) showed that the predicted force development increased progressively in caudal direction. The intradiscal pressure (IDP) values calculated were in good correlation with previous *in vivo* measurements showing the ability of the model to capture realistic internal load distributions. Then, to represent standing posture, the gravity loads were defined by considering the heterogeneous distribution of body

volumes and densities along the trunk. This simulation was also coupled to a previous simulation of 8-hour free IVD swelling to mimic the disc hydration taking place overnight. Disc swelling led to muscle activation and muscle force distributions that seemed particularly appropriate to counterbalance the anterior body mass effect in standing, pointing out the likely existence of a functional balance between stretch-induced muscle activation and IVD multiphysics.

A geometrical extension of the generic FE model was then performed to incorporate all relevant tissues of the full lumbar osteoligamentous spine and include in total 94 muscle fascicles arising from the L1-S1 levels. Simulations of standing and lying position were repeated and the effect of previous rest (PR) and muscle presence (MS) on internal loads was explored. Predictions of muscle forces revealed that notably higher muscle activations were required in simple standing, while when PR was considered, the total load transferred to the LS was altered from compressive to tensile forces. Overnight, the predicted IDP increase reproduced previous *in vivo* measured data. Both PR and MS were found to affect the intersegmental rotations (ISR) particularly at the upper lumbar levels. When degenerated material properties were used for the discs, up to 14 times higher active forces were developed in standing with PR, and the IDP was decreased at all levels but L5/S1 compared to the values predicted with healthy discs.

At last, the previous workflow was coupled to a L1-S1 FE model of a patient LS model that was simulated using patient-specific (P-SP) and condition-dependent tissue material properties. In standing, an asymmetrical fascicle activation with increased shortening of the left side fascicles and a lateral bending of the trunk was predicted. The decreased swelling capacity of the degenerated discs was associated to an increase of the muscle activations needed to balance the gravity loads that tended to flex forward the P-SP spine model. In standing without MS and PR, an alternating pattern of forward-backward bending especially between the upper two levels was predicted. Comparisons in terms of IDP predictions for both generic and P-SP models with healthy disc properties revealed that introducing P-SP geometries gave better correlations with *in vivo* data. Given the difficulties to evaluate the predicted muscle forces against *in vivo* measurements, such outcome greatly contributed towards a full validation of the methodology proposed. In spite of some limitations, this approach allowed to explicitly and rationally explore the interactions between muscle function and passive tissue biomechanics in the LS. The information provided could help clinical decision for patients whom source of back pain is unclear.

Resum - La columna vertebral proporciona suport mecànic al tors alhora que protegeix la medul·la espinal i els nervis de les forces externes transferides durant les activitats diàries. Aquestes forces són controlades en gran part pels músculs espinals i influeixen en la regulació biofísica dels discos intervertebrals (IVD). Els models numèrics han estat eines importants per a la traducció de les forces externes en càrregues internes que d'altra manera no poden ser fàcilment mesurades directament. Aquesta tesi utilitza la capacitat predictiva de les equacions constitutives per considerar les propietats mecàniques dels discs lumbars i dels músculs i explorar la interacció IVD-múscul a la columna vertebral sana i degenerada.

Es va realitzar una revisió de l'estat de l'art dels mètodes reportats per l'estimació de les càrregues, i es van detallar particularment el model muscular de Hill i les formulacions poro-hiperelàstics utilitzades per a la modelització del disc. Es va proposar un model novedós d'equacions constitutives implicant un paràmetre actiu controlat a través de criteris basats en la deformació, i quatre paràmetres passius. Per aquests últims, es van definir uns valors inicialment basats en la literatura, mentres que pel paràmetre actiu es va realitzar un estudi paramètric per proposar els llindars d'activació relacionats amb l'estirament. A continuació, es va desenvolupar un esquema d'optimització per definir un conjunt complet de valors calibrats per fascicle utilitzant estimacions de forces d'un model de cos rígid de la literatura basat en la cinemàtica de les vèrtebres mesurada.

Per comprovar la robustesa del mètode, es va desenvolupar un model L3-S1 d'elements finits (FE) incloent 46 fascicles musculars i tots els teixits passius. La simulació de flexió anterior va mostrar que les forces musculars predites van augmentar en direcció caudal. Les prediccions de pressió intradiscal (IDP) es van correlacionar amb mesures in vivo mostrant així la capacitat del model per capturar les càrregues internes reals. Per simular la posició d'empeus, les càrregues de gravetat es van definir considerant la distribució heterogènia dels volums del cos al llarg del tronc. A més, aquesta simulació es va acoblar amb un inflament previ del IVD de 8 hores per imitar la hidratació del disc durant la nit. L'inflament del disc va induir activació muscular i una distribució de forces que semblaven particularment apropiades per a contrarestar les càrregues de gravetat, assenyalant la probable existència d'un equilibri funcional entre l'activació muscular i la multifísica del disc.

Després es va realitzar una extensió geomètrica del model per incorporar tots els teixits pertinents de la columna lumbar completa incloent un total de 94 fascicles. L'efecte del repòs previ (PR) i la presència de múscul (MS) sobre les càrregues internes va ser explorat en posició d'empeus i estirada. Durant la nit, l'augment de l'IDP computat va confirmar dades anteriors in vivo. Quan es van definir propietats degenerades als discs, es va predir una disminució general de l'IDP i una activació fins a 14 vegades més alta en peu amb PR. Per últim, les simulacions es van repetir utilitzant un model L1-S1 FE de pacient amb propietats del material específics pel pacient (P-SP) i dependents de la condició del teixit. D'empeus, es va predir una activació asimètrica a la banda esquerra i inclinació lateral. La disminució de la capacitat d'inflament dels discs degenerats es va associar a un augment de l'activació muscular necessària per equilibrar les forces de gravetat que tendeixen a flexionar el tronc. La bona correlació dels resultats de l'IDP en el model P-SP amb discos sans amb dades in vivo va contribuir a la validació del mètode presentat. Malgrat les seves limitacions, aquest enfoc va permetre explorar de manera explícita i racional les interaccions entre la funció muscular i la biomecànica dels teixits passius i contribuir a l'enteniment de l'origen de mal d'esquena.

Contents

List of Figures

List of Tables

Abbreviations

AF	Anulus Fibrosus
AP	Articular Process
BEP	Body Endplate
BM	Body Mass
BW	Body Weight
CEP	Cartilage Endplate
CNS	Central Nervous System
CSA	Cross-Sectional Area
CSYS	Coordinate System
DOF	Degrees of Freedom
FE	Finite Element
IST	Intersegmental Translation
ISR	Intersegmental Rotation
IVD	Intervertebral disc
LBP	Low Back Pain
LS	Lumbar Spine
MP	Mamillary Process
mfMRI	Muscle Functional MRI
MS	Muscle Presence
MSL	Musculoskeletal
MT	Musculo-Tendon
NP	Nucleus Pulposus
PCSA	Physiologic Cross-Sectional Area
PNS	Peripheral Nervous System

PR	Previous Rest
PSIS	Posterior Superior Iliac Spine
P-SP	Patient-Specific
RB	Rigid Body
SIS	Superior Iliac Spine
SOTA	State-Of-The-Art
SP	Spinous Process
TP	Transverse Process
VB	Vertebral Body
3D	Three-dimensional

Chapter 1

Introduction

1.1 Background and motivation

Recent findings suggest that prolonged times of sedentary behaviour in modern societies, as well as the lack of physical activity, highly increase the risk of chronic musculoskeletal disorders. Though statistics vary among different epidemiological studies, low back pain (LBP) is one of the major health problems in industrialized countries resulting as one of the largest causes of absence from work [1]. To quote the definition given by the World Health Organization (WHO): *"LBP is neither a disease nor a diagnostic entity of any sort. The term refers to pain of variable duration in an area of anatomy afflicted so often that it has become a paradigm of responses to external and internal stimuli (...) such pain ranks high (often first) as a cause of disability and inability to work, as an interference with the quality of life, and as a reason for medical consultation"* [2].

Based on regional cross-sectional data available in the literature, the incidence and one year prevalence of LBP are roughly the same the world over (Fig. 1.1). In terms of lifetime prevalence, studies reported that the percentage might overcome 80% [3]. Back pain affects both men and women and most frequently occurs between 30 and 50 years of age. As pain episodes can be either punctual or periodic, it is suggested that prevalence numbers related to a specific period may give a more accurate picture of the problem. That is, while about 20-40% of adults may experience LBP over a period of one month, when a one-year period is considered, these percentages may rise up to 72% in Europe and Canada [4]. Although these numbers might seem very high, estimates also vary in relation to the severity and to the duration of the symptoms, and depend on whether the pain limits daily activities. For example, LBP can be classified by duration as acute (short-term, usually less than 6 weeks), sub-chronic (lasts 6 to 12 weeks) or chronic/severe, that may last for years. Actually, in the latter case, the prevalence per year may fall to around 12% [5]. Several studies performed so far to evaluate the social and economic impact of LBP used a number of variables such as lost salaries, lower productivity and company profitability. Findings showed that back pain imposes an enormous economic burden on individuals, families and governments. Particularly in Europe, work absenteeism accounts for 75% of a total of 7000€ annual direct cost of LBP per patient prior to any rehabilitation intervention [6], whereas in the USA, the respective cost may reach up to $20 billions per year [7].

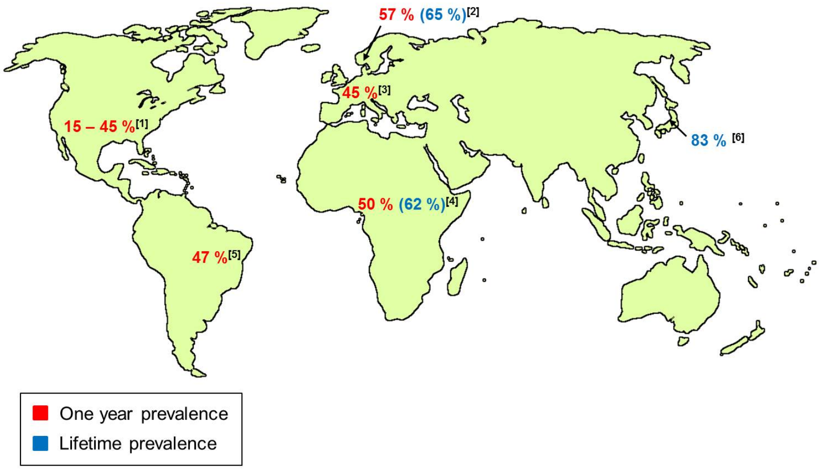

[1] Andersson (1999); [2] Sjolie (2004); [3] Eurofound (2012); [4] Louw *et al.* (2007); [5] Meziat Filho *et al.* (2015); [6] Fujii and Matsudaira (2013).

Figure 1.1: Annual and lifetime prevalence of back pain based on previous regional cross-sectional studies.

Nowadays, the most common ways to treat LBP is with analgesics, steroid injections or surgical interventions, such as discectomy, laminectomy, fusion or IVD substitutes. Alternative strategies include rest, rehabilitation, acupuncture or exercise programs involving stretching and strengthening. In short-term, such practices may offer an important pain relief to the patient. However, they do not stand for effective treatments in the mid/long-term resulting often to pain resurgence. Indeed, because of its anatomy, the spine structure protects the major nerve root of the human body and as such, an inappropriate treatment technique may quickly lead even to recurrent surgery [8].

Surprisingly, the origins of LBP are rarely addressed and only in few instances does a direct link to some defined organic disease exist. The possible pain mechanisms are several and likely complex, such as irritation of nerve roots caused by disc protrusion in the spinal canal or immunological and inflammatory responses of the surrounding spine tissues ([9], [10]). Premature ageing changes that can alter the mechanical behavior of the disc [11], neuropathic alterations like nerve ingrowth into degenerated discs ([12],[13]) and disc bacterial infections in patients with sciatica [14] could also explain the feeling of pain. Yet, evidence suggests that the major cause of back-related symptoms, such as muscle spasms ([15], [16]), is IVD degeneration. Altered disc condition was suggested to be significant also in sciatica and lumbar spinal stenosis ([17], [18]). However, the extent of such role of the disc is still unclear. Studies over the past decade associate disc degeneration to age, gender, smoking [19], and to genetic [18] and occupational factors, e.g. improper lifting and vehicular vibration [20]. At the same time, multi-variable analyses reveal that an important figure between 25 and 50% of occurrences and progression of disc degeneration especially at the lower lumbar region remains unexplained [21]. These unidentified factors are likely to involve complex mechanobiological and multiphysics interactions in the IVD [22] under the influence of the external mechanical loads transferred through the back muscles.

As such, careful analysis of the muscle activity is needed for the translation of the external loading into specific distributions of internal loads among the surrounding spine tissues. Still, to our knowledge, limited research has been conducted to include the *contribution* of muscle mechanics in spine studies, either through experimental or numerical models. Experimentally, the obvious complexity of direct measurement of muscle loads has been addressed through alternative, indirect techniques to quantify the muscle activity, such as EMG signals or force plate measurements.

A way to interpret these data as load magnitudes is to use mathematical formulations. For instance, kinematical models can derive the muscle forces at different spine levels by performing inverse dynamics or/and optimization analyses based on the measured motion data ([23],[24]). Nonetheless, these approaches do not take into account neither the muscle mechanical properties nor the parameters affecting the force development, such as force-length, force-velocity relations. Furthermore, few, if any, consider the nonlinear and time-dependent passive resistance of the intervertebral joints that is probably another important limitation. Meanwhile, weakness or fatigue of back muscles is thought to be another risk factor for LBP ([25], [26]) raising an issue on whether such condition has an impact on the functional biomechanics of the spine. Recently, different studies intended to address this concern by representing the muscle dynamics through force-generating springs and damper systems in kinematical models ([27], [28]). This concept increases our understanding of spine kinematics, such as lumbar lordosis variations between the reference and final positions. However, its predictive ability remains limited given the dependence of the estimated set of forces on the specific kinematical input. Above all, though, these approaches still cannot address the possible connections between IVD and muscle function to decipher the cause-effect relations that influence the spine mechanical response. Therefore, a predictive lumbar MS model that combines as many of the mechanical and biological aspects above-mentioned would be of a great clinical interest to explore the degenerated spine biomechanics in a patient-specific manner.

1.2 General aims and outline of the thesis

The ambition of this thesis is the application of continuum mechanics theories to capture the functional interactions between muscle activation and IVD multiphysics using a FE-predictive lumbar spine model. The present work aspires to apply constitutive formulations for the hyperelastic and osmo-porohyperelastic behaviour of the muscle and disc tissues, respectively, and predict the load transfers of external static forces to the surrounding spine tissues in different trunk positions. The objective involves: (i) the coupling of such models to different generic and P-SP FE musculoskeletal (MSL) geometries of the LS, (ii) the exploration of the effect of condition-related material properties based on P-SP experimental data and mathematical formulations, and (iii) the analysis of the contribution of muscle function to the mechanical stabilization of the healthy and pathologic spine. The aims are discussed and organized as follows:

- **Chapter** 2 includes a detailed description of the anatomy, physiology and biomechanics of the most important tissues of the human LS, i.e. the vertebrae, IVD, ligaments and muscles, with a literature review focused on the physical properties of the latter. Previous experimental and numerical studies reported for the estimation of spinal loads will be extensively reviewed. The Hill-type three-element theoretical model for the simulation of muscle contraction, and the poro-mechanical theory for the modeling of the solid and fluid parts of the IVD tissues will be presented as well.
- **Chapter** 3 presents a novel hyperelastic, quasi-incompressible and transversely isotropic constitutive assembly developed to model the active and passive behavior of the lumbar muscles. A literature-based exploration of the muscle material parameter values will be detailed as well as a parametric study for the definition of the active parameter. Moreover, an optimization study will be developed and discussed for the P-SP calibration of all muscle material parameters per fascicle using force estimations from a kinematics-driven (KD) analysis of a previously reported LS patient model.
- **Chapter** 4 describes the development of a generic L3-S1 FE MSL model of a healthy spine based on an already existing model of the L3-L5 osteoligamentous spine. The creation of the muscle network involving the fascicles of the multifidus, erector spinae, and psoas major muscles through uni-directional truss elements and the coupling with the osteoligamentous mesh will be detailed. The L3-S1 model will be used to simulate two different postures: flexion and standing. The scheme designed for the definition of the gravity load distribution in standing will be described. In order to evaluate the robustness of the proposed constitutive model, the predictions of muscle loads, strains and IDP

per level in both postures will be discussed and when possible compared to other experimental and numerical studies.

- **Chapter** 5 is dedicated to the development and analysis of full L1-S1 FE models, both healthy (generic) and degenerated (P-SP). The extension of the muscle network described in Chapter 4 will be presented here. Different sets of healthy and condition-related material parameters for the IVD will be summarized for each model based on reported studies in the literature. The same spine postures will be simulated: standing and lying (night rest). Explorations will include the prediction of active and total muscle forces, fascicle strains, IDP and spine kinematics using both geometries. Particular focus will be given in the assessment of the interactions between the IVD multiphysics and muscle activity overnight and the effect of such interplay on the load transfers in standing. Comparisons between the IDP predictions using the generic and P-SP geometries and either sets of IVD material properties against *in vivo* measurements will be also performed for an indirect validation of the approach proposed.
- **Chapter** 6 summarizes the conclusions and general discussion of the main outcomes of the present thesis as a whole.

Chapter 2

Functional anatomy of the human lumbar spine: state-of-the-art

2.1 The whole spine

The human *spine* or *vertebral column* is a complex anatomical structure composed of bony and cartilaginous elements and supported by robust spinal ligaments and muscles. All of these elements are important to the structural integrity of the spine. The spine provides three vital functions: protection of the spinal cord and nerves, mechanical support of the body, and mobility by acting as a flexible axis for movements of the head and torso. As such, the vertebral column can be considered as a scaffold for the entire body positioned posteriorly at the midline.

2.1.1 Structure

The normal spine (Fig. 2.1) consists of 24 articulating vertebrae named according to the distinct section of the spine, and 9 fused vertebrae at the sacrum and coccyx region. At the upper segment, the cervical spine is composed of seven vertebrae (C1-C7, from superior to inferior). The atlas (C1) articulates the spine with the skull enabling to nod forward (flexion) or tilt back (extension), while the axis (C2) allows the skull and atlas to rotate axially. In the middle segment, 12 vertebrae

(T1-T12) are articulated to the rib cage via synovial joints forming the thoracic spine. The lumbar spine follows between the rib cage and the pelvis consisting of five vertebrae (L1-L5), which are the largest of the vertebral column and will be detailed in Section 2.2. All articulating vertebrae but C1/C2 are separated from each other by IVDs. Inferior to the lumbar vertebrae and at the lowermost section of the spine, five fused vertebrae comprise the sacrum (S1-S5), a large triangular bone wedged between the two hip bones, and three to five fused vertebrae compose the coccyx, the final segment of the vertebral column often referred to as the human tailbone.

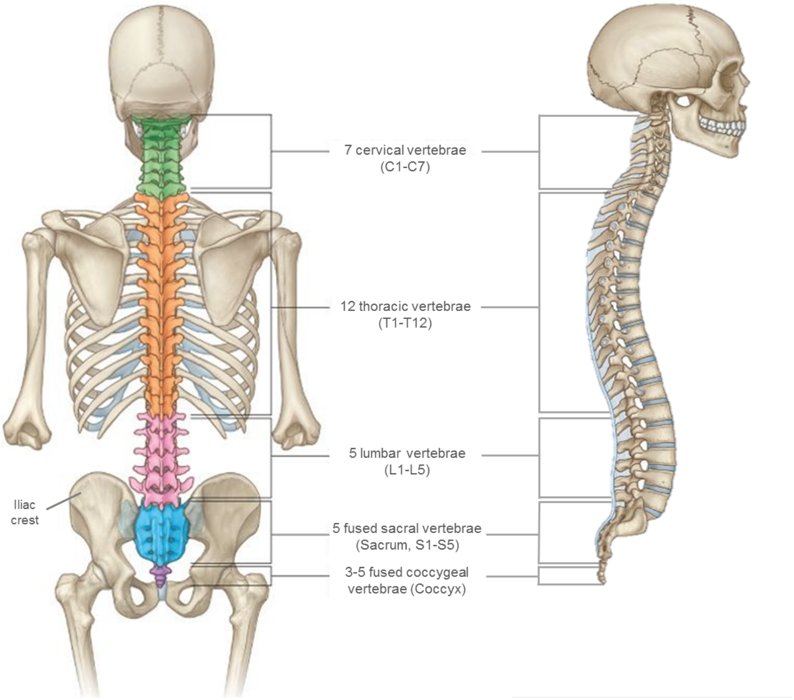

Figure 2.1: Representation of the human spine geometry and its various parts (figure adapted from [29]).

2.1.2 Spinal vertebrae

In general, the articulating vertebrae have quite similar geometry and their size increases in caudal direction. The increase of the transverse diameter may be explained by the successively greater load needed to be carried as we move from top to bottom.

Fig. 2.2 shows the common vertebral shapes in the cervical, thoracic and lumbar spine. A typical vertebra can be divided in two basic regions: a vertebral body (VB), which is the weight bearing part of the bone, and a vertebral arch anchored posteriorly where a number of processes arise for muscle and ligament attachment and for articulation with the adjacent vertebrae. The bone in both regions is composed of an outer cortical shell that is thin on the superior and anterior surfaces of the VB and thicker in the vertebral arch and the processes. The functional anatomy of each region is detailed for the LS in Section 2.2. Together, these parts form the *vertebral canal* or *foramen*, i.e. the central opening that encloses and protects the spinal cord. The foramen is the main pathway of the nervous system for information and extends from the brainstem to the lumbar region.

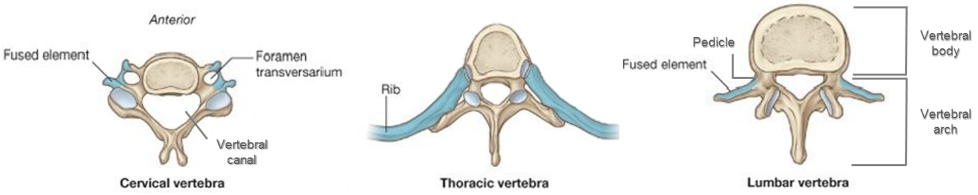

Figure 2.2: Superior view of common vertebral shapes in the cervical, thoracic and lumbar spine (adapted from [29]).

2.1.3 Shape

In the womb and as a newborn infant, the human spine is concave anteriorly forming one primary (P) C-shaped curve from the cervical down to the lumbosacral region [30], and another one through the pelvis anterior inclination known as kyphoses (Fig. 2.3A). As the infant begins to lift their head from the prone position (about 3 to 4 months after birth), cervical muscles gain strength forcing the formation of a secondary (S) antagonistic curve with a concave posterior shape, i.e. the cervical lordosis, between T2 and T12. The cervical lordosis is further accentuated by the age of 9 months when the infant gradually sits upright and stabilizes their head. When he or she begins walking upright (between 9 and 18 months after birth), the abdominal wall muscles are toned and the centre of gravity is shifted into a vertical line. To sustain the body in an erect position, the erector spinae muscle (extensor group of the human back) pulls the LS creating the lumbar lordosis, the second posteriorly concave curvature that extends from T12 to the L5/S1 IVD. The greatest portion of the curve is at the lower LS. Generally, the lumbar lordosis is more prominent than the cervical lordosis.

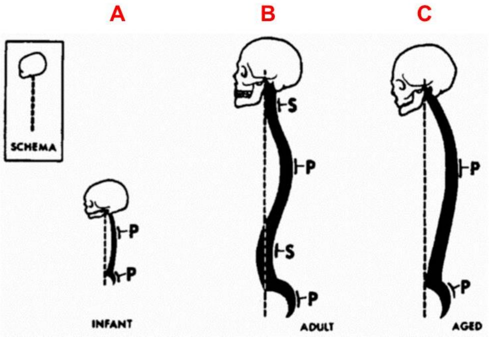

Figure 2.3: Evolution of primary (P) and secondary (S) curvatures of the vertebral column from (A) infants to (B) adult, and (C) aged subjects (adapted from [30]).

Eventually, a natural sinusoidal shape is seen in the sagittal plane in adult spines consisting of two kyphoses and two lordoses (Fig. 2.3B). The spine curves, along with the IVDs and VBs, act to dissipate the increased loads that would occur during daily activities in case of a straight spine [31]. Previous measurements revealed that the spine shape is adapted depending on the posture in order to maintain the balance of the trunk. The lumbar lordosis and the thoracic kyphosis are increased when passing from supine to standing position [32]. In standing, De Carvalho et al. reported that the lumbar lordosis is greater than in sitted position [33]. During forward flexion, Black *et al.* found that the increase of the cervical lordosis compensates the decrease of the lumbar lordosis [34]. Interestingly, aged adult spines may show an increased kyphosis angle (Fig. 2.3C) that may simply cause pain or even cause multiple MSL and neuromuscular impairments in the case of hyperkyphosis [35].

2.1.4 Spinal innervation

The spine is associated with a variety of nerves, the central focus of which belongs in the peripheral nervous system (PNS). The PNS communicates the central nervous system (CNS), i.e. the brain and spinal cord, to the rest of the body through the spinal and cranial nerves. The spinal nerves are attached to the spinal cord by a posterior and an anterior root and have a mixed sensory and motor aspect.

Peripherally, i.e. outside the spine, each spinal nerve branches into a dorsal (posterior) and a ventral (anterior) ramus (Fig. 2.4). The dorsal ramus innervates the intrinsic muscles, such as the multifidus and erector spinae, and the adjacent skin of the back and across the iliac crest. Divisions of its medial branch supply also the zygapophysial joints (Z joints) of the vertebra that are discussed in Section 2.2.1.3. Nerves arising from the ventral ramus are much larger, like the sciatic nerve, and innervate the remaining anterior parts of the trunk and the upper and lower limbs, e.g. the diaphragm, abdominal and limb muscles. Spinal innervation can be affected in cases of IVD herniation or bone-loss pathologies, such as osteoporosis, which narrow the size of the foramen where the nerves branch off of the spinal canal.

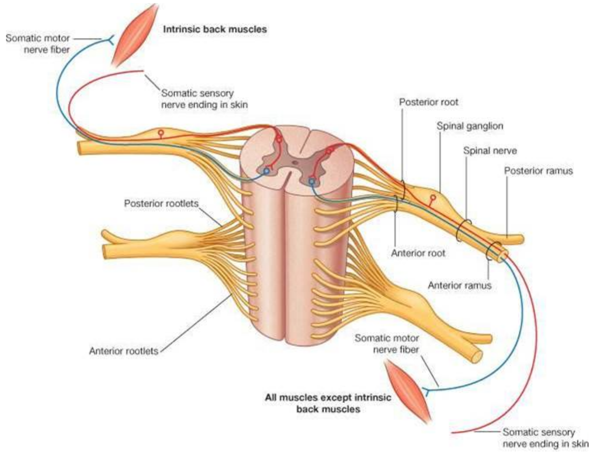

Figure 2.4: Spinal nerve organization (adapted from [29]).

2.2 The lumbar back

This section focuses on the functional anatomy of the bony, ligamentous, cartilaginous, and muscular elements related to the lumbar part of the spine. The objective of this introduction is to familiarize the reader with the terminology and specific anatomy of the LS for a better understanding of the numerical analyses presented in the following chapters of this thesis.

2.2.1 Vertebrae

The lumbar vertebrae are the largest segments of the human spine and are named L1 to L5 starting at the top. They form the skeletal support for the posterior abdominal wall and help sustain the body weight (BW) and allow movement. The lumbar vertebrae are kidney-shaped and are distinguished from vertebrae in other regions by the lack of articulating facets with the ribs (thoracic vertebrae) and the absence of the foramen transversarium in the transverse process (cervical vertebrae) (Fig. 2.2). A schematic representation of the anatomical details of a typical lumbar vertebra is shown in Fig. 2.5.

2.2.1.1 Vertebral body

The VB is a box-shaped block of bone surrounded by an outer shell of solid, cortical bone. It is flattened or slightly concave at the top and bottom, concave posteriorly and constricted in front and at the sides [29]. Its core comprises the trabecular (or spongy) bone that endows the VB with weight-bearing thanks to the capacity of the network of trabeculae struts to sustain both the vertical and shear loads felt by the vertebrae (Fig. 2.6). As such, VB are optimally designed with the least amount of bone mass to provide the greatest amount of strength [36]. The cavities between the trabeculae can be used as channels for nerves and blood supply towards the bone margins and at the cranial and caudal end of IVDs. In some cases, they are also a convenient site for the production of blood cells [37]. From a geometrical standpoint, Masharawi *et al.* [38] found that VB at L4 and L5 were successively wider and posteriorly wedged, i.e. taller anteriorly than behind, while the reverse was true at L1 and L2. L3 VB measurements revealed non-wedged geometries. According to Pal *et al.* [39], the VB and the IVD constitute the anterior column for weight transmission in the lower thoracic and lumbar regions, while the successive articulations of laminae define the posterior spine.

The cranial and caudal aspects of the VB named *vertebral* or *bony endplates* (BEP), are vascularized osseous layers located between the VB and the cartilaginous layer (*cartilage endplates*, CEP) adjacent to the IVD. Together they form the *endplate*, a

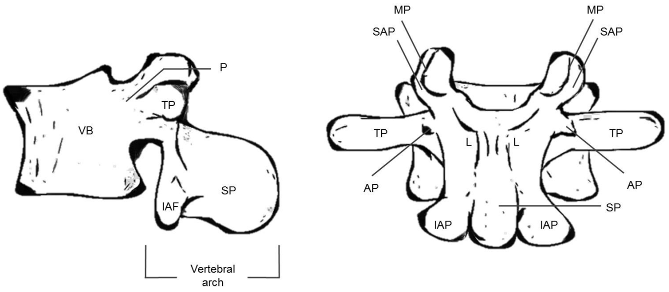

Figure 2.5: Left lateral and posterior view of a typical lumbar vertebra and its anatomic details: AP=accessory process; IAF=inferior articular facet; IAP=inferior articular process; L=lamina; MP=mamillary process; P=pedicle; SAP=superior articular process; SP=spinous process; TP=transverse process; VB=vertebral body.

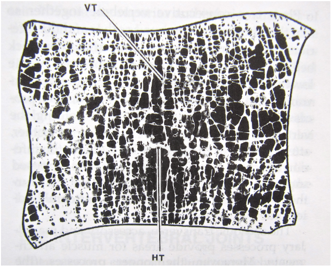

Figure 2.6: Sagittal section of a lumbar VB. Vertical (VT) and horizontal (HT) trabeculae are shown (adapted from [37]).

thin osseochondral structure that is fundamental for the regulation of cell metabolism in the IVD [40]. *The endplate acts as a mechanical interface between stiff bone and resilient disc by preventing the penetration of the nucleus pulposus into the VB.* Actually, the capillaries of the VB penetrate the permeable BEP and ensure the delivery of nutrients (glucose, oxygen) to the avascular IVD tissues through the CEP by diffusive transport [41]. The lumbar BEP is fairly flat, relatively weak and thin in the central region but stronger postero-laterally [42] according to the local resistance to the mechanical loads transmitted by the anulus fibres. Previous morphological measurements reported that endplates become more elliptical shape from L1 to L5, and both their depth and areas tend to increase caudally up to L4/L5 level and decrease at L5/S1 [43]. Davis [44] and Pal *et al.* ([45]) observed a similar reduction of the VB surface area from L4 to L5. A priori, the lumbosacral level is expected to sustain most of the upper compressive loads and a decrease in VB transversal cross sections would compromise the axial load resistance. Nevertheless, the reduced surface of the

L5 body seems to be compensated by the presence of strong pedicles and increased articular facet area at L5/S1 level [45]. Clearly, the functional shape of the posterior and anterior VB, together with the spine curvature and the muscles are important elements for the load transfers to the spine.

2.2.1.2 Vertebral arch

The posterior elements of the vertebra are the pedicles and the laminae that form the vertebral or neural arch, and the processes (Fig. 2.5). The irregular geometric form of the vertebral arch is a natural adaptation of the vertebrae to receive forces in different directions. Actually, the role of the pedicles, i.e. the pair of bone elements that connect the VB with the vertebral arch, is to transmit tension and bending forces anteriorly. The pedicles are more compact and thicker in regions with more motion, for instance in the upper lumbar regions compared to the almost immobile pedicles in the thoracic spine. A pair of skew bony plates, the laminae, arise from each pedicle and progress towards the midline where they fuse. Previous studies on the trajectory architecture of the trabeculae in the lumbar VB showed that, in the transverse plane the trabeculae bundles run to reinforce the bone from the VB towards the laminae and TP as shown in Fig. (2.7) [39].

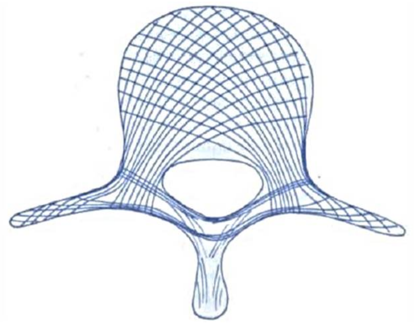

Figure 2.7: Transverse section of a lumbar vertebrae showing the pattern of trabeculation along the lines of greatest stress (adapted from [37]).

The junction of the two laminae in the midline forms the SP, while at the lateral fusion of each lamina and pedicle start the TP, a pair of long flattened bony bars. At the root of each TP, i.e. from the junction of the lamina and pedicle, rise the AP that extend upwards and downwards forming the superior (SAP) and inferior (IAP) articular processes, respectively (Fig. 2.5). The AP possess a hyaline cartilage-lined articular surface, the *articular facet cartilage* or *facet*. Particularly in the lumbar region, facets have a sagittal orientation facing posteromedially (superior, SAF) or anteromedially (inferior, IAF) that defines their biomechanical function accordingly. This cartilage layer on the facet surfaces is a low-friction interface that, along with a fibrous articular capsule that surrounds the facet, facilitate the motion and give stability to the healthy spine. The processes provide areas for muscle and ligament attachments. The TP are generally thin and long except for the TP at L5, where they are thicker and cone-shaped for the attachment of the iliolumbar ligaments joining the L5 vertebra with the ilium [29]. The TP and SP act also as levers for the attached muscles, e.g. longissimus thoracis (lumbar fibers) or back extensors like multifidus, respectively. It has been suggested that at L5/S1, about 23% of the total weight is borne by the posterior elements [45] and is then transmitted to the VB through the pedicles and the laminae. In case of injured laminae or after laminectomy surgery, such load transfer to the anterior column would be compromised resulting probably to excessive strain on the posterior elements. When humans are sitting erect, or standing in a slightly flexed posture, the loads transmitted per motion segment[1] (Fig. 2.8) move the IAF that is pressed against the SAF of the adjacent vertebra forming two synovial joints, named *zygapophysial*, *facet* or simply *Z joints* in order to support the spine. The articular facets are not designed to support or transmit axial compressive loads. However, previous experimental studies found that in a range between 3 and 25%, facet joints resist about 16% of the compressive forces in erect standing position (slight extension) [46]. A third joint formed between the vertebral bodies, i.e. an intervertebral symphysis, is the main weight-bearing joint that transfers most of this axial load to the vertebra through the IVD. It can be concluded thus that multiplanar motion of the spine strongly depends on this three-point support (Fig. 2.8).

---

[1] Also called functional spinal unit, is the smallest part of the spine representing all the main biomechanical features. It consists of two consecutive lumbar vertebra with its posterior elements and facets, the IVD between and the surrounding ligaments, without muscles.

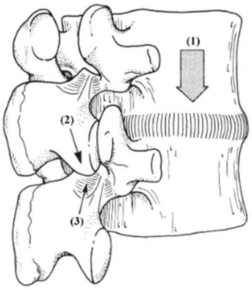

Figure 2.8: Load transmission in a motion segment through the interbody joint (1) and the Z joints (2,3) (adapted from [37]).

2.2.1.3 Zygapophysial joints

The functional role of the lumbar facets involves preventing excessive bending and translation between adjacent vertebrae. The ability of the facets to achieve this depends on their particular morphology that governs the magnitude and direction of the load transmission. In the transverse plane, the facet curvature varies by spinal level and also between subjects from almost planar, i.e. flat, to different curvatures. According to Horwitz and Smith [47], the facets tend to have a flat, planar surface in the lower LS, while at L2/L3 and L3/L4 levels they are more likely to be curved. Their orientation defined as the angle made by the plane of the joint with respect to the sagittal plane, ranges from parallel to vertical [37]. The lumbar facets receive innervation from the medial branch of the dorsal ramus not only at the level of the joint but also the adjacent superior and inferior levels [48]. This multilevel innervation is suggested to explain why the feeling of LBP from a Z joint is described clinically as referring to regions innervated by higher lumbar segments [49]. In the case of narrowed intervertebral space, i.e. in patients with decreased height of one or more IVD, there is an increased pressure applied on the facet surfaces that grows further in postures involving extension of the lumbar region. Therefore, there is a strong interaction between facet joints and the IVD in order to control the functional biomechanics of the spine.

2.2.2 Intervertebral discs

The IVD is an organ that lays between two adjacent VBs and articulates the anterior spine. It is the largest avascular structure in the human body with the lowest concentration of nutrients (e.g. oxygen, glucose) and the highest concentration of metabolic wastes (e.g. lactic acid) in its center [50]. Nonetheless, the oxygen concentration at the interface with the VBs is around 50% thanks to the nutrient pathway via capillaries in the endplates, the latter being the major path of nutrient supply and waste product elimination.

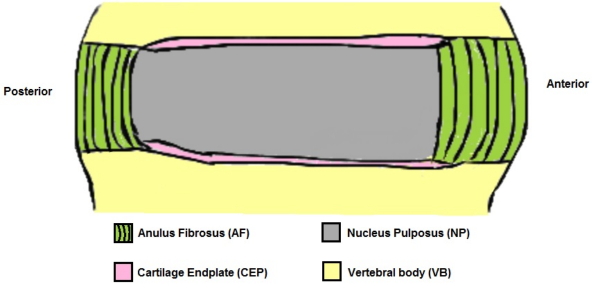

Figure 2.9: Schematic representation of the anatomy of the IVD and its components (sagittal cut).

Biomechanically, each IVD is considered to be fully functional when it fulfills the following roles: (i) load transmission from one vertebra to the other without collapsing, (ii) spine mobility without being injured, and 3) accommodation of the rocking movements of the vertebrae through its deformation without compromising its strength. IVDs are made of three major tissues (Fig. 2.9): a central *nucleus pulposus* (NP), surrounded by a peripheral *anulus fibrosus*[2] (AF), and two *cartilage endplates* (CEP) that cover the top and bottom ends.

Like other cartilagenous structures, the disc is mainly composed of water, collagen fibers (mainly type I and II), proteoglycans, and of cells distributed throughout the collagen-proteoglycan matrix. Despite a low cell density in comparison to other human tissues, disc cells (primarily chrondrocytes and fibroblasts) play a vital role in the production and break down of the matrix components. Once synthesized inside the cell, the proteoglycan molecules bind to the collagen, and the negative

---

[2] Often spelled also as *annulus*, despite the word derivation from the Latin *anus* meaning *ring*.

charges of these molecules (carboxylic (COO^-), sulphate (SO_4^{2-})) attract the mobile positive ions of the interstitial fluid leading to disc swelling pressure [37]. The IVD is an osmotic system that is sensitive to mechanical load and to tissue condition [51]. When the IVD is healthy, loading of the spine leads to an outflow of fluid from the disc that increases the swelling pressure and results in disc height loss. As long as the fluid flow is controlled, the deformability of the disc is sufficient to offer the required spine flexibility while the hydrostatic pressure in the center (Fig. 2.10A) supports the weight-bearing capacity of the disc [52]. In rapid unloading of the spine, the IVD height increases to return to its former state. In prolonged loading however, because of the viscoelastic behavior of the disc, its height decreases further, while the swelling pressure increases.

2.2.2.1 Nucleus Pulposus

The NP forms 25-50% of the disc transversal area. Its rather posterior than central location in the lumbar IVD may be considered as an optimal structural adaptation to sustain compressive stresses. The NP is a semi-fluid mass of mucoid material with a high swelling capacity that reaches maximum hydration in adults between the age of 20 and 30 years [53]. Its primary function is to redistribute external loads by exerting pressure in all directions thanks to its fluid nature (Fig. 2.10A). Hence, its mechanical communication with the AF is really important. In normal conditions, apart from water (70-90%), proteoglycans account for 65% of the dry weight of NP, and collagen II represents 15-20% of the dry weight [31]. Such tissue organization attributes high hydrostatic pressure in the disc that is particularly beneficial for weight-bearing [54] and also provides viscoelasticity acting as a shock absorber, as discussed previously. During daily activities, the NP can change its position and shape depending on the external loads [55]. It has been reported that when the body leans forward to a flexed posture, the NP moves posteriorly [56] and the IDP increases in relation to its value in erect standing position [57]. MRI [58] and ultrasound [59] techniques have highlighted the importance of frequent diurnal variation of activities in order to regain the IVD height. Moreover, previous *in vivo* studies reported that in lying position, after 7-8 hours of sleep, the IDP has increased approximately by 240% [60] and the body has restored its total height [59]. Interestingly though, prolonged rest has been shown to lead to disc dehydration after 5 weeks of continuous bed rest [61] and to selective back muscle atrophy after 60 days [62].

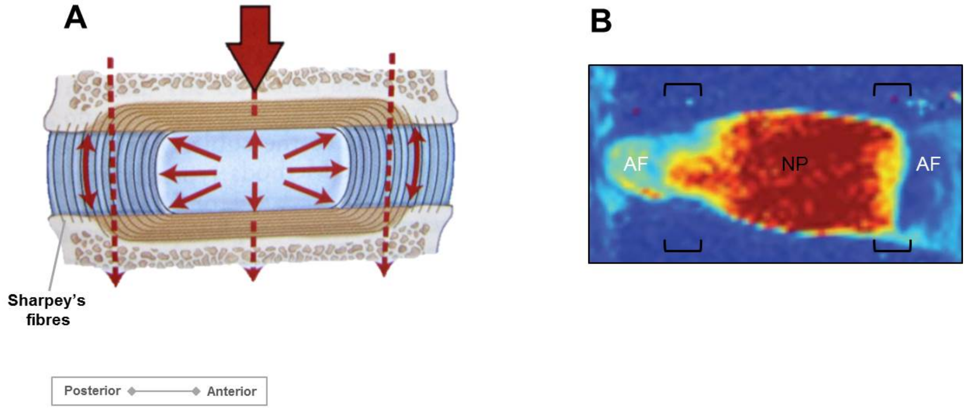

Figure 2.10: (A) Action of the hydrostatic pressure of the NP on the AF and stress transmission to the adjacent vertebrae through the CEP (adapted from [63]), (B) Quantitative T2*MRI mapping of a L4/L5 IVD showing the AF, NP and transition zone (adapted from [64]).

2.2.2.2 Anulus fibrosus

Embryologically, the determination of the AF region is highly associated to the NP formation. The latter develops from the notochord whose cells are progressively replaced by fibrocartilage over time. When the outer NP blends with the inner AF layer [31], a determination of a clear boundary between the two regions is difficult. Rather, a transition zone (Fig. 2.10B) with a nearly fibrocartilage composition has been imaged [64] followed by a radial composition gradient towards different layers of the AF [65]. The consideration of a transition zone with homogenized material parameters has been also numerically suggested to address the fluid flow oscillations otherwise seen in fast loading of the IVD due to such material discontinuity [66] (discussed in 2.5.3). From a biochemical standpoint, the AF has a high concentration of collagen I and II (50-60% of its dry weight) [31] and low content of proteoglycans (20% of its dry weight). Cells of the outer AF receive their nutrients directly from capillaries in the surrounding soft tissues. This can explain why in case of injury (e.g. IVD tears), the outer AF heals or scars in comparison to the inner AF or NP regions that do not.

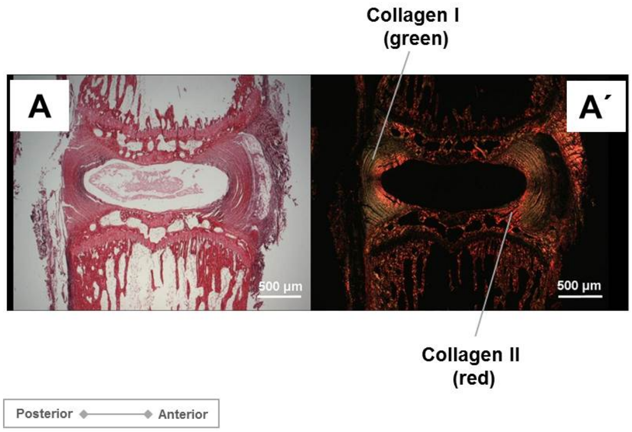

Figure 2.11: Histology and polarizing microscopy images showing the collagen type and fiber orientation in the IVD (adapted from [67]).

Collagen fibers are arranged in concentric layers (lamellae) that peripherally surround the NP. Collagen type I is stiffer than type II and is largely concentrated in the outer AF [68] (Fig. 2.11) whose thin posterior portion creates IVD structural weakness. Indeed, the presence of the posterior longitudinal ligament (PLL) that penetrates the outer AF layer and blends with the collagen fibers posteriorly is suggested to further attribute to the disc resilience. Collagen type II is found in higher concentration towards the center of the disc as shown in Fig. 2.11. Type I fiber orientation in all lamellae is between $65-70°$ to the vertical axis [37], while between adjacent lamellae, a criss-cross pattern is present. Biomechanically, such organization makes the AF be functionally adapted to withstand any type of shear deformations. In the outer region, some lamellae extend directly to the vertebrae via Sharpey's fibers (Fig. 2.10A), while the inner fibers (about 2/3 of AF) are anchored to the CEP [31]. Therefore, in healthy conditions, by totally enclosing the NP, the AF fibers resist the lateral pressure exerted by the NP and assist the load-bearing capacity of the IVD.

2.2.2.3 Cartilage endplate

The CEP is a cartilaginous layer at the BEP/IVD junction with a heterogeneous composition similar to that in articular cartilage; proteoglycans account for 20% (mean value) and water for 55% [40] of its dry weight. It owes its fibrocartilage nature to the collagen fibers of the inner AF that, as discussed before, insert into the endplate and run parallel to the plane that separates the CEP and the NP, forming more or less a capsule around the NP [37] (Fig. 2.10A). Because of these fibrous attachments, the CEP is strongly bound to the IVD but not the VB bone. As such, it is susceptible to mechanical failure. Actually, previous numerical [69] and autopsy [70] studies confirm that the endplate first becomes separated from the subjacent bone and then herniated from the IVD. Yet, its role on the mechanical function of the spine remains unclear. In fact, its mechanical characterization has been only recently studied experimentally [71]. CEP poromechanics has been suggested to control the fluid exchanges between the IVD and the vertebrae in a direction-depended way and are, thus, responsible to ensure that all the fluid expelled during loading is recovered during rest states ([72], [73]). The fact that the CEP assumes an essential gateway for nutrient transport into the inner region of the IVD correlates well with the measurements of thinner CEP and BEP at the centre [40] as well as the higher porosity reported for the BEP in the region [74].

2.2.3 Ligaments

The ligaments, together with the muscles and tendons, are the elements that reinforce and support the joints between the vertebrae during rest and activity. Importantly, they help to prevent injuries of the spine due to excessive motions, such as hyperextension and hyperflexion. From a topographic point of view, the lumbar ligaments can be classified into four groups; the ventral or anterior ligaments that interconnect the VB, the dorsal or posterior connecting the bony posterior elements, the iliolumbar ligament, and the minor ligaments, such as the intertransverse ligament, that connect two distinct points of the same VB.

The ventral group comprise the anterior (ALL) and posterior (PLL) longitudinal ligaments. Both ALL and PLL have polysegmental disposition throughout the spine and are richly innervated which makes them highly sensitive to pain [49]. Since they are mainly composed by collagen fibers, they have high tensile strength, and their viscoelastic behavior acts synergistically with the creep behavior of the IVD tissues discussed before. The dorsal ligaments in an antero-posterior order of location are the ligamentum flavum (LF), the capsular (CL), the supraspinous (SSL) and the interspinous (ISL) ligaments. As reported by Bogduk [37], these ligaments form a continuous network and their primary function is to resist externally applied flexion of the spine [46].

The existence of Iliolumbar ligament (ILL) has been controversial among previous studies; it has been reported to be present by 11.5 weeks of gestation in the study of [75], whereas Luk *et al.* [76] suggested that it is muscular at birth and not a fully developed ligament until the third decade of life. The anatomy and morphology of the ligament has been also reported in many articles with considerable discrepancy ([76], [75], [77], [78], [37], [79]). As a whole, the ligament is a strong bond between the L5 vertebra and the ilium functioning to stabilize the L5/S1 junction and to prevent forward sliding of L5 [37]. Aihara *et al.* [80] concluded that its short posterior portion is associated to great disc degeneration at L4/L5 level with the L5/S1 disc being protected. The ILL also limits flexion, extension, lateral bending and axial rotation of the last lumbar vertebra [81]. The intertransverse ligament (ITL) comprises sheets of connective tissue extending from the upper edge of one TP to the lower edge of the TP above without specific lateral borders. A previous numerical study showed that, under rotation, ITL removal had very limited effect on the ROM of a L3-L5 osteoligamentous configuration, but it was suggested to play a role in the load distribution to the spine tissues [82].

2.2.4 Muscle anatomy and physical properties

Muscles are another important structure of the back thanks to their multiple role in the normal functioning of the spine. They are voluntarily controlled and belong to the skeletal type, i.e. elements attached to the skeleton via tendons. Apart from their ability to create a variety of spinal movements, several of the back muscles also serve to maintain posture [83] and to disperse the externally applied loads with the purpose of protecting the spine [84]. Hence, since the mechanical behavior of the muscle-tendon unit is highly determined by the muscle architecture, a thorough understanding of the anatomy and function of skeletal muscles is fundamental. The following sections describe the physiology and structural arrangement of these muscles and their effect on force and/or rate of contraction via the force-length, force-velocity and activation relationships.

2.2.4.1 Anatomy

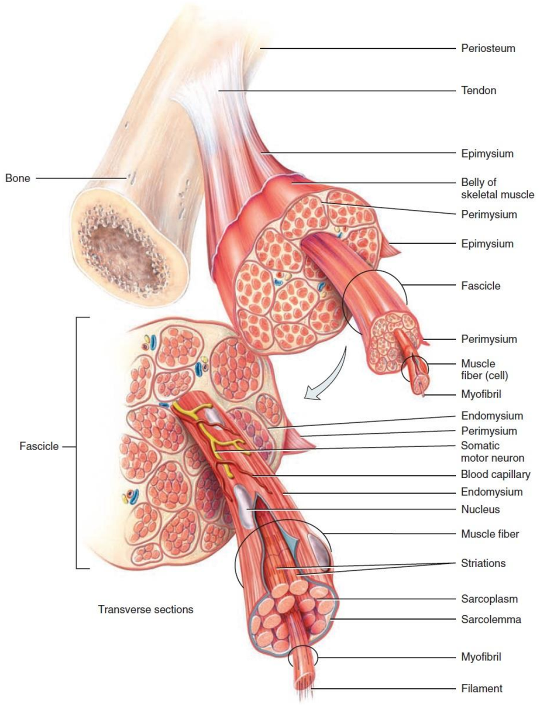

Figure 2.12: Structural hierarchy of skeletal muscle from muscle to myofilaments.

Muscles are separated by the *fascia*, a band of connective tissue that surrounds and stabilizes the muscles and other internal organs. Interiorly, each muscle is covered by another connective sheath, the *epimysium*, which in its turn encloses the *perimysium*, a layer of collagenous connective tissue that surrounds the *fascicles*. The latter are bundles of *muscle fibers* (also called *myocytes*) bound together via the *endomysium* tissue that provides pathways for the passage of blood vessels and nerves. The fibers are long and cylindrical, multi-nucleated cells that are the smallest contractile units of the skeletal muscles. They develop from a fusion of precursor cells known as myoblasts in the process of myogenesis, and they run parallel to each other within a muscle. Like other cells, fibers have a cytoplasm, called *sarcoplasm*, which is filled with significant amounts of glycogen and myoglobin, and mitochondria between parallel bundles of *myofibrils*.

The myofibrils attach to the *sarcolemma*, the plasma membrane that is the site of action potential conduction, and they are surrounded by the *sarcoplasmic reticulum* that serves to store the calcium ions needed to cause a muscle contraction. They are composed of long proteins, such as actin, myosin, and titin. These proteins are organized in filaments that repeat along the length of the myofibril and form the units known as *sarcomeres* attributing the characteristic striated appearance to the muscle. The sliding between the myofilaments to form cross-bridges is the essential mechanism of muscle contraction.

2.2.4.2 Cross-bridge theory

The consecutive articles of H.E.Huxley and Hanson [85] and A.F.Huxley and Niedergerke [86] introduced the idea that muscle shortening during contraction of striated muscles is probably caused by the sliding between actin (thin filament) and myosin (thick filament), named the *sliding filament theory*. The hypothesis proposed that the sliding happens using the energy produced by the hydrolysis of adenosine triphosphate molecules (ATP). This chemical process causes a sequential formation of cross-bridges, i.e. independent force generators, such that the whole muscle fiber shortens and the muscle contracts. The mechanism was published in 1957 as the *cross-bridge theory* [87], and the dynamic nature of this interaction was proved in a later study [88].

Fig. 2.13 outlines the stages of the often called *cross-bridge cycle*: (A) A molecule of ATP binds to the back of the myosin head causing a conformation which cannot bind actin, (B) The head is displaced along the filament about $5nm$ as ATP hydrolysis occurs. At this stage the adenosine diphosphate (ADP) and inorganic phosphate (Pi) produced remain bound to the myosin, (C) When the Pi is released, the head binds tightly to the actin. The actin binding sites are uncovered by the release of calcium ions from the sarcoplasmic reticulum, (D) The release of Pi triggers the *power stroke*, i.e. the force generating change in shape during which the head loses

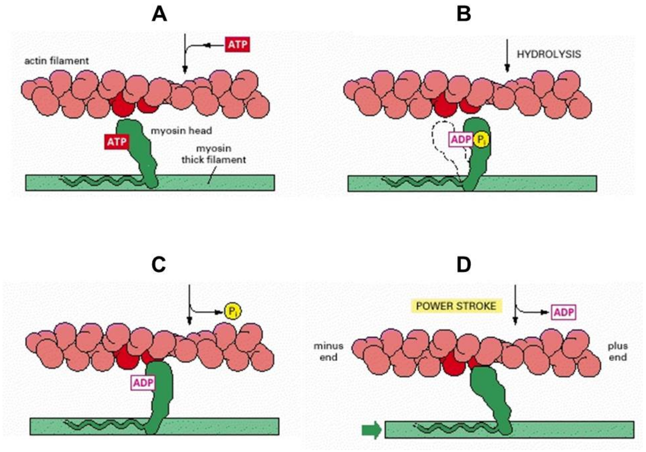

Figure 2.13: The cross-bridge cycle (adapted from [89]).

its bound ADP and moves to a new position on the actin filament (*rigor mortis*) to start a new cycle.

2.2.4.3 Fiber types and arrangement

The fiber properties play an important role in muscle contraction basically because of the different metabolic pathways through which fibers can generate ATP, and because their type determines the rate of energy release that dictates the velocity of contraction [90]. Given the substantial role of ATP for the cross-bridge cycle described before, histochemical staining for myosin ATPase activity is a common method to differentiate fibers. Accordingly, the types found in human are the following:

- type I (SO)[3], which are mainly characterized by slow contraction time (or twitch, ST), high resistance to fatigue (endurance) and oxidative (aerobic) capacity, but low force production because of their relatively small diameter (cross-section).
- type II (FT) can be broken down into two types: type IIA (FOG), with fast contraction time, intermediate resistance to fatigue (endurance), intermediate-high oxidative (aerobic) and glycolytic (anaerobic) capacity and high force

---

[3] S=Slow; F=Fast; T=Twitch; O=Oxidative; G=Glycolitic.

production; type IIX (FG), very fast contraction time, high glycolytic capacity that is advantageous for anaerobic activities, generally larger diameter and thus higher force production but only for short periods (low endurance) because of their low oxidative (aerobic) capacity.

Some additional differentiation types have been also reported, such as IIB and IIC [90], but they are either rare, or there is no consensus on whether they are also expressed in humans besides other mammals ([91], [92]). Although a motor unit, i.e. a group of muscle fibers innervated by the same single motor neuron, comprises one type of fibers, most muscles consist of a mixture of ST and FT.

The fiber physical arrangement at the macroscopic level is part of the muscle's architecture and is another influencing factor for the mechanical function of the muscle. Among the numerous ways of muscle fiber arrangement, there are three general types of fiber architecture defined based on the angle between their longitudinal direction and the force-generating axis (*pennation angle, a*) :

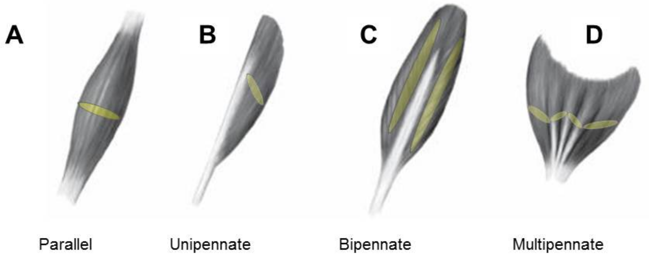

Figure 2.14: General types of muscle fiber arrangements and corresponding physiologic cross-sectional areas. (A) Parallel, (B) Unipennate, (C) Bipennate, (D) Multipennate (adapted from [93]).

- Muscles composed of fibers that extend parallel to the force-generating axis of the whole muscle-tendon complex are called *parallel* arranged (Fig. 2.14A). Previous experimental studies in mammalian muscles reported that these fibers do not extend the entire length of a muscle or probably not even that of a fascicle ([94], [95]). Examples of parallel arranged muscles are the rectus abdominis, psoas major and biceps muscles.

- Muscles composed of fibers at a single pennation angle relative to the axis of force generation (varying from about 0° to 30° in mammals [96]) inserting all on the same side of a central tendon, such as the extensor digitorum longus muscle of the leg, are called *unipennate* arranged (Fig. 2.14B).
- Muscles composed of fibers at two or several pennation angles are called *bipennate* (Fig. 2.14C), or *multipennate* (Fig. 2.14D) arranged, respectively. Multipennate muscles, such as the deltoid and gluteus, form the most general category to which most muscles belong.

Between two muscles with the same volume but different architecture, parallel fiber arrangement involves longer but less muscle fibers (in number) and has a smaller cross-sectional area (CSA) than a pennate muscle. As such, force transmission to the tendon is 100% efficient compared to pennate muscles, where the force is distributed also to the fiber direction and therefore the force magnitude depends on the pennation angle. Nonetheless, a pennate is stronger than a parallel since the maximum isometric force (tetanic, T_0) a muscle can exert depends on its *physiologic cross-sectional area* (PCSA), i.e. the area of the cross-section of the muscle perpendicular to its fibers[4], that is greater in pennate muscles. The effect of the muscle architectural parameters together with its physical properties are discussed in the following sections through the definition of the force-length, velocity and activation relationships.

2.2.4.4 Force-length relationship

The *force-length* (f-l) curve is the most prominent and important physical property of skeletal muscle function. It relates the maximal force of a muscle (or fiber or sarcomere) measured during isometric contractions[5] and maximal muscle activation to its length. Over a century ago, Blix [98] first demonstrated experimentally that isometric force on frog striated muscles increased with increasing lengths, reached a plateau, and then decreased. Such force generation was suggested to be based

---

[4] Based on [97], PCSA is commonly calculated and defined as the ratio between the muscle volume and the fiber length.

[5] Muscle (or fiber or sarcomere) contraction that occurs with no change in muscle length.

on the shortening of the myofilaments. Several decades later, Gordon *et al.* [99] published the results of a classical study on isolated frog muscle fibers that for the first time suggested a dependence of the active force production on the known cross-bridge theory. Among the assumptions of this theory were the uniform distribution of the cross-bridges along the thick filaments (i.e. myosin), and the capacity of each cross bridge to exert on average the same amount of force as any other cross-bridge. Considering the previous hypotheses together with the limited attachment range of the cross-bridges due to their small size, it was implied that the maximal isometric force of a sarcomere is linearly related to the magnitude of the overlap between the myofilaments [100].

Fig. 2.15 shows the f-l curves based on the experimental results in frog [99], and human fibers of different muscles ([101], [102]). The shift to the right in the human optimal sarcomere lengths (SLo) (plateau) compared to that of frog (2.0-2.2 μm [99]) corresponds basically to the higher actin (thin filament) lengths measured in humans. In all cases, though, it has been demonstrated that skeletal muscles generate higher forces when operating at intermediate lengths and the force remains constant in the plateau phase.

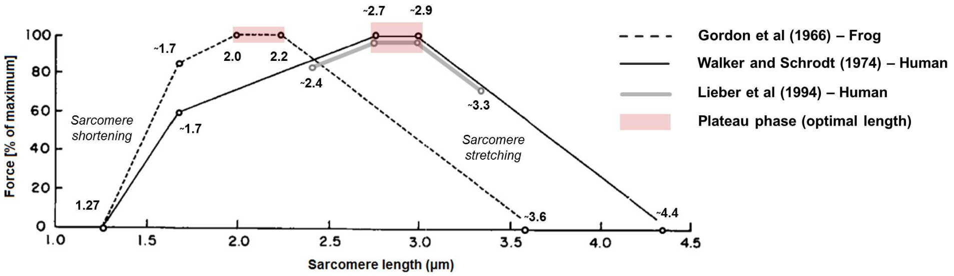

Figure 2.15: Force-length relationship of frog and human skeletal muscles based on the results of Gordon *et al.* [99], Walker and Schrodt [101], and Lieber *et al.* [102]. (Sarcomere shortening=ascending limb; Sarcomere stretching=descending limb).

The SLo results in [101], [102] were both between 2.7-2.9 μm, although the authors reported different physiological operating ranges of the sarcomeres presumably due to inter-muscular differencies. Variations have been also reported for the plateau region that probably depended on the scale of the experiment, i.e. organ or fiber level; 2.6-2.8 μm from measurements on intact muscles of the lower limbs [103], 2.37-2.95 μm on the SLo of human gastrocnemius fibers [104].

When stretched beyond the plateau, the active muscle force was found in all previously referred studies to decrease and should become zero at a sarcomere length of about 3.6 μm (frog) and 4.4 μm (human) where no overlap of the myofilaments occur. The linear relation between the active force and length reported by Gordon *et al.* [99] at the descending limb (sarcomere stretching) (Fig. 2.15, 2.16A) was questioned experimentally by several authors, such as ter Kreus *et al.* [105] who found a non-linear f-l relation (Fig. 2.16B).

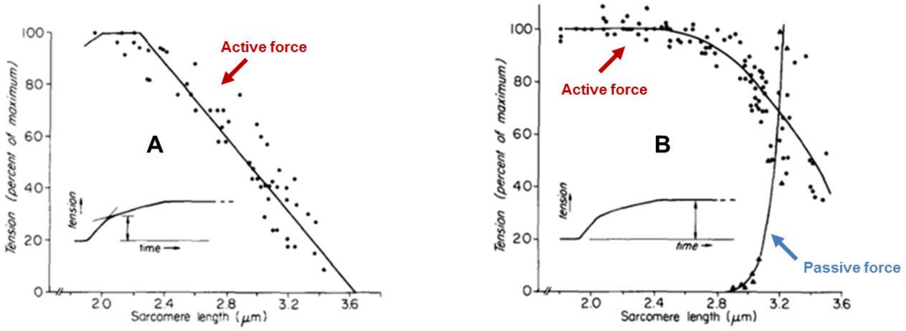

Figure 2.16: Tension-sarcomere length relationship results in frog muscles as presented by (A) Gordon *et al.* [99], (B) ter Keurs *et al.* [105] (adapted from [105]).

The main difference in the protocols used was that the study was keeping either the sarcomere (linear behavior) or the fiber (non-linear behavior) lengths constant. This latter condition appears to approach actual physiologic conditions more appropriately especially in studies at organ level since they allowed for non-uniform changes in sarcomere length.

Fig. 2.17 depicts the differences in the f-l relationship between muscles with different PCSA and different or same fiber length. Muscles with long fibers generate lower tensions than short-fibered muscles due to smaller PCSA, but they work over larger ranges of deformation (Fig. 2.17B). Thus, it can be concluded that muscles with short fibers and large PCSA are better designed for force production.

In addition to the aforementioned active f-l behavior of the muscle, the *passive force* developed without stimulation when a muscle is stretched contributes as well to the

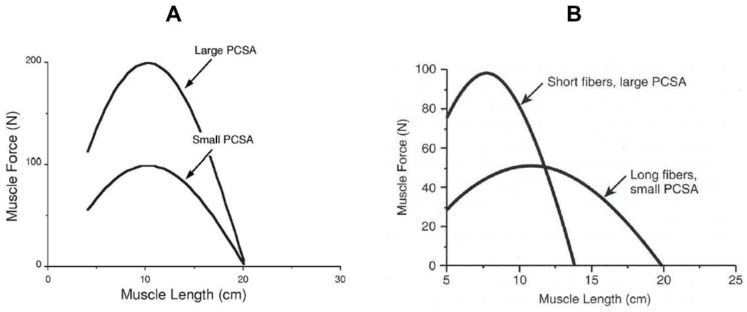

Figure 2.17: Force-length relationships of two muscles with different architecture: (A) Different PCSA but same fiber length, (B) Different PCSA and fiber length (adapted from [106], [90]).

final muscle f-l properties. Previous studies have identified the protein titin between the thick myofilaments as the source of this passive resistance ([107], [108], [109], [110]). The measurements of ter Keurs *et al.* [105] in frogs showed that passive tension was almost zero near the optimal length but increased exponentially with muscle stretch when the sarcomere length became larger than 2.8 μm (known as *passive slack length*) (Fig. 2.16B). Gollapudi *et al.* [104] reported an average passive slack length of 2.22 $\pm 0.08 \mu$m and a similar exponential increase in humans (Fig. 2.18A). Passive properties have been shown to differ also among muscle groups in humans [111]. Finally, the theoretical *total force-length relationship* is derived by the sum of both active and passive properties of the muscle and its normalized form is shown in Fig. 2.18B. In practice, active force cannot be measured directly. Nonetheless, the experimental measurements of passive and total forces directly (e.g. using servomotor length controllers, force transducers ([112], [113]), and load cells [114]), or indirectly (e.g. through elastography techniques [115]), are used to calculate the active force curve as (total force - passive force) [113].

2.2.4.5 Force-velocity relationship

Although the f-l relationship describes well a muscle's behavior under isometric conditions (i.e. constant length), several movements involve isotonic muscle contractions (i.e. constant load, muscle length changes) and therefore, the speed of muscle contraction needs also to be considered. The *force-velocity* (f-v) curve relates the rate

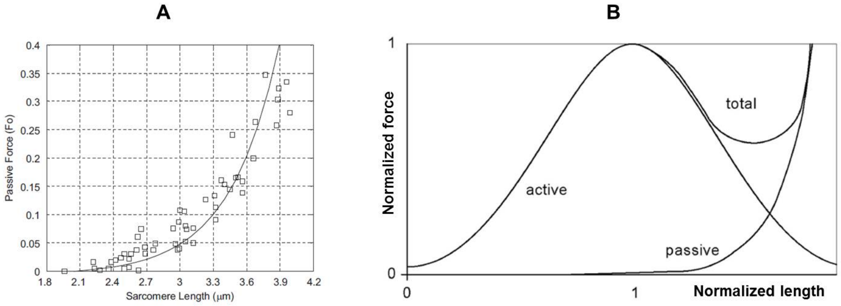

Figure 2.18: (A) Passive tension [104], (B) Active, passive and total normalized force-length relationship.

of muscle (or fiber) length change to the maximal force the muscle (or fiber) can generate. Actually, like the f-l relationship, the f-v curve is not continuous but is rather obtained by interpolating the force and velocity data measured in distinct experiments under maximal activation conditions. Its general form is shown in Fig. 2.19. Although Fenn and Marsh [116] were the first to perform experiments on f-v properties of the muscle, the classical papers of Hill [117] (later summarized in [118]) and Katz [119] on frog skeletal muscles, determined the effect of load on the speed of shortening.

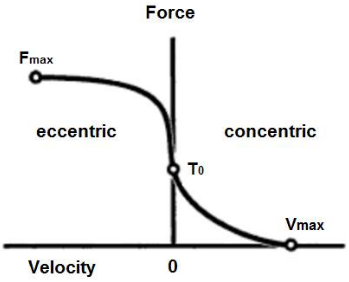

Figure 2.19: Schematic force-velocity curve of a skeletal muscle during shortening (concentric) and lengthening (eccentric) contractions (adapted from [120]).

When a muscle is maximally activated to balance an external load that is less than the maximum tetanic force (T_0) it can generate, the muscle shortens allowing a contraction known as *concentric* (Fig. 2.19). The muscle force developed is always less than T_0 and decreases as the velocity of contraction increases [117] until finally becomes zero when the velocity reaches its maximum value (ν_{max}). Huxley [87] found a good agreement comparing the normalized f-v relationship proposed by Hill with his theoretical predictions of the cross-bridge theory. The study suggested that, as the muscle shortens with increasing velocity, force decreases because of the lower number of cross-bridges attached [31]. The mathematical form proposed was a rectangular hyperbolic equation [117]:

$$(F + a) \cdot \nu = b \cdot (T_0 - F), \tag{2.1}$$

where a is a constant with units of force that depends on the PCSA of the muscle and the level of activation, b a constant in units of velocity that defines the absolute rate of energy liberation during contraction, ν the shortening velocity, F the muscle force, and T_0 the maximum tetanic force at zero velocity and optimal sarcomere length. For ν=ν_{max} the force is zero (F=0), and the velocity can be calculated as:

$$\nu_{max} = \frac{bT_0}{a} \tag{2.2}$$

where the ratio a/T_0 is approximately constant (≈ 0.25) [117].

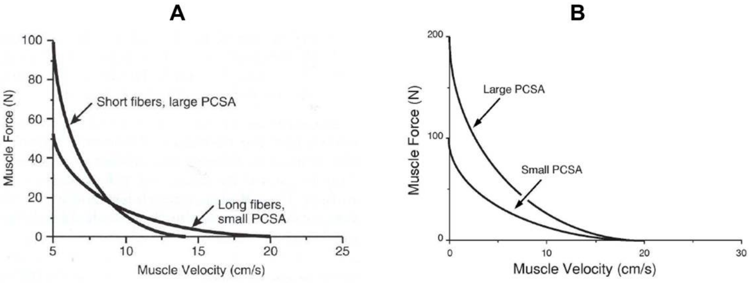

Figure 2.20: Force-velocity relationships of two muscles with different architecture: (A) Different PCSA and fiber length, (B) Different PCSA but same fiber length (adapted from [106], [90]).

Fig. 2.20 illustrates how the potential speed of contraction is influenced by the muscle architectural parameters (PCSA and fiber length). The long-fibered muscle has a much greater ν_{max} than that of the short-fibered (Fig. 2.20A), while for fibers of the same length, muscles with greater PCSA produce more force (Fig. 2.20B).

The muscle force increases in eccentric contraction (lengthening) much faster than it decreases in concentric contraction. The maximum force values range from about 1.5 to 2 times T_0 and are relatively independent of the lengthening velocity (Fig.

2.21). Nonetheless, experimental evidences demonstrate that such high force values cannot be achieved only through voluntary contractions, but require additional electrical stimulation [121]. Generally, in activities that involve cyclic contraction and relaxation (such as running or swimming), among the principal functions of locomotor muscles is to lengthen and do negative work. That is, to absorb the work supplied by its antagonists or by energy dissipation in the bones to which they are attached [122]. However, the cross-bridge theory does not successfully describe this muscle function. As such, there is a strong interest in studying the mechanics of muscle lengthening given its important role on total muscle performance.

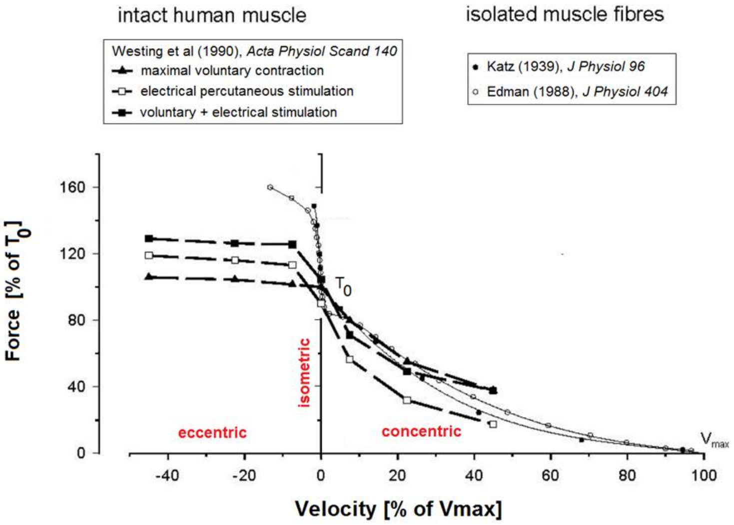

Figure 2.21: Force-velocity relationships obtained during concentric and eccentric contractions of isolated muscle fibers and during voluntary, electrical and combined stimulation of intact human muscles (adapted from [123]).

2.2.4.6 Force-activation relationship

An important mechanical characteristic of skeletal muscles that should be also taken into account is the role of the level of activation in both f-l and f-v relationships. The results derived from previous studies shown in Fig. 2.22 demonstrate that optimal fiber length increases (i) while the speed of contraction decreases [124], and (ii) with the decrease of the activation.

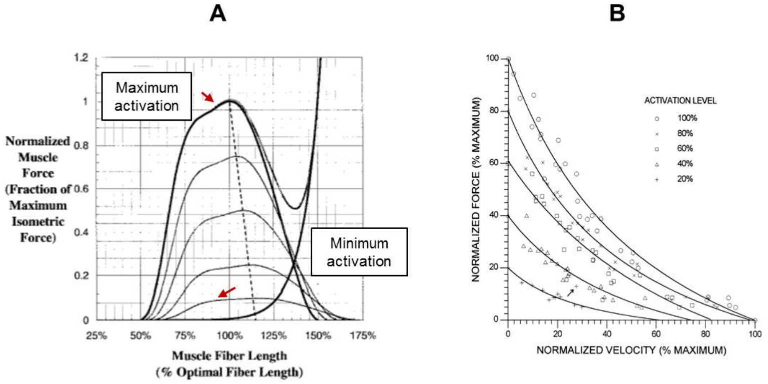

Figure 2.22: Normalized (A) force-length (adapted from [125]), and (B) force-velocity ([124]) curves for different levels of activation.

2.2.5 Back muscles

Back muscles perform individually or in coordination, as agonists (prime mover), synergists or antagonists depending on the movement. During flexion of the LS from lying (supine) position, for example, the psoas major acts as a prime mover together with the abdominal muscles At the same time, the erector spinae muscles contract synergistically to help to control the trunk motion at the fully flexed posture. Such muscle coordination, though, may vary depending on the condition of the body. That is, in case of muscle fatigue [126] or pain, the CNS will alter the muscle activity accordingly in order to produce the motion of the body.

Several approaches have been proposed for the organization of the back muscles, either based on their location around the spine, such as lateral, posterior etc, or their superficial or deeper position (extrinsic or intrinsic muscles, respectively). Bogduk [37] divided the lumbar muscles based on their position and their particular functions into three groups: (i) the psoas major, which covers the anterolateral aspects of the LS, (ii) the intertransversarii laterales and quadratus lumborum, which join the TPs anteriorly, and (iii) the back deep muscles that lie posteriorly and either attach directly or act on the LS (Fig. 2.23).

A particular focus is given on the anatomical descriptions of the psoas major and the back deep muscles (particularly the multifidus and erector spinae groups), given their major role in the mechanical stability of the LS during daily activities.

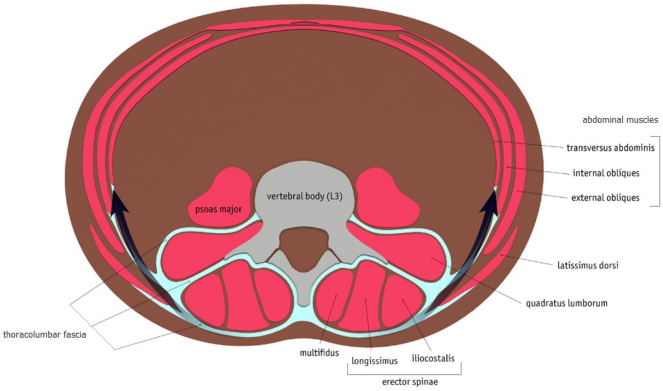

Figure 2.23: Transverse view of the spine and the major back muscles.

2.2.5.1 Psoas Major

The psoas major (PS) is the largest muscle in CSA at the lower lumbar region and its fascicles are approximately similar in length [127]. The PS is essentially considered as a muscle of the thigh [37]. Nonetheless, in absence of hip movement, such as in standing position or performing sit-ups, the muscle can act on the LS [128]. The PS fascicles arise from the anterior surfaces of the TPs, from the antero-lateral aspects of the L1 and L5 VBs, and from the rim of the IVDs with the adjacent vertebrae from T12/L1 to L4/L5. They descend along the pelvic brim, deep to the inguinal ligament, and insert via a tendon into the lesser trochanter of the femur. Such femoral insertion is common with the iliacus muscle (Fig. 2.24A), and both muscles are often referred to as one unit or as the iliopsoas ([129], [130]). The PS has important fascial connections. The medial fascia that encloses the muscle, also called *psoas fascia* (Fig. 2.24B), forms a tendinous arch over the lateral aspects of the VBs [37], allowing passage between this arch and the spine for nerves and vessels. As it surrounds the muscle, the fascia passes under the medial arcuate ligament superiorly and continues to the diaphragm. It becomes thicker caudally [131] and is continued by the iliac fascia under the inguinal ligament where both form the iliopectineal arch.

The deep location of the PS into the body does not favor *in vivo* activity registration to better explore its function. In fact, there is lack of consensus in the literature

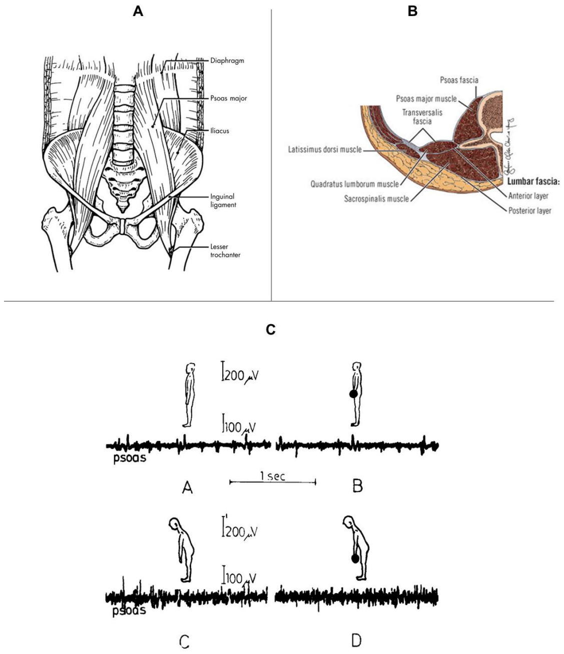

Figure 2.24: (A) Anatomy of the PS and iliacus muscles (adapted from [132]), (B) Transverse view of the back muscles and fascia (adapted from [133]), (C) EMG activity of the PS of a healthy subject in upright standing and forward flexed postures with and without load in hands (adapted from [57]).

about the PS function. Nachmeson ([57],[134]) used invasive needles at the level of the L3/L4 disc to capture the PS activity and supported the idea that, besides its role as a hip flexor, the muscle is a spine stabilizer in upright postures (sitting and standing) (Fig. 2.24C). Recently, deGroot *et al.* [135] used, for the first time so far, surface EMG electrodes placed in supine position to quantify the role of the PS in the dysfunction of the sacroiliac joint via leg raising tests. There are several hypotheses as regards the biomechanical function of the PS: dominant flexor of the hip joint ([128], [136], [137], [138], [139]); lateral flexor of the LS ([140], [138]); flexor of the LS on the pelvis ([141], [138], [84]); stabilizer of the LS ([57], [134], [142], [143], [136], [144]); stabilizer of the hip ([139], [128], [137]); controller of lumbar lordosis ([128], [37], [145]) and pelvic tilt [145], as well as power source for bipedal walking and running ([146], [147]). Insights into the PS function related to symptomatic population have emerged recently using advanced imaging techniques. A reduction of the CSA of the muscle was reported in patients with herniated discs [148] or unilateral LBP [149], while the contrary was found after prolonged bed rest [150] both for the PS and for the rectus abdominis groups.

2.2.5.2 Multifidus

The multifidus (MF) is the most medial and largest muscle of the paraspinal muscle groups spanning the lumbosacral junction [151] (Fig. 2.25A). It consists of a series of muscular and tendinous fasciculi that arise from the posterior aspect of the sacrum and superior iliac spine (SIS). Fasciculi run upwards along the spine ascending two to four vertebrae levels until they attach to a SP (MPs in the lumbar region, TPs in the thoracic region and APs in the cervical region except for the atlas) [84]. An extensive literature exists about the MF morphology, and descriptions vary in terms of number ([152], [151], [153], [143], [154]) and attachments ([155], [29], [156], [157]) of its lumbar fascicles, of fascicle orientations ([158], [159], [160]), and of its architecture ([161], [162]). Nonetheless, there is a common conclusion on the multi-segmental arrangement of the MF fascicles in distinct bands in the lumbar region where the muscle is most developed.

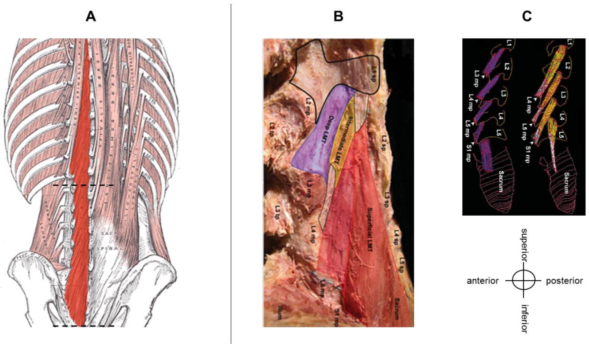

Figure 2.25: (A) Location of the MF among the back muscles (dashed lines showing the lumbosacral region of interest) (adapted from [29]), (B) Dissection and (C) three-dimensional reconstruction of the digital specimen showing the superficial (red), intermediate (yellow) and deep (blue) regions of the lumbar MF [162].

Based on the primary and widely accepted description of Macintosh *et al.* [151], the MF fascicles can be divided in five bands, i.e. one per lumbar level, and three layers; superficial, intermediate and deep (Fig. 2.25B) at all lumbar levels but L5/S1, where the absence of intermediate fascicles was confirmed [162]. The fascicles of the deep layer are the shortest. They stem from the laminae of each vertebra and insert into the MP of the vertebra two levels more caudally [37]. Some of the deepest MF fibers, for example those of the L1 laminar fascicle, attach to the facet capsule of lower levels [154], and as mentioned in 2.2.3, they reinforce the function of the CL to protect the capsule during movement [37]. At L5, the deep layer fascicles insert directly into the sacrum just above the first sacral foramen. The remaining two fascicle layers (i.e. intermediate and superficial) form the bulk of the lumbar MF and are long fascicles with oblique postero-anterior orientation. They arise from the SPs of each segmental level and radiate caudally until they attach into lower MPs, the iliac crest and the sacrum. Such fascicle disposition along with the single level innervation pattern imply that the muscle is designed to act principally on individual SPs [151] and only indirectly on any interposed vertebrae. Actually, since the long MF fascicles lie behind the lordotic curve, it has been suggested that a secondary action of the muscle is the accentuation of the lumbar lordosis [37].

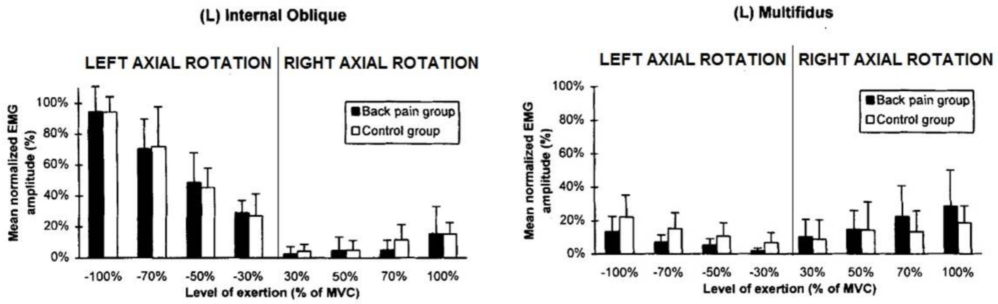

Figure 2.26: Normalized EMG amplitude of the (L)eft Internal Oblique and MF during axial rotation in back pain (black) and control (white) groups (adapted from [163]).

Macintosh *et al.* [151] and Bogduk [37] suggested that the MF is primarily a posterior sagittal rotator, i.e. an extensor of the LS. The role of the muscle in rotation is antagonistic to the flexion effect of the abdominal muscles as the latter produce rotation. Ng *et al.* [163] captured such antagonistic activity during axial rotation using EMG in healthy subjects (control group) and patients with back pain (Fig. 2.26). Lonneman *et al.* [154] interpreted the muscle function as a whole and considered the MF as a multi-functional muscle that stabilizes the LS and potentially minimizes the shear and compression loads on the facets.

2.2.5.3 Erector Spinae

The erector spinae (ES), also known as *sacrospinalis*, is a large muscular and tendinous mass that lies laterally to the MF and spans the entire length of the spine. Because of their location, the muscles that comprise the ES share the same primary functions, that is posterior sagittal rotation (i.e. extension) and lateral flexion of the spine [84]. They arise from a broad, thick tendon (also called *erector spinae aponeurosis*, ESA) that attaches to the posterior surface of the sacrum, the iliac crest, the SSL and the sacral, lumbar and lower thoracic spinous processes ([29], [164]). Posteriorly, the mass is covered by the thoracolumbar fascia, and the nuchal ligament that continues the SSL in the cervical region. Because part of the caudal fibers of the ES are continuous with the gluteus maximus, when the latter is contracted, tension is generated in the ES and in the superficial layer of the thoracolumbar fascia, in order to provide spinal stiffness [165].

Anatomically, in the upper lumbar region, the ES splits into three vertical muscle columns (Fig. 2.27): a lateral (*Iliocostalis*), an intermediate (*Longissimus*), and a medial (*Spinalis*). Each of these muscles can be further subdivided regionally depending on the general area of the spine to which they insert, i.e. lumborum, thoracis, cervicis, and capitis [84]. According to Gray [29], the lumbar portion of ES crosses the region without attachment to the lumbar vertebrae. Later studies ([166], [167], [168], [169]), however, reported that it can be considered as a common muscle consisting of two divisions; *Longissimus thoracis* medially, and *Iliocostalis lumborum* laterally, each of which has lumbar (*pars lumborum*) and thoracic (*pars thoracis*) fibres. The tendons of the ES thoracic fibers (Fig. 2.28C) as well as the upper lumbar fibers of the MF have been reported to

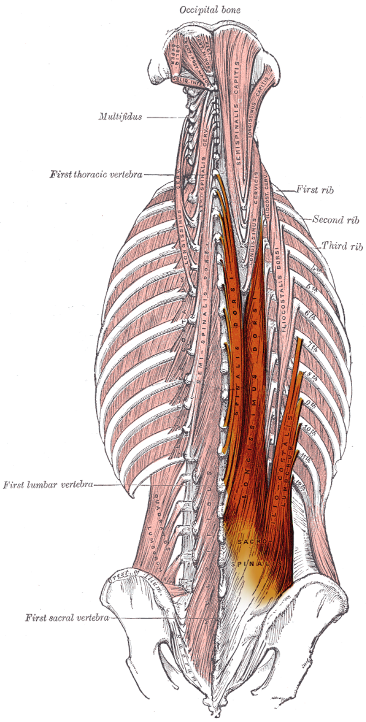

Figure 2.27: Subdivisions of the ES muscles per region (adapted from [29]).

basically form the ESA [164]. The Spinalis group
muscles run caudally down to the upper thoracic spine and therefore are out of the scope of the current thesis.

2.2.5.3.1 Longissimus Thoracis

In the lumbar region, Macintosh and Bogduk [168] identified five fascicles occurring from the AP and TP of each lumbar vertebra (Fig. 2.28 A,B) that comprise the *Longissimus Thoracis pars lumborum* (hereafter abbreviated as *LTpL* or lumbar LT). The L1 to L4 fascicles have tendon caudal ends that eventually form a common tendon of insertion, the *lumbar intermuscular aponeurosis* (LIA) that attaches to the medial surface of the posterior SIS (PSIS). The L5 has a direct muscular insertion medially to the upper LTpL fascicle insertions. Despite the implications of previous studies [167], Bogduk [37] found no attachment of the lumbar fascicles to the ESA. Instead, these fascicles anchor the lumbar vertebrae directly to the ilium meaning that the LTpL acts independently from the rest of the ES. Indeed, each of its fascicles can be resolved into a large vertical (parallel to the longitudinal axis) and a considerably smaller horizontal (parallel to the anteroposterior axis) line of action (Fig. 2.28A) with varying size depending on the spinal level and the muscle contraction [168]. As such, the capacity of LTpL as a posterior sagittal rotator, i.e. back extensor, increases rostrally in line with the larger vertical vectors, while its capacity for posterior translation is greater at lower lumbar levels where the fascicles have a more dorso-ventral orientation. Importantly, though, the muscle is not able to exert posterior sagittal rotation without simultaneously exerting whatever horizontal rotation [37].

The *Longissimus Thoracis pars thoracis* (hereafter abbreviated as *LTpTh* or thoracic LT) is the intermediate and largest of the vertical muscle columns of the ES. It consists of 11 or 12 pairs of thoracic fascicles that proximally attach to the TPs and ribs of the thoracic vertebrae via tendons (Fig. 2.28C) that may merge medially from T5 down to T12 [37]. The fascicle muscle bellies are small and the ones from the upper levels overlap those from the lower levels [170]. Eventually, the LTpTh

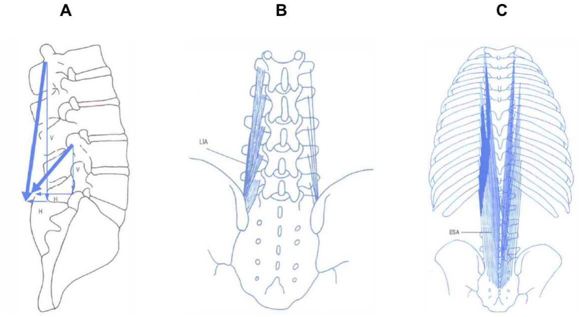

Figure 2.28: (A) Lateral view of the vertical and horizontal action of the lumbar LT fascicles, (B) The lumbar and (C) thoracic fascicles of the Longissimus Thoracis from a posterior view. (LIA=lumbar intermuscular aponeuris; Darkened areas: fascicle muscle belly (flesh)) (adapted from [37]).

fascicles end in large caudal tendon insertions that form the ESA and insert into the lumbar and sacral SPs, the sacrum, and the ilium. For example, the fascicles from the T2/T3 level attach to the L3 SP, and those from T8/T9 to T12/L1 extend down to the S3 SP and to the caudal extent of the PSIS. The principal action of the LTpTh is on the thoracic vertebrae and the ribs. Nonetheless, the LTpTh fascicles between T6/T7 and T12/L1 levels span the entire lumbar region and can act on the lumbar vertebrae. Bilateral contraction of the muscle results to an indirect increase of the lumbar lordosis through the ESA. When contracted unilaterally, the thoracic LT principally flexes the thoracic spine laterally and secondary it produces lateral flexion of the LS [164].

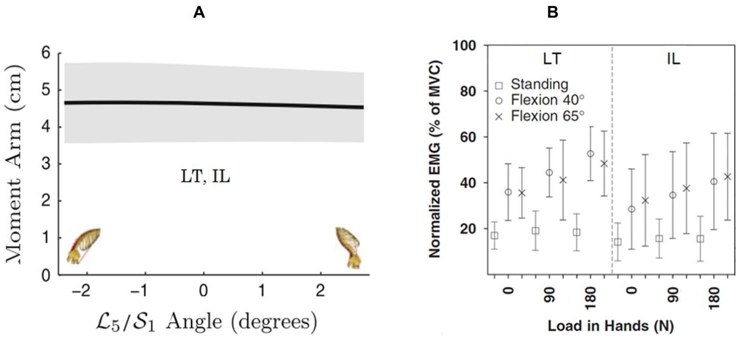

Figure 2.29: (A) Sagittal plane moment arms calculated about the L5/S1 IVD between fully extended and flexed postures (adapted from [27]), (B) Normalized EMG of the LT and IL in standing and flexed posture with varying load in hands (adapted from [171]).

The distribution of the LT fascicles allowed quantification of the muscle architecture parameters and its activity using different *in vivo* techniques, such as radiographs, MRI and EMG measurements. For instance, the decreasing sagittal plane moment arms[6] calculated through the model of [27] from neutral to flexed positions were in a similar range with the ones previously quantified using images ([172], [173]). Tveit and colleagues [174] found also a decrease in the moment arms when the subjects were passing voluntarily from maximum lordosis to kyphosis in supine position. The lumbar LT and IL activity captured through EMG signals in [171] was significantly higher in forward flexions compared to standing under identical external loads (Fig. 2.29B).

2.2.5.3.2 Iliocostalis Lumborum

The *Iliocostalis Lumborum pars lumborum* (ILpL or lumbar IL), i.e. the lumbar component of the Iliocostalis Lumborum (IL), consists of four fascicles arising from the tips of the L1-L4 TPs and from the thoracolumbar fascia (Fig. 2.30A). Caudally, they insert directly on the iliac crest and on the posterior surface of the PSIS laterally to the LTpL [168]. The literature does not describe any fascicles that arise from L5. Rather, according to [37], this ”lacking” part of the ILpL seems to be represented by the ILL. The ILpL fascicles have similar disposition to that of the lumbar LT and their action can be resolved respectively into a predominant vertical and a smaller horizontal vector. Such vectors act directly on the lumbar vertebrae and are not independent. When contracted bilaterally, the lumbar IL can act mainly as a posterior sagittal rotator producing extension and simultaneously exerting axial rotation that is greater at the lower lumbar levels. When contracted unilaterally, the fascicles can produce lateral flexion and the TP attachments stand for suitable lever arms to produce axial rotation [37] and extension at the same time. When the abdominal muscles act to rotate the trunk, the ILpL cooperates with the MF to resist the flexion effect produced by the rotation (Fig. 2.31).

The *Iliocostalis Lumborum pars Thoracis* (ILpTh or thoracic IL) represents the thoracic component of IL and consists of fascicles that arise via flattened tendons

---

[6] Also known as *lever arm* of a force system is the perpendicular distance from an axis to the line of action of a force.

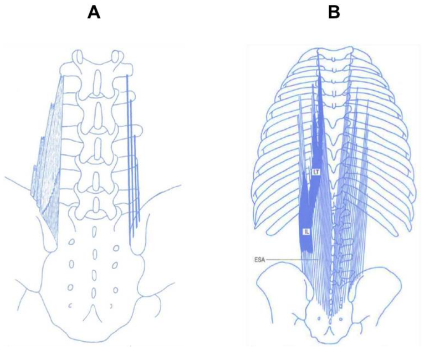

Figure 2.30: Posterior view of the (A) lumbar IL, and (B) thoracic IL and LT fascicles. Darkened areas: fascicle muscle belly (flesh) (adapted from [37]).

from the lower seven or eight ribs as shown in Fig. 2.30B. The thoracic IL fascicles are not related to the Iliocostalis Thoracis muscle present between the first six thoracic ribs (see Fig. 2.27). The ILpTh possess longer muscle bellies than the thoracic LT but similar to the latter, they have tendon caudal ends that contribute to the ESA and ultimately attach to the ilium and to the sacrum [37]. They span the LS but they have no direct attachment to it [164]. The ILpTh has similar actions to the LTpTh; it exerts an indirect "bowstring effect" on the LS when contracted bilaterally that results in an accentuation of the lumbar lordosis [164]. When contracted unilaterally, like the lumbar IL, it laterally flexes the LS and can also have a small axial rotator role (Fig. 2.31).

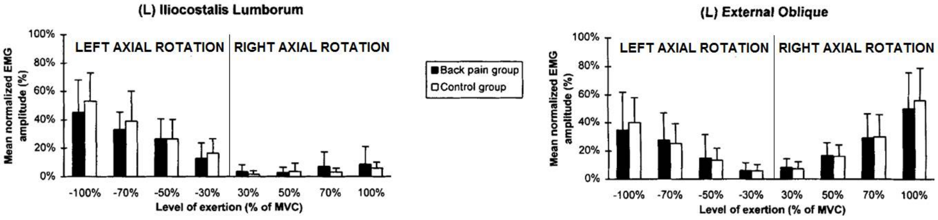

Figure 2.31: Normalized EMG of the (L)eft External Oblique and IL during axial rotation in back pain (black) and control (white) groups (adapted from [163]).

2.3 Estimation of spinal loads

2.3.1 Experimental explorations

Despite its great importance for the research on back pain, loading of the spine is still not well quantified or even understood. Apart from the ethical difficulties involved, direct *in vivo* measurement of spinal loads is generally avoided mostly because of the invasiveness of placing a force cell, intramuscular electrodes or pressure needles. For the muscles, the non-linearities of the tissue and importantly, the redundant number of muscle actuators in complex systems, like the human back, are great limitations on the acquisition of muscle load magnitudes *in situ*. For the IVDs, pressure needle measurements may have pathological consequences in a long term as shown with discography examination [175] and, therefore, are normally avoided or made over a small number of patients ([176], [177], [60]). Similarly, the necessary disruption of the facet capsule makes the measurement of facet contact forces hard to perform. As such, the necessity of estimating how much load is transferred to the different components of the spine has been addressed experimentally using different *in vivo* and *in vitro* techniques. Still, the data available in the literature remain limited.

For the *in vivo* estimation of muscle loads, surface EMG electrodes have been often used to capture the real time activation levels of the most superficial back muscles during different exercises ([171], [178], [163], [179], [180]). Unfortunately, given the complicated anatomy of the back, capturing deep muscle fiber signals as well as isolating muscle activity is quite sensitive to the protocol used for the electrode placement. Yet, although the measurements do not permit direct force magnitude estimations, the electric potentials measured are useful for detecting abnormal muscle activity in both the healthy and the pathologic spine. Alternatively, Rohlmann *et al.* used implanted spinal fixators to measure inter-segmental forces and moments in patients ([181], [182]). These studies are suitable for load estimation during occupational activities, but measurements cannot be included in a clinical routine and neither permit the conclusion of general patterns for healthy subjects. Towards non-invasive approaches, the study of Bogduk *et al.* [183] proposed an image-based technique to determine the individual fascicle forces of lumbar muscles. The three-dimensional (3D) orientation of the fascicles derived from anatomic studies ([168], [151]) was plotted onto radiographs of healthy spines taken in upright position. For each fascicle, the PCSA was calculated[7] and was related to the T0 through a force coefficient k equal to 0.46 MPa to match the L5/S1 moment estimations with the respective measurements in [184]. Importantly, because the parameter value was based on different reported ranges ([97], [185], [186]), the estimated force results are subjected to variance depending on the fascicle anatomic data. Other studies reported moments and strength/endurance data measured using dynamometers during trunk extension exercises ([187], [188], [189], [190]). In the last decade, muscle functional MRI (mfMRI) was explored for the assessment of the lumbar extensors during similar exercises ([191], [192], [180]). Comparison of the T2 relaxation time values to EMG showed similar, linear patterns ([192], [180]). Accordingly, the linear relationship identified between T2 and exercise intensity for MF and ES supports the use of mfMRI to evaluate muscle recruitment both in healthy volunteers and patients in order to improve current rehabilitation strategies.

For the intradiscal loads, experimental evaluation has been explored mainly *in vivo* but unfortunately remains limited given the invasiveness of most of the techniques. In 1960s and 1970s, a series of pioneering studies by Nachemson in LBP patients showed that, for instance, sitting increases the IDP when compared with standing, from around 0.8 to 1.2 MPa mean values ([193], [176], [177], [57], [194]). Later static *in vivo* measurements in healthy volunteers qualitatively confirmed Nachemson's outcome, although lower IDP values and varying physiological ranges were reported (Table 2.1). Wilke *et al.* ([60], [195]) performed dynamic measurements during a variety of postures and exercises and reported absolute IDP values and anthropometric measurements for a healthy volunteer that complemented the state-of-the-art (SOTA) at the moment. During many exercises, the results in these studies correlated with Nachemson's data and confirmed the suggestion that there is a significant relationship between lumbar IDP and different body positions. However, the authors

---

[7] The *physiologic cross-sectional area* (PCSA) was defined as the ratio between the measured fascicle volume and rest length.

reported slightly increased pressure values in relaxed standing in comparison to sitting position (between 0.44-0.50 MPa). These differences may be explained by the different transducers and calibration accuracy used, compared to Nachemson's work. Although they were acquired for one subject only, the measurements of Wilke and colleagues confirmed previous findings from an indirect method using stadiometry [196], and another one using an instrumented spinal fixator [197]. Quantitatively, the large spread of the measured IDP values has been related to the large variation in the number of volunteers, the inter-subject variation [198], as well as to the disc level and condition ([199], [200], [201]). Certainly, there are multiple interactions involved in the mechanical response both of the healthy and the pathologic spine that the information obtained by such *in vivo* techniques might be too local to help towards their understanding. Nonetheless, such measurements are unique and hence, they are very valuable for the validation of numerical models of the spine.

Table 2.1: Mean *in vivo* IDP (MPa) measured in standing and sitting postures.

	Standing	**Sitting**
Andersson *et al.* [202]	0.36	0.41
Schultz *et al.* [203]	0.27	0.32
Sato *et al.* [198]	0.54	0.62

Previous *in vitro* stress profilometry studies showed large stress peaks in the posterior AF during flexion/extension motions [204]. These stress values were further increased when prior creep [205] and age-related changes [201] were considered. Steffen *et al.* [206] confirmed such findings under asymmetrical external loading by instrumenting cadaveric spines with multiple pressure sensors. This possible mechanical overload found in the postero-lateral AF under combined axial rotation with postural changes may lead to mechanical IVD failure in the pathologic spine. However, it requires further investigation in different external loading cases. In fact, one of the main challenges of *in vitro* evaluations of spine biomechanics is the experimental simulation of reliable external loads involving set-ups with various degrees of freedom. Muscle action lines represented by cable tractions were used to simulate the effect of back and abdominal muscles on the mechanical response of LS specimens to different rotation motions. The results showed that including muscles significantly affected the IDP and the load-deformation values ([207], [208], [209]). By comparing *in vivo* and *in vitro* IDP in different lumbar levels, estimations of approximations of muscle loads expected *in vivo* were achieved through different load combinations in standing and flexion/extension positions [210]. Unfortunately, previous semi-experimental methods suggested that the amount of *in vivo* data available remains too low in comparison to the high number of degrees of freedom (DOF) to be adjusted for multilevel muscle force determination [23]. As such, simplified experimental set-ups using moment-controlled hybrid rotations [211] and follower compressive forces [212] were studied giving useful outcomes for the evaluation of static motions. Still, stability issues are suggested to relate with the transient, long-term spine response [213] that requires other techniques of exploration of the mechanical load distributions through the different spine tissues.

2.3.2 Computational explorations

Considering the difficulty to capture experimentally the physical phenomena related to the functional behavior of the spine, computational models seem to be indispensable tools towards a better understanding of the spine biomechanics. So far, the LS models developed intended to capture the spinal function through often relatively simplified assumptions, e.g. on the anatomy, geometry, passive properties and gravity loads, that consequently affected the accuracy of the results. Free body diagrams (usually a transversal cut at L4/L5 or L5/S1 disc) and advanced 3D thoracolumbar or LS models have been reported, involving various combinations of rigid bodies (RB) and deformable bodies using the FE approach. The latter is a widely accepted method used in biomechanics since 70s [214] and can provide information that laboratory experiments cannot apprehend. On one hand, among other FE modeling allows the simulation of complex loading conditions, the prediction of stress distributions in the different spine tissues under large strains, the exploration of a practically unlimited set of physiological conditions, the simulation of complex geometrical structure and non-linear material properties. RB modeling, on the other hand, has lower computational cost and can be combined with deformable models in applications that require numerous calculations and/or extensive geometrical models. For example, when complex spine kinematics with multi-level incorporation of muscle fascicles is investigated, stress-strain computations within the vertebrae are not of major interest. Therefore, vertebrae can be modeled as RB in stability and equilibrium analyses that focus on muscles and passive soft tissues, such as IVD.

Accordingly, the proposed LS assemblies often combined rigid vertebrae models with IVDs simulated as custom joints ([215], [216], [27], [24], [217], [218]), beam-like with a given passive stiffness ([215], [219], [178], [220]) or 3D geometries modeled as hyperelastic composites ([221], [222], [223], [224]). To account for the stabilizing action of the muscles on the trunk, different methods were employed. On one hand, considering that the segmental compressive forces followed the axial axis, *follower* loads were applied directly as punctual forces [225], or via a path of unidirectional connector elements [226]. Since the accuracy of such approximations depends on the definition of the antero-posterior location of the path [227], the application of a surface pressure was suggested alternatively by Noailly *et al.* [228]. Nonetheless, it is unclear whether such concentration of forces on the VB can represent the balance of BW and muscle effects. Clearly, simulation of boundary conditions through explicit muscle modeling was expected to better capture the effect of muscle function on trunk stability. Hence, an early attempt of a full lumbar MSL FE model including the ES fascicles was reported by Zander *et al.* [221]. More advanced models incorporating the fascicles of several back and abdominal muscles relevant to the thoracolumbar area were developed in the recent years with increasing complexity and realism ([178], [171], [24], [27], [217], [218]). Interestingly, although antagonistic activation of abdominal muscles was seen in extension, lateral bending and axial rotation [229], the unclear effect of the intra-abdominal pressure on the decrease of spinal loading and increase of spine stabilization needs to be further addressed ([230], [231], [232]).

As discussed previously, the main challenge of MSL models has been the quantification of the back muscle loads developed in different trunk positions. For a given motion described through kinematical data, such as motion capture and EMG signals, inverse dynamics approaches are used to solve the motion equations of the system. Since unknown muscle forces significantly outnumber the equilibrium equations, optimization ([233], [234], [203]), EMG-driven ([235], [236]) and a combination of EMG-assisted optimization methods ([237], [238]) have been used so far to tackle such kinematic redundancy in the LS. That is, optimal muscle recruitment able to minimize the muscle activation was formulated through an objective function, and the intersegmental forces and internal joint moments and forces were estimated so to fulfill the trunk stability for the specific motion. Comparisons between single- and multi-joint equilibrium models have shown that muscle and spinal load estimations using single-level equilibrium are inadequate to satisfy the mechanical equilibrium at remaining levels either using only optimization techniques [238] or EMG-driven methods ([239], [240], [23], [24]). From a biomechanical point of view, such outcome seems coherent with the back muscle anatomy. The multi-level spanning design of most back muscles makes uncertain the reliability of estimations performed using cutting plane analyses, since in reality the CNS attempts to balance external moments at all levels simultaneously and not at one single joint. In their study, Arjmand *et al.* attempted to quantify such differences [239]. On one hand, for the shear forces and muscle activations levels, a clear task and level dependency was found. Axial compression loads, on the other hand, appeared to be less sensitive among any of the used approaches. More recently, Arjmand *et al.* [241] used a FE thoracolumbar KD model previously created [171] together with regression methods to propose predictive equations for the quantification of spinal loads at the L4/L5 and L5/S1 levels in symmetric lifting tasks. The results were comparable to previous L4/L5 compression loads measured *in vivo* under identical tasks [195] suggesting that the proposed method is promising for fast risk prevention analyses and simulations of realistic external loading *in vitro*. However, a limitation of the study was that the predictive equations did not consider subject anthropometric data among the independent variables (e.g. height). Han *et al.* [217] explored the effect of varying BW and height on the intersegmental forces using a full spine MSL model from the Anybody software (AnyBody Technology, Aalborg, Denmark). The authors found a high dependence for both variables in different static postures and lifting tasks that was especially stronger for the BW. Recently, Hajihosseinali *et al.* [218] used a FE thoracolumbar KD model that was similar to the one used in [241] to verify the effect of increasing BW on the L5/S1 compression while scaling the moment arms and PCSA of the muscles accordingly [242].

Certainly, muscle dynamics is one of the major considerations to expect reliable results through such biomechanical models, as described in detail in 2.2.4. Based on a thorough literature review, the first attempt reported for the LS was in 2012 by Christophy and colleagues through the OpenSim platform [243]. A full thoracolumbar RB model was coupled to 238 muscle fascicles with prescription of force-generating springs and damper systems based on an improved approach over the basic Hill-type[8] muscle model [244]. That is, the muscle behavior was described by prescribing all parameters needed to scale the f-l and f-v curves already implemented in the software. Hence, the model could be used for the inverse estimation of the muscle forces developed as an optimized set of values that fulfill the equilibrium equations for the simulated motion and therefore, are directly linked to the kinematical input. However, this concept limits the predictive ability of a biomechanical model to calculate the intersegmental loads produced *under different conditions*. Such results could not give either information on the decoupled contribution of the passive and active role of the muscle sub-tissues (e.g. fibers). Moreover, in spite of the recognized complexity of the model, the effects of the passive structures, i.e. IVDs, ligaments and facet joints, were not sufficiently incorporated. The consideration of a three DOF[9] LS model representing the intervertebral joint kinematics definitely is not enough for the simulation of coupled motion since it has been suggested that rotation and lateral bending are usually followed by motion in the other two DOF [245]. An alternative approach would be, for example, the definition of a non-diagonal stiffness matrix that may possibly include also the ligament effect. The consideration of the constraining role of facet forces would also permit the exploration of the synergistic action between facet joints and muscles in spine stabilization as proposed previously [246]. Probably the most important limitation of the discussed study was its generality, i.e. the lack of wide inter-subject variation in lumbar geometry and muscle strength. Nevertheless, the model's high physiological

---

[8] The Hill-type model is presented in detail in 2.4. In brief, the model represents the muscle contraction through a contractile and a series element arranged in parallel with a third spring that represents the passive behavior of the muscle when unactivated.

[9] Flexion-extension, axial rotation, and lateral bending.

complexity and some preliminar results of the calculated moment arms allowed its consideration as the most detailed non-commercial tool for the exploration of the LS biomechanics at that time. Actually, the open-source nature of this model encouraged the development of a P-SP lumbar MSL model by Dao *et al.* [28] based on anatomical images (CT, MRI). The model included 126 muscle fascicles and considered the anatomical landmarks, modeling properties and Hill-based muscle behavior implemented by Christophy *et al.* [27]. Following the concept of inverse force calculations, the authors reported fascicle force estimations ranging from 3 to 40 N for a simulated extension-like trunk motion (hyperlordosis) based on dynamic MRI. Since it was the first P-SP model documented for the LS so far, the results were partially correlated with previous generic models in terms of order of magnitude (11-70 N) [247]. However, similar to other RB analyses, the quantification of the muscle active forces as well as the passive resistance offered by muscles and discs could not be addressed.

In this sense, the exploration of FE MSL models of the LS involving continuum mechanics theories could help to overcome this limitation. Such models consider the constitutive behavior of the IVDs and muscles and, hence, are able to predict the spinal loads developed under any simulated load state and under large deformations. Such approximation has been already proposed to explore the mechanical response of the cervical spine [248]. A combination of passive non-linear solid and active Hill-type elements were used to model the cervical muscles, which were represented as a 3D continuum model previously validated ([249], [250]). The coupled model allowed the prediction of different distributions of neck muscle load and strains in impact-induced motions. Yet, at the moment of writing, no such predictive models have been explored for the LS despite the high clinical relevance of translating lumbar external loads into internal forces under any deformation and at any strain rate. In the following section, a brief presentation and literature review is given on the predictive models proposed so far from the 1D Hill's model up to 3D extended variations of the same and multi-scale formulations coupling sub-cellular to organ processes taking place during muscle contraction.

2.4 Muscle modeling: from Hill-type to biophysically-based models

In 1938, A.V. Hill set the basis for the approximation of the skeletal muscle contraction through a simple phenomenological model. In particular, the Hill model is composed of three elements (Fig. 2.32) :

- an active contractile element (CE) that is fully extensible when unactivated (at rest), but capable of shortening (contracting) when activated; the force generated in this component is the result of the number of active cross-bridges formed by the sliding actin and myosin filaments described in 2.2.4.
- a series element (SE) which is a non-linear spring that provides an energy storing mechanism and is arranged in series with the CE; the SE is usually associated with the intrinsic elasticity of the myofilaments and the tendon.
- a parallel element (PE) that is a non-linear spring arranged in parallel with the other two elements and is responsible for the passive behavior when the muscle is stretched even when the CE is not activated, i.e. at rest. The PE represents the passive force of the connective tissues (fascia, epimysium, perimysium and endomysium).

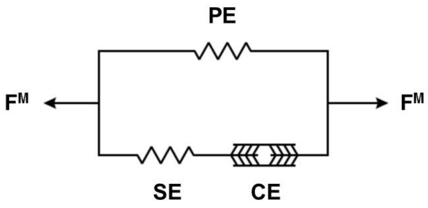

Figure 2.32: Hill-type three-component model (PE=Parallel elastic element; SE=Series elastic element; CE=Contractile elastic element).

In this model, the CE is considered to have *f-l* and *f-v* characteristics similar to those described in 2.2.4.4-2.2.4.5. The muscle force, F^M, is the sum of the forces developed by the PE and SE, with the latter being equal to the force generated in the CE ($F^{SE}=F^{CE}$). When viscous effects are taken into account, variations of the

Hill model can be used considering a non-linear viscous element instead of the PE, or a dashpot instead of the CE to incorporate viscosity as a function of time, strain and strain rate ([117], [251]).

To date, the Hill-type three-element model remains the model of choice for most modeling studies of muscle movement systems mainly because of its computational simplicity and the ease with which model parameter values can be estimated. That is, the formulation is based on interpretations of input-output data obtained from controlled experiments on isolated fibers or a single muscle [252]. Therefore, it is a phenomenological approximation. However, one of the main weaknesses of the Hill's model is its one-dimensional (1D) formulation. Because of this, the muscle mass, geometrical characteristics and shape change during contraction cannot be considered, neither its architectural characteristics, such as fiber orientations. Hence, in order to explore complex 3D geometries and simulate the muscle contraction, continuum constitutive models have been used as a 3D extension of Hill's model. Such models consider the muscle as a fiber-reinforced continuum tissue that most commonly is described as a hyperelastic material. For a quasi-incompressible behavior, the strain energy per unit volume of the reference configuration is written as the sum of a fiber term (U_F), and a term related to the matrix, that is often further decoupled into a deviatoric (U_I) and a dilatational (volumetric) (U_J) component:

$$U = U_F + U_I + U_J \tag{2.3}$$

Accordingly, the constitutive models proposed in the literature were of varying complexity depending on the levels represented (e.g. tissue or motor unit level), the type of conditions simulated (i.e. static or dynamic), or the number of muscle model parameters involved. For instance, in the 3D Hill-type skeletal model developed by Kojic *et al.* [253], the CE and SE accounted for the active behavior of the muscle, while the PE represented the surrounding matrix considering linear isotropic properties but not incompressibility constraints. In total this model involved ten material parameters. In the same year, Martins and colleagues [254] proposed a 3D Hill-type skeletal muscle model inspired from the passive cardiac model of Humphrey and Yin [255]. The authors extended that model to include the active muscle behavior such that the final model was consistent with the 1D formulation of Zajac [256] for skeletal muscles. The muscle was modeled as a fiber-reinforced composite with a reduced number of only four material parameters among which a strain-like quantity was used to control the activation in the CE. A few years later, this parameter was modified by splitting the fiber stretch into a contractile and elastic stretch adding therefore one more material parameter [257]. Still, the limited number of five parameters remained one of the main advantages of this model in terms of parameter value calibration. The same year, Blemker et al. [258] proposed a fiber-reinforced model for the biceps brachii with transversely isotropic material symmetry influenced by the study of Weiss [259] that moreover considered the microstructure of the muscle, i.e. the fiber orientations. The authors used a similar generic form of the strain energy function as described above for a nearly incompressible muscle based on the strain invariants [260]: they separated the material's mechanical response to stretch in the fibers, shearing along and transverse the fibers. In total the model included 14 material parameters among which some properties, such as the resistance to shear parallel to the fiber direction, that had not been addressed experimentally. Actually, this is a common restriction of representing muscles as a continuum with complex fascicle geometry. To overcome this, authors often make geometrical assumptions or simplifications in order to reduce the number of material parameters in the model. The constitutive relation of Lu *et al.* [261] was based on previous approaches ([262], [258]) and considered a 3D hyperelastic muscle model coupled with active contraction of muscle fibers and a total of 13 material parameters. In this study, a sensitivity analysis was performed to help understand how some parameters influence the total muscle stress depending on whether their values can be experimentally determined, whether they come from reported ranges or they can be tuned to predict experimental data.

The phenomenological nature of Hill-type muscle models means that few of the parameters can have direct physical counterparts. In turn, biophysically based models can predict the muscle response as emerging from the underlying physiology of the system, i.e. including structural and functional characteristics of skeletal muscles. As such, physiologically based, multi-scale skeletal muscle FE models together with a model of motor-unit recruitment can compute the electro-physiological behavior of single muscle fibers within motor units and link it to a continuum-mechanical constitutive law (Fig. 2.33) ([263], [264]).

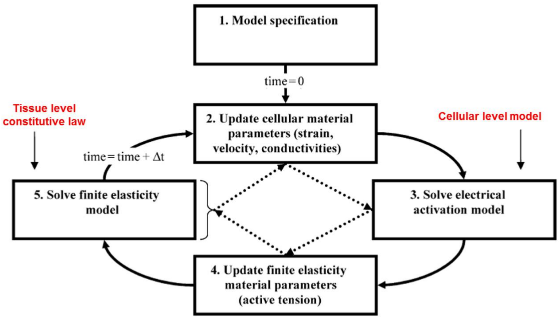

Figure 2.33: Illustration of the algorithm typically used to numerically simulate models of cellular-tissue coupled active mechanics (adapted from [263]).

In the last decade, Röhrle and colleagues progressively included a much larger array of anatomical and physiological properties in their multi-scale constitutive law that bridged the cellular and organ level via a direct coupling of the active contribution to a detailed skeletal muscle model of the sub-cellular process [265]. The feasibility of their model was tested on a tibialis anterior FE muscle geometry [266]. The result was an elegant and detailed model able to give a better understanding of skeletal muscle function during fiber recruitment and of the effect of alterations of muscle properties due to injuries and diseases on the mechanical force generation. A qualitative validation of the model was also attempted by the authors and their results fitted within known experimental ranges. Yet, a more in-depth validation procedure would be needed among different subject-specific models. The complexity and versatility of the model are key elements and main weaknesses at the same time, since they require a large set of input variables that can be very difficult to obtain for a subject-specific case. Hence, such advanced frameworks that still require rigorous validation are suggested to be more suitable for individual muscle explorations when investigating physiological diseases rather than for high complex anatomical systems, as the human spine.

2.5 Modeling of the IVD

As discussed in 2.2.2, the IVD is a multiphasic material that contains water and a network of collagen and elastin fibers embedded in a matrix composed principally of proteoglycans and cells. In terms of simplicity, this material can be considered containing two phases, i.e. a solid phase composed of structural macromolecules and cells, and a fluid phase consisting in water and solutes. In order to describe the IVD mechanical behavior, two different approaches have been adopted based on the concepts of the continuum mechanics: (a) the *biphasic* or *mixture* theory that considers that each material part is occupied by a solid and a fluid particle [267], and (b) the *Biot poroelastic* theory that considers each material part as a continuum point that is a homogenized or average combination of solid and fluid phases [268]. Both theories use the same concept of porosity[10] but their difference lies mainly on the averaging procedure. Actually, it has been reported that the two approaches are equivalent when solid and fluid phases are incompressible both for linear and non-linear finite deformation cases ([269], [270]). A brief description of the Biot poroelastic theory is given next.

2.5.1 Poro-hyperelastic models

In the frame of poromechanics, all IVD tissues are modeled as fluid-saturated porous media. The solid phase is considered as a compressible drained porous skeleton the pores of which are filled with an incompressible fluid. The total Cauchy stress $\boldsymbol{\sigma}$ is expressed as a decomposition into the volumetric (expressed through the pore pressure, p) and the effective (or deviatoric) ($\boldsymbol{\sigma^s_{eff}}$) stress term:

$$\boldsymbol{\sigma} = \boldsymbol{\sigma^s_{eff}} - p\mathbf{I} \tag{2.4}$$

where $\mathbf{I}$ is the second-order unit tensor.

In linear poro-elasticity, the solid stress follows the linear elasticity form given by the generalized Hooke's law. Whether such behavior presents a realistic description

---

[10] If saturation is assumed, the solidity n^s and porosity n^f satisfy the equation $\mathrm{n}^s + n^f = 1$.

of the CEP material was recently questioned experimentally [71]. Indeed, the poro-hyperelasticity has been suggested as a better approximation since it considers the non-linear effect of geometry under large deformations [271]. Hence, for the AF and NP, a hyperelastic formulation can be used and the total stress can be expressed as:

(Cauchy stress)

$$\boldsymbol{\sigma} = \frac{1}{J}\frac{\vartheta U}{\vartheta \mathbf{F}}\mathbf{F}^T - p\mathbf{I} \tag{2.5}$$

or

(2nd Piola-Kirchhoff stress)

$$\mathbf{S} = \mathbf{F}^{-1}\frac{\vartheta U}{\vartheta \mathbf{F}} - p\mathbf{I} \tag{2.6}$$

where $\mathbf{F}$ is the deformation gradient tensor involved in the calculation of the strain tensor based on [272], and U is the strain energy function. Among many different relations presented in the literature, a Neo-Hookean model can be used for the poro-hyperelastic solid matrix taking into account its deviatoric and volumetric components:

$$U_M = \frac{G}{2}(I_1 - 3) + \frac{K}{2}(J-1)^2 \tag{2.7}$$

where G is the shear modulus, I_1 the first invariant of the right Cauchy-Green strain tensor C, and K the bulk modulus of the porous solid skeleton. For the NP, this corresponds the total strain energy function ($U = U_M$). For the AF, the total strain energy U is the additive contribution of the previous matrix formulation (U_M) and an anisotropic term (U_F) that considers reinforcement with fibers that are orientated in a criss-cross pattern ([273], [274]):

$$U_F = \frac{K_1}{K_2}\sum_{\alpha=1}^{2}\left\{\exp\left[K_2\left\langle \overline{E}_\alpha \right\rangle^2\right] - 1\right\} \tag{2.8}$$

where K_1 and K_2 are fiber stiffness-related parameters, and $\overline{E}_\alpha$ is a strain-like quantity representing the square of the stretch in the two directions of the fibers.

For the fluid phase of all tissues (AF, NP, and CEP), Darcy's law can be used to integrate the pore pressure p through the relation of the fluid mass flow rate to the spatial gradient of the pore pressure:

$$\nu_f n = -\frac{\kappa}{\mu}\nabla p \tag{2.9}$$

ν_f being the fluid velocity, n the porosity tensor of the material, κ the intrinsic permeability and μ the dynamic viscosity of the fluid (i.e. water) within the porous solid. Note that biomechanical studies often report directly the *hydraulic permeability* (i.e. the ratio $\frac{\kappa}{\mu}$). It has been suggested that the large deformations present in the disc possibly make the permeability κ decrease with deformations and so, strain-dependent models have been proposed for its calculation ([275], [276]). The exponential constitutive law proposed by [275] was the following:

$$\kappa = \kappa_0 \left[\frac{e(1+e_0)}{e_0(1+e)}\right]^2 \exp\left[M\left(\frac{1+e}{1+e_0}-1\right)\right] \tag{2.10}$$

where e is the current void ratio, i.e. the ratio between fluid and solid matrix, κ_0 and e_0 the initial permeability and void ratio, respectively, and M an empirical coefficient. The two phases were assumed to be nearly incompressible, and the void ratio varied with the porosity of the tissue according to:

$$e = \frac{n}{1-n} \tag{2.11}$$

The experimental complexity of perturbing soft materials is high and as a consequence, direct measurement of the tissue poro-mechanical properties is not an easy task. Accordingly, definition of healthy disc osmo-poro-hyperelastic properties is often based on calibrations of the proposed constitutive laws in order to reproduce simple mechanical test results ([277], [278]).

2.5.2 Tissue damage criteria

In case of degenerated tissues, due to the lack of experimental values, the poro-mechanical disc response is often described by decreasing the porosity and swelling capacity (i.e. p) and increasing the stiffness parameters (e.g. K) ([279], [280]). However, from a biological standpoint, the multiphysics changes induced by disc degeneration, such as tissue dehydration and crack occurrence, cannot be captured through similar parameter value adjustments. Moreover, these models have not been validated so far. Recently, Malandrino and colleagues explored the effect of an introduced damage criterion on the bulk (K), shear (G) and porosity (n) parameters [281] by simulating both the AF and NP as cracked continuums [282] inspired by the theory of micromechanics. One of the main outcomes of the study was that the consideration of tissue damage coupled to the classical IVD poro-mechanical models achieved to represent known degenerative changes. Furthermore, it gave degeneration-dependent material properties related to osmotic pressure ($\Delta\pi$) and water loss, and to increased fibrosis. Such approach allowed validation of specimen-specific IVD models suggesting possible anticipation of degeneration mechanisms via *in situ* geometrical consideration of the disc morphology.

2.5.3 Load velocity effect

Most of the FE models including poro-elastic disc formulations in the literature explored important long-lasting phenomena, such as swelling and solute transport ([279], [283], [284]). However, only scarce information exists on IVD numerical studies simulating rapid loads, i.e. loading at rates as fast as 1 Hz, that the IVD experiences along activities such as walking. Actually, Rohlmann *et al.* [182] found that the disc load can increase from 100 to 1000 N in just one 1s. Based on their results, Stokes *et al.* [285] reported that poro-elastic models may become unstable under such kind of fast loads and hence, the disc mechano-biological simulated response could be significantly affected. Under a 1h compressive load, Schröeder *et al.* [276] calculated unexpected stress peaks at the AF-NP boundary that could be attributed to the material discontinuities existing in this specific zone. Ruiz *et al.* [66] confirmed this hypothesis simulating fast load rates in a poro-hyperelastic IVD model. To limit such discontinuity effect, the authors proposed the creation of a material transition zone with a combined gradient of material properties and local mesh refinements. This strategy would improve the ability of poro-mechanical disc models to link tissue level biomechanics with lower level phenomena, such as solute diffusion.

Chapter 3

Development of a novel active lumbar spine muscle model

3.1 Description of the constitutive terms

In this chapter, the development of a new constitutive assembly is presented for the description of the contraction of lumbar back muscles. Similar to previous 3D extension approaches of Hill's model, the muscle is described as a fiber-reinforced, transversely isotropic composite material with hyperelastic behavior assuming that the respective strain energies of the matrix and the embedded muscle fibers can be decoupled [259].

Fibers were modeled including the PE, SE and CE elements based on [117] (Fig. 2.32) with the mathematical representation of the respective contributions inspired from [254]. Accordingly, the strain energy stored in the muscle fibers (U_F) was given by:

$$U_F(\overline{\lambda}_f, \zeta^{CE}) = T_0 \int_{1}^{\overline{\lambda}_f} f_{PE}(\lambda) d\lambda + T_0 \int_{1}^{\overline{\lambda}_f} f_{SE}(\lambda, \zeta^{CE}) d\lambda \tag{3.1}$$

where $\overline{\lambda}_f$ is equal to $\sqrt{N^T \overline{C} N}$, N is the orientation vector of the fiber in the undeformed fascicle, and $\overline{\mathbf{C}}$ the deviatoric part of the right Cauchy–Green strain tensor $\mathbf{C}$. $\overline{\lambda}_f$ is equivalent to $J^{-1/3}\lambda_f$, where λ_f is the longitudinal fascicle stretch ratio. T_0

is the maximum tetanic stress, and ζ^{CE} is the contraction amplitude reflecting the muscle activation level of the CE: this parameter is further described in Eq. 3.9.

For the matrix, the dilatational (U_J) and deviatoric (U_I) strain energy densities were also decoupled considering a Neo-Hookean formulation for the U_I and the definition of [259] for the U_J. As such:

$$U_I(\overline{I}_1) = \frac{G}{2}(\overline{I}_1 - 3) \tag{3.2}$$

is the strain energy associated with the deviatoric response of the matrix, and

$$U_J(J) = \frac{K}{2}\ln(J)^2 \tag{3.3}$$

is the strain energy associated with the volume change.

All in all, the overall strain energy of the muscle was given by:

$$U = U_F(\overline{\lambda}_f, \zeta^{CE}) + U_I(J) + U_J(\overline{I}_1) \tag{3.4}$$

In Eqs. 3.2 - 3.4, J is the Jacobian determinant of the deformation gradient tensor $\mathbf{F}$, $\overline{I}_1$ is equal to $J^{-2/3}trC$, that is the first invariant of $\overline{\mathbf{C}}$, and G and K the matrix shear and bulk modulus, respectively.

When non-activated, stretched muscles produced a positive fiber stress that developed only in the PE branch of the model (Fig. 3.1):

$$\sigma^{PE} = T_0 \cdot f_{PE}(\overline{\lambda}_f) \tag{3.5}$$

where

$$f_{PE}(\overline{\lambda}_f) = \begin{cases} A(\overline{\lambda}_f - 1)^2 & \text{if } \overline{\lambda}_f > 1 \\ 0 & otherwise \end{cases} \tag{3.6}$$

Chen and Zeltzer [286] measured the passive force on frog muscles and proposed the quadratic form presented in Eq. 3.6 to express the experimental f-l curve, where A is a dimensionless material parameter defined through fitting with this curve.

When muscles are activated, a stress response is additionally produced in the SE of the active branch of the Hill-type assembly, in interaction with the CE. The total active stress is given by:

$$\sigma^{SE} = T_0 \cdot f_{SE}(\overline{\lambda}_f, \zeta^{CE}) \tag{3.7}$$

where

$$f_{SE}(\overline{\lambda}_f, \zeta^{CE}) = \begin{cases} 0.1\exp[100(\overline{\lambda}_f - 1 - \zeta^{CE})] - 1 & \text{if } \overline{\lambda}_f > 1 + \zeta^{CE} \\ 0 & otherwise \end{cases} \tag{3.8}$$

is the contractile stress-stretch function (Fig. 3.1). The non-zero expression of Eq. 3.8 represents the muscle response at the ascending (concentric) or descending (eccentric) limb of the active f-l curve (Fig. 2.22), depending on the value of the strain-like parameter ζ^{CE} that can be decoupled as:

$$\zeta^{CE} = \frac{L^{CE} - L_0^{CE}}{L_0^M} = \frac{L_0^{CE}}{L_0^M}\left(\frac{L^{CE} - L_0^{CE}}{L_0^{CE}}\right) = C_{CE} \cdot \varepsilon \tag{3.9}$$

Eq. 3.9 means that ζ^{CE} is proportional to the engineering strain $\varepsilon = \left(\frac{L^{CE} - L_0^{CE}}{L_0^{CE}}\right)$ and hence avoids explicit input of the activation level to describe active contraction in the CE in agreement with the phenomenological approach of [254]. In other words, the parameter controls the level of stretch-induced fascicle activation through the *active parameter* C_{CE}, i.e. the length between the resting (L_0^{CE}) and the optimal (L_0^M) fascicle lengths. Since no quantitative information could be retrieved from the existing literature about the mentioned fascicle lengths, the hypothesis proposed by [243] was adopted; the length ratio $\frac{L_0^{CE}}{L_0^M}$ was considered equivalent to the ratio between optimal and resting sarcomere lengths as follows:

$$L_0^M = L_0^{CE} \times \frac{L_0^S}{L^S} \Leftrightarrow \frac{L_0^{CE}}{L_0^M} = \frac{L^S}{L_0^S} \tag{3.10}$$

where L^S and L_0^S are the resting and optimal sarcomere lengths, respectively. Accordingly, the C_{CE} value was considered consistent among all fascicles of a given muscle group and was calculated by normalizing the L^S estimations reported in [27] per fascicle with L_0^S set equal to 2.8 μm based on [101], [102]:

$$C_{CE} = \frac{L_0^{CE}}{L_0^M} = \frac{L^S}{2.8} \tag{3.11}$$

Similar to [254] and [287], the model considered the velocity of deformation of the CE as the time derivative of the parameter ζ^{CE} here implicitly calculated as the rate of ε change along the simulations. As such, the velocity values depended on the strain ε, and on the muscle group via the value of C_{CE}. The maximum contraction velocity (v_{max}) was reached when the muscle force was zero (Fig. 2.19), i.e. when $\overline{\lambda}_f$ was lower or equal to $1 + \zeta^{CE}$ based on the criterion of Eq. 3.8.

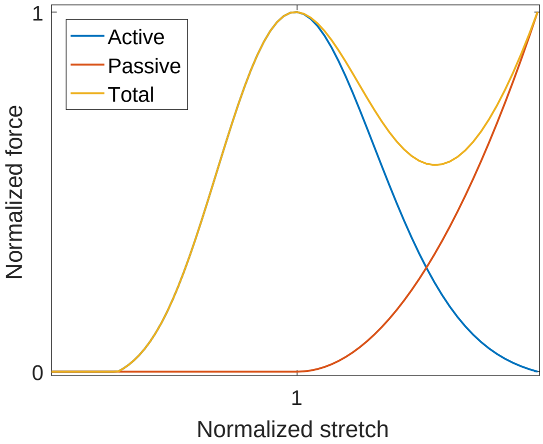

Figure 3.1: Active, passive and total normalized f-l relationship of the proposed model based on Eqs. 3.6, 3.8.

Finally, the second Piola-Kirchhoff stress tensor $\mathbf{S}$ was obtained from the derivation of the overall strain energy function (Eq. 3.4) with the substitution of the related terms from Eqs. (3.1-3.3):

$$\mathbf{S} = 2\frac{\vartheta U}{\vartheta \mathbf{C}} = \frac{G}{2}\left(2J^{-2/3}\mathbf{I} - \frac{2}{3}\overline{I}_1\mathbf{C}^{-1}\right) + K \ln J\mathbf{C}^{-1} + U_F' \left[J^{-2/3}\overline{\lambda}_f^{-1}(N \otimes N) - \frac{1}{3}\overline{\lambda}_f\mathbf{C}^{-1}\right] \tag{3.12}$$

where

$$U_F' = U_{PE}'(\overline{\lambda}_f) + U_{SE}'(\overline{\lambda}_f, \zeta^{CE}) \tag{3.13}$$

with

$$U_{PE}'(\overline{\lambda}_f) = T_0 \cdot f_{PE}(\overline{\lambda}_f) \tag{3.14}$$

and

$$U'_{SE}(\overline{\lambda}_f, \zeta^{CE}) = T_0 \cdot f_{SE}(\overline{\lambda}_f, \zeta^{CE}) \tag{3.15}$$

Using Eqs. 3.12 - 3.15 and according to the continuum mechanics theory, the Cauchy stress $\boldsymbol{\sigma}$ was related to the second Piola-Kirchhoff stress tensor $\mathbf{S}$ by the following relation:

$$\boldsymbol{\sigma} = \frac{1}{J}\mathbf{FSF^{-T}} = \frac{G}{2J}\left(2\overline{\mathbf{B}} - \frac{2}{3}\overline{I}_1\mathbf{I}\right) + \frac{K\ln J}{J}\mathbf{I} + \frac{T_0}{J}\left[(f_{PE} + f_{SE})\left(\overline{\lambda}_f(n \otimes n) - \frac{1}{3}\overline{\lambda}_f\mathbf{I}\right)\right] \tag{3.16}$$

where n is the fiber direction in the deformed state, $\mathbf{I}$ the second-order unit tensor, and $\overline{\mathbf{B}}$ the deviatoric part of the left Cauchy-Green tensor $\mathbf{B}$. The expressions f_{PE} and f_{SE} were calculated based on Eqs. 3.6, 3.8.

All in all, the constitutive model proposed involved five material parameters; three passive (A, G, K), one active (C_{CE}) and the maximum tetanic stress (T_0).

3.2 Literature-based exploration of the model parameters

For the passive parameters, thorough literature review showed that no specific values have been reported for back muscles. As such, initial parameter definition was based on the existing data for skeletal muscles.

Since the matrix was represented as nearly incompressible, K was prescribed to be 1000 times G ([258], [288]), the value of G being derived from [254]. As for A, a parameter value set to 4 gave the best fit to the experimental curve based on the measurements of [286] in frogs. Given the similar striated form of human and frog skeletal muscles, this value was later used in human muscle constitutive models, such as in [254] and [261], and was also adopted in the present model. T_0 has been found to vary both from species to species and from subject to subject. According to the reported range of 0.16-1 MPa reported for skeletal muscles [256], an average value equal to 0.46 MPa was used similar to [183]. Parameter values are summarized in Table 3.1.

Table 3.1: Literature-based definition of the constitutive model parameters (A, K, G, T_0).

PE parameters		Matrix parameters	
A (dimensionless)	4·2	G (MPa)	$16{\cdot}420\times10^{-4}$
T_0 (MPa)	0·46	K (MPa)	1·642

In [254], the authors controlled the muscle contraction through different ζ^{CE} values each of which represented a different deformation state of the simulated muscle. That is, the ζ^{CE} parameter was treated directly as muscle strain ε. In this framework, the ζ^{CE} was rather considered as strain adjusted via the active parameter C_{CE} for each muscle (Eq. 3.9). Nonetheless, no C_{CE} values could be found in the literature. Hence, a first set of values was calculated for the MF, PS, IL and LT muscles (Table 3.2) based on Eq. 3.11 and the L^S estimations per muscle as reviewed in [27].

Table 3.2: Literature-based definition of the C_{CE} parameter.

CE parameters		
C_{CE} (dimensionless)	MF	0·811
	LTpL, LTpTh	0·825
	ILpL	0·846
	PS	1·111

However, when tested for single fascicle elements, these values did not always allow fulfilling the strain-based criteria (Eq. 3.8) in order to induce activation. Therefore, a parametric analysis was performed to explore the C_{CE} in a range of strain levels potentially achieved during loading of the spine.

3.3 Parametric study of the C_{CE} parameter

Based on Eq. 3.8, the active parameter C_{CE} controls the muscle contraction through the value of the criterion:

$$f_{crit} = \overline{\lambda}_f - 1 - \zeta^{CE} \tag{3.17}$$

where $\overline{\lambda}_f$ is the modified fascicle stretch. For any differential line element, $\overline{\lambda}_f$ can be related to the engineering strain ε through:

$$\overline{\lambda}_f = J^{-1/3}\lambda_f = \lambda_f^{2/3} = (\varepsilon_{11} + 1)^{2/3} \tag{3.18}$$

considering that when the truss element (i.e. fascicle) is aligned with the x_1-axis the Jacobian determinant $J = \lambda_1 = \lambda_f$. As such, using Eqs. 3.9 and 3.18, the criterion in Eq. 3.17 can be rewritten as:

$$f_{crit} = (\varepsilon_{11} + 1)^{2/3} - 1 - \varepsilon_{11} C_{CE} \tag{3.19}$$

The above formulation was used to define: (i) two C_{CE} values as activation thresholds and, (ii) a specific set of values based on these thresholds for each simulated muscle when the latter is concentrically (C_{CE1}) and eccentrically (C_{CE2}) contracted. Only values allowing to fulfill the strain-based criteria for muscle activation were accepted ($f_{crit} > 0$). The explored strains ranged between ±30% considering previous experimental models reporting that sustained compression over 20% [289] or excessive stretching above 30% strain [290] may increase the risk of cytoskeletal damage [291]. Actually, numerical simulations showed that only one fascicle deformed up to 19% in flexion, and around ±2% in standing (Chapters 4 and 5).

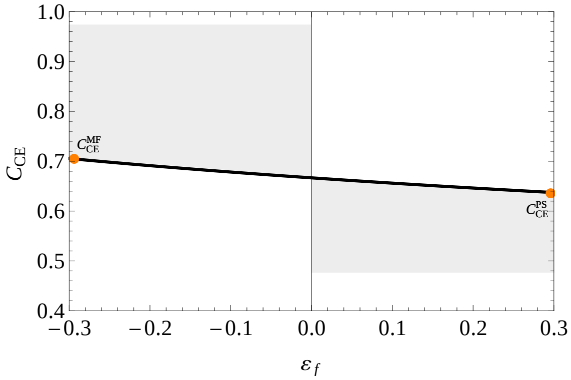

Figure 3.2: Activation thresholds (C_{CE}^{MF}, C_{CE}^{PS}) calculated from Eq. 3.9, and suggested range of C_{CE} values (shadow regions) under different deformation levels.

As shown in Fig. 3.2, two limit C_{CE} values were calculated: 0.706 in maximum concentric contraction and 0.637 in maximum eccentric contraction. In order to suggest a set of C_{CE} values per muscle (one for each type of contraction), a hypothesis was made based on the morphometric data reviewed in [27]: since MF had the shortest sarcomeres in length (L^S) among the studied muscles, it was assumed that the limit value found in concentric contraction should be assigned to MF. Then the C_{CE} for the rest of the muscles were calculated by preserving the proportion of activation between each muscle and MF as described in Eq. 3.20 below. The same concept was used in eccentric contraction where the limit C_{CE} value was assigned to PS (longest sarcomeres) and therefore the proportions were calculated related to this muscle as follows:

$$C_{CE} = \begin{cases} C_{CE}^{MF} \times \dfrac{L^S}{L_{MF}^S} & \text{if } \varepsilon_f < 0 \\ \\ C_{CE}^{PS} \times \dfrac{L^S}{L_{PS}^S} & \text{if } \varepsilon_f > 0 \end{cases} \tag{3.20}$$

where L^S values were derived from [27], C_{CE}^{MF} is equal to 0.706, and C_{CE}^{MF} to 0.637. The values were considered to be consistent among all fascicles of the same muscle and are summarized in Table 3.3. Grey shadow regions in Fig. 3.2 show the range of the C_{CE} values suggested in both types of contraction.

Table 3.3: C_{CE} parameter values per muscle based on the parametric study (CE1=Concentric contraction, CE2=Eccentric contraction).

CE parameters		C$_{CE1}$/C_{CE2}
C_{CE} (dimensionless)	MF	0.706/0.465
	LTpL,LTpTh	0.718/0.473
	ILpL	0.737/0.485
	PS	0.967/0.637

As such, in order to calculate the active contraction of each muscle through Eq. 3.8, an updated ζ^{CE} was considered per muscle depending on whether the fascicles were shortened (C_{CE1}) or stretched (C_{CE2}):

$$\zeta^{CE} = \begin{cases} C_{CE1} \cdot \varepsilon_f & \text{if } \varepsilon_f < 0 \\ C_{CE2} \cdot \varepsilon_f & \text{if } \varepsilon_f > 0 \end{cases} \tag{3.21}$$

In total, a set of six parameter values was required for the full definition of the material properties of each muscle: four parameter values for the (A, K, G, T_0) as described in Table 3.1 that were common for all simulated muscles, and another set of two values for the active parameter C_{CE} as reported in Table 3.3 that was different per muscle.

3.4 Patient-specific calibration of the model parameters

A step forward would be the definition of a personalized set of muscle parameters, hereafter named *patient-specific*, in order to represent more realistically the muscle function of a patient based on kinematical data of subjects with LBP. An indirect way to perform this is through correlations between KD-driven and FE-predictive force results. That is, KD fascicle force estimations derived from a previously reported RB model of a degenerated spine using inverse dynamics analysis and static optimization [28] were compared with the (FE) force predictions based on the constitutive model presented. The objective was the calculation of an optimum set of muscle parameter values that match the fascicle force results.

3.4.1 Design of the optimization scheme

The optimization scheme was designed to calculate the values of all five muscle parameters per fascicle and per lumbar level. At first, FE models were developed using single truss elements in the FE commercial software ABAQUS (Simulia, Providence, RI, USA) for all the fascicles of the MF, ILpL and LTpL with attachments between L1/L2 and L5/S1 levels. For their definition, geometrical properties were derived from [183]. In [28], a hyperlordosis (extension-like) motion was simulated based on the kinematical range of motion and spinal curvature derived from *in vivo* dynamic MRI of a patient with LBP. Therefore, to reproduce the motion, each fascicle model was deformed according to the calculated musculo-tendon (MT) length changes that were provided by the authors (UMR CNRS 7338 Biomechanics and BioEngineering group, UTC, Compiègne, FRANCE).

An objective function was defined as the average least square difference between the KD and FE estimated fascicle forces during hyperlordosis motion as follows:

$$X_{hyp} = \frac{\sum_{j=1}^{N} (KD_j - FE_j)^2}{N} \tag{3.22}$$

where

$$FE_j = \boldsymbol{\sigma_j}(x(k)) \cdot PCSA_j \tag{3.23}$$

with $\boldsymbol{\sigma}(x(k))$ calculated as in Eq. 3.16 for each fascicle j, and N the number of points considered for the optimization between the reference (supine) and the final deformed (max extended) position. When only maximum extended position is considered, then $N = 1$. The downhill simplex method was run in the commercial software MATLAB R2009a (The Mathworks, Inc., Natick, MA) through a user-defined script to minimize the objective function (Eq. 3.22) and to calculate an optimum vector $x(k)$ for the constitutive parameters, where $k = 1, ..., 5$ corresponded to T_0, G, K, A, C_{CE}, respectively. The values for the initial vector $x_0(k)$ to be optimized were chosen based on Tables 3.1 for T_0, G, K, A, and Table 3.3 for C_{CE1} or C_{CE2} depending on the type of contraction. For all parameters but T_0 values were constrained to be positive, while for T_0 the reported range between 0.16 and 1 MPa [256] was used as a constraint.

FE-predicted forces (FE) were obtained by coupling the constitutive equation scheme (Eqs. 3.1 - 3.16) to each fascicle model via user-defined material subroutines (UMAT) and imposing the displacement as calculated by the MT length change (Table 3.5). KD force estimations (KD) were directly derived from [28]. All in all, the optimization scheme was defined as follows:

$$\text{minimize } X_{hyp}$$

subject to:

$$0.16 < x(1) < 1.0, \;\; x(2) > 0, \;\; x(3) > 0,$$
$$x(4) > 0, \;\; x(5) > 0,$$
$$x_0(k) = (0.46,\, 0.001642,\, 1.642,\, 4.0,\, C_{CE1} \text{ if } \; \varepsilon_f < 0, \; or \; C_{CE2} \text{ if } \varepsilon_f > 0)$$

Optimizations were run for 25 single truss models of the local fascicles, i.e. MF, lumbar IL and LT. The parameter set for thoracic LT was not optimized since these fascicles were not represented in the KD-model [28].

3.4.2 Optimized muscle parameter values per fascicle and lumbar level

Optimization results were obtained for all 25 fascicles in low real time (about 4 hours per fascicle). The algorithm was tested using either one or multiple points N resulting in minor differences on the optimized values. Hence, only the results with one point are reported here. Fig. 3.3-3.5 were used to analyze the values obtained per level and per fascicle.

For T_0, optimization results (0.47 - 0.51 MPa) varied up to maximum 10% from the initial T_0 (0.46 MPa). Particularly, for MF (Fig. 3.3), the maximum variation calculated among fascicles of the same level was approximately 3% at L2/L3. For ILpL (Fig. 3.4) and LTpL (Fig. 3.5), the max T_0 value (L5/S1) was around 4 and 6% higher than the minimum value calculated for each muscle, respectively. The optimized values lied around the mean of the suggested range from 0.23 to 1.0 MPa for different skeletal muscles available in the literature ([233], [292], [293], [183], [294], [295], [296]). Still, since T_0 values have not been previously explored per fascicle, no straightforward correlation could be performed.

For G, low variation around 2 and 3% was calculated from the initial guess (1.642 x 10^{-3} MPa) for most muscle fascicles. Maximum optimization value was calculated for MF (Fig. 3.3) and ILpL (Fig. 3.4) at L2/L3 level (1.695 x 10^{-3} MPa). For K, the proportion of 1000 times the G value to simulate a nearly incompressible tissue was preserved for most fascicles after the optimization (Table 3.4). For MF, K optimization values at all levels but L4/L5 were around 1.46 MPa being approximately 12% lower than the initial value (1.642 MPa) (Fig. 3.3). The results for ILpL and

LTpL had a similar inter-level variation with values decreasing caudally down to 1.407 MPa at L5/S1 (Fig. 3.4, 3.5).

As discussed previously, A is a phenomenological parameter that was fitted against f-l measurements performed in frogs [286]. For the majority of the fascicles, the optimized parameter values ranged around the initial guess equal to 4.0 corresponding to the best experimental fit (Table 3.4). Optimizations gave minimum value of 3.4 for MF at the uppermost lumbar level, while the results for all other MF fascicles and the other two muscles were slightly lower than 4.0 (Fig. 3.3, 3.5).

For C_{CE}, the optimization algorithm calculated 25 values, that is one per fascicle and per level as listed in Table 3.4. Fig. 3.3-3.5 show that, for all muscles studied, the results presented a small caudal inter-level increase of the activation value. Parameter C_{CE} ranged from 0.81 to 0.91 among the fascicles of all three groups and it was always higher than the initial guess (C_{CE1} or C_{CE2}) (Table 3.3). By calculating the average per muscle, mean optimized values of 0.84, 0.83 and 0.84 were found for MF, ILpL and LTpL, respectively. Compared to the morphology-based calculations performed previously (Table 3.2), small relative differences were calculated demonstrating the realistic nature of the values obtained. Indeed, deformation of full FE LS models showed that assigning one C_{CE} (optimized value) per fascicle without strain criteria allowed always muscle activation for the simulated activities where muscles were never strained over ±20% (Chapters 4, 5). Moreover, towards the general objective of fully personalized models, the consideration of one P-SP C_{CE} value per fascicle is also advantageous since it reduces the necessary number of parameter values to be defined per model.

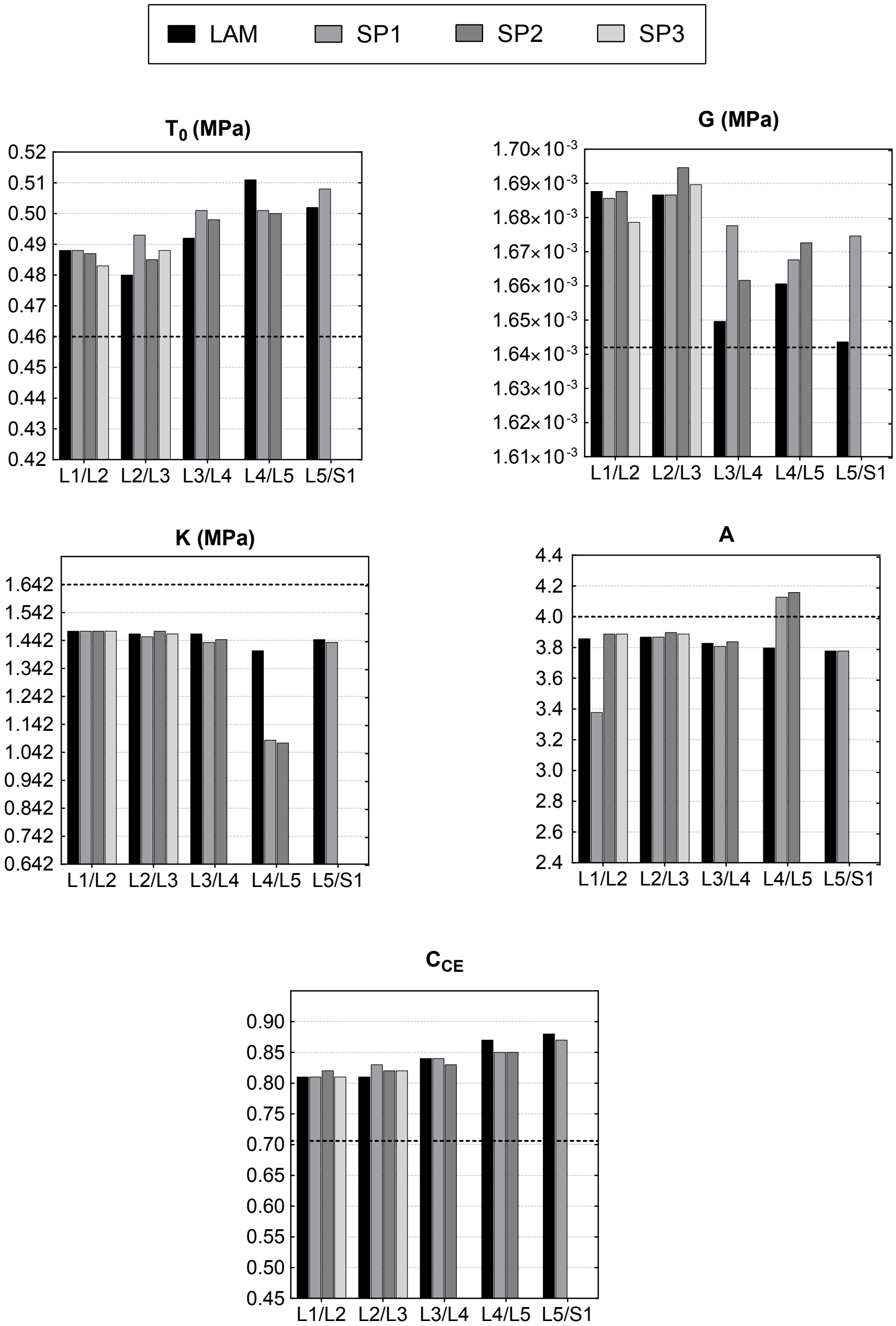

Figure 3.3: Variation of the optimized parameter values for MF calculated per level and per fascicle. Dashed lines correspond to the generic parameter values.

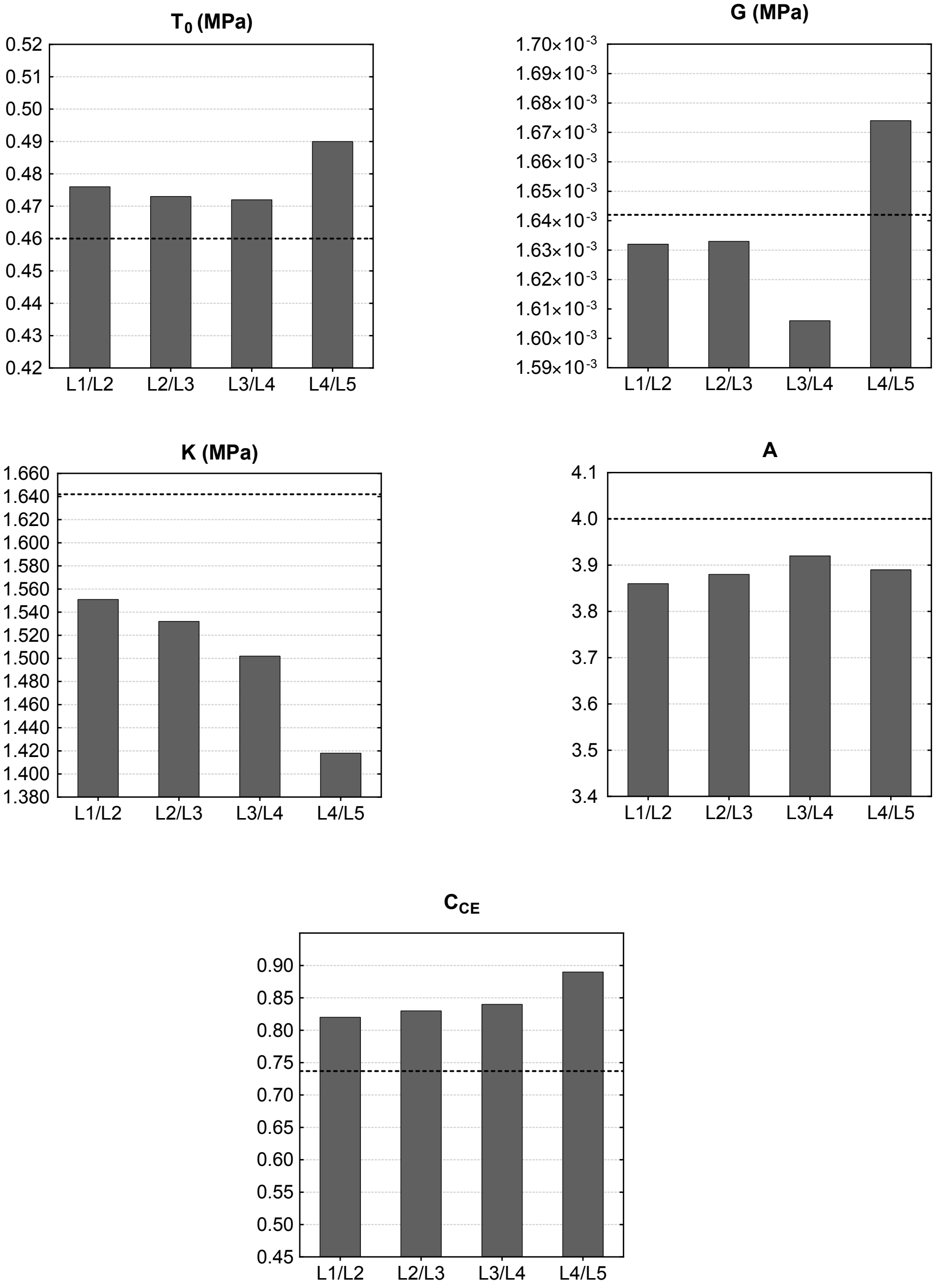

Figure 3.4: Variation of the optimized parameter values for ILpL calculated per level and per fascicle. Dashed lines correspond to the generic parameter values.

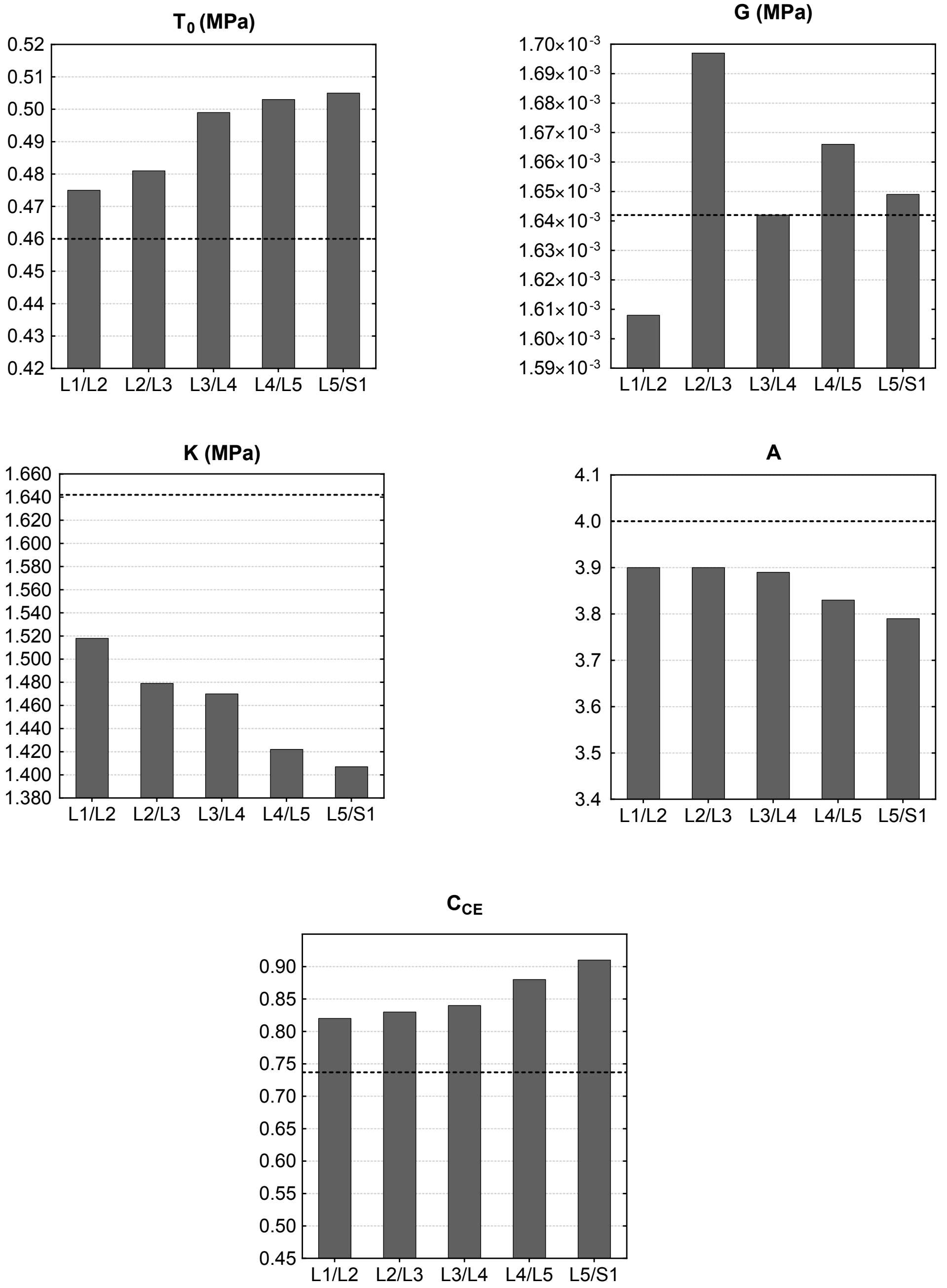

Figure 3.5: Variation of the optimized parameter values for LTpL calculated per level and per fascicle. Dashed lines correspond to the generic parameter values.

Table 3.4: Optimization results of the muscle parameters calculated for the MF and lumbar IL, LT per level and fascicle.

MF			**Muscle parameter**		
Level	T_0 (MPa)	G (MPa)	K (MPa)	A	C_{CE}
L1L2	0.488/0.488/0.487/0.483	1.688/1.686/1.688/1.679 x 10^{-3}	1.476/1.478/1.478/1.479	3.87/3.39/3.90/3.90	0.81/0.81/0.82/0.81
L2L3	0.480/0.493/0.485/0.488	1.687/1.687/1.695/1.690 x 10^{-3}	1.475/1.462/1.478/1.473	3.88/3.88/3.91/3.90	0.81/0.83/0.82/0.82
L3L4	0.492/0.501/0.498	1.650/1.678/1.662 x 10^{-3}	1.469/1.436/1.448	3.84/3.82/3.85	0.84/0.84/0.83
L4L5	0.511/0.501/0.500	1.661/1.668/1.673 x 10^{-3}	1.476/1.090/1.077	3.81/4.14/4.17	0.87/0.85/0.85
L5S1	0.502/0.508	1.644/1.675 x 10^{-3}	1.451/1.442	3.79/3.79	0.88/0.87

ILpL			**Muscle parameter**		
Level	T_0 (MPa)	G (MPa)	K (MPa)	A	C_{CE}
L1L2	0.476	1.632 x 10^{-3}	1.551	3.86	0.82
L2L3	0.473	1.633 x 10^{-3}	1.532	3.88	0.83
L3L4	0.472	1.606 x 10^{-3}	1.502	3.92	0.84
L4L5	0.490	1.674 x 10^{-3}	1.418	3.89	0.89
L5S1	-	-	-	-	-

LTpL			**Muscle parameter**		
Level	T_0 (MPa)	G (MPa)	K (MPa)	A	C_{CE}
L1L2	0.475	1.608 x 10^{-3}	1.518	3.90	0.82
L2L3	0.481	1.697 x 10^{-3}	1.479	3.90	0.83
L3L4	0.499	1.642 x 10^{-3}	1.470	3.89	0.84
L4L5	0.503	1.666 x 10^{-3}	1.422	3.83	0.88
L5S1	0.505	1.649 x 10^{-3}	1.407	3.79	0.91

Next, the FE force predictions before and after the optimization were studied in relation to the KD estimations from [28]. As listed in Table 3.5, a remarkable decrease was calculated for all fascicle forces and particularly for those arising from the upper lumbar levels. The perfect agreement in the force values between the two models achieved after the optimization demonstrated the robustness of the designed scheme. Interestingly though, such significant reduction in the force magnitudes did not correlate with the small variation of the parameter values obtained.

Table 3.5: Fascicle forces calculated using the FE-predictive model before and after the optimization.

Muscle	Level	**Fascicle forces (N)**		
		FE	FE$_{opt}$	KD[a]
MF[b]	L1L2	13.30/27.76/22.53/26.44	0.09/0.19/0.16/0.28	0.09/0.19/0.16/0.28
	L2L3	27.81/16.94/60.93/53.09	0.10/0.44/0.44/0.45	0.10/0.44/0.44/0.45
	L3L4	53.09/27.76/16.12	0.25/0.24/0.24	0.25/0.24/0.24
	L4L5	20.01/4.91/4.83	0.14/0.22/0.21	0.14/0.22/0.21
	L5S1	12.14/14.19	0.33/0.10	0.33/0.10
ILpL	L1L2	52.23	0.96	0.96
	L2L3	64.92	1.69	1.69
	L3L4	53.14	1.46	1.46
	L4L5	23.20	2.92	2.92
	L5S1	-	-	-
LTpL	L1L2	41.77	0.35	0.35
	L2L3	41.77	0.40	0.40
	L3L4	25.54	0.47	0.47
	L4L5	11.72	0.48	0.48
	L5S1	11.72	0.50	0.50

[a] Dao et al. [28]

[b] First value corresponds to the fascicle arising from the laminar process (LAM) and the following to those arising from the spinous processes (SP) varying in number between one and three depending on the level.

As aforementioned, in order to reduce the computational cost of the procedure, initial FE predictions were made using single fascicle elements instead of full LS MSL models. As a result, the predicted fascicle forces in each case did not take into account the synergistic effect of other muscles. Such limitation might explain the significantly higher FE force values calculated before the optimization. Furthermore, since the optimization scheme was coupled to isolated muscle fascicles, the minimization of the objective function was also performed each time for the particular fascicle without considering, for example, the mechanical response of the rest of the fascicles at that level. The KD force estimations on the contrary were obtained after a simultaneous minimization of the fascicle activations using a full lumbar kinematical model [28]. Therefore, such simplifications in the configuration used might explain the small deviation of most optimized values from the initial parameter vector x_0.

A closer analysis of the relation between parameter sensitivity and the minimization of the objective function X_{hyp} was necessary to better interpret the results. For each fascicle, parameter values were plotted against the corresponding values of the objective function until the X_{hyp} reached its global minimum value and each parameter was optimized. As such, for instance, for ILpL, five plots were generated per fascicle, making in total 20 plots for this muscle. The C_{CE} variation pattern was found to clearly follow the minimization profile of the objective function for most fascicles (Fig. 3.6), while among the passive parameters a more irregular pattern was seen (Fig. 3.7).

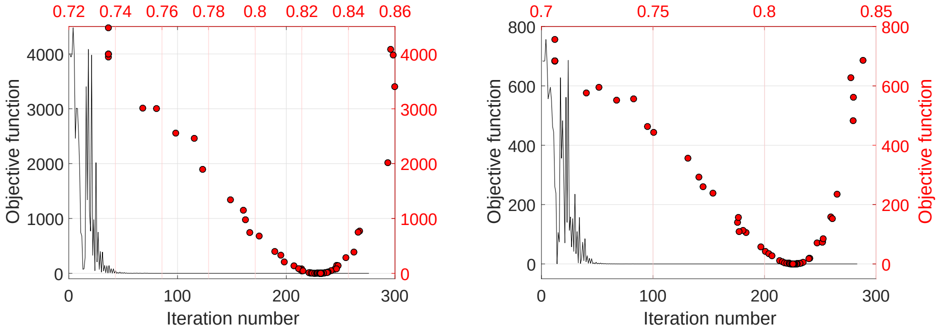

Figure 3.6: Variation of the C_{CE} values (red horizontal axis) during the minimization of the objective function: L2 ILpL (left) and L1 MFS3 (right).

In some cases, such as the ILpL at L4/L5 and MF at L5/S1 (Fig. 3.8), apart from the C_{CE}, parameters K and A also showed an important effect on the reduction of the X_{hyp}. It was suggested therefore, that the combined effect of the minimizing

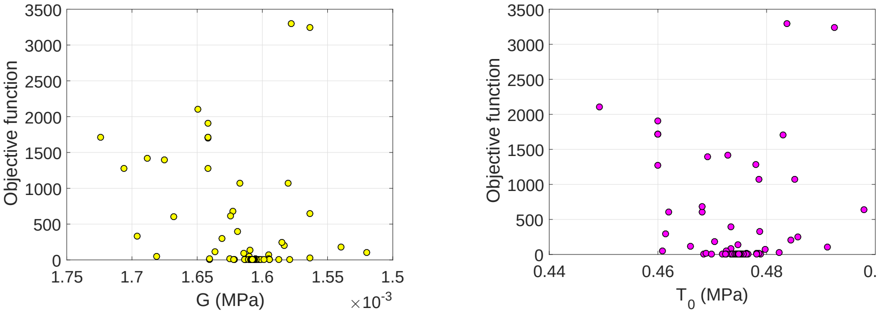

Figure 3.7: Variation of the G (left) and T_0 (right) parameter values for the L1 LTpL.

pattern of three parameters (i.e. C_{CE}, K, A) might be related to the dramatic decrease in force predictions.

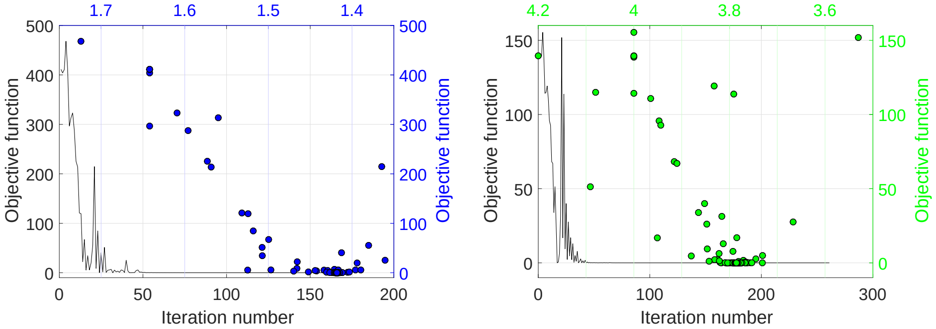

Figure 3.8: Variation of the K (blue horizontal axis) and A (green horizontal axis) during the minimization of the objective function: L4 ILpL (left) and L5 MF (right).

To sum up, a P-SP set of five parameter values was defined for each of the 25 fascicles optimized making in total a number of 80, 25 and 20 parameter values defined for the MF, lumbar LT and lumbar IL fascicles, respectively (Table 3.4). Whether the optimized set of values would vary significantly if KD estimations were calculated under a different physical task, such as flexion, or if a multi-objective optimization algorithm was used ([297], [298]) cannot be anticipated. Ideally, a specific set of muscle parameter values must be defined per each subject studied.

All in all, with all limitations in mind, the methodology proposed managed to address the following points:

- The development of a novel constitutive equation assembly that involved a limited number of five parameters able to be personalized using, for instance, elastography [115] or dynamic MRI techniques [28].
- The numerical exploration of the range of values of the basic muscle mechanical parameters, such as the T_0, G and K, for the first time for the lower back muscles.
- The suggestion of an optimized set of parameter values per fascicle that seems particularly appropriate to calculate realistic f-l curves using the constitutive formulation proposed.

Chapter 4

Development of a generic L3-S1 FE musculoskeletal model

4.1 Introduction

In Chapter 3, a novel hyperelastic, constitutive formulation was presented aiming to describe muscle contraction by decoupling the active and passive contributions of its components (matrix and embedding fibers). In this chapter, a L3-S1 FE MSL model will be developed to test the ability of this methodology to simulate the function of major back muscles in three spine postures: flexed, standing and lying, the latter mimicking the trunk position during night rest. The definition of the loading conditions applied to simulate each posture, and the material properties assigned to the tissues involved, i.e. IVD, vertebrae, ligaments and muscles, will be detailed. For all simulations, the muscle/osteoligamentous spine relationship will be assessed by studying the predicted muscle activation patterns, muscle strains and forces, as well as the IDP. The load distributions obtained after rest will be used to address the existence of possible interactions between muscle function and IVD multiphysics. As an indirect validation of the method proposed, experimental data from previous studies will be used for correlations with the IDP values predicted by the model.

4.2 Methods

For the osteoligamentous geometry, a bi-segment FE model developed previously [299] featuring the L3-L5 lumbar levels was used as a base model. This assembly was first extended to include the lumbosacral joint (L5/S1) whose sagittal balance was proportionally related to the model's lordosis according to anatomical measurements ([300], [183]). Fig. 4.1 shows the generic (healthy) FE MSL model developed involving the L3-S1 lumbar levels. The model has four different groups of element-type: shell elements (vertebrae), hexahedral elements (discs and facets), truss elements (muscles and ligaments), and beam elements (network for load application).

4.2.1 Modeling the back muscle network

4.2.1.1 Geometry

A muscle architecture was developed representing the major local (attached to lumbar vertebrae and sacrum: MF, LTpL, ILpL) and global (attached moreover to thoracic and femur levels; LTpTh, PS) muscles related to the lumbar region. The bony insertions of the relevant muscle fascicles were adapted on the specific anatomy of the previously described FE model. Overall, the L3-S1 muscle network consisted of 23 sagitally symmetric fascicle pairs (13 local and 10 global) as presented in Fig. 4.1. Unidirectional elements (T3D2 element type) with straight lines of actions were used to model all fascicles without considering muscle wrapping. Fascicle 3D orientations and equivalent PCSA were based on anatomic studies and radiographic measurements as reported by ([183],[128],[27]). Table 4.1 summarizes the PCSA and the MT rest lengths defined per fascicle and level.

For the MF, a multi-segmental arrangement was simulated following previous anatomical descriptions ([162],[37]). Three antero-posterior groups were introduced for the deep, intermediate and superficial fascicles with insertions distributed along the lumbar and sacral levels. In total, the MF involved eight fascicle pairs.

The geometry of each LTpL and ILpL fascicle with a known origin O was represented according to the approximation proposed in [183] (Fig. 4.2). A set of axial (X_a)

Table 4.1: Geometrical muscle modeling parameters per fascicle between L3 and S1.

Muscle	Fascicle	PCSA (mm^2)	$L_0^{CE}(mm)$
MF	L3	23	41.32
	$S_{3,1}$	52	76.22
	$S_{3,2}$	52	136.14
	L4	17	41.46
	$S_{4,1}$	47	68.70
	$S_{4,2}$	47	111.37
	L5	36	169.99
	$S_{5,1}$	23	69.83
ILpL	L3	182	86.91
	L4	189	50.31
LTpL	L3	103	106.60
	L4	110	66.86
	L5	116	26.67
LTpTh[a]	L3	56	63.01/173.40/81.93
	$L_{4,1}$	45	92.98/129.11/108.49
	$L_{4,2}$	44	61.36/202.47/55.27
	L5	64	91.72/176.10/60.67
PS	TP_3	173	252.42
	L3L4	191	233.06
	TP_4	120	224.57
	L4L5	119	205.58
	TP_5	36	195.21
	VB_5	79	184.54

[a] The multiple L_0^{CE} values per level correspond to the short fascicles attached between the lumbar and thoracic levels. For instance, LTpTh3 consists of one fascicle with insertions into L3 and L1 TP, and another two between L1, T7 and T7, T3 levels.

and shear (X_s) lines of action was resolved in the local Coordinate System (CSYS) of the vertebra of origin and of each successively lower level k interposed between the origin and insertion points as follows:

$$X_{a_0} = X_{sag} \cdot cos\lambda, \qquad X_{a_m} = \frac{X_{a_0} \cdot cos\left(\lambda_0 - \sum_{k=1}^{m} \beta_k\right)}{cos\lambda_0} \tag{4.1}$$

$$X_{s_0} = X_{sag} \cdot sin\lambda, \qquad X_{s_m} = \frac{X_{s_0} \cdot sin\left(\lambda_0 - \sum_{k=1}^{m} \beta_k\right)}{sin\lambda_0} \tag{4.2}$$

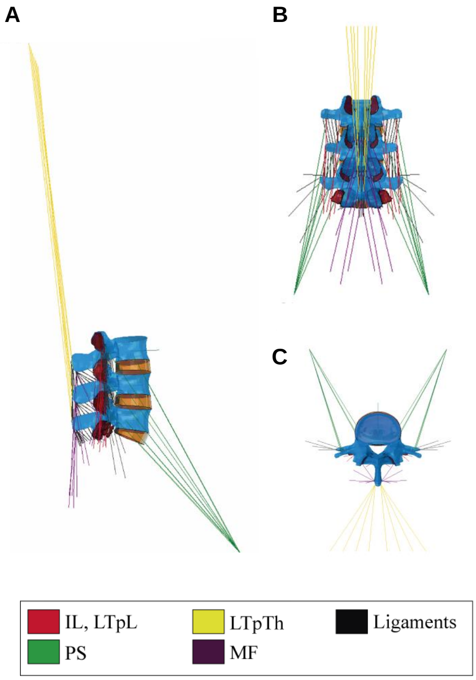

Figure 4.1: (A) Right sagittal, (B) frontal and (C) top transverse views of the L3-S1 FE MSL spine model.

where X_{sag} the sagittal fascicle projection, λ the angle between the fascicle and the long axis of the vertebra, and β and β_k the intersegmental lordotic angles at the level of origin or at each successive level k. X_{sag} and λ values were directly derived from [183], while β, β_k angles were calculated based on the FE lumbar spine geometry of each model. For the LTpL, one fascicle pair was simulated per lumbar level, i.e. in total three pairs for the L3-S1 model. For the ILpL, two fascicle pairs were modeled according to the descriptions discussed in 2.2.5.

Due to the lack of thoracic cage representation in the models, the LTpTh fascicles were modeled with cranial insertions reconstructed to simulate the lines of action that virtually reach the T3–T6 levels of the thorax. For the initial configuration explored, i.e. L3-S1 model, a common MT rest length was assumed for all thoracic elements based on the L3 LTpTh length reported in [27]. Accordingly, a common rostral insertion of the fascicle cranial ends was hypothesized as an enlarged transverse process of the third thoracic vertebra (T3) and was modeled as a rigid rod as shown in Fig. 4.1A. In total, four fascicles of the LTpTh were incorporated on each side of the L3-S1 model.

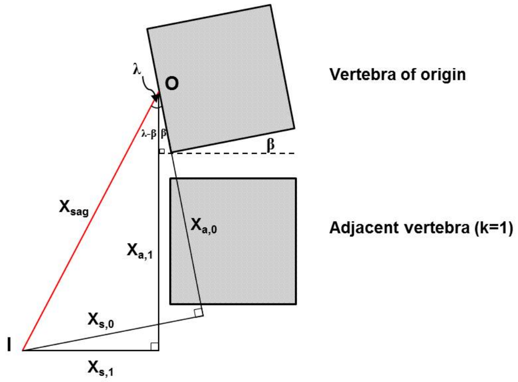

Figure 4.2: A diagram of a motion segment showing the relationship between the (a)xial and (s)hear vectors of the fascicle OI (O=origin; I=insertion point).

As for the PS, in lack of femur geometry, the site of the common caudal insertion (femoral lesser trochanter) was approximated in relation to the PS rest lengths reported by ([27], [128]), to the sacral attachments of the longest fascicles of the model, i.e. the MF superficial fascicles, and to the femur FE model of [301]. That is, based on [37], the caudal attachment points of the L3/L4 MF superficial fascicles lie lateral to the 4th posterior sacral foramina site. In an average human pelvis, this foramina could be approximately considered as horizontally aligned to the femoral head in the frontal plane (Fig. 4.3). Accordingly, the axial distance between the femoral head and the lesser trochanter eminence in the configuration of [301] was used as a proportion for the definition of the PS femoral insertion based on the modeled MF superficial fascicle insertions into the sacrum. In addition, manual calculations of the sacrum and vertebra proportions

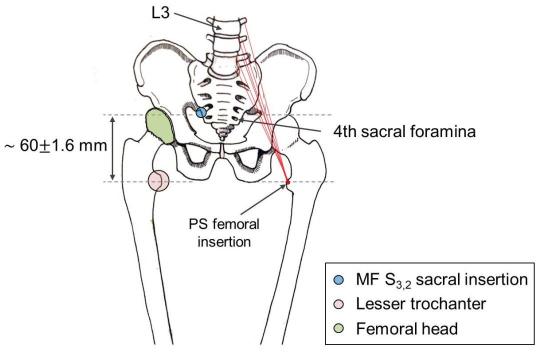

Figure 4.3: Definition of the PS fascicle femoral insertion. MF S3,2 refers to the MF superficial fascicle arising from L3/L4.

between a human skeleton (male subject, Sawbone) and the spines measured in [37] were performed ($\sim 1.7{:}1$) in order to confirm a realistic representation of the muscle anatomy in the model. In total, six overlapping segmental fascicles were incorporated on each side between the anterolateral aspects of the vertebra and the lesser trochanter of the femur.

4.2.1.2 Material parameters

In the L3-S1 FE model, the passive parameter values for all muscles were defined as in Table 3.1. For the active parameter C_{CE}, the values calculated from the parametric study reported in Table 3.3 were assigned.

4.2.2 Description of the material behavior of the passive tissues

4.2.2.1 Ligaments

The model included seven groups of ligaments (ALL, PLL, LF, CL, SS, IS, ITL) represented by truss elements as in [228]. Non-linear elastic tensile behavior, modeled through a power law for the toe region and via a linear stress-strain relationship for the linear region was defined for all groups involving in total three material parameters (A, B and C) [82]. Parameter values based on experimental data were assigned to the ligaments per level as reported in Table 1 of the cited study.

4.2.2.2 VB

The shells that represented the VB were modeled as a quasi-rigid material using isotropic elastic properties. A Young's modulus equal to 30 GPa and Poisson's ratio of 0.3 were prescribed to all lumbar VB levels.

4.2.2.3 IVD

As described in 2.5.1, poro-hyperelastic behavior for the AF and NP and poro-elastic for the CEP with strain-dependent permeability (Eq. 2.10) were considered for all disc sub-structures (NP, AF, CEP) based on the Biot theory and previously reported studies ([302], [279]). For the NP, an osmo-porohyperelastic law (Eqs. 2.5, 2.7) involving the tissue swelling capacity was implemented via user-defined material subroutines (UMAT). The AF was modeled as anisotropic poro-hyperelastic material reinforced with two families of fibers through the Holzapfel-Gasser-Ogden form already implemented in Abaqus libraries (Eqs. 2.7, 2.8). No material transition zone was included between the AF and NP. The CEP behavior was defined via a poroelastic material also implemented. At all lumbar levels, poromechanical properties for healthy discs were assigned per region (Table 4.2) to conduct simulations for healthy subjects.

Table 4.2: Set of poromechanical properties for the simulated healthy discs.

	e_0[a]	κ_0 (mm^4/N s)[a]	M[a]	G (MPa)[b]	K (MPa)	$\Delta\pi$ (MPa)[a]
AF	3.0	0.0002	8.5	0.95	0.37[a]	-
NP	4.9	0.0009	8.5	0.47	0.16[a]	0.15
CEP	4.0	0.0025	8.5	8.55	10.10[b]	-

[a] Derived from [279].
[b] Calculated based on the mechanical properties (E, ν) reviewed in [302].

4.2.3 Boundary conditions and simulated postures

4.2.3.1 Boundary conditions

For the local muscles, displacements of the sacral attachment points were constrained in all directions ($U_i = 0$, $i = x, y, z$ direction). For the LTpTh, the rigid rod discussed before was only constrained in the sagittal plane for the simulation of standing position ($U_y = 0$). The lower endplate of the L5/S1 IVD as well as the upper facets of S1 that were included in the model were fixed in all directions for all simulations. A condition of free fluid flow was simulated at the external disc boundaries by considering nil external pore pressure ($P = 0$).

4.2.3.2 Simulated postures

- **Flexion**

An anterior sagittal rotation of 10° was simulated on the uppermost lumbar level of the model, i.e. L3/L4, along a time step of 80 sec. The rotation vector was applied to a central node so that it would be transferred to the spine along a beam network attached to the L3 BEP as shown in Fig. 4.4.

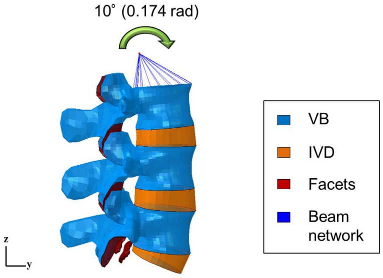

Figure 4.4: Point of application of the 10° rotation to simulate forward flexion.

- **Lying**

In order to represent rest position, a free IVD swelling condition due to an initial gradient of osmotic pressure $\Delta\pi$ between the NP and the IVD boundaries was considered at all levels according to [303]. A swelling equal to 0.15 MPa was applied in the NP (Fig. 4.5) and was simulated for a period of 8 hours aiming to mimic a typical overnight rest.

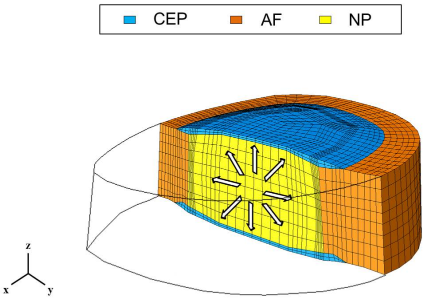

Figure 4.5: Osmotic pressure equal to 0.15 MPa was applied to the NP of all discs to simulate lying position (night rest).

- **Standing**

For the simulation of standing posture, a heterogeneous distribution of body volumes and densities along the spine was considered according to ([304], [305]). The magnitude and point of application of an equivalent gravity load per simulated level was calculated for a given BW (70.8 kg for the L3-S1 model). To do this, the body mass (BM) distributions were translated into punctual static loads in function of the contribution expected from the rest of the upper body. In order to place these vertical loads, an eccentric path passing through the different segmental centers of mass, *COM*, anterior to the vertebral center, *VC*, was defined. Accordingly, the postero-anterior distance, R_i, between *VC* and *COM* was calculated per lumbar level. Fig. 4.6 shows the definition of this path according to the *COM* and *VC* locations. The methodology used was generalized in order to be useful for simulations at full L1-S1 LS models that will be detailed in Chapter 5. As such, the data presented in the following tables refer to all lumbar levels from L1 to S1.

For the loads associated to the weight of the head and the cervical spine (C1-C7), the percentages of BM per i^1 segment, $BM_i(\%)$, with respect to the total BW were defined based on previous average estimations for an adult subject [306]. The values of the mass moment of inertia, Iz_i,^{2} were derived directly from the cited study, while the $BM_i(\%)$ values were calculated proportionally to the simulated BM. For the loads induced by the BM in the thoracic (T1-T12) and lumbar (L1-S1) regions, the $BM_i(\%)$ were recalculated relative to the simulated BW and the Iz_i values were adapted to these $BM_i(\%)$ in function of the R_i values reported in [304]. Table 4.3 presents all BM_i and Iz_i values used for the calculation of the effective loads at all lumbar levels.

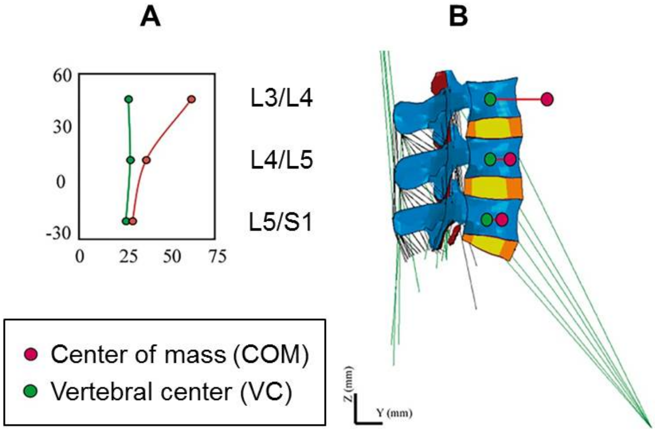

Figure 4.6: (A) The eccentric path for the gravity load distribution passing through the segmental *COM*, (B) *VC* and *COM* sites per level.

In order to compute the effective moment of inertia, $Iz_{,eff(Lj)}$, at the uppermost lumbar level j of a model, i.e. at L3/L4 for a L3-S1 model (j=*3*) , or at L1/L2 for

---

[1] i refers to HD and all vertebrae from C1 to L5.

[2] z is the axial direction

a L1-S1 model (*j=1*), the Huygens-Steiner theorem was taken into account for all i upper segments. That is, for a configuration including only the lumbar levels between L3-S1, the $Iz_{,eff(Lj)}$ considers 14 levels (from T1-T12 and L1-L3), while for a L1-S1 model, the $Iz_{,eff(Lj)}$) would take into account 12 levels (from T1-T12). As such, the moment of inertia, $Iz_{i,Lj}$, of each of the aforementioned i spinal segments was calculated with respect to the vertical axis, COM_j, passing through the L_j/L_{j+1} COM. For instance, for the L3-S1 model, the $Iz_{i,L3}$ was the product of $BM_i(kg)$ with the square of the perpendicular distance, d_i, between the axis COM_3, and the vertical axis, COM_i, that passes through the COM of level i. The following equation is given in a generalized form ready to be used for both FE models:

$$Iz_{i,Lj} = BM_i \cdot d_i^2 \tag{4.3}$$

with *j=1* for the L1-S1 FE model, *j=3* for the L3-S1 model.

All COM_i axes were adapted to each model geometry according to the measurements reported in [304]. Importantly, since no relevant d_i values could be found in the literature for the head and cervical spine levels, the cervical curvature was hypothesized to move only slightly from the lumbar lordotic curve in the antero-posterior direction. That is, it was assumed that the respective d_i for each cervical segment i would be lower than the one reported for T1 (0.8 cm). As such, based on Eq. 4.3, the squared perpendicular distances d_i^2 would be even smaller and so the contribution of these levels on $Iz_{eff(Lj)}$ could be neglected. Overall, for the L3-S1 FE model, the total moment of inertia was calculated by summing the 14 $Iz_{i,L3}$ contributions (from T1-T12 and L1-L3) with the Iz_3 at L3/L4 with respect to COM_3. Similarly, for the L1-S1 FE model, the total moment of inertia $Iz_{eff(L1)}$ at L1/L2 was the sum of 12 $Iz_{i,L1}$ contributions (from T1-T12) plus the local moment of inertia, Iz_1, at L1/L2 with respect to COM_1 (Eq. 4.4, *j=1*). The generalized form of estimating the $Iz_{eff(Lj)}$ at the uppermost lumbar level of each model was as follows:

$$Iz_{eff(Lj)} = \sum_{T1}^{L_j} Iz_{i,Lj} + Iz_j \tag{4.4}$$

Table 4.3: Sagittal moment of inertia, moment arm, and mass properties used to calculate gravity loads.

i	Body mass (%)	Body mass (kg)[a]	$Iz_{i,tot}(kg \cdot cm^2)$[a]
HD	4.7	3.300	160.00
C1	0.6	0.404	0.63
C2	0.7	0.508	1.10
C3	0.5	0.363	0.45
C4	0.5	0.366	0.47
C5	0.5	0.371	0.49
C6	0.6	0.439	0.69
C7	0.7	0.505	1.19

i	Body mass (%)[b]	Body mass (kg)[b]	$Iz_i\,(kg \cdot cm^2)$	$Iz_{i,L1}/Iz_{i,L3}\,(kg \cdot cm^2)$
T1	1.1	0.811	4.98×10^{-1}	2.43 / 4.67
T2	1.1	0.780	0.13×10^{1}	2.34 / 4.49
T3	1.4	0.976	0.39×10^{1}	2.73 / 4.72
T4	1.3	0.920	0.72×10^{1}	2.39 / 3.68
T5	1.3	0.945	1.06×10^{1}	2.17 / 2.73
T6	1.3	0.932	1.39×10^{2}	2.05 / 1.34
T7	1.4	0.976	1.83×10^{1}	2.64 / 0.48
T8	1.5	1.049	2.22×10^{1}	3.15 / 0.17
T9	1.6	1.096	2.39×10^{1}	3.62 / 0.01
T10	2.0	1.419	2.99×10^{1}	5.11 / 0.06
T11	2.1	1.479	2.88×10^{1}	5.77 / 0.37
T12	2.5	1.767	2.97×10^{1}	7.24 / 0.87
L1	2.4	1.677	2.08×10^{1}	- / 0.60
L2	2.4	1.689	1.24×10^{1}	- / 0.27
L3	2.3	1.670	0.53×10^{1}	- / -
L4	2.6	0.180	2.18×10^{-1}	- / -
L5	2.6	0.182	2.92×10^{-2}	- / -

[a] Values are derived from [306].
[b] Values are derived from [304].

Finally, the effective distance $R_{eff(Lj)}$ at which the effective gravity load has to be applied at L_j/L_{j+1} was estimated through the resultant Iz_i and BM_i values in order to consider those superior levels not included in each model. For the lumbar levels caudal to L_j, e.g. from L4 to S1 at the lower lumbar model, local boundary loads were simply calculated by using the BM_i and Iz_i values derived from [304] (Table 4.3). Based on the above calculations, a total gravity load of 276 N was estimated for the L3-S1 model corresponding to about 40% of the simulated body weight for a 70.8 kg subject. Estimated magnitudes and distribution is summarized per lumbar level in the following table.

Table 4.4: Total gravity load distribution per level for a 70.8 kg subject.

	L3/L4	**L4/L5**	**L5/S1**
Load (N)	239.8	18.1	18.1
R_i (mm)	41.4	11.0	4.0

Simulations of all three postures were performed with the FE commercial software ABAQUS (Simulia, Providence, RI, USA) under large displacements and large strains using a coupled fluid-solid FE approach. Results were analyzed at maximum loading (e.g. at fully flexed posture in flexion) in terms of pore pressure (center of the NP), axial stress (AF and NP), muscle forces and strains (fascicle elements).

4.3 Results

4.3.1 Flexion

4.3.1.1 Muscles stresses and strains

In 10° flexion, the analysis showed activation of all fascicles and large strains over ±5% for almost half of the fascicles involved in the model. As reported in Table 4.5, at fully flexed posture the local fascicles, i.e. MF, ILpL, LTpL, were eccentrically contracted (stretched) and traction total stresses were exerted with values up to 3.09 MPa for the L5 MF. For the PS and thoracic elements the model predicted concentric contraction (shortening) and compression total stresses up to 0.015 and 0.27 MPa, respectively.

As shown in Fig. 4.7, at the beginning of the simulation, the most rostral fascicles developed traction tensile stresses while being shortened and contributed, as such, to the forward flexion of the trunk. The stress profile of these fascicles showed the dominating role of the active constitutive term predicted for strains below -2% that led to an increase of the total stress developed in the rest of the simulation.

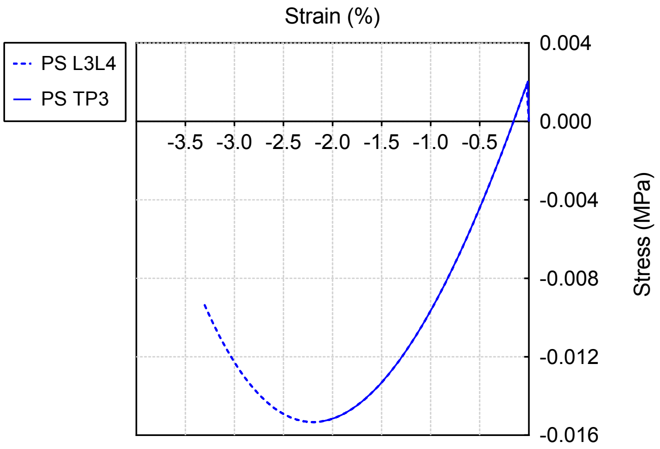

Figure 4.7: Stress-strain curve of the L3/L4 fascicles of PS in flexion.

Table 4.5: Muscle strain and total muscle stress results per fascicle and per level in flexion.

Muscle	Fascicle	Strain (%)	Stress (MPa)
MF	L3	2.6	0.13
	$S_{3,1}$	4.4	0.23
	$S_{3,2}$	5.6	0.30
	L4	6.8	0.39
	$S_{4,1}$	7.7	0.46
	$S_{4,2}$	5.9	0.33
	L5	19.2	3.09
	$S_{5,1}$	7.5	0.45
ILpL	L3	3.0	0.15
	L4	5.0	0.25
LTpL	L3	3.3	0.16
	L4	4.0	0.20
	L5	9.2	0.57
LTpTh	L3	-8.2	-0.27
	$L_{4,1}$	-6.2	-0.19
	$L_{4,2}$	-6.5	-0.20
	L5	-4.4	-0.14
PS	TP_3	-2.1	-0.015
	L3L4	-3.3	-0.009
	TP_4	-1.3	-0.012
	L4L5	-1.9	-0.015
	TP_5	-0.4	-0.003
	VB_5	-0.7	-0.006

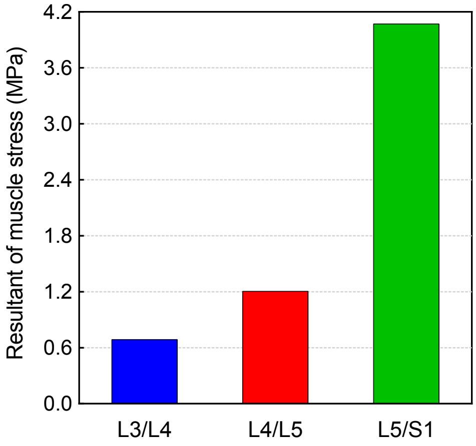

Figure 4.8: Total resultant stress per level in the L3-S1 FE model in flexion.

Calculation of the stress resultants for the local muscles showed that the model predicted increased activation towards the caudal levels, while the global muscles exerted higher stresses at L4/L5 (Table 4.6).

Table 4.6: Muscle resultant stresses per level in the L3-S1 FE model in flexion.

Muscle	L3/L4	L4/L5	L5/S1
MF	0.66	1.18	3.66
ILpL	0.14	0.25	-
LTpL	0.16	0.20	0.57
$\sum \sigma_{local}$	0.97	1.62	4.23
LTpTh	-0.27	-0.40	-0.14
PS	-0.02	-0.02	-0.02
$\sum \sigma_{global}$	-0.28	-0.42	-0.16

A tendency to increase muscle loads was also reflected by the inter-level distribution of the resultant stresses; the L5/S1 level was subjected to around 4 MPa which was about six times higher than the total stress exerted at L3/L4 (Fig. 4.8).

4.3.1.2 Internal loads

For the estimation of the internal loads applied on the discs, the IDP was calculated at fully flexed posture with and without muscles. A region in the center of the NP was selected as shown in Fig. 4.9 and mean±SD values were calculated in the studied volumes per disc.

(a) L3/L4 **(b)** L4/L5

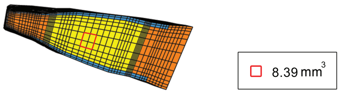

(c) L5/S1

Figure 4.9: Selected region (red) of four hexahedral elements in the center of NP for the calculation of mean±SD IDP values. Region volumes per disc are given in the legends (Undeformed state).

Results were correlated to experimental values retrieved from the literature and are presented in Fig. 4.10 and Table 4.7. With muscle presence (MS), mean IDP prediction was found to decrease from 1.15 MPa at L3/L4 to 0.8 MPa at the lumbosacral level. Absence of MS resulted in considerably lower IDP values with small variations along the lumbar levels; highest mean IDP without muscles was calculated at L4/L5 equal to 0.22 MPa.

Stress profilometry analysis per disc showed that with MS, the calculated profiles differed moderately between the L3/L4 and L4/L5 levels (Fig. 4.11). At L5/S1, a peak compressive stress around 3 MPa was predicted in the posterior AF, whereas without MS a smoother profile with a peak around 0.8 MPa was calculated (Fig. 4.12C). Comparative results shown in Fig. 4.12 present the effect of MS on the axial stresses at all three levels.

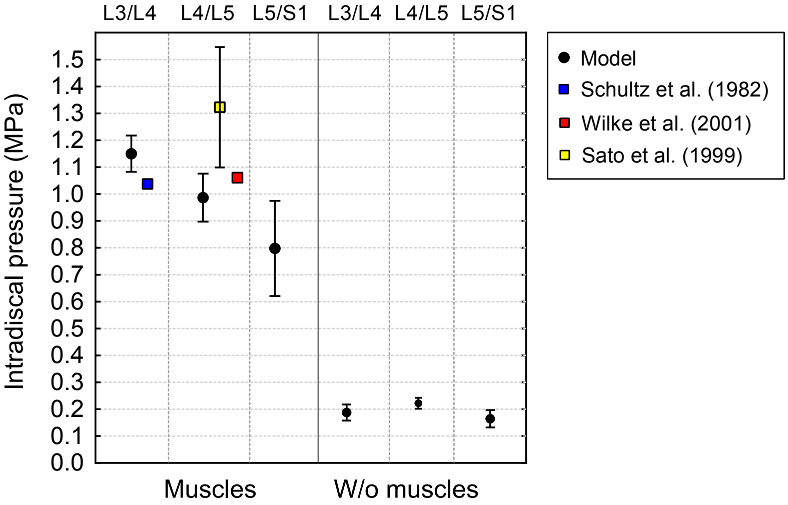

Figure 4.10: Effect of MS on the IDP predictions per level using the L3-S1 FE model in flexion.

Table 4.7: Intradiscal pressure (MPa) values in the center of NP for the L3-S1 FE model in flexion.

	L3/L4	L4/L5	L5/S1
FE model[a]			
Flexion (MS)	1.15±0.07	0.99±0.09	0.80±0.18
Flexion (~~MS~~)	0.19±0.03	0.22±0.02	0.17±0.03
***In vivo* studies**			
Schultz et al. [203]	1.04[b]	-	-
Sato et al. [198]	-	1.32±0.22[a]	-
Wilke et al. [195]	-	1.08[b]	-

[a] Mean±SD value.
[b] [203]: Mean value measured in 30° sagittal flexion; [195]: Measured in 36° sagittal flexion.

4.3.1.3 Reaction moment

The effect of MS was also quantified in terms of reaction moment. Under 10° flexion, simulation of muscles in the model predicted a 4.52 Nm moment at the node where the rotation was applied. Without MS, the respective calculated value was raised to 45.2 Nm for the same rotation.

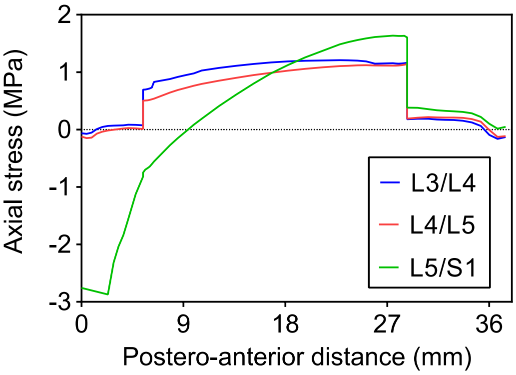

Figure 4.11: IVD stress profilometry in the L3-S1 FE model in flexion.

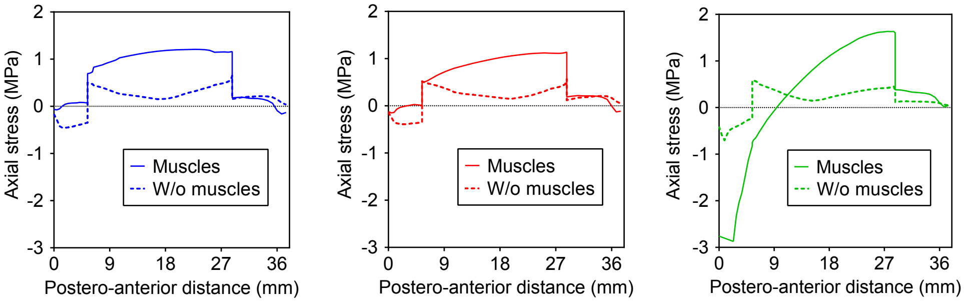

Figure 4.12: Effect of MS on the IVD stress profilometry in the L3-S1 FE model in flexion.

4.3.2 Standing

4.3.2.1 Muscles forces and strains

In standing position without previously simulated rest (PR), muscle force calculations revealed activation of all muscles particularly of the local groups (Fig. 4.13). Among the global fascicles, the lowest contribution was predicted for the thoracic components of LT (Fig. 4.13 right). At the upper levels, i.e. L3/L4 and L4/L5, the MF and ILpL fascicles transferred compression forces equal to 3.5 and 6.5 N, respectively, to the vertebrae and IVD over which they span (Fig. 4.13 left).

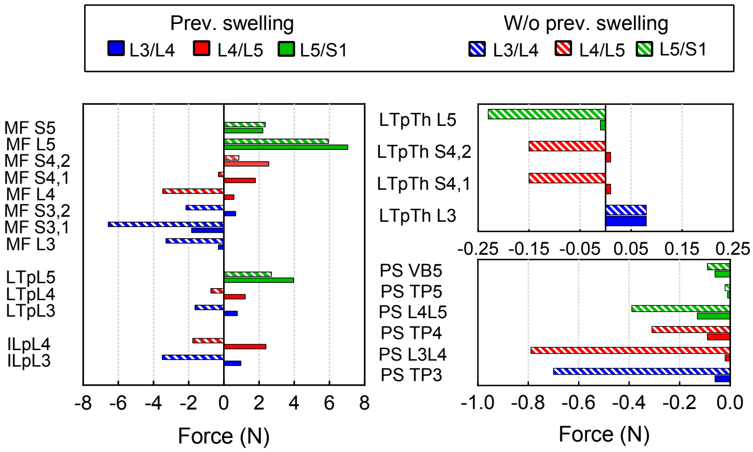

Figure 4.13: Effect of PR on total force distribution per level and fascicle in the L3-S1 FE model in standing.

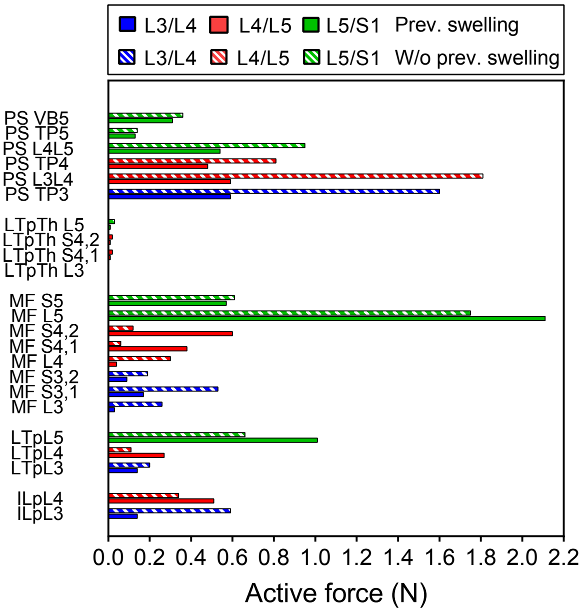

Figure 4.14: Effect of PR on the muscle activation per level and fascicle in the L3-S1 FE model in standing.

Among the local back muscles, the highest active forces were predicted for the L5 MF fascicles accounting for more than 1.5 N (Fig. 4.14) over a total force of about 6 N developed at this level without PR (Fig. 4.13). In the case of PS, the total compression forces developed were up to 0.8 N with important contribution of active forces at all levels (Fig. 4.14). Fig. 4.15 includes the relative contribution of passive and active forces to the total force predicted without PR for the fascicles with highest activation.

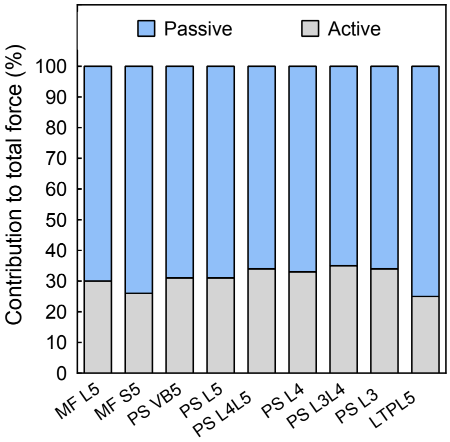

Figure 4.15: Relative constitutive term contribution to the total force predicted in standing without PR.

When PR was considered, increased muscle function was predicted for the caudal dorsal fascicles with positive total forces of up to about 7 N (Fig. 4.13). For MF, the model calculated active forces over 2 N at the lowermost level. For the global fascicles, the fascicles of PS were less activated at all levels (Fig. 4.14) and developed compression forces that did not exceed 0.13 N at L5/S1 level. The contribution of LTpTh was minor.

Studying the total force distribution per level revealed that when standing followed previous disc swelling, total muscle forces increased linearly from L3/L4 to L5/S1 (Fig. 4.16). The maximum resultant force was around 12 N at the L5/S1 level, i.e. nearly 67% larger compared to the total force predicted at L4/L5. Without PR, load concentration was calculated at L3/L4 (-18 N) followed by a nearly 10 N resultant force at the lumbosacral level (Fig. 4.16). Fascicle strain calculations in simulated standing showed that with PR, most of the dorsal fascicles were stretched, whereas without PR shortening was predicted for most of these fascicles as shown in Fig. 4.17.

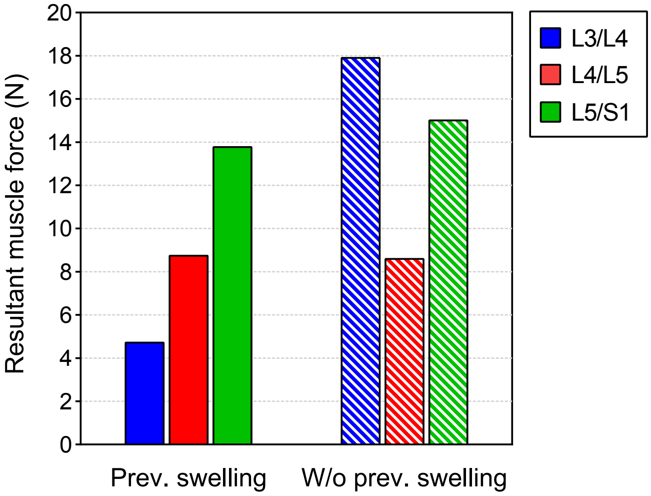

Figure 4.16: Effect of PR on total force distribution per level in the L3-S1 FE model in standing.

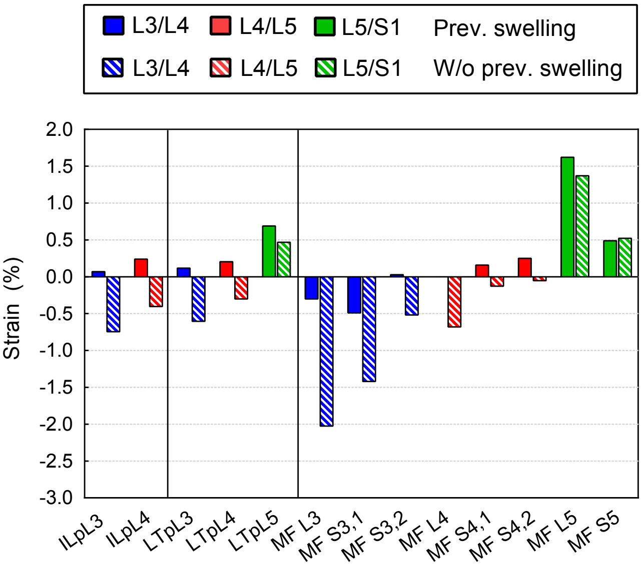

Figure 4.17: Effect of PR on dorsal fascicle strains in the L3-S1 FE model in standing.

Indeed, during the disc swelling simulated for the 8 hours of rest, active forces were developed by the dorsal muscles while the latter were stretched. As presented in Figure 4.18, the highest activation was calculated for the L3 and L4 MF fascicles.

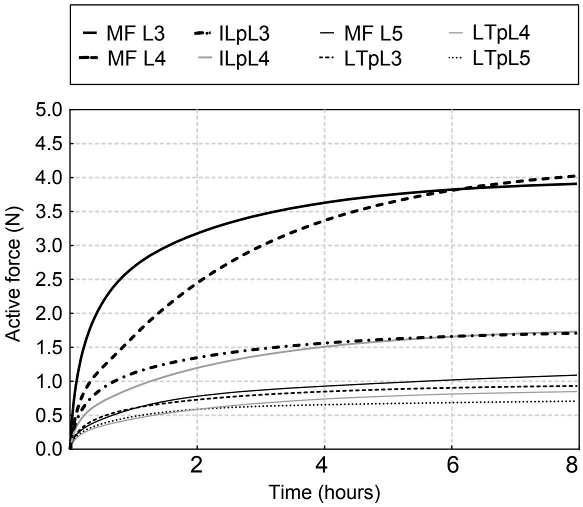

Figure 4.18: Dorsal muscle activation during 8 hours of simulated rest.

4.3.2.2 Intradiscal pressure

For the estimation of the internal loads applied on the discs, the IDP was calculated at the end of simulated standing (Fig. 4.19) and lying (Fig. 4.20) posture analyzing the effect of previous disc swelling and muscle contribution on the predicted pressures. The same region in the center of the NP was selected as was depicted in Fig. 4.9 and mean±SD values were calculated per disc. Because the variation found among the IDP values in the region of interest was very low, i.e. SD was never over 0.01 (Table 4.8), only mean values are included in the figures. As presented in Fig. 4.19, the IDP in standing with PR was 0.22 MPa at L3/L4 and L4/L5, while it was 0.28 MPa in the lumbosacral disc. Simulation of 8 hours of rest increased the pressure in standing by 34-43% along the lumbar levels. The prediction was 0.31 MPa at L3/L4 where the *in vivo* measurement of Schultz et al. [203] gave 0.27 MPa, and where the values measured by Andersson et al. [202] ranged between 0.26 and 0.42 MPa with a mean value equal to 0.34. At L4/L5, the IDP calculated was 0.32 MPa and was close to the mean IDP reported by [307] (0.35 MPa). Also, the prediction laid within the range of values measured *in vivo* by Sato et al. [198] (0.22-0.75 MPa) but seemed to be slightly underestimated statistically (Table 4.8). Interestingly, calculations without MS showed that inclusion of the latter contributed to decrease the

IDP in standing position by up to 9% when previous lying was not simulated.

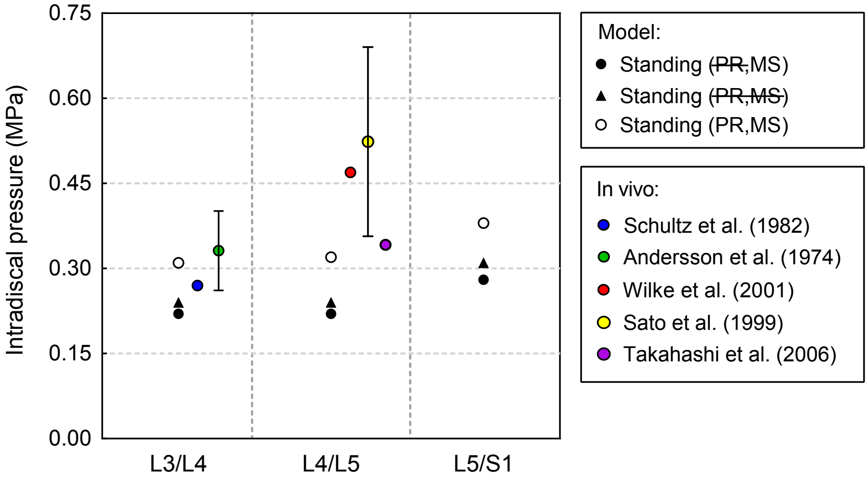

Figure 4.19: IDP predictions per level using the L3-S1 FE model in standing position.

Figure 4.20 shows that after 8 hours of swelling (lying) and no external loads, the overall pressure increased by 0.14 MPa at all levels. At a healthy L4/L5, Wilke et al. [195] recorded the IDP continuously over a 7-hour rest and report a pressure increase from 0.10 to 0.24 MPa, i.e. of 0.14 MPa.

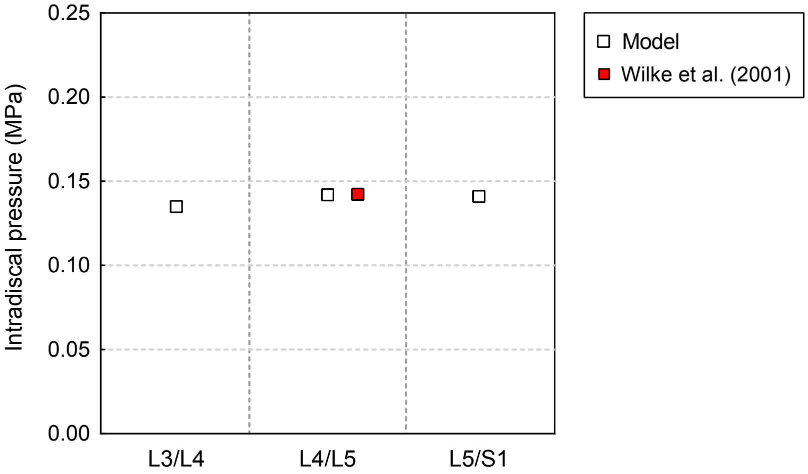

Figure 4.20: IDP predictions per level using the L3-S1 FE model after 8-h rest.

Table 4.8: Intradiscal pressure (MPa) values in the center of NP for the L3-S1 FE model in standing and lying position. (PR=Prev.swelling; MS=Muscle presence)

	L3/L4	L4/L5	L5/S1
FE model[a]			
Standing (PR, MS)	0.31±0.01	0.32	0.38
Standing (~~PR~~, ~~MS~~)	0.24±0.01	0.24	0.31±0.01
Standing (~~PR~~, MS)	0.22±0.01	0.22	0.28
Lying (8 hours rest, MS)	0.14±0.01	0.14	0.14
***In vivo* - Standing**			
Schultz et al. [203]	0.27[b]	-	-
Andersson et al. [202]	0.34±0.08[a]	-	-
Wilke et al. [195]	-	0.50	-
Takahashi et al. [307]	-	0.35[b]	-
Sato et al. [198]	-	0.54±0.18[a]	-
***In vivo* - Lying (rest)**			
Wilke et al. [195] (7 hours rest)	-	0.14	-

[a] Mean ± SD.
[b] Mean value.

4.4 Discussion

In the present chapter, a novel constitutive law was applied to lumbar muscle models in an attempt to improve our understanding of (a) back muscle dynamics, (b) the effect of mechanical stretch on fascicle activation, and (c) the possible interaction between muscle function and IVD multiphysics. Although the components of the Hill-type muscle model have been already used in previous formulations ([258], [254]), the current assembly was applied for the first time to the back muscles. The model was computationally efficient, which allowed its successful integration into a MSL FE model of the lower LS.

Validation of the constitutive muscle model is challenging mostly due to the scarcity of direct reported data (e.g. fascicle forces, segment displacements/rotations) or indirect force estimations through for example, myoelectrical activity, since their reliability for model evaluation is questionable. On the contrary, the geometry of the bi-segment osteoligamentous model used for the development of the L3-S1 FE MSL model was previously validated by [299]. The adopted poroelastic IVD model was also validated before by [308] against *in vitro* data [309]. The ligament formulation used has shown as well its capacity to lead to the validation of different LS FE models ([299], [281]). As discussed further below, the coupling of the lumbar musculature model with geometrically and mechanically valid osteoligamentous components of the LS allowed valuable assessments of the predicted muscle action in all simulated postures.

4.4.1 Flexion

Simulation of unsupported forward flexion showed that the stretching induced by the applied external rotation resulted in activation of all muscles involved in the L3-S1 FE model. In fully flexed posture, the calculated stretching for the dorsal fascicles fluctuated between 2.4 and 19.2%, while for the global fascicles the shortening range was between -0.7 and 8.2%. Despite a thorough literature review, no previous experimental measurements could be found to contrast the strain results per fascicle or per lumbar level. Nevertheless, the predicted ranges were considered reasonable since they did not exceed the strain thresholds (-20% and 30%) reported to increase the risk of cytoskeletal damage ([289], [290], [291]).

Fascicle stress distribution showed that, on one hand, the dorsal fascicles fully resisted the motion by exerting traction total stresses while being stretched all along the flexion. On the other hand, the PS fascicles that were constantly shortened were found to help the forward trunk flexion by developing tensile loads (Fig. 4.7) at the beginning of the simulation the PS; total stresses up to 0.002 MPa $\approx$ 0.36 N were calculated per fascicle in the first 30-40% part of the simulation. Nonetheless, such behavior changed in the rest of the simulation until the fully flexed position (10° flexion). Although its fascicles were constantly shortened, the PS was developing compressive loads towards the spine showing a resistance to the motion.

Among the dorsal muscles, analysis of the resultant stresses showed that the MF had the highest participation with linearly increasing loads up to almost 3.7 MPa at L5/S1 (Table 4.6). Similar tendency was found for the sum of all dorsal stresses with the lumbosacral level being subjected to four times higher loads than the L3/L4 level. As reported in Table 4.6, the model predicted that the MF and the lumbar ES play a dominant role in the load distribution per level during light forward flexion, while the contribution of the global muscles is low. Indeed, for the LTpTh, bilateral contraction was captured with a significant activation at L4/L5 level (Table 4.6). As discussed previously (2.2.5.3.1), such action could accentuate the lumbar lordosis, an effect that was slightly seen on the deformed spine shape. Nevertheless, the modeling hypothesis of a common thoracic insertion that resulted in longer fascicle lengths (e.g. L4 components) than the ones according to dissection studies was suggested to affect the load magnitudes calculated. As such, a rather qualitative evaluation of the LTpTh role is more adequate for the current model configuration.

In terms of IDP, a region of interest with volume between 8.4-11.3 mm^3 was selected in the NP per disc (Fig. 4.9) in order to perform IDP calculations in a comparable area to the one covered by 1.2 [198] and 1.5-mm-diameter [195] needles used in previous *in vivo* studies. The model calculated a notable decrease at the NP per level in the 10° flexed position when muscles were not included in the model (Fig. 4.10). For instance, at L3/L4, the mean IDP results were up to six times higher with MS (1.15 MPa) compared to those without MS (0.19 MPa). Such outcome revealed the key role of muscle action on disc loading in activities involving flexion of the LS. In the center of the L3/L4 IVD, the SD calculated ranged the pressures between 1.08 and 1.22 MPa, whereas at L4/L5 the predictions were lower, from 0.89 to 1.08 MPa. Previous *in vivo* measurements in healthy subjects reported IDP equal to 1.04 MPa (L3/L4 [203]) and 1.08 MPa (L4/L5 [195]) for a 30 and 36° forward flexion of the whole LS, respectively (Fig. 4.10). Based on the range of motion reported by [245], the L1/L2 and L2/L3 levels could reach on average a total of 26° motion in flexion and thus, the experimentally measured flexions would correspond to approximately 10° flexion at L3/L4. Sato and colleagues [198] also registered a wide range of L4/L5 IDP values measured *in vivo* in forward trunk flexion (1.32 ± 0.22 MPa). Even though the boundary conditions simulated in the present FE model did not account for the BW load, and despite the geometrical limitations, correlations with the cited *in vivo* studies suggested that the model achieved to capture realistic IDP values.

When muscle action was not simulated, an important effect quantified as a tenfold rise of the reaction moment was calculated at the uppermost level of the model.

Interestingly, though, only minimal differences were found along the lumbar levels between the predicted loads either in the center (Fig. 4.11) or the mid-sagittal path of the discs (Fig. 4.12). When muscle function was included in the model, part of the posterior L5/S1 NP was under compression, unlike the other two discs. The peak stresses calculated both at the anterior and posterior region of the L5/S1 AF (Fig. 4.11) may be attributed to geometrical artifacts since the disc geometry was a result of an adaptation between the pre-existing L5 VB [299] and a sacrum model available in the laboratory and has not been validated yet.

4.4.2 Standing

In standing posture simulation, active forces counteracted the anterior BW effect and pulled back the spine segment, resulting in the shortening of the majority of the fascicles (Fig. 4.17). When PR was considered, active force predictions revealed that global muscle activity was reduced by up to 68%, while local muscle activity was increased by up to 85% (Fig. 4.14), increasing thus the effective pull back forces. In particular, during night rest, the model predicted that the slight axial spine distraction induced by the swelling of the IVD stretched all the fascicles (Fig. 4.17). This stretch led to heterogeneous fascicle activation through the different lumbar levels (Fig. 4.18); up to 73%, 48%, and 24% higher activation was calculated at L3/L4 than at L5/S1 for MF, PS and lumbar LT, respectively. Such increased activation at L3/L4 was explained as a result of the cumulative effect of IVD swelling from L5/S1 to L3/L4. According to this higher pre-activation at L3/L4 and L4/L5, once standing was simulated, the total loads transferred to the L3/L4 level decreased drastically compared to standing without PR (Fig. 4.16). Remarkably, eventual fascicle strain was positive in standing with PR, even though the absolute stretch values were lower compared to the standing case alone (Fig. 4.17). Such outcomes suggest that swelling involved in previous rest may limit muscle strain when standing position follows but it also improves the capacity of the fascicles to mechanically stabilize the spine.

Given the lack of direct muscle force measurements in the literature, comparisons of the predicted force distribution with reported KD model estimations allowed for a primary qualitative assessment of the muscle model. In [239], the force estimations in upright posture for the dorsal muscles using the KD model showed an increasing tendency from L3/L4 to L5/S1 level: 7-24 N (MF), 5-13 N (ILpL), 2-14 N (LTpL) (Table 1 in the cited study). The force variation calculated by the presented L3-S1 FE model per muscle in standing position with PR showed a similar increasing pattern from L3/L4 to L5/S1 level: 2.1-4.6 N (MF), 0.5-1.2 N (ILpL), 0.4-2 N (LTpL) (Fig. 4.13). Even though for some L3/L4 fascicles the FE-driven results agreed in order of magnitude with the KD estimations in [239], they were generally underestimated compared to the KD results. Nevertheless, the authors in the cited study simulated upright position via a distributed gravity load equal to 378 N (i.e. 37% higher than the one in the FE model) combined with a 180 N anterior load that was not present in the current FE model. As such, a quantitative comparison could not be performed in order to assess the present methodology.

Indeed, literature review showed that previous studies reported the application of a single vertical load placed anteriorly at a point that represented the center of gravity at L1/L2 ([219], [223]), or at the different lumbar levels [221] to mimic the BW. In the present L3-S1 FE model, the gravity load was distributed over the model and the resultant of 276 N obtained at L5/S1 stood for about 40% of the total BM for a 70.8 kg subject. Regarding the magnitude, such estimation was close to the 260 N load reported in [223] for a 56 kg subject (i.e. approximately 46% of the total BM), applied as a single vertical load at T12/L1 in an effective distance R_i of 30 mm. From a qualitative viewpoint, this value correlated well with the calculated R_i distance equal to 41.4 mm used at the L3/L4 level of the present FE model. Good agreement was found also with the study of Shirazi-Adl *et al.* [222], where a 245 N gravity force was estimated and distributed eccentrically per level as follows: 205.6 N (applied between L1/L2 - L3/L4), 19.3 N (L4/L5) and 20.1 N (L5/S1 level).

An alternative way of evaluating the model's robustness was through the calculations of internal loads, i.e. disc pressure, for which comparisons with experimental data was more straight-forward (Fig. 4.19). After eight hours of simulated rest, the IDP increased at all different levels by about 0.14 MPa (Table 4.8), falling in the *in vivo* range measured at a healthy L4/L5 disc after seven hours of rest [60]. When standing position followed the rest, increased IDP values were predicted in comparison to simple standing simulation (Fig. 4.19, white and black circles). Importantly, these values were able to reproduce previous *in vivo* data, reflecting as such the ability of the disc model to capture the osmotically-induced disc turgor. In particular, at L3/L4, the IDP prediction (0.31 MPa) correlated well with the pressure measured *in vivo* by Schultz et al. [203] (0.27 MPa) for a healthy person with a slightly lower BW (63 kg). The predicted IDP laid also close to the mean value reported by Andersson et al. [202] (0.34 MPa) when measuring healthy subjects with BW ranging from 53 to 77 kg (Table 4.8). At L4/L5, the IDP result (0.32 MPa) agreed well with the mean value measured by [307] in healthy subjects with similar weight (0.35 MPa, 72.3 kg average BW). Moreover, the predicted IDP was among the measurements reported by Sato et al. [198] for eight healthy volunteers with BW ranging from 60 to 96 kg, whereas compared to the single measurement of Wilke et al. [195] (0.5 MPa), it was relatively underestimated.

Regarding the possible functional relations between IVD and back muscles, the conclusions shared by previous experimental and numerical studies have been controversial. For instance, in the *in vitro* tests reported by [310], back muscle action was simulated via loading external cables fixed to the LS and the IDP was measured in different positions. The results showed a substantial pressure increase by more than 200% in neutral position (i.e. no external loads), and 130% in flexion when muscle forces were considered. The L3-S1 FE model presented here predicted as well a significant increase of the IDP up to about 500% in flexed position with MS (Table 4.7). Similar to [310], Goel et al. [311] applied nodal forces to simulate the back muscles but used a L3/L4 osteoligamentous FE model instead. Unlike in the former study though, the authors calculated a loss in the IDP by about 18% in flexion. In simple standing, the current L3-S1 FE model predicted a decrease of approximately 8-10% in the IDP as reported in Table 4.8. A possible explanation could be that because of the action of the anterior BW, muscle fascicles imparted both anterior and posterior mechanical support to the osteoligamentous spine and therefore the pressure in the discs decreased. The IDP increase at the end of simulated night rest (0.14 MPa at all levels) reflected the increased load-bearing role of water within the disc captured by the model that also agreed perfectly with the *in vivo* IDP range

(0.10-0.24 MPa) in [60]. Indeed, given the simulated effect of PR on the inter-level load distributions when standing followed (Fig. 4.16), combination of disc swelling and muscle activation might give a further insight on the effect of muscle function on IDP in standing position. Although muscle tone could be suggested as a factor of the muscle tension calculated during rest for the dorsal muscles that were passively stretched (up to 1.6% for MF) [312], the limited ability of the proposed approach to capture intrinsic tensions does not allow any relevant discussion.

The outcomes of this study contribute to the first educated exploration of a possible interaction between disc swelling and muscle function. However, the FE model used has its limitations. From a geometrical viewpoint, extension of the model's configuration to include the upper lumbar VB, i.e. L1/L2 and L2/L3, and all related soft tissues (ligaments, muscles, discs) is remarked as necessary. Such improvement would alter the gravity load distribution and muscle activation allowing hence for more realistic load predictions. Certainly, an extended model able to capture larger kinematical changes should confirm whether, for instance, a wider network of pre-strained muscles is more efficient in restricting forward trunk rotation in upright standing. Another limitation to be addressed is the modeling of the thoracic fascicles by considering a more pragmatic representation of the fascicle attachments between T1-T12. For example, for the L3-S1 MSL assembly presented in this chapter, it was assumed that the axial alignment of L3 VB and the third rib (common rostral insertion) should be preserved. Yet, such approximation would be more correct if L1 was taken as a reference instead of the L3. Even more important, the simplification of a common rostral insertion affected the lengths of the L4 and L5 thoracic fascicles compared to the MT lengths reported for each fascicle in [27]. Therefore, some overestimation of the predicted LTpTh forces might be expected, although the predominant role of the dorsal and PS fascicles suggests that this limitation might not affect the current model interpretations.

Still, from a biomechanical point of view, one of the main objectives remains the exploration of muscle and internal loads in symptomatic population. Therefore, a next step should also involve the development of P-SP LS FE models using personalized geometries and material properties. Previous studies have quantified how tissue condition alters the disc multiphysics and ligament behavior and sets of degenerated material parameters have been proposed accordingly [281]. Concerning the muscle parameters, however, no specific data for the back muscles could be retrieved from the existing literature. Alternatively, the optimized set of values presented in Chapter 3 can be used given its personalized nature.

To sum up, the highlights of the results obtained in the simulations presented in this chapter are:

- The constitutive muscle model proposed was successfully coupled with a L3-S1 FE MSL model and achieved to capture muscle activation in forward flexion.
- A new scheme for the definition of gravity loads in simulated standing and its distribution along an anteriorly placed eccentric path was developed using the body volumes and densities per spine level.
- The internal load distributions predicted in both flexion and standing positions were able to reproduce previous *in vivo* IDP measurements.
- Overnight disc swelling led to muscle activation and load distributions that seemed appropriate to balance the anterior body mass effect when standing followed.
- The likely existence of functional interactions between the IVD multiphysics and stretch-induced muscle activity was suggested.

Chapter 5

Development of generic and patient-specific L1-S1 FE musculoskeletal models

5.1 Introduction

In this chapter, the methodology proposed in Chapter 3 will be applied on two L1-S1 FE models developed using generic and P-SP osteoligamentous geometries. The muscular network detailed in Chapter 4 will be extended to incorporate all fascicles of the modeled muscles arising between the L1 and L5 and will be coupled to both geometries. As such, the final FE MSL assemblies will represent the full LS region, both healthy (generic) and degenerated (P-SP). The same spine postures will be simulated: standing and lying position (night rest). The P-SP model will address some of the restrictions of Dao's et al. model [28] through the personalization of the muscle constitutive parameters and the quantification of active forces. Moreover, for the first time in a patient LS MSL model, the poro-mechanical response of the IVD will be taken into account via condition-dependent material properties [281]. For both generic and P-SP configurations and both postures, the analyses will include prediction of muscle strains and spinal loads, i.e. muscle and joint forces, and assessment of the interactions between the IVD multiphysics and muscle contraction as studied for the L3-S1 FE model (Chapter 4). The influence of the relation between disc height reduction and degeneration that has been previously questioned [313] will be also explored through comparisons of the predicted load distributions and muscle activation along the lumbar levels between the models.

5.2 Methods

A generic L1-S1 osteoligamentous model was developed as an extension of the previously presented L3-S1 geometry (Chapter 4). The methodology used to obtain L1, L2 was similar to that reported in [299], while the intervertebral spaces, i.e. disc heights, were validated against MRI data from previous studies ([314], [315]) (Fig. 5.1). For the P-SP configuration, a morphed L1-S1 FE model with subject-specific osteoligamentous geometries developed in the framework of the EU-funded project *My SPINE* was provided [281]. For the incorporation of muscles in both FE models, the L3-S1 muscle architecture presented in Fig. 4.1 was extended to include the relevant muscle fascicles arising from L1-L2.

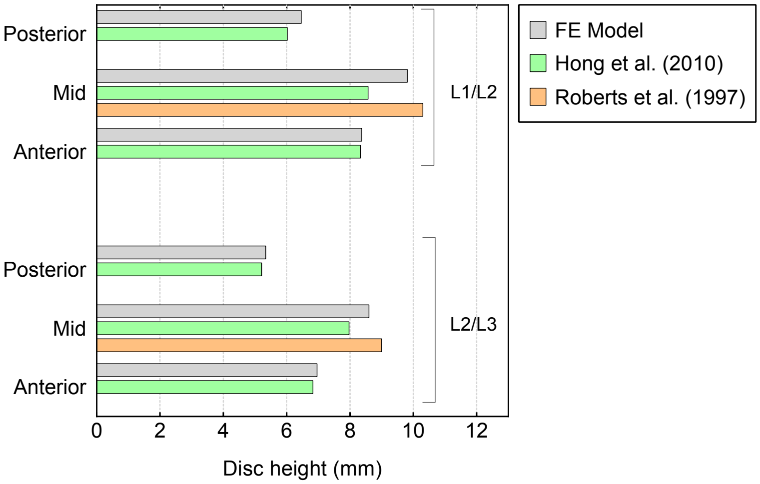

Figure 5.1: L1/L2 and L2/L3 IVD height validation against MRI data reported in the literature ([314], [315]).

5.2.1 Extension of the muscle network

For all fascicle representation, unidirectional elements with straight lines of actions were used as in Chapter 4 deriving the 3D orientations and equivalent PCSA from the literature ([183],[128],[27]). For the MF, 17 fascicle pairs were modeled in total between L1-S1 using the information reported in ([162],[37]). For the LTpL and ILpL, five and four fascicle pairs were simulated, respectively, following the modeling approach proposed in [183] as detailed in 4.2.1. For the extended LTpTh network, a more realistic representation was used compared to the L3-S1 FE model; different MT rest lengths and sagittal orientations were simulated per fascicle based on [27] (Table 5.1). In total, 18 fascicle pairs were modeled with rostral attachments between T1-T10 levels of the thorax each of these attachments simulated as an enlarged transverse process that was modeled as rigid rod (Fig. 5.2). Among them, only ten fascicle pairs had at least one attachment on the lumbar levels. As for the PS, 11 overlapping segmental fascicles were incorporated in total on each side based on the approximations discussed in 4.2.1.

All in all, the L1-S1 muscle network consisted of 94 fascicles, i.e. 47 fascicle pairs, 21 global and 26 local sets that represented the MF, LTpL, ILpL, LTpTh and PS as reported in Table 5.1. The muscles were then coupled to both L1-S1 FE osteoligamentous assemblies. In the generic model (Fig. 5.2A), the muscle network was sagitally symmetric like in the previous lower LS model. In the case of the P-SP model, however, attachment points had to be geometrically adjusted and orientated accordingly to match the morphed FE mesh of the patient model as shown in Fig. 5.2B.

5.2.2 Material parameters

5.2.2.1 Generic model

Similar to the L3-S1 FE model, all tissues in the generic L1-S1 model were simulated as healthy to represent an asymptomatic subject. In particular, for the IVD, the

Table 5.1: Geometrical muscle modeling parameters per fascicle between L1 and S1.

Muscle	Fascicle	PCSA (mm^2)	$L_0^{CE} (mm)$
MF	L1	19	34.94
	$S_{1,1}$	40	72.82
	$S_{1,2}$	42	149.11
	$S_{1,3}$	36	140.96
	$S_{1,4}$	60	104.95
	L2	22	34.20
	$S_{2,1}$	39	76.13
	$S_{2,2}$	39	109.06
	$S_{2,3}$	99	128.19
	L3	23	41.32
	$S_{3,1}$	52	76.22
	$S_{3,2}$	52	136.14
	L4	17	41.46
	$S_{4,1}$	47	68.70
	$S_{4,2}$	47	111.37
	L5	36	169.99
	$S_{5,1}$	23	69.83
ILpL	L1	108	166.06
	L2	154	129.41
	L3	182	86.91
	L4	189	50.31
LTpL	L1	79	193.23
	L2	91	151.05
	L3	103	106.60
	L4	110	66.86
	L5	116	26.67
LTpTh[a]	L1	29	$\underline{165.45}$/121.25
	L2	57	$\underline{195.71}$/101.76
	L3	56	$\underline{63.01}$/$\underline{173.40}$/81.93
	$L_{4,1}$	45	$\underline{92.98}$/$\underline{129.11}$/108.49
	$L_{4,2}$	44	$\underline{61.36}$/$\underline{134.26}$/68.57/55.27
	L5	64	$\underline{91.72}$/$\underline{129.27}$/47.17/60.67
PS	TP_1	61	312.51
	VB_1	211	319.34
	L1L2	211	292.74
	TP_2	101	282.70
	L2L3	161	260.98
	TP_3	173	252.42
	L3L4	191	233.06
	TP_4	120	224.57
	L4L5	119	205.58
	TP_5	36	195.21
	VB_5	79	184.54

[a] The multiple L_0^{CE} values per level correspond to the short fascicles attached between the lumbar and thoracic levels. For instance, LTpTh3 consists of one fascicle with insertions into L3 and L1 TP, and another two between L1, T7 and T7, T3 levels. Fascicles with at least one lumbar attachment are underlined.

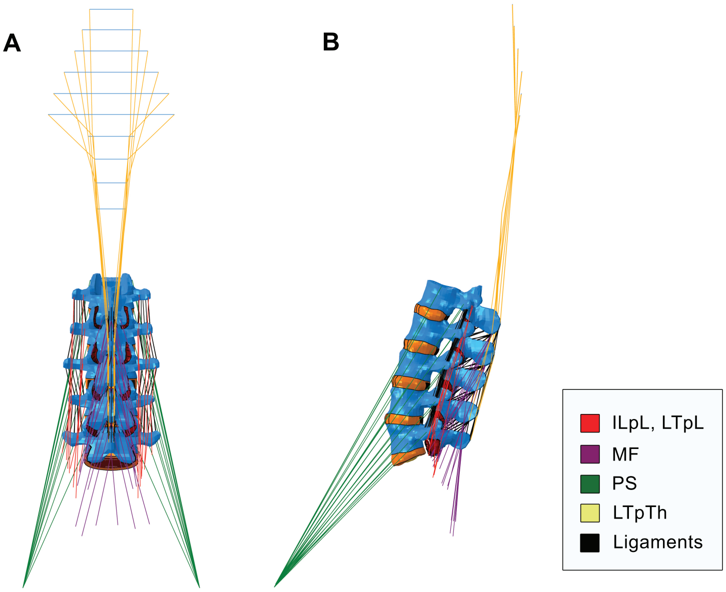

Figure 5.2: (A) Generic L1-S1 FE model (posterior view), (B) P-SP L1-S1 FE model (left sagittal view).

poromechanical properties used per region are the ones reported in Table 4.2. Non-linear elastic tensile behavior was modeled for all seven groups of ligaments based on the study of Noailly et al. [228] as described before (4.2.2.1). Between L3-S1, the material parameter values were derived from [82] and [228]. For the L1-L2 ligaments, values came from an optimization strategy proposed in the literature [281] aiming for a more realistic modeling of the curve stiffness proposed by [228]. All parameters used are summarized in Table 5.2. For the VB, isotropic elastic properties were assigned as described in 4.2.2.2. For the muscles, the individualized sets of parameter values calculated in 3.4.2 were used for MF, LTpL and ILpL (Table 3.4). Material parameter values for the PS and LTpTh were defined based on Table 3.1 and 3.3.

5.2.2.2 Patient-specific model

According to the anthropometric data provided by the EU-funded project *My SPINE*, the patient geometry belongs to a 64 y/o female subject of 64 kg diagnosed with

Table 5.2: Summary of the material parameter values used per ligament.

Ligament	*A*	*B (MPa)*	*C (MPa)*
ALL[a,b]	3.18	7.28×10^{2}	25.70
PLL[a,b]	1.68	0.68×10^{2}	26.60
LF[a,c]	5.64	3.10×10^{5}	47.30
IS[a,b]	4.07	4.66×10^{2}	6.53
SS[a,b]	15.76	8.70×10^{9}	7.70
ITL L1L2	3.77	34.70×10^{-2}	424.98
ITL L2L3	3.77	66.00×10^{-2}	424.98
ITL L3L4	3.77	69.20×10^{-2}	424.98
ITL L4L5	3.77	61.70×10^{-2}	424.98
CL L1L2	13.59	40.40×10^{-2}	92.57
CL L2L3	13.59	22.90×10^{-2}	92.57
CL L3L4	13.59	17.00×10^{-2}	92.57
CL L4L5	13.59	15.30×10^{-2}	92.57

$dS = k(E)dE$, where E is the dependent unidirectional longitudinal stiffness in the fiber direction, and $k(E)$ the Green-Lagrange strain[c]:

$$k(E) = \begin{cases} 0 & \text{if } E \leq 0, \\ ABE^{A-1} & \text{if } 0 < E \leq E_t, \\ C & \text{if } 0 < E \leq E_t \end{cases}$$

[a] Same set of parameter values were used for all lumbar levels.
[b] Based on [82].
[c] Based on [228].

disc herniation. The IVDs were graded by an experienced radiologist in terms of degeneration Pfirrmann score [316] as follows: L1/L2, L2/L3, L3/L4 (grade 3), L4/L5 (grade 4), L5/S1 (grade 2). A set of grade-dependent material properties (G, K, $\Delta\pi$) was derived from the literature [281] for each disc sub-tissue as reported in Table 5.3.

Table 5.3: Set of grade-dependent material properties per IVD sub-region defined in [281].

	G (MPa)[a]	K (MPa)[a]	$\Delta\pi$ (MPa)[b]	Disc level
Grade 2	0.069	0.487	0.24	L5/S1
Grade 3	0.333	0.548	0.08	L1/L2, L2/L3, L3/L4
Grade 4	0.425	1.543	0.09	L4/L5

[a] Same values were used for AF, NP and CEP.
[b] The osmotic pressure $\Delta\pi$ was applied in the NP.

For the ligaments, the material properties used were the ones presented in Table 5.2. For the dorsal muscles, the individualized sets of parameter values reported in Table 3.4 were assigned. Indeed, the subject modeled in the current P-SP FE mesh was the same used in [28] to perform the KD force estimations that were considered in the optimization study in 3.4.2.

5.2.3 Boundary conditions and simulated postures

5.2.3.1 Boundary conditions

The models were restricted using boundary conditions similar to those used with the L3-S1 FE model studied in Chapter 4. Displacements of the sacral attachment points of dorsal muscles were constrained in all directions ($U_i = 0$, $i = x, y, z$ direction). For the LTpTh, all rigid rods representing the thoracic ribs were constrained in the sagittal plane for the simulation of standing position ($U_y = 0$). The lower endplate of the L5/S1 IVD as well as the upper facets of S1 that were included in the model were fixed in all directions for all simulations. A condition of free fluid flow was simulated at the external disc boundaries by considering nil external pore pressure ($P = 0$).

5.2.3.2 Simulated postures

- **Lying**

Similar strategy was used as in the L3-S1 FE model: a free IVD swelling condition due to an initial gradient of osmotic pressure $\Delta\pi$ between the NP and the IVD boundaries was considered at all levels according to [303]. Such swelling was applied in the NP and was simulated for a period of 8 hours aiming to mimic a typical overnight rest (see Fig. 4.5). For the generic model, a $\Delta\pi$ equivalent to 0.15 MPa was defined at all five IVDs. For the P-SP model, grade-dependent values were chosen per disc based on [281] (Table 5.3).

- **Standing**

The methodology presented in 4.2.3.2 was used to calculate the gravity load distribution along the lumbar levels for both L1-S1 meshes. In order to compare the effects of geometry and tissue condition on each model, a common BW was considered based on the patient's data (64 kg). Accordingly, the effective distance $R_{eff(L1)}$ at which the effective gravity load had to be applied at L_1/L_2 was estimated through the resultant Iz_i and BM_i values in order to consider those superior levels not included in each model (i.e. HD, C1-C7 and T1-T12). For each lumbar level caudal to L_1, i.e. from L2 to S1, local boundary loads were simply calculated by using the BM_i and Iz_i values derived from [304] (see Table 4.3). All in all, based on the above calculations, a total gravity load of 249.3 N was estimated corresponding to about 40% of the simulated BW for a 64 kg subject. Estimated load magnitudes and effective distances per level are given in Table 5.4. The eccentric paths of the load distribution for each model are shown in Fig.5.3

Finally, both generic and P-SP FE meshes had four different groups of element-type: shell elements (vertebrae), hexahedral elements (discs and facets), truss elements (muscles and ligaments), and beam elements (network for load application). All simulations of both postures were performed with the FE commercial software ABAQUS (Simulia, Providence, RI, USA) under large displacements and large strains using a coupled fluid-solid FE approach. Results were analyzed at maximum loading (e.g. at the end of standing simulation) in terms of pore pressure (center of the NP), axial stress (AF and NP), muscle forces and strains (fascicle elements).

Table 5.4: Total gravity load distributions per level for a 64 kg subject.

	L1/L2	**L2/L3**	**L3/L4**	**L4/L5**	**L5/S1**
Load (N)	187.2	15.1	14.4	16.3	16.3
R_i (mm)	44.4	27.0	18.0	11.0	4.0

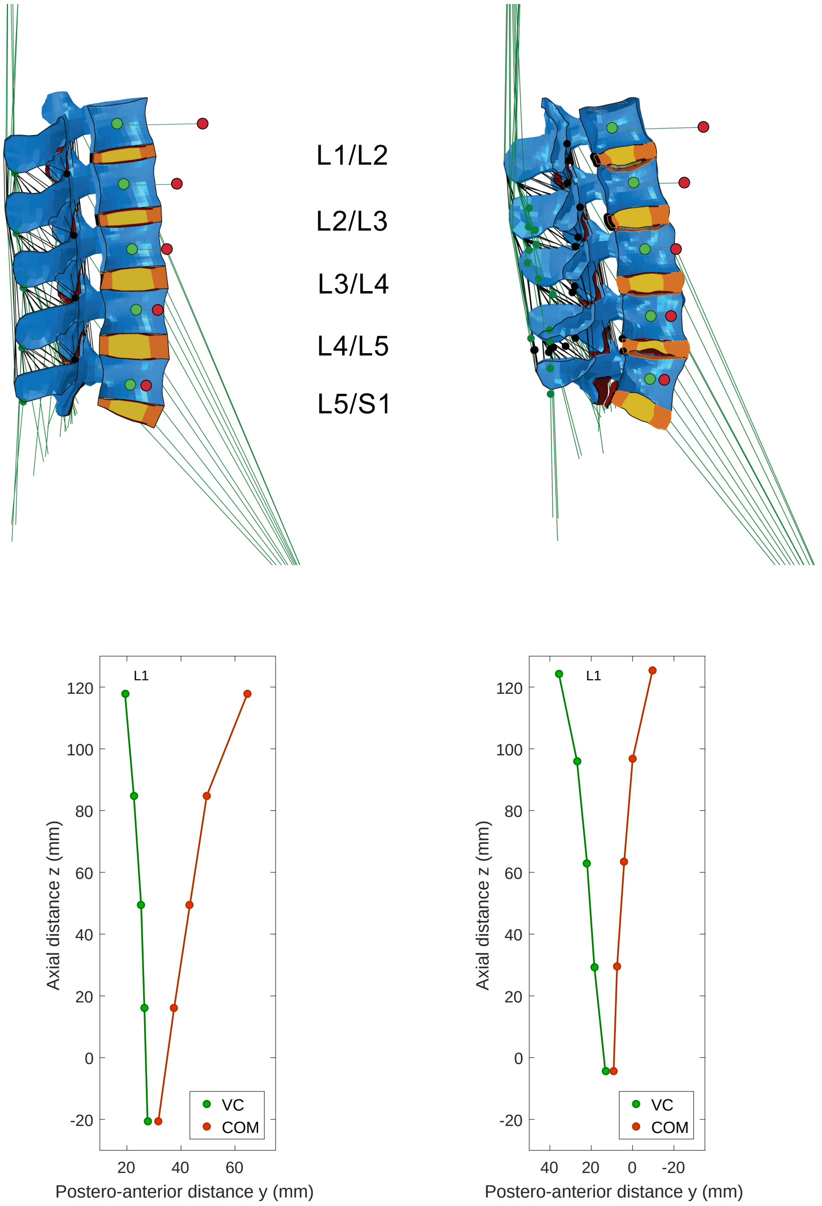

Figure 5.3: Definition of the eccentric gravity load path through the segmental *COM* in the (A) generic and (B) P-SP L1-S1 FE models.

5.3 Results

5.3.1 Generic model

5.3.1.1 Muscle forces and strains

Force-strain results showed that the muscle model captured activation of all fascicles under gravity loads. Simulation of standing without PR resulted in higher loads between L3-L5 for the trunk extensors (Fig. 5.4 ILpL, LTpL, MF) whose fascicles also tended to suffer more shortening (Fig. 5.5). When PR was considered, a different force distribution was calculated along the levels (Fig. 5.6). Particularly for the local fascicles, previous disc swelling was found to have a notable effect on the muscle behavior when standing followed. For instance, without PR, ILpL fascicles were shortened up to approximately 0.65% (L4/L5) (Fig. 5.5) developing compression forces from 0.8 (L1/L2) to about 3 N (L3/L4, L4/L5) (Fig. 5.4).

When PR was considered, these fascicles were pre-stretched. Maximum traction forces equal to 1.4 N at L1/L2 (Fig. 5.6) and fascicle lengthening up to 0.41% (Fig. 5.7, L4/L5) were calculated in standing. PR had a similar effect both on strain and force patterns for most of the MF and LTpL fascicles. In standing without PR, MF fascicles transferred mainly compression loads with a peak around 1.3 N (Fig. 5.4). Most of the global fascicles, in turn, exerted traction forces to the spine and hence their role in the movement depended on the type of deformation: without PR, all PS and L4-L5 LTpTh fascicles were shortened and therefore actively contributed to the forward trunk flexion. When PR was considered before standing, these fascicles were lengthened up to 0.13% (Fig. 5.7) and they exerted tensile forces up to almost 2.4 N.

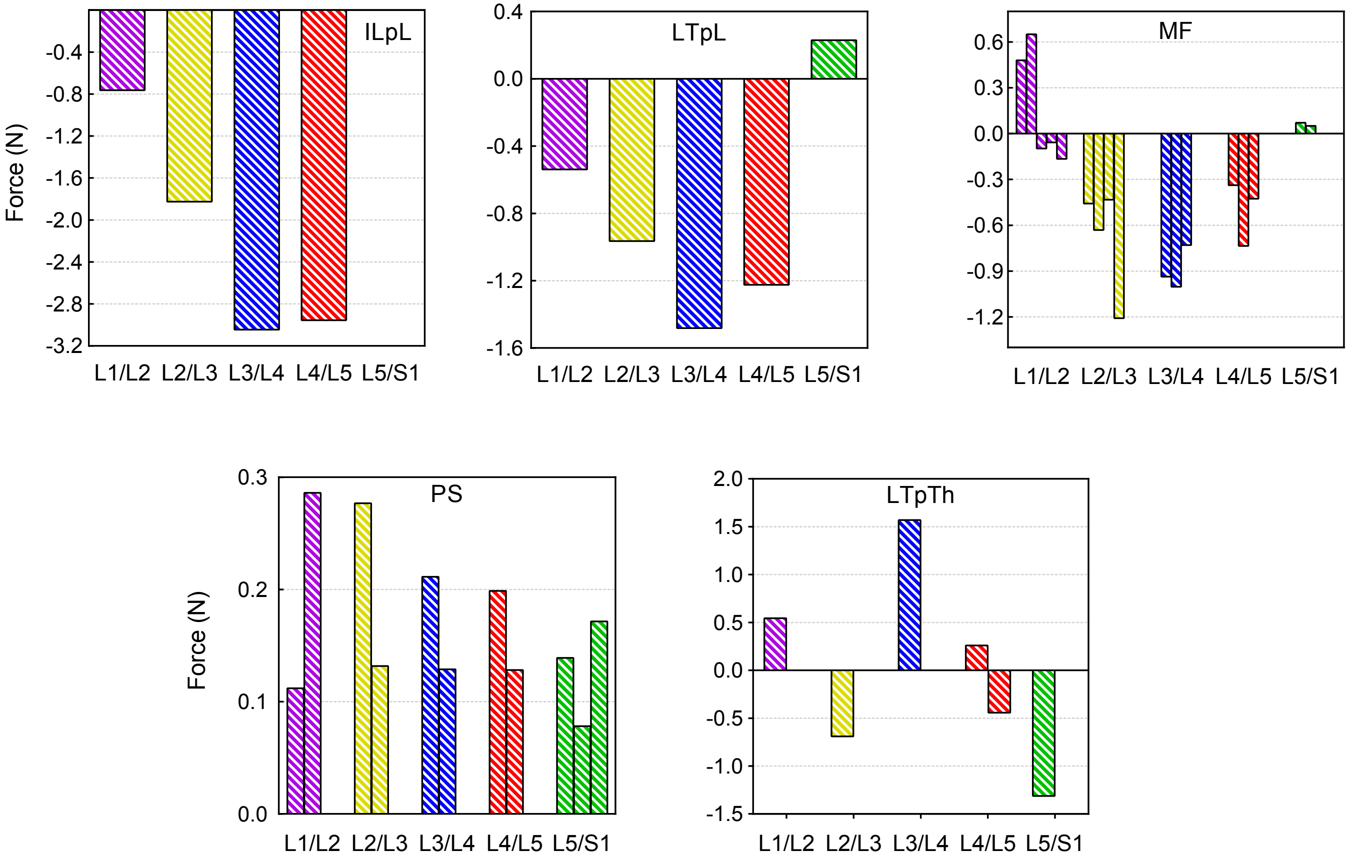

Figure 5.4: Muscle forces per lumbar level and fascicle in the generic L1-S1 FE model in standing.

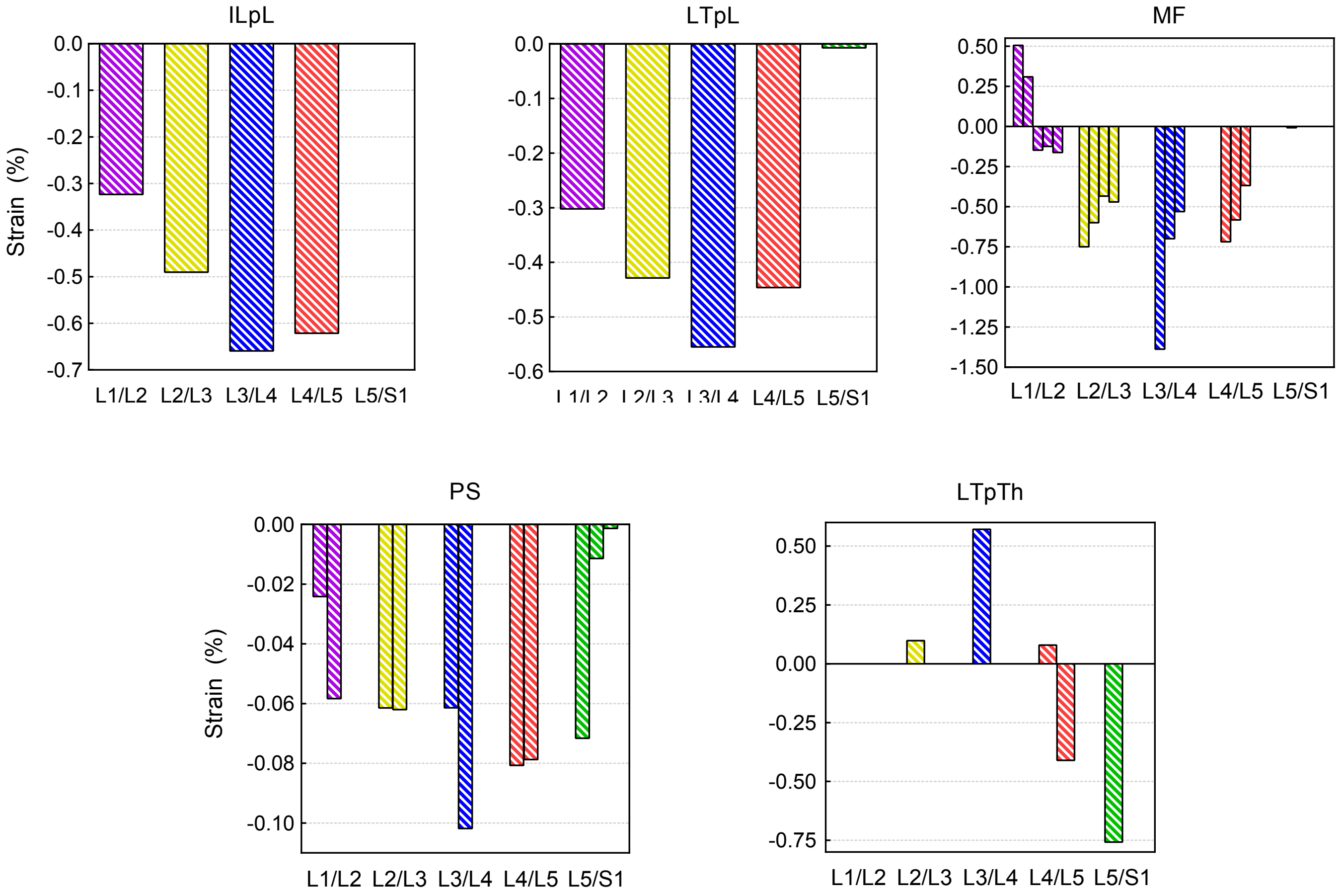

Figure 5.5: Muscle strain per lumbar level and fascicle in the generic L1-S1 FE model in standing.

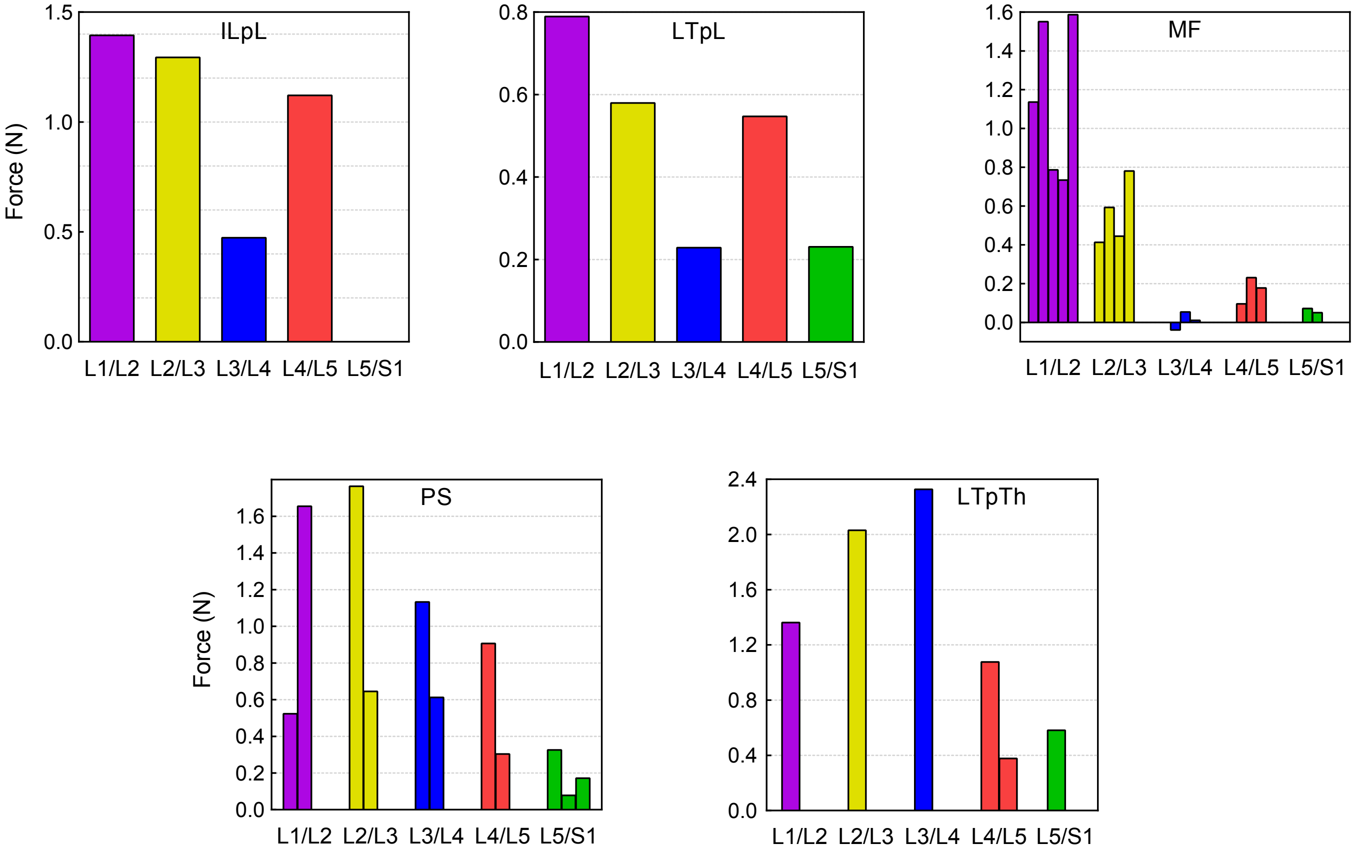

Figure 5.6: Muscle forces per lumbar level and fascicle in the generic L1-S1 FE model in standing with PR.

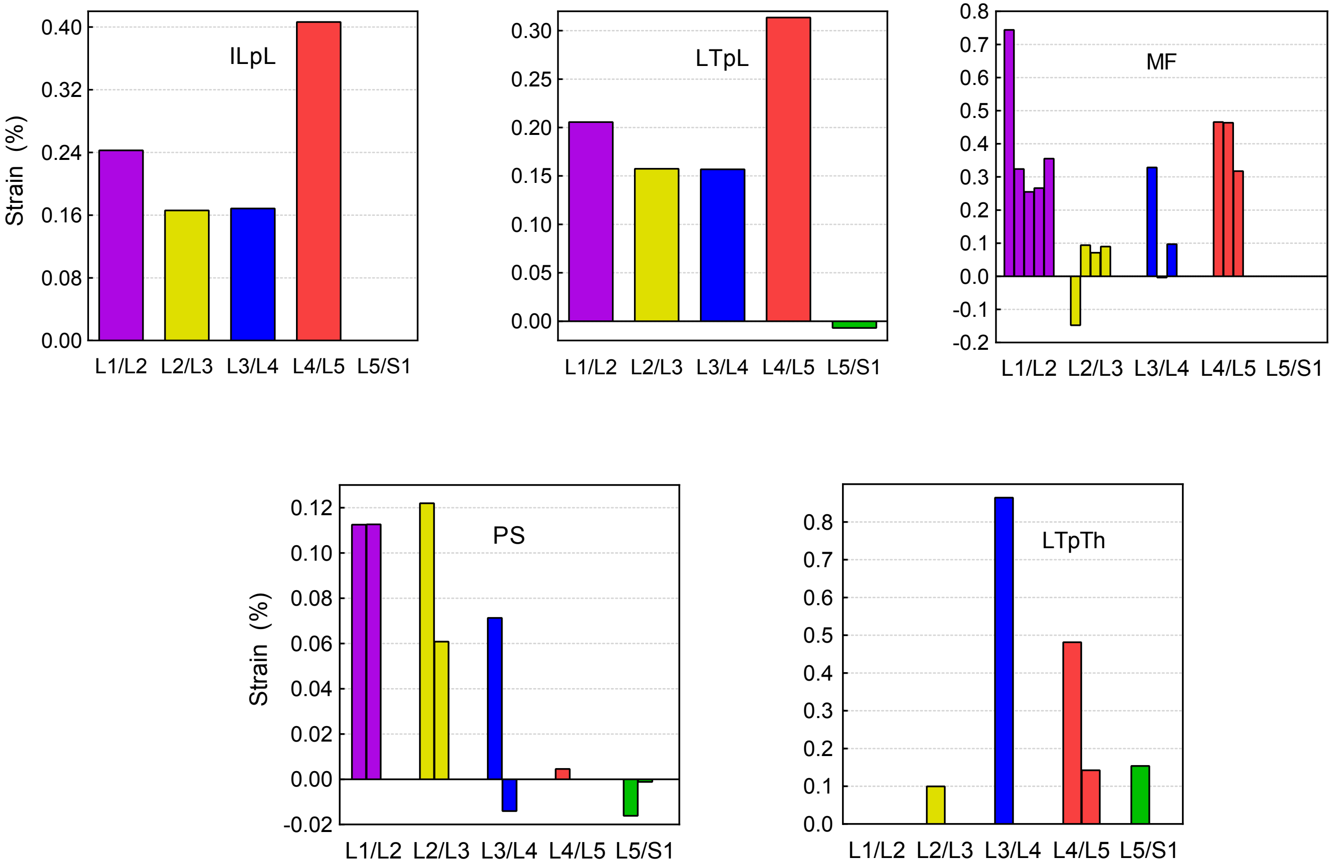

Figure 5.7: Muscle strain per lumbar level and fascicle in the generic L1-S1 FE model in standing with PR.

Figure 5.8 presents the variation of muscle activation per lumbar level in standing position with and without PR. As shown, in the latter case, highest activations were calculated in the mid lumbar zone, i.e. between L2/L3 and L4/L5 (~3 N per level). Consideration of PR required significantly less muscle activation at all lumbar levels: from 28% up to 95% lower active forces at L1/L2 and L4/L5, respectively. That is, previous disc swelling contributed to the stabilization of the spine against the external loads and therefore, less muscle work was needed to fulfill the system's equilibrium.

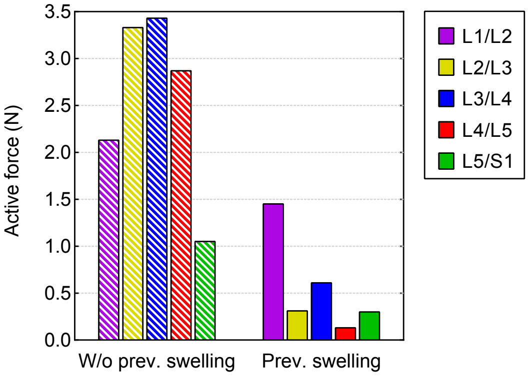

Figure 5.8: Effect of PR on the muscle activation per level for the generic L1-S1 FE model in standing.

The distribution of total muscle forces along the levels changed drastically from compression (without PR) to traction forces (with PR) (Fig. 5.9). The maximum load magnitude predicted in standing without PR was around 6 N at L3/L4 (absolute value), while when PR was simulated, the maximum was localized at L1/L2 level with a value that was about two times higher. At this level, without PR, a traction force around 0.5 N was calculated. Between L3/L4 and L4/L5, muscle load predictions followed a qualitatively similar pattern between the two simulations, i.e. first decrease and then slightly increase again.

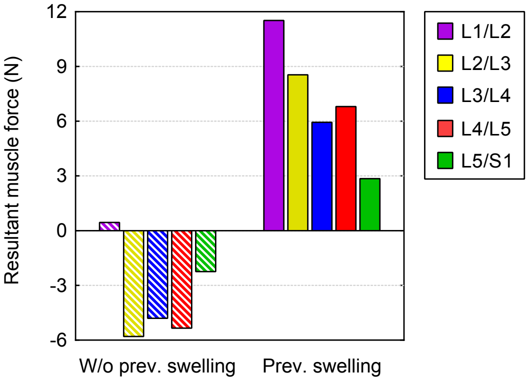

Figure 5.9: Effect of PR on total force distribution per level in the generic L1-S1 FE model in standing.

5.3.1.2 Intradiscal pressure

The IDP was calculated in the center of the NP of each of the five discs in regions with similar volume as the ones selected for the L3-S1 model (Fig. 4.9): 9.79 mm^3 (L1/L2), 8.22 mm^3 (L2/L3), 11.32 mm^3 (L3/L4), 11.50 mm^3 (L4/L5), 8.25 mm^3 (L5/S1). Accordingly, mean±SD values were estimated per disc in four different simulation cases studying the effect of PR and MS (Table 5.5):

- Case 1: Standing with previous swelling, with muscle presence (PR, MS)
- Case 2: Standing without previous swelling, with muscle presence (~~PR~~, MS)
- Case 3: Standing with previous swelling, without muscle presence (PR, ~~MS~~)
- Case 4: Standing without previous swelling, without muscle presence (~~PR~~, ~~MS~~)

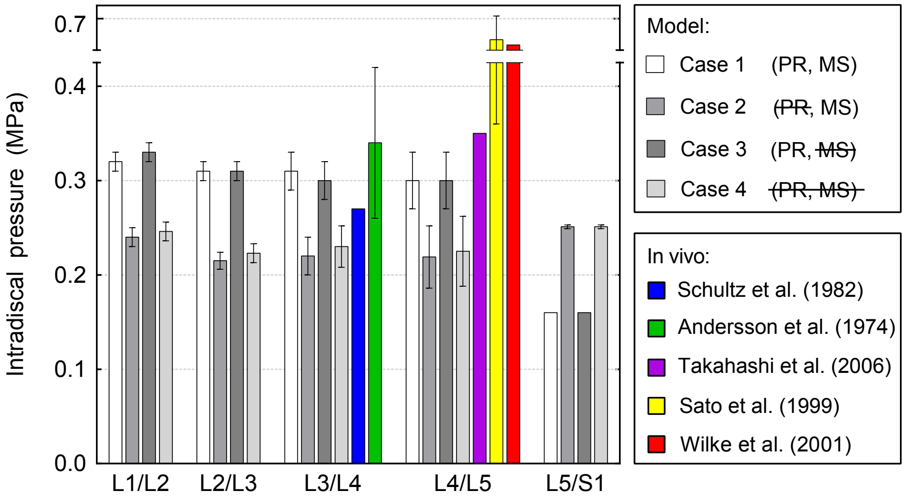

Figure 5.10: Effect of PR and MS on the IDP predictions per level using the generic L1-S1 FE model in standing.

As shown in Fig. 5.10, when PR was simulated, muscles were found to slightly vary the IDP at L1/L2 and L3/L4 levels (3%), while at the remaining two levels no change was seen (Case 1, Case 3). Mean IDP values around 0.30-0.33 MPa were calculated between L1/L2 and L4/L5 in both cases, at the same time that the predicted L5/S1 IDP was equal to 0.16 MPa either with or without MS. Muscle inclusion was found to have a similar effect on IDP when PR was not simulated (Cases 2,4), although generally lower mean pressures were calculated between 0.22-0.25 MPa (Table 5.5). Exploration of the effect of PR with muscle presence (Cases 1,2) revealed a significant variation of disc pressures at all levels: 25% to 29% lower mean IDP values were calculated between L1/L2 and L4/L5 when PR was not considered, while the mean L5/S1 disc pressure increased by about 36% (0.25 MPa). An analogous pattern was predicted for the effect of PR on IDP values when muscles were not present (Cases 3,4; Fig. 5.10). At L3/L4, the IDP predictions in standing with PR (0.31±0.02 MPa) correlated well with the *in vivo* measurements of [203] (0.27 MPa) and laid within the reported range in [202] (0.34±0.08 MPa) (Table 5.5). At L4/L5, the predicted range of disc pressure, i.e. 0.30±0.03 MPa, was in agreement with the mean IDP in [307] (0.35 MPa), and within the range measured by Sato et al. [198] (0.22-0.75 MPa) although they were statistically underestimated as reported in Table 5.5.

Fig. 5.11 presents the calculated effect of muscle simulation on the IDP after 8 hours of rest. Mean pressure increase of 18 and 8% was calculated at L1/L2 and L3/L4, respectively, while at the lowest two lumbar levels the IDP remained constant between 0.14 and 0.15 MPa (Table 5.5). Such values agreed perfectly with the 0.14 MPa increase measured overnight by Wilke et al. [195] on a single healthy L4/L5 disc.

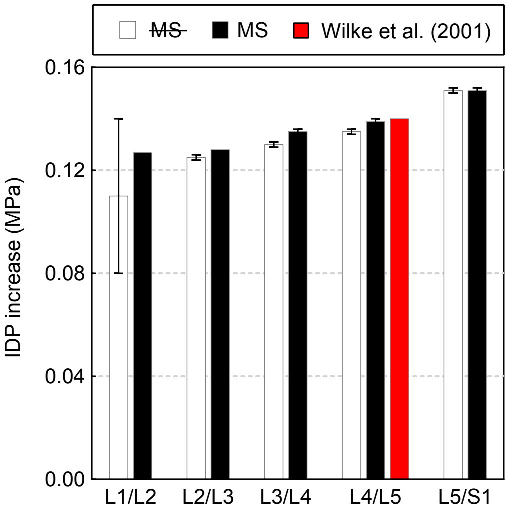

Figure 5.11: Effect of MS on the IDP increase per level using the generic L1-S1 FE model after 8 hours of simulated rest.

Table 5.5: Intradiscal pressure (MPa) values in the center of NP in the generic L1-S1 FE model. (PR=Prev.swelling; MS=Muscle presence)

	L1/L2	L2/L3	L3/L4	L4/L5	L5/S1
FE model-Standing[a]					
Case 1 (PR, MS)	0.32±0.01	0.31±0.01	0.31±0.02	0.30±0.03	0.16
Case 2 (~~PR~~, MS)	0.24±0.01	0.22±0.01	0.22±0.02	0.22±0.03	0.25
Case 3 (PR, ~~MS~~)	0.33±0.01	0.31±0.01	0.30±0.02	0.30±0.03	0.16
Case 4 (~~PR~~, ~~MS~~)	0.25±0.01	0.22±0.01	0.23±0.02	0.23±0.04	0.25
FE model-Lying (8-h rest)[a]					
MS	0.13	0.13	0.14	0.14	0.15
~~MS~~	0.11±0.03	0.13	0.13	0.14	0.15
***In vivo*-Standing**					
Schultz et al. [203]	-	-	0.27[b]	-	-
Andersson et al. [202]	-	-	0.34±0.08[a]	-	-
Wilke et al. [195]	-	-	-	0.50	-
Takahashi et al. [307]	-	-	-	0.35[b]	-
Sato et al. [198]	-	-	-	0.54±0.18[a,c]	-
***In vivo*-Lying (7-h rest)**					
Wilke et al. [195]	-	-	-	0.14	-

[a] Mean±SD.
[b] Mean value.
[c] Measured range: 0.22-0.75 MPa.

5.3.1.3 Lumbar lordosis and intersegmental motion

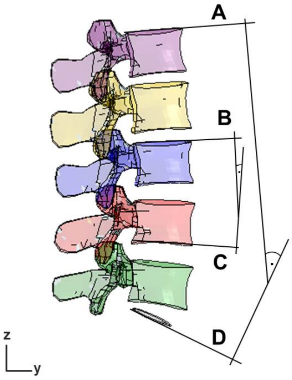

Figure 5.12: Schematic representation of the measurement of the L1-S1 (A-D) and L3-L4 (B-C) Cobb angles.

The Cobb method [317] was used to assess the sagittal plane deformity of the generic FE model for all the four aforementioned simulated cases of standing position. The technique was employed for the measurement of both monosegmental angles (i.e. from L1-L2 to L4-L5) and the lumbosacral curvature (L1-S1) as illustrated in Fig. 5.12. For instance, the L3-L4 lordotic angle was measured between the superior L3 and the inferior L4 endplates, and the L1-S1 between the superior L1 and inferior S1 endplates. Results for each case are listed in Table 5.6. In standing with PR (Case 1), the

Table 5.6: Monosegmental and L1-S1 Cobb angles (°) in the generic L1-S1 FE model in standing.

	Case 1	Case 2	Case 3	Case 4	Effect of PR (%) (Case 1,2)	Effect of MS (%) (Case 1,3)
L1-L2	0.13	0.27	0.20	0.20	-51.9	-35.0
L2-L3	0.39	0.33	0.36	0.36	15.4	7.7
L3-L4	3.90	3.66	3.84	3.76	6.2	1.5
L4-L5	6.94	7.10	7.32	7.03	-2.3	-5.2
L1-S1	30.33	30.33	30.34	30.32	0.00	0.03

calculated L1-S1 curvature was 30.33°, same as in simulated standing without PR (Case 2). Subtle differences were also predicted between Cases 1,3 (with PR) or Cases 2,4 (without PR) (Table 5.6). However, in terms of ISR, notable variations were found between the simulated cases (Table 5.6). For example, consideration of PR decreased the L1-L2 angle by about 52%, i.e. the spine was rotated forward at this level, although such motion was compensated for the levels in the midst (up to 15.4% backward rotation at L2-L3). Similarly, the forward rotation seen at L1-L2 when MS was considered was again balanced between L2-L4 levels. On the effect of either studied factors (PR, MS), a trend of forward rotation at L4-L5 was generated and captured by the model.

For all four studied cases of standing, the centers of each vertebral body were obtained, and centroids were plotted in the sagittal plane to assess the intersegmental translations (IST). In the axial direction, without MS (Case 3), bigger upward translations were predicted for the upper three VB compared to Case 1 (Fig. 5.13A), whereas without PR (Case 2), downward centroid motion was seen (Fig. 5.13B). The combined effect of PR and MS on the lower lumbar spine was found to be more important at L3-L4 (Fig. 5.13C, D). In the antero-posterior direction (Fig. 5.14), the IST gradually decreased from L1-L2 to L3-L4 (3.03-1.03 mm[1]), and increased again at L4-L5 (1.22 mm[1]). In standing without PR (Case 3), around 27% higher posterior translation was calculated at L3-L4 level compared to Case 1. However, when muscles were not present (Cases 2,4), the absence of PR resulted to 33% smaller translation at this level.

---

[1] Mean value calculated among the four cases.

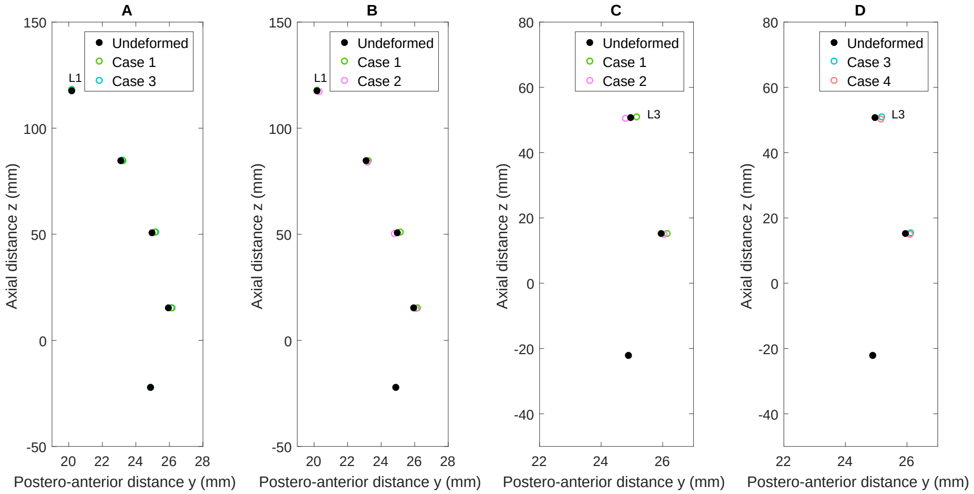

Figure 5.13: Effect of (A) MS, (B) PR on the L1-L5 centroid position; Effect of PR on the L3-L5 centroid position (C) with and (D) without MS (generic L1-S1 FE model, standing).

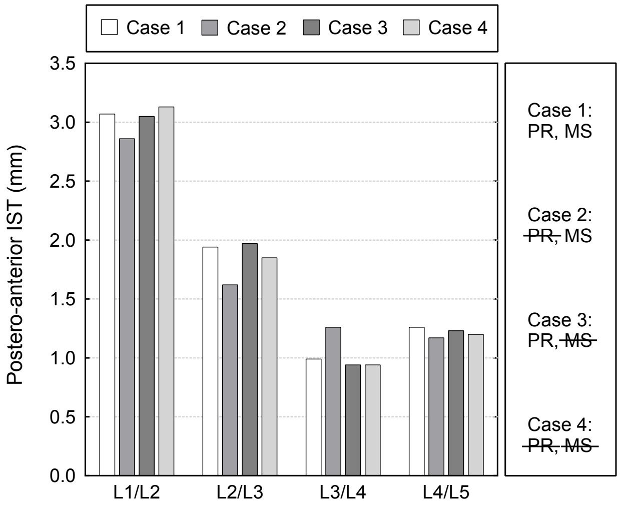

Figure 5.14: Postero-anterior IST in the generic L1-S1 FE model in standing.

5.3.1.4 Effect of IVD condition in generic geometries

To investigate the effect of disc condition on internal loads and muscle activation predictions, comparisons were performed between two identical generic L1-S1 FE models with the same IVD geometries (Fig. 5.3A) but different sets of disc material properties: one healthy (Table 4.2) and one degenerated (Table 5.3) set. Accordingly, the presented results from the generic FE model with healthy disc properties will be hereafter called ”Healthy” (Case 1 with MS, Case 3 without MS) and results from the model with degenerated disc properties as ”Degenerated” (Case 5 with MS, Case 6 without MS).

First, the effect of disc degeneration was analyzed in terms of IDP in standing (Fig. 5.15) and after rest (Fig. 5.16). For both postures, simulations were run with PR once with MS and then without MS. In standing (Fig. 5.15), mean IDP for healthy discs was from 0.16 to 0.33 MPa either with (Case 1) or without MS (Case 3), even though a slightly different intralevel distribution was predicted among the cases. The healthy L5/S1 disc had always had the lowest IDP among all levels (0.16 MPa). When degenerated discs were simulated, the IDP ranges changed to 0.21-0.29 MPa with MS (Case 5) and 0.21-0.30 MPa without MS (Case 6). As it can be observed, muscle function did not seem to affect the pattern predicted: degenerated discs decreased the IDP at all levels but L5/S1 (Fig. 5.15). In both Cases 5 and 6 of standing with degenerated discs, the IDP at the lumbosacral disc remained constant at 0.21 MPa that was approximately 31% higher than the result calculated for healthy discs. Moreover, even though all three upper IVDs were classified as grade 3 and hence had the same material properties, different IDP were predicted between them in either cases of standing, i.e. with or without muscles (Fig. 5.15).

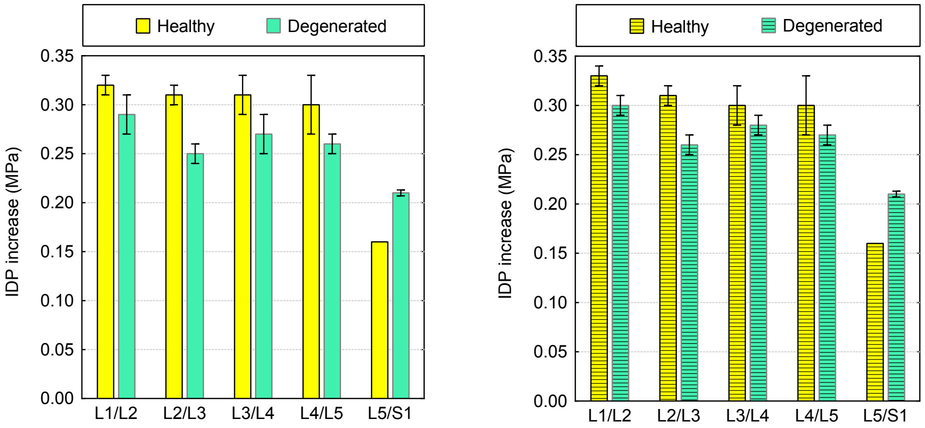

Figure 5.15: Effect of disc condition on the IDP predictions (mean±SD) using the generic L1-S1 FE model in standing position: with (left) and without (right) MS.

In lying position after 8 hours of rest (Fig. 5.16), disc condition was found to have a crucial effect on the IDP increase. When muscles were included (Fig. 5.16 left), simulation with degenerated discs gave 53-59% lower IDP between L1/L2 (grade 3) and L4/L5 (grade 2), but 40% higher IDP at L5/S1 (grade 2) compared to the simulation with healthy discs. Pressure increase at the degenerated discs was between 0.06-0.21 MPa, whereas at healthy discs the respective values varied from 0.13 to 0.15 MPa.

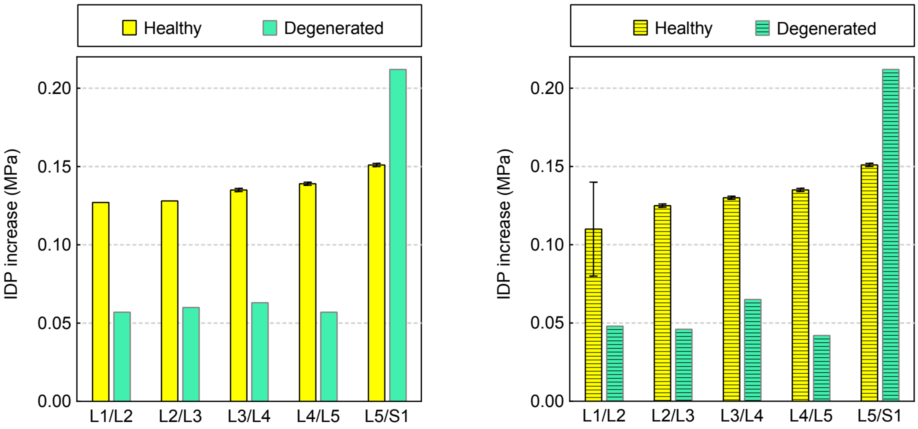

Figure 5.16: Effect of disc condition on the IDP predictions (mean±SD) using the generic L1-S1 FE model after 8-h rest: with (left) and without (right) MS.

Without MS (Fig. 5.16 right), such tendency was even more pronounced: 63% and 69% lower IDP increase was predicted at L2/L3 (grade 3) and L4/L5 (grade 4), respectively, compared to the healthy case, even though the geometry of all discs was kept intact between the models. At L5/S1 (grade 2), no effect was observed for the muscles on the IDP increase overnight, remaining equal to 0.15 MPa for healthy properties and 0.21 MPa for degenerative properties.

In order to further explore any possible relation between the disc condition and the muscle function, the active forces developed were studied in standing position with PR for both Case 1 and Case 5. As presented in Fig. 5.17, disc condition did not affect the prediction of muscle activation at L1/L2, where active forces remained around 1.45 N. Between L2 and L5, nonetheless, a significant increase was predicted in the simulation with degenerated discs. Active forces at L2/L3, L3/L4 (discs of grade 3) were almost 3 N per level, i.e. about ten and five times, respectively, higher than with healthy discs. At the L4/L5 level (IVD of grade 4), active forces passed from 0.13 to 1.84 N (Fig. 5.17). That is, at this level muscles developed 14 times higher loads when degenerated discs were considered. At the lumbosacral level, active forces with healthy discs were 0.3 N, whereas with degenerated discs, the corresponding load magnitude was about 0.9 N. Table 5.7 lists the active forces developed per each muscle and per level in standing with previous disc swelling and either healthy or degenerated disc propeties.

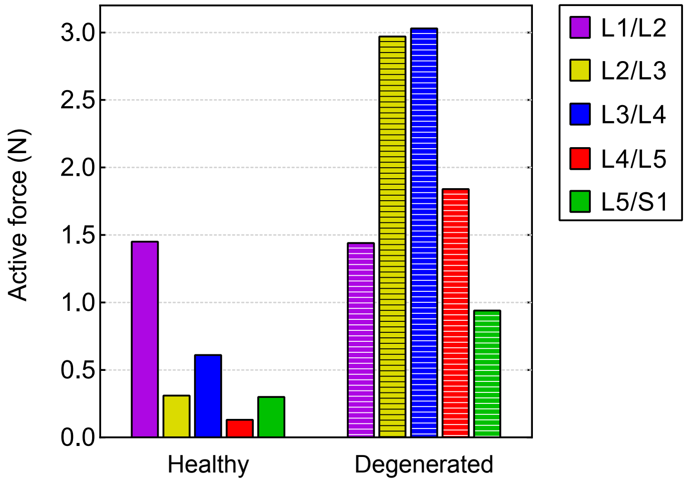

Figure 5.17: Effect of disc condition on muscle activation per level using the generic L1-S1 FE model in standing with PR.

Table 5.7: Active forces (N) in standing position using the generic L1-S1 FE model and healthy/degenerated disc material properties.

Muscle	**Lumbar level** **L1/L2** **H/D**[a]	 **L2/L3** **H/D**	 **L3/L4** **H/D**	 **L4/L5** **H/D**	 **L5/S1** **H/D**
MF	1.05/0.36	0.03/1.29	0.00/0.64	0.03/0.41	0.00/0.58
ILpL	0.00/0.25	0.00/0.50	0.00/0.82	0.00/0.22	-/-
LTpL	0.00/0.16	0.00/0.25	0.00/0.39	0.00/0.09	0.01/0.01
PS	0.06/0.57	0.06/0.76	0.05/1.03	0.01/0.92	0.03/0.23
LTpTh	0.34/0.09	0.23/0.16	0.56/0.15	0.10/0.20	0.26/0.13
Sum per level	1.45/1.43	0.32/2.96	0.61/3.03	0.14/1.84	0.30/0.95

[a] H=Healthy; D=Degenerated.

Mid sagittal heights were also calculated for each disc in standing with PR and MS and with either sets of disc parameters, i.e. healthy (H, Case 1) or degenerated (D, Case 5), as summarized in Table 5.8. With healthy material properties, the largest increase from the initial disc height was calculated between L1/L2 (1.4%) and L2/L3 (1.5%). With degenerated material properties, the disc heights at these levels showed no variation, whereas between L3-L5 they lost about 1.8 and 1.3% of their initial mid disc height.

Table 5.8: Mid sagittal disc heights (mm) in standing and difference from the initial values (%) for the generic discs with healthy/degenerated[a] properties.

IVD	Initial	H	D	H-Initial (%)	D-Initial (%)
L1/L2	8.72	8.84	8.73	1.4	0.1
L2/L3	9.92	10.07	10.00	1.5	0.8
L3/L4	13.10	13.21	12.87	0.8	-1.8
L4/L5	14.33	14.41	14.14	0.5	-1.3
L5/S1	10.34	10.34	10.34	-0.03	-0.02

[a] H=Healthy; D=Degenerated.

5.3.2 Patient-specific model

5.3.2.1 Muscle forces and strains

In standing without PR, all fascicles between L1 and L3 transferred compression forces with maximum values at L3/L4 (around 1.5-2 N for ILpL-LTpTh) (Fig. 5.18). The fascicle force magnitudes predicted between L1/L2 and L2/L3 were similar in LTpL and MF. At the lower lumbar levels, traction forces were calculated for most fascicles except for LTpTh for which total forces were compressive. The highest contribution was seen for the dorsal elements, i.e. L4 ILpL (0.53 N) and L5 LTpL (0.25 N), followed by the PS forces at L5/S1 (up to 0.17 N).

When rest was simulated before standing (Fig. 5.19), similar force distributions per level with generally decreased magnitudes were computed especially for the dorsal muscles compared to simple standing. Moreover, traction forces about 0.02 N were calculated for the upper PS fascicles arising from the L1 and L2 vertebrae, and from the IVD-vertebra interfaces at L2/L3. At these levels, the LTpL and MF transferred comparable compression forces per level ranging up to 1 N. For the LTpTh fascicles, previous disc swelling had a clear effect particularly in the higher lumbar spine: at L2/L3, the total fascicle force increased to 2 N (absolute value), whereas at L3/L4, it almost dropped to 0 (Fig. 5.19).

Strain results in standing showed bilateral contraction for most muscles. However, notable differences were predicted between the two sides of the muscle, i.e. left-right. Therefore, the fascicle strain-activation was analyzed per side instead of per pair, as performed previously for the generic model (Fig. 5.5, 5.7). The following tables list the strain and active force predictions per fascicle and per side in standing (Table 5.9) and standing with PR (Table 5.10). In either simulations of standing, shortening was predicted for all fascicles but for ILpL, LTpL fascicles at L4/L5 that were both lengthened. An initial evaluation of the effect of PR on the overall strain levels revealed that smaller strains were predicted for all muscle fascicles in standing when previous disc swelling was considered compared to simple standing (Table 5.10, Fig. 5.20-5.21). Actually, given the stretch-induced activation criteria of the muscle model, such decrease in strain levels resulted also in lower active force values. Nonetheless, previous disc swelling had no effect on the zero deformation and activation captured by the model for all L5 MF, LTpL and PS fascicles in both standing cases (Table 5.9, Table 5.10).

Similar behavior was seen for the LTpTh arising from L1/L2 and for most of the shorter fascicles with attachments to the ribs. Maximum shortening was predicted for the L3 laminar MF fascicle attached between the L3 and L5 vertebrae: -1.87% in standing (Fig. 5.20), -1.59% when standing followed PR (Fig. 5.21). For all muscles but PS, larger fascicle compression was calculated at the left side fascicles in comparison with the right side in either simulations. In fact, for instance for L3 ILpL, such asymmetric muscle contraction between the two sides (-1.06%/-0.07% strain in standing) resulted in up to 17 times higher active forces developed on the spine tissues at the left side of the trunk (Fig. 5.20). For the PS, however, higher compression and activation was predicted at the right side of the muscle for all fascicles but the one attached to the L2 transverse process (Table 5.9, Table 5.10).

In standing (Table 5.9), the highest active forces at the left side were developed by the lumbar IL and LT at L3/L4 (1.16 N) and L4/L5 (0.69 N), respectively, followed by the L1L2 PS (0.50 N) and MF S2 (0.40 N) fascicles (Fig. 5.20). In standing with PR (Table 5.10), muscle activation showed a similar tendency although for the MF S2 active forces were slightly higher than for the L1L2 PS (0.35 versus 0.31 N, respectively). On the right side, the highest activation for ILpL, PS and LTpL was predicted at the two uppermost levels; with PR, maximum active forces were 0.66, 0.48 and 0.16 N, respectively (Fig. 5.21), while without PR, the corresponding predictions were 0.77, 0.57 and 0.53 N (Table 5.9). For the thoracic LT, low contribution was calculated in either cases of standing.

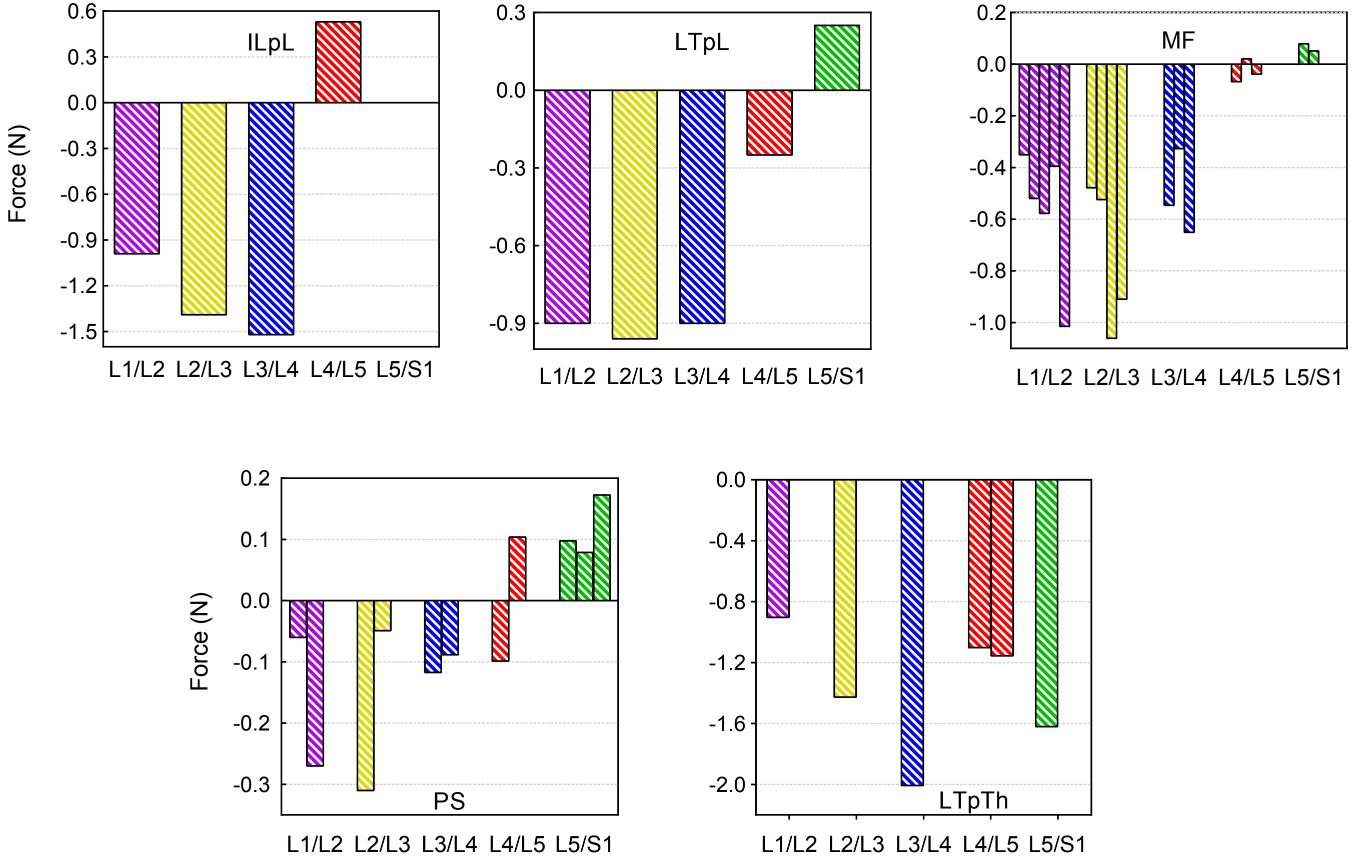

Figure 5.18: Muscle forces per lumbar level and fascicle in the P-SP L1-S1 FE model in standing.

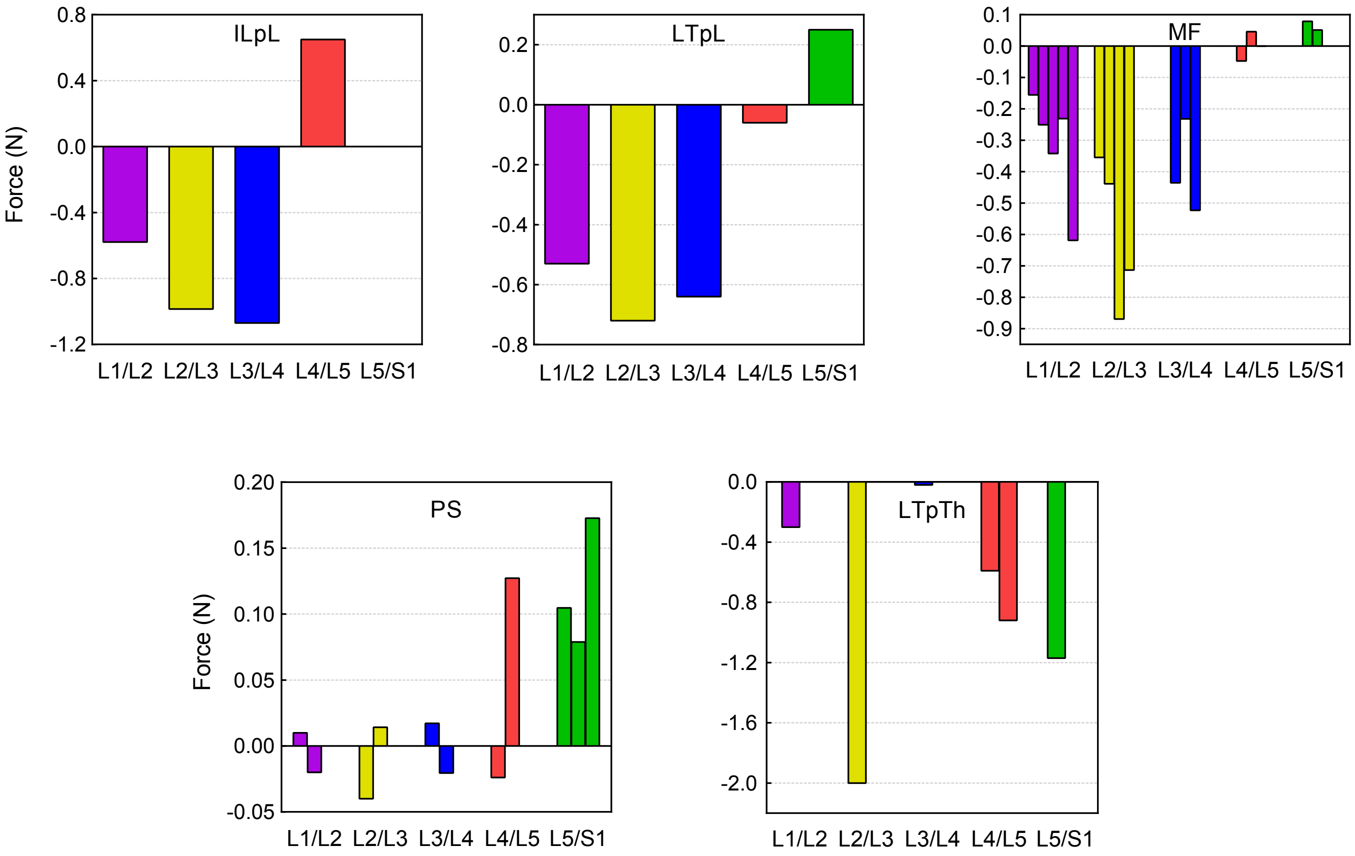

Figure 5.19: Muscle forces per lumbar level and fascicle in the P-SP L1-S1 FE model in standing with PR.

Table 5.9: (L)eft/(R)ight fascicle strain and active force predictions in standing using the P-SP L1-S1 FE model.

Muscle	Fascicle	Strain (L/R) (%)	Active force (L/R) (N)
MF	L1	-0.99/-1.12	0.10/0.11
	$S_{1,1}$	-0.90/-0.64	0.18/0.13
	$S_{1,2}$	-1.09/-0.56	0.24/0.12
	$S_{1,3}$	-0.81/-0.52	0.14/0.09
	$S_{1,4}$	-0.74/-0.55	0.00/0.00
	L2	-1.40/-1.03	0.16/0.11
	$S_{2,1}$	-1.15/-0.56	0.25/0.12
	$S_{2,2}$	-0.80/-0.52	0.40/0.26
	$S_{2,3}$	-0.69/-0.48	0.35/0.24
	L3	-1.87/-1.12	0.27/0.16
	$S_{3,1}$	-0.54/-0.47	0.17/0.14
	$S_{3,2}$	-1.02/-0.68	0.32/0.21
	L4	-0.58/-0.33	0.07/0.04
	$S_{4,1}$	-0.20/-0.19	0.06/0.06
	$S_{4,2}$	-0.39/-0.31	0.12/0.09
	L5	0.00/ 0.00	0.00/0.00
	$S_{5,1}$	0.00/ 0.00	0.00/0.00
ILpL	L1	-0.59/-0.49	0.33/0.27
	L2	-0.20/-0.91	0.16/0.77
	L3	-1.06/-0.07	1.16/0.07
	L4	-0.51/ 0.27	0.75/0.00
LTpL	L1	-0.69/-0.65	0.28/0.26
	L2	-0.93/-0.31	0.60/0.15
	L3	-0.35/-1.05	0.22/0.53
	L4	-0.80/ 0.05	0.69/0.00
	L5	0.00/ 0.00	0.00/0.00
LTpTh[a]	L1	0.00 / 0.00	0.00/0.00
	L2	-0.14/-0.11	0.01/0.01
	L3	-0.52/-0.38, 0.00/ 0.00	0.05/0.03, 0.00/0.00
	$L_{4,1}$	-0.86/-0.75, 0.00/ 0.00	0.06/0.05, 0.00/0.00
	$L_{4,2}$	-0.86/-0.85, -0.16/-0.23	0.06/0.06, 0.01/0.02
	L5	-0.82/-0.84, -0.19/-0.23	0.08/0.08, 0.02/0.02
PS	TP_1	-0.21/-0.25	0.12/0.15
	VB_1	-0.25/-0.26	0.49/0.52
	L1L2	-0.25/-0.28	0.50/0.57
	TP_2	-0.29/-0.10	0.28/0.09
	L2L3	-0.11/-0.31	0.17/0.49
	TP_3	-0.08/-0.31	0.13/0.51
	L3L4	-0.10/-0.29	0.18/0.53
	TP_4	0.00/-0.19	0.00/0.21
	L4L5	-0.04/-0.16	0.04/0.18
	TP_5	0.00/ 0.00	0.00/0.00
	VB_5	0.00/ 0.00	0.00/0.00

[a] Each second set of values corresponds to the fascicle part between the last lumbar and the first thoracic attachment; e.g. for LTpTh L3, it is the fascicle part between L1-T7 levels.

Table 5.10: (L)eft/(R)ight fascicle strain and active force predictions in standing with PR using the P-SP L1-S1 FE model.

Muscle	Fascicle	Strain (L/R) (%)	Active force (L/R) (N)
MF	L1	-0.45/-0.60	0.04/0.06
	$S_{1,1}$	-0.54/-0.31	0.11/0.06
	$S_{1,2}$	-0.80/-0.27	0.18/0.06
	$S_{1,3}$	-0.58/-0.28	0.10/0.05
	$S_{1,4}$	-0.52/-0.32	0.00/0.00
	L2	-1.08/-0.78	0.12/0.08
	$S_{2,1}$	-1.03/-0.44	0.23/0.09
	$S_{2,2}$	-0.71/-0.42	0.35/0.20
	$S_{2,3}$	-0.59/-0.38	0.30/0.19
	L3	-1.59/-0.82	0.23/0.11
	$S_{3,1}$	-0.43/-0.36	0.13/0.11
	$S_{3,2}$	-0.88/-0.53	0.27/0.16
	L4	-0.49/-0.23	0.06/0.03
	$S_{4,1}$	-0.14/-0.13	0.04/0.04
	$S_{4,2}$	-0.30/-0.21	0.09/0.06
	L5	0.00/ 0.00	0.00/0.00
	$S_{5,1}$	0.00/ 0.00	0.00/0.00
ILpL	L1	-0.41/-0.31	0.23/0.17
	L2	-0.05/-0.80	0.04/0.66
	L3	-0.98/ 0.07	1.06/0.00
	L4	-0.50/ 0.31	0.73/0.00
LTpL	L1	-0.45/-0.41	0.18/0.16
	L2	-0.93/-0.15	0.47/0.07
	L3	-0.79/-0.19	0.51/0.12
	L4	-0.75/ 0.15	0.66/0.00
	L5	0.00/ 0.00	0.00/0.00
LTpTh[a]	L1	0.00 / 0.00	0.00/0.00
	L2	-0.05/-0.02	0.00/0.00
	L3	-0.17/ 0.00, 0.00/ 0.00	0.01/0.00, 0.00/0.00
	$L_{4,1}$	-0.57/-0.45, 0.00/ 0.00	0.04/0.03, 0.00/0.00
	$L_{4,2}$	-0.78/-0.76, -0.03/-0.10	0.05/0.05, 0.00/0.01
	L5	-0.67/-0.69, -0.05/-0.09	0.07/0.07, 0.01/0.01
PS	TP_1	-0.13/-0.16	0.07/0.09
	VB_1	-0.16/-0.17	0.31/0.34
	L1L2	-0.16/-0.19	0.31/0.37
	TP_2	-0.24/-0.05	0.24/0.05
	L2L3	-0.05/-0.25	0.07/0.39
	TP_3	-0.05/-0.28	0.08/0.47
	L3L4	-0.07/-0.26	0.12/0.48
	TP_4	0.00/-0.18	0.00/0.21
	L4L5	-0.03/-0.16	0.03/0.17
	TP_5	0.00/ 0.00	0.00/0.00
	VB_5	0.00/ 0.00	0.00/0.00

[a] Each second set of values corresponds to the fascicle part between the last lumbar and the first thoracic attachment; e.g. for LTpTh L3, it is the fascicle part between L1-T7 levels.

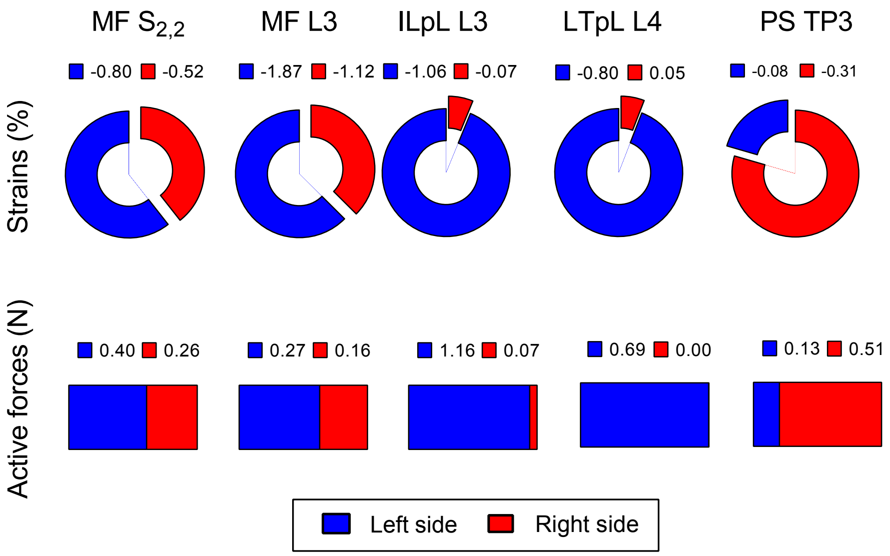

Figure 5.20: Strains and active force predictions per side for the fascicles in the P-SP L1-S1 FE model in standing.

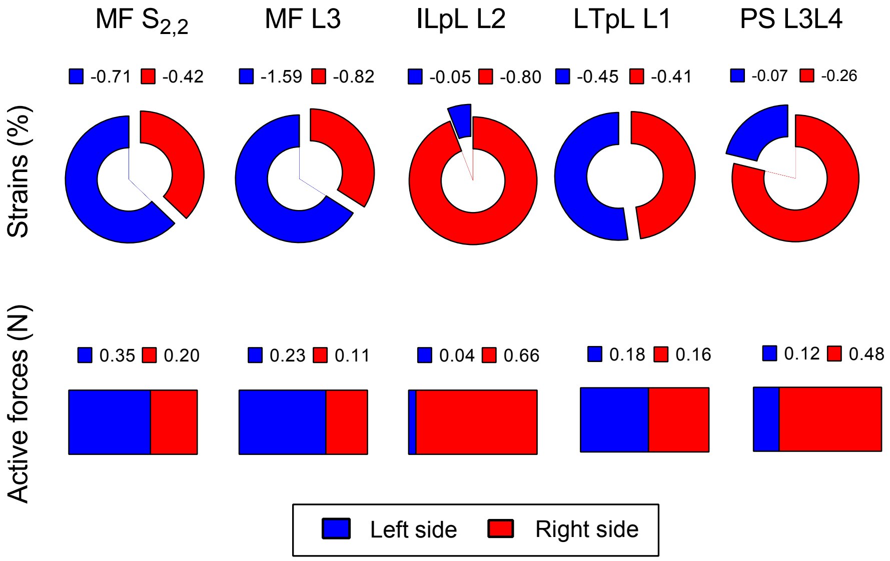

Figure 5.21: Strains and active force predictions per side for the fascicles in the P-SP L1-S1 FE model in standing with PR.

Figure 5.22 presents the variation of muscle activation per lumbar level in standing position with and without PR taking into account the contribution of all fascicles. As observed, the active force development followed an almost bell-shaped distribution along the lumbar spine with highest predictions between L2/L3 and L3/L4 levels in either case. Without previous disc swelling (Fig. 5.22), the results ranged from 1.55 (L5/S1) to 5.11 N (L2/L3, L3/L4). In standing with PR, the corresponding values varied from 1.24 to 3.98 N, respectively. In other words, simulation of PR required 15-39% less activation of the back muscles to achieve mechanical stability of the system in standing.

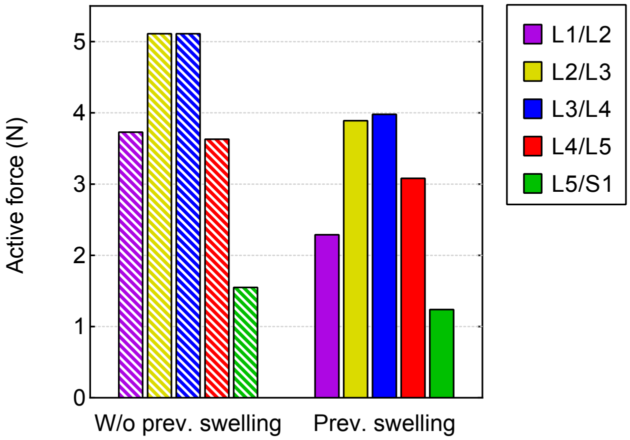

Figure 5.22: Effect of PR on the muscle activation per level in the P-SP L1-S1 FE model in standing.

When passive muscle resistance was also considered in order to calculate the total muscle forces, PR was found to have an important effect on the force magnitudes and its concentration between L2 and L3. For instance, as shown in Fig. 5.23, the total force increase-decrease pattern predicted from L1/L2 to L3/L4 was similar between the two simulations. Nevertheless, although results at L2/L3 were comparable (-7.1, -6.1 N), at L1/L2 and L3/L4 a twofold increase of the compression forces was predicted in standing without PR. Similar situation was seen at L4/L5 (around 53% difference). Interestingly, at the lower lumbar spine, total forces decreased by approximately 17% from L4/L5 to L5/S1, while when PR was simulated before standing, a total force increase of about 16% was calculated.

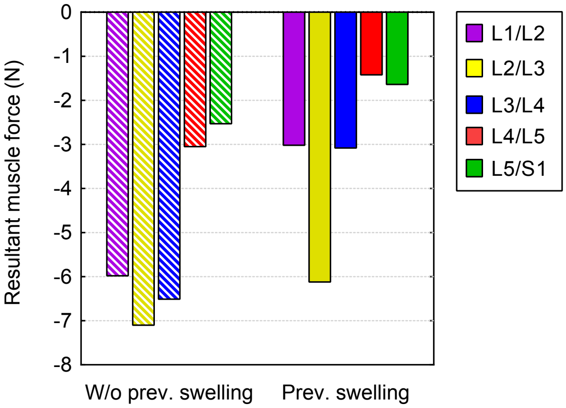

Figure 5.23: Effect of PR on total force distribution in the P-SP L1-S1 FE model in standing.

5.3.2.2 Intradiscal pressure

IDP was calculated at the center of NP of all five discs following the same methodology as described in Chapter 4 and used for the generic models. Due to the altered disc geometry of the patient model, selecting the region was adapted to the disc mesh. For example, at L3/L4 and L4/L5, the mesh was more refined than at other levels and therefore, more integration points were considered for the calculation of the mean IDP (Fig. 5.24). Accordingly, the volumes per NP were: 8.75 mm^3 (L1/L2), 5.06 mm^3 (L2/L3), 8.29 mm^3 (L3/L4), 14.54 mm^3 (L4/L5), 6.27 mm^3 (L5/S1). In order to explore the effect of PR and MS, mean±SD values were estimated in four different simulation cases of standing posture like in 5.3.1.2.

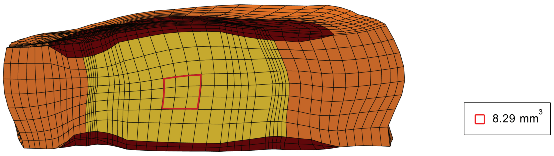

Figure 5.24: Selected region (red) in the center of the L3/L4 NP for the calculation of mean±SD IDP value. Region volume is given in the legend (Undeformed state).

Disc pressures were also predicted after 8 hours of rest with and without muscle simulation (Fig. 5.26). All results are summarized in Table 5.11 and graphed in Fig. 5.25.

Table 5.11: Mean±SD intradiscal pressure (MPa) values in the center of NP in the P-SP L1-S1 FE model in standing and lying. (PR=Prev.swelling; MS=Muscle presence)

	L1/L2 (3)[a]	**L2/L3** (3)[a]	**L3/L4** (3)[a]	**L4/L5** (4)[a]	**L5/S1** (2)[a]
Standing					
Case 1 (PR, MS)	0.28±0.01	0.27±0.003	0.34±0.02	0.42±0.04	0.19±0.004
Case 2 (~~PR~~, MS)	0.24±0.02	0.22±0.010	0.31±0.02	0.38±0.04	0.40±0.010
Case 3 (PR, ~~MS~~)	0.29±0.01	0.29±0.003	0.37±0.02	0.41±0.04	0.20±0.004
Case 4 (~~PR~~, ~~MS~~)	0.26±0.02	0.24±0.010	0.33±0.02	0.37±0.04	0.41±0.010
Lying (8-h rest)					
MS	0.06	0.06	0.07	0.08	0.20±0.004
~~MS~~	0.06	0.05	0.06	0.06±0.01	0.20±0.004

[a] Disc degeneration grade.

In standing with previous disc swelling (Case 1), the mean IDP varied between 0.19-0.42 MPa (Fig. 5.25). Without PR (Case 2), lower IDP were predicted at all levels from L1/L2 (0.24±0.02 MPa) to L4/L5 (0.38±0.04 MPa). At L5/S1, the model captured a mean pressure increase from 0.19 MPa to 0.40 MPa. When muscles were not simulated (Cases 3,4), a similar tendency was predicted regarding the effect of previous disc swelling on disc pressure. Particularly, without PR (Case 4), mean IDP values between L1/L2 and L4/L5 were 0.26, 0.24, 0.33 and 0.37 MPa, i.e. 10.3, 17.2, 10.8 and 9.8% lower than in Case 3. At the lumbosacral level, however, the IDP without PR and without MS (0.41 MPa) was more than two times higher than in Case 3 (0.20 MPa).

Analysis of the muscle role in standing with (Cases 1,3) and without (Cases 2,4) previous disc swelling revealed that muscle absence constantly increased the mean IDP at all levels except for L4/L5 (Fig. 5.25). In all cases of simulated standing, the highest SD was calculated at L4/L5 where severe degeneration was clinically identified (grade 4).

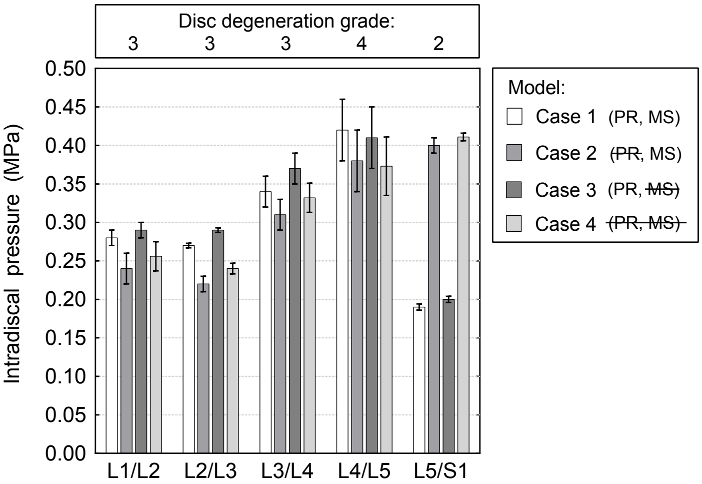

Figure 5.25: Effect of PR and MS on the IDP predictions per level using the P-SP L1-S1 FE model in standing.

After 8 hours of rest, the IDP increased on average by 0.06 MPa at L1/L2-L3/L4 discs (grade 3), 0.08 MPa at L4/L5 (grade 4) and 0.20 MPa at L5/S1 (grade 2). That is, like in the generic model, most discs were subjected to a pressure that was only a fraction of the one in standing position. Without muscle action, small variations were predicted (Fig. 5.26). For this simulation, no experimental data on symptomatic population after rest could be retrieved from the literature in order to evaluate the results obtained.

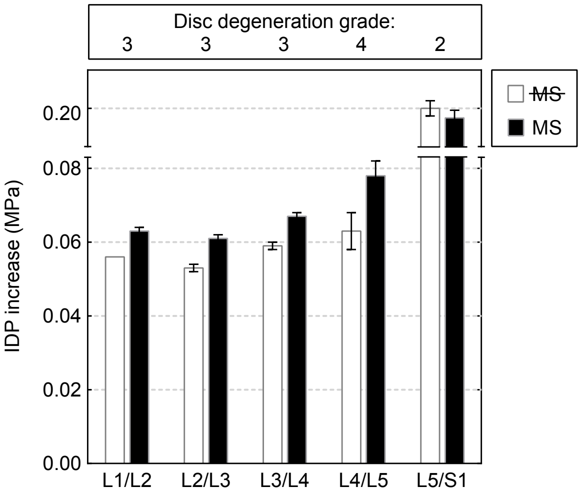

Figure 5.26: Effect of MS on the IDP increase per level using the P-SP L1-S1 FE model after 8 hours of simulated rest.

5.3.2.3 Lumbar lordosis and intersegmental motion

Calculations based on the model in standing position showed that previous disc swelling affected mainly the ISR at the upper two lumbar levels (Table 5.12) even though the effect between such levels was different. Specifically at L1-L2, the calculated segmental angle decreased when PR was included, whereas at L2-L3 a slight increase was predicted. Between L3-L5, the low swelling capacity of the relevant discs (grade 3, 4) resulted in similar ISR predictions between Cases 1 and 2 (about 8.4°, 21.1° at each level respectively). On the contrary, MS had a significant effect at most levels. That is, at L1-L2, the ISR was about 7.2% lower when muscle were not simulated (Case 3), and when PR was not considered either (Case 4) the monosegmental angle predicted was 12.3% smaller than in Case 1 (Table 5.12). In comparison with the ISR predictions obtained with the generic L1-S1 model (Table 5.6), the monosegmental angles calculated in the degenerated spine were larger at all lumbar levels. For instance, in Case 1, the results at the patient model from up to downwards were 93%, 92%, 54% and 67% higher.

In terms of lordotic angle, the L1-S1 curvature calculated for the patient model in standing position was 41.24° either with or without PR. Such value was approximately 36% higher than the lordotic angle calculated for the generic L1-S1 model in the same cases of simulated standing (Table 5.6). As reported in Table 5.12, previous disc swelling was found to have no effect on the total lordotic angle of the patient model even when it was combined with muscle absence (Cases 3,4).

Table 5.12: Monosegmental and L1-S1 Cobb angles (°) in the P-SP L1-S1 FE model in standing.

	Case 1	Case 2	Case 3	Case 4	Effect of PR/MS/PR+MS (%)
L1-L2	1.95	2.02	1.81	1.71	-3.5/7.2/12.3
L2-L3	5.06	4.96	5.16	5.25	2.0/-2.0/-3.6
L3-L4	8.44	8.42	8.55	8.60	0.2/-1.3/-1.9
L4-L5	21.10	21.17	21.04	21.01	-0.3/0.3/0.4
L1-S1	41.24	41.24	41.28	41.28	0.00/0.11/0.11

Similar tendencies were reflected by the analysis of the vertebral movement at the different planes (Fig. 5.27-5.29). When standing followed PR (Case 1), the VB centroid positions showed a slight axial compression together with lateral bending of the degenerated spine towards the left side. This behavior was further marked at both frontal (Fig. 5.27 left, 5.28A) and transverse (Fig. 5.28C) planes when muscles were absent (Case 3).

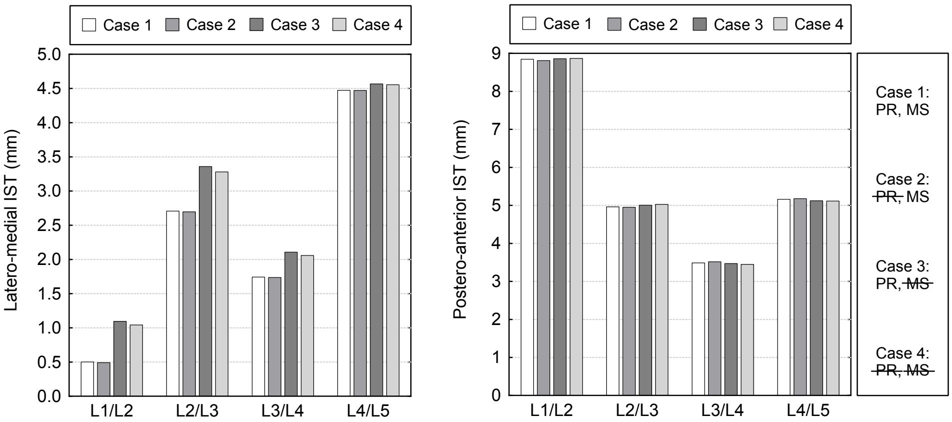

Figure 5.27: IST in the frontal (left) and sagittal (right) plane using the P-SP L1-S1 FE model in standing.

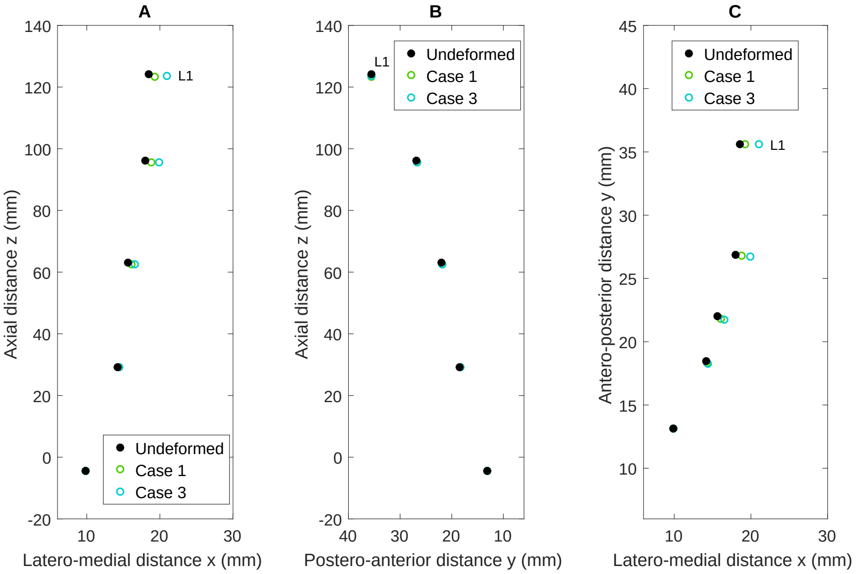

Figure 5.28: Effect of MS on the L1-L5 centroid position in (A) frontal, (B) sagittal and (C) transverse plane. (P-SP L1-S1 FE model, standing)

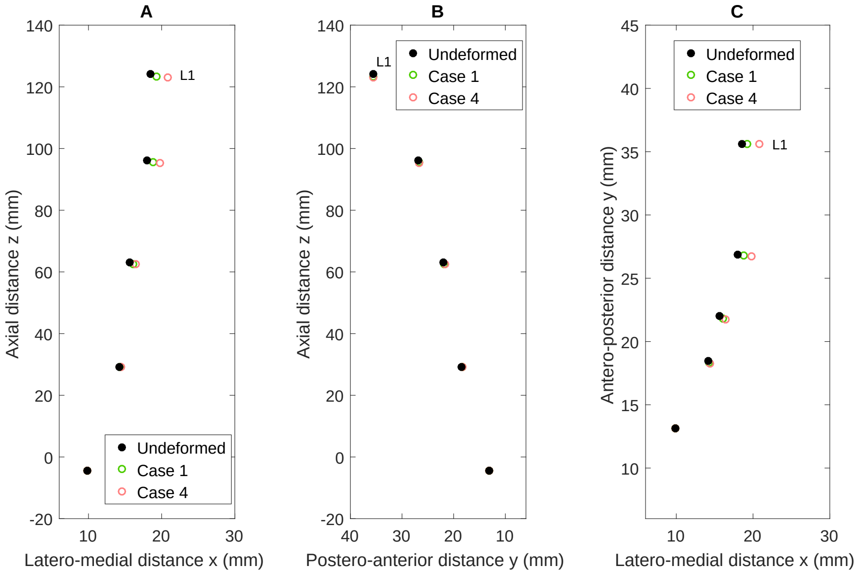

Figure 5.29: Combined effect of MS and PR on the L1-L5 centroid position in (A) frontal, (B) sagittal and (C) transverse plane. (P-SP L1-S1 FE model, standing)

Indeed, as presented in these figures, such left lateral bend was principally observed at the upper L1-L3 levels and was in line with the increased fascicle shortening predicted at those levels (Table 5.10). When both PR and MS were excluded from the simulation (Case 4), the obtained profiles in standing (Fig. 5.29) were comparable with Case 3. However, the lack of disc swelling resulted to a slightly increased downward movement of the upper VB centers compared to Case 3 (Fig. 5.28B, Fig. 5.29B). Still, at the lower lumbar levels, the difference captured on the VB positions was null. Compared to the generic model (Fig. 5.14), the postero-anterior IST on the sagittal plane was very small (Fig. 5.27 right).

Calculations of anterior (at anterior AF), mid (at NP center) and posterior (at posterior AF) disc heights revealed that body weight did not have an important effect on disc heights in any of the studied cases of standing (Fig. 5.30). In terms of disc geometry, the significant intralevel differences of especially the mid and posterior heights at all standing states followed the same pattern as for the initial configuration. The increased anterior disc heights compared to the posterior values at L1/L2 and L5/S1 (about 43% lower in either levels) reflected the wedge shaped geometry of these joints. Particularly for L5/S1 (grade 2), height values in any standing case showed that the disc preserved its vertical dimensions at all three regions; anterior, mid and posterior (Fig. 5.30). Taking into account the restricted motion of the L5/S1 lower endplate, such outcome suggested that all aforementioned changes in the NP pressure at this level (Cases 1-4, Fig. 5.25) led to a radial expansion of the disc that was seen as symmetric posterior and anterior bulging of the annulus.

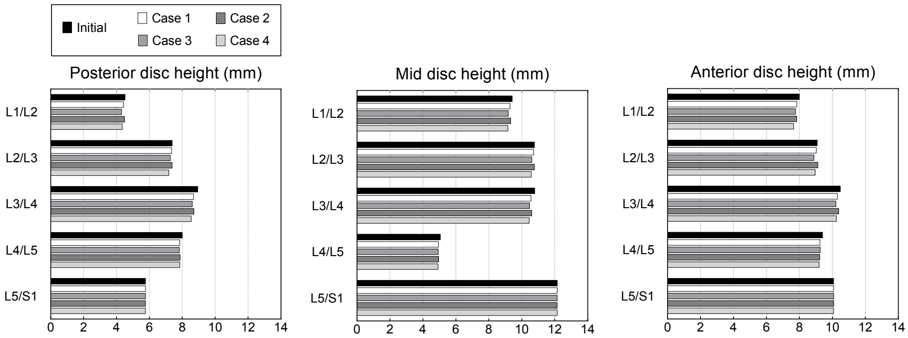

Figure 5.30: Posterior, mid and anterior disc heights per level and per simulated case of standing.

Table 5.13 lists the mid height values calculated at the NP of all discs of the generic and P-SP lumbar spine models at the undeformed (initial) shape and the percentage variation calculated per level when standing with PR was simulated for each model (Case 1). In the undeformed configuration, the patient model had thicker discs at L1-L3 and L5/S1 levels than the generic model. The patient L3/L4 and L4/L5 IVDs on the contrary were clearly more flattened. Particularly at L4/L5, the NP height of the healthy disc was three times larger than the one of the degenerated disc which had a rather collapsed geometry (grade 4).

Table 5.13: Initial mid disc height (mm) and height difference calculated per level in the generic and P-SP L1-S1 FE models in standing with PR (Case 1).

	Generic		**P-SP**	
IVD	**Initial**	**Height difference**	**Initial**	**Height difference**
L1/L2	8.72	1.36%	9.41	-1.33%
L2/L3	9.92	1.49%	10.77	-0.45%
L3/L4	13.10	0.83%	10.78	-2.01%
L4/L5	14.33	0.56%	5.06	-2.47%
L5/S1	10.34	0.00%	12.15	0.00%

5.3.2.4 Effect of IVD condition and geometry

At first, the effect of disc condition was explored by repeating the simulations of Cases 1 and 3 for the patient model using healthy disc properties, i.e. the material properties used in the generic model simulations (Table 4.2). In lying position at the end of the 8 hours of rest, the IDP variation predicted using the patient model with muscles and either sets of disc material properties at most levels was very similar to the results presented previously for the generic model (Fig. 5.31 left). Pressure increase in the degenerated discs after 8-h rest were between 0.06-0.20 MPa (with muscles) and 0.05-0.20 MPa (without muscles), whereas the mean ranges in healthy discs were 0.14-0.15 MPa (with muscles) and 0.13-0.15 MPa (without muscles). When muscles were included (Fig. 5.31 left), simulation with degenerated discs gave 45-56% lower pressure increase between L1/L2 (grade 3) and L4/L5 (grade 4), but 22% higher IDP at L5/S1 (grade 2) than in the simulation with healthy discs. When muscles were not included (Fig. 5.31 right), the respective variations of the IDP increase overnight were similar: 53-57% between L1/L2 and L4/L5, 25% at L5/S1. Muscles were found to have almost zero effect on the simulated L5/S1 IDP increase overnight independently of the disc condition.

In standing position, healthy material properties always increased the IDP predictions at most levels but L5/S1 compared to the degenerated disc definitions, likewise observed in the generic model with or without muscle presence (Fig. 5.32). Mean IDP ranges were 0.15-0.42 MPa (healthy) and 0.19-0.42 MPa (degenerated) when muscles were included (Fig. 5.32 left), whereas the corresponding ranges without muscle presence were 0.15-0.43 MPa and 0.20-0.41 MPa (Fig. 5.32 right). Unlike the outcomes of the generic model, the pressure predictions between L1-L3 increased in caudal direction when healthy discs were simulated either with or without muscles. Among all lumbar levels, the maximum IDP value for the patient model was calculated at L4/L5 (average: 0.42 MPa) and was approximately 27% higher than the maximum IDP calculated for the generic model (average: 0.31 MPa at L1/L2).

At L5/S1, the muscle effect was almost null either with healthy (0.15, 0.15 MPa)

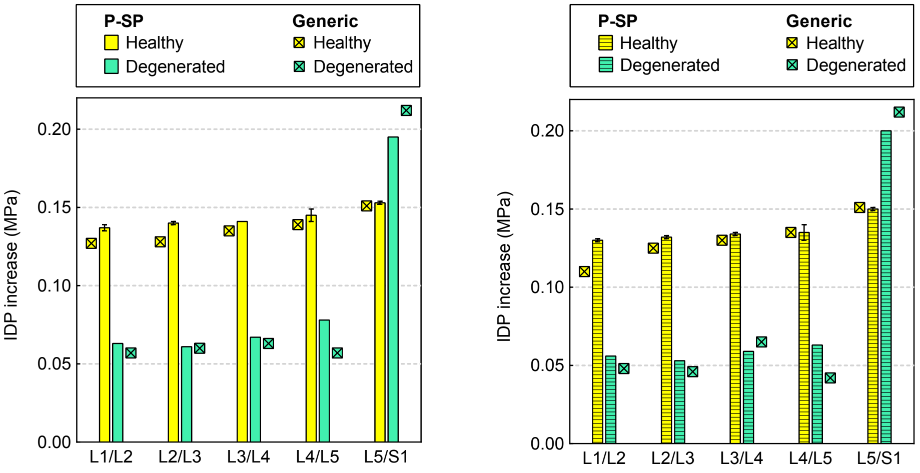

Figure 5.31: Effect of disc condition on the IDP predictions (mean±SD) using both the P-SP and generic L1-S1 FE models after 8-h rest: with (left) and without MS (right).

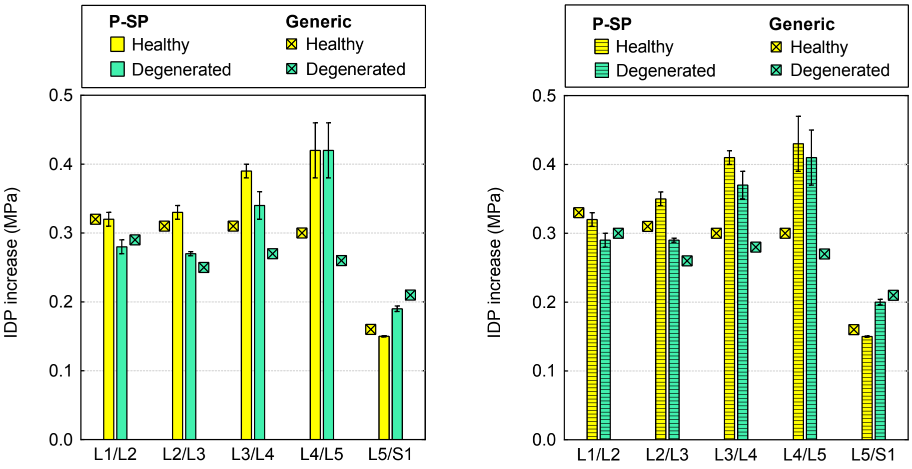

Figure 5.32: Effect of disc condition on the IDP predictions (mean±SD) using both the P-SP and generic L1-S1 FE models in standing: with (left) and without MS (right).

or degenerated (0.19, 0.20 MPa) disc properties, whereas the effect of disc condition resulted in about 21-25% higher IDP pressures when degenerated discs were simulated. The latter was comparable to the effect of disc condition quantified as approximately 24% at L5/S1 for the generic model. When muscle action was not taken into account, the mean IDP was slightly decreased when degenerated disc properties were assigned (0.41 MPa). Interestingly, when muscles were included, identical IDP was calculated at L4/L5 with either set of material parameters (0.42 MPa). In other words, disc condition had no effect on the disc pressure magnitude probably because the already collapsed geometry of the disc defined the limited load bearing ability at this level. In fact, analysis of the combined effect of disc geometry and disc condition on the IDP results supported such idea. Fig. 5.33 presents the IDP predictions in standing with PR for the generic and P-SP L1-S1 models considering degenerated disc material properties for all discs in either model. In spite of the identical material definition, the IDP increase calculated at L3/L4 (about 26%) and L4/L5 (around 61%) where highest NP height decrease was discussed before could be associated with the altered disc geometry of the patient discs. Indeed, the L4/L5 IDP in the P-SP model (0.42±0.04 MPa) gave better correlations with previous *in vivo* measurements (0.54±0.18 MPa, [198] and 0.50 MPa, [195]) than the corresponding IDP found in the generic model. Such outcome greatly contributed towards the validation of the proposed methodology when P-SP configurations are introduced in the simulations.

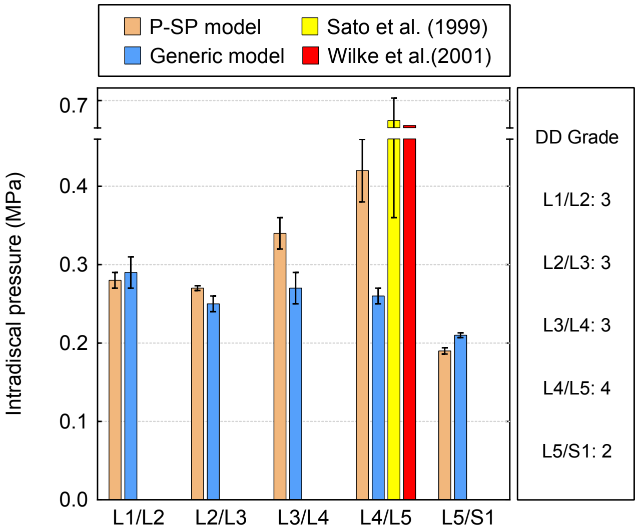

Figure 5.33: Effect of disc geometry on the IDP predictions in standing with PR using degenerated disc material properties.

In standing position with PR, the calculated active forces were also compared for the patient model using the two different sets of disc properties (Fig. 5.34). From a qualitative viewpoint, the relevant inter-level force distributions were similar with either healthy or degenerated disc parameters. That is, active forces increased progressively from L1/L2 to L3/L4, where the peak value was predicted, and then decreased in the caudal direction. The predicted active loads per level ranged between 1.24-3.98 N (degenerated) and 0.42-1.92 N (healthy) revealing, as such, the significantly higher muscle activation required to balance the gravity loads in a degenerated spine. Particularly, at L1/L2, the active forces with degenerated discs were equal to 2.29 N, i.e. more than five times higher than the corresponding value with healthy discs (0.42 N), while at the levels between L2 and S1, a twofold increase was predicted on average. In either simulations, similar activation was predicted between L2/L3 and L3/L4 levels. Indeed, the relative force distribution pattern in the patient model with degenerated discs correlated well with the respective predictions in the generic model with the same degenerated disc properties (Fig. 5.17).

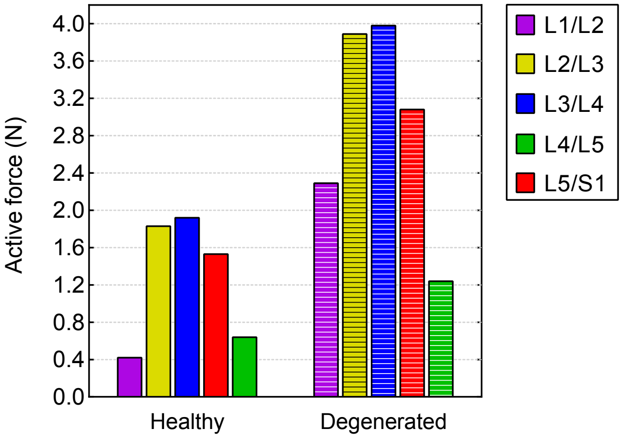

Figure 5.34: Effect of disc condition on muscle activation per level using the P-SP L1-S1 FE model in standing with PR.

For a general evaluation of the spine loads predicted in standing posture, comparisons were performed between the generic and P-SP L1-S1 models with and without previous disc swelling. To do so, the results of simulated Cases 1 and 2 for each model were considered here with healthy disc material properties. Accordingly, Fig. 5.35 presents the effect of previous disc swelling on the active force predictions per level for the generic and P-SP models. For the generic model, simulation of previous disc swelling led to notably different activation needs to mechanical stabilize the trunk in standing, both in terms of magnitude and inter-level variation. For instance, without PR, the highest active forces were concentrated between L2/L3 and L3/L4 (around 3.4 N), whereas with PR, the highest active forces were more than 50% lower and were localized at L1/L2. For the degenerated spine, the effect of PR was reflected by decreased magnitudes of active forces needed rather than by modifications of the inter-level of relative activation (Fig. 5.35). Nonetheless, in both lumbar spine models, the minimum values of activation were always calculated at the lumbosacral level and were further decreased when PR was simulated before standing, particularly for the generic model (about 71%).

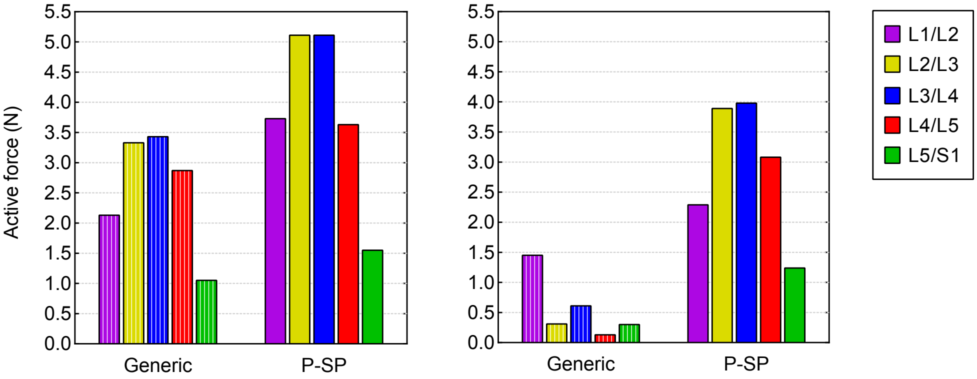

Figure 5.35: Comparison of the active forces per level between the generic and P-SP models in standing without (left) and with (right) PR.

Similar analysis of the resultant muscle forces per lumbar level in both models with (Fig. 5.36 left) and without PR (Fig. 5.36 right) revealed the crucial effect of swelling mainly on the generic spine. More specifically, although in simple standing the muscles in the generic model developed compressive loads at most levels but L1/L2, the increased swelling capacity of the discs resulted in the development of high tensile loads when standing followed PR. Indeed, in that case, the load distribution per level decreased craniocaudally for the generic spine.

In standing, the model captured concentration of compressive loads at the upper lumbar spine in the degenerated spine (Fig. 5.36 left). At L4/L5, the total muscle load magnitude predicted was about half compared to the value obtained for the generic model. In standing with PR, relevant differences between the two models were calculated: up to 74 and 79% smaller loads in absolute values were developed

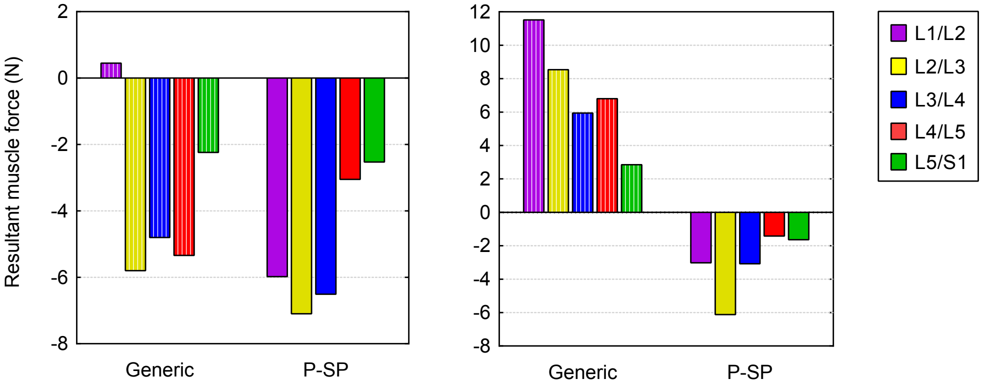

Figure 5.36: Comparison of the total muscle forces per level between the generic and P-SP models in standing without (left) and with (right) PR.

at L1/L2 and L4/L5, respectively, in the P-SP model (Fig. 5.36 right). Nonetheless, the average deformation of the muscle network was 0.35% in the P-SP model, that is almost two times higher than in the generic model (0.18%). Without PR, both mean deformation values were somewhat larger: 0.45% and 0.30%, respectively.

5.4 Discussion

5.4.1 Generic model

The first half of this chapter focused on employing the methodology proposed in Chapter 3 for the biomechanical study of a full lumbar spine FE model with a generic geometry.

In standing position, the effects of two factors were explored upon load predictions and spine kinematics: previous disc swelling (PR) and muscle presence (MS). In terms of forces, without PR, the model predicted a high load concentration between L2-L4 levels, with active forces varying in the range of 2.7-3.3 N (Fig. 5.8). The resultant forces predicted at these levels were between -2 and -6 N (Fig. 5.9) and important contributions of all dorsal and L4-L5 LTpTh fascicles were seen (Fig. 5.4). Interestingly, at L1/L2, despite the high loads exerted mainly by ILpL and LTpL (-1.3 N), the resultant muscle force was positive and equal to 0.5 N. Such behavior was attributed to the short L1 fascicles of MF (LAM1, SP1) for which analysis of the constitutive stress terms revealed high volumetric contribution. Particularly, the lengthening predicted in standing for these two fascicles (Fig. 5.5) created about 74% higher passive forces compared to the active forces at this level. In total, the tensile load developed together with the PS and LTpTh fascicles was over 2 N, that is 128% higher than the compression forces applied by the rest of muscles at this level.

When PR was simulated, traction total forces were calculated by the model at all levels with a decreasing tendency from L1/L2 (11.5 N) to L5/S1 (2.9 N) (Fig. 5.9). The significant effect of PR on the L1/L2 total force magnitude (0.5 N against 11.5 N) was explained by an overall muscle contribution with increased tensile forces (Fig. 5.6). In that case, the active force distribution followed a rather asymmetric pattern with the highest active forces calculated at L1/L2 (1.5 N) and L3/L4 (0.6 N) (Fig. 5.8). Given the healthy condition of the discs, previous IVD swelling offered mechanical stabilization to the spine and so, when standing followed, generally lower muscle activation was needed to satisfy the system equilibrium. The IDP predictions also reflect such behavior (Fig. 5.10): simulation of PR increased the disc pressure between L1/L2 and L4/L5 by up to 41% reaching IDP values that were in agreement with *in vivo* measured data in standing (Table 5.5). At L5/S1, however, the IDP decreased. Analysis of the stress components (Eq. 2.4) immediately after the 8-h rest revealed that the IDP value captured by the model was basically attributed to the deviatoric stress term developed in the center of this disc (approximately 0.15 MPa, absolute value). Application of the gravity loads gave similar stress values at L5/S1, although for the other discs, the significant increase of the volumetric stress term justified the overall IDP increase calculated (Fig. 5.10). Indeed, in standing without PR, the increase of the L5/S1 IDP was associated with the higher contribution of the volumetric stress component. Since healthy material properties were considered using an identical set of values for all discs, the low IDP values at the lumbosacral disc could be related to the disc wedged shape, and mostly to the restricted kinematics of this joint defined at the inferior CEP in lack of sacrum representation. Actually, such restriction resulted in zero L5 VB translations (Fig 5.14) in all simulated cases of standing position.

In terms of ISR (Table 5.6), larger anterior sagittal rotations of approximately 52% at L1-L2, and 2% at L4-L5 were captured in standing when PR was not simulated. For the levels at the midst (i.e., L2-L3 and L3-L4), posterior sagittal rotations of around 15 and 6% lower magnitude were predicted, respectively. Such intersegmental variance probably justifies the similar L1-S1 curvatures calculated in standing with and without PR (Table 5.6). In fact, in spite of the functional and clinical importance of the lumbar lordosis for the assessment of postural abnormalities, there is no consensus among the scientific and clinical community on the most accurate method of measurement and the establishment of a widely accepted range of values for healthy spines ([318], [319], [320]). For the generic L1-S1 FE model that was hypothesized to represent a healthy subject, the L1-S1 lordosis calculated using the Cobb Method was equal to 30.33±0.01 (mean±SD among the cases). The calculated lordosis correlated with [319] even though being slightly underestimated compared to the cited study (33 to 89° for asymptomatic volunteers). The geometric limitation of absent sacrum in the model has most probably affected the calculations. Accordingly, the general 3D orientation of the L1-S1 model considered as a reference for the definition of the vertical gravity loads might have introduced some error on the angle calculation and hence should be taken into account. Study of the IST translation predictions (Fig. 5.14) showed a concentrated effect of PR between L2-L3 that was quantified as 19% anterior more translation of the L2 VB while the L3 moved to the opposite direction by 21% compared to standing with PR.

Evaluation of the effect of MS on the spine kinematics showed a 35% (L1-L2) and 5% (L4-L5) larger anterior sagittal rotation when muscles were not present, while for L2-L3 and L3-L4, a smaller posterior sagittal rotation was calculated (Table 5.6). It has been reported elsewhere that either the abdominal (spinal flexors) and back muscles (spinal extensors) as separate groups of muscles [321], or the relationship between them [322] can be related to pelvis inclination and lumbar lordosis while in upright posture. In the present model where no abdominal fascicles were included, the results in upright standing between normal function (Case 1) and complete muscle absence (Case 3) of back muscles revealed only a small effect (0.03°) of MS on the L1-S1 lordotic angle.

In terms of IDP, the model in standing posture was less sensitive to muscle inclusion than to disc swelling simulation. In standing without MS (Case 3), the maximum pressure increase (about 3%) was calculated at L1/L2 (Fig. 5.10), whereas at L5/S1 no difference in the IDP value was predicted, apart from decreased L5 fascicle deformation (Fig. 5.7) and low stretch-induced activation (Fig. 5.8). In lying rest position, however, muscle absence decreased the IDP by 15% at L1/L2 (0.11 MPa), and by 7% at L3/L4 (0.13 MPa) (Fig. 5.11). At L4/L5, even though muscle function was not found to affect the disc pressure, the FE-driven IDP prediction (0.14 MPa) laid in the measured range reported by [195] (0.10-0.24 MPa) for a volunteer with a similar weight.

When the variations of the two factors (MS, PR) were combined (Cases 1, 4), the results revealed an interesting behavior. For instance, in Case 1, IDP values from L1/L2 to L4/L5 were 28-41% higher than in Case 4, where simple standing was simulated without muscles and without previous disc swelling (Fig. 5.10). That is, in Case 4 the low IDP calculated at most discs were far from reported experimental measurements. In terms of vertebral rotation, 35% higher anterior sagittal rotation at L1/L2 was captured compared to Case 1. Although such motion was compensated by the backward rotation between L2/L3 and L3/L4 levels, a slight forward rotation was also generated at L4/L5. The relative rotations in Case 4 were comparable to Case 3 where PR was simulated (Table 5.6). Nonetheless, magnitudes were smaller especially at the lower region principally because the spine was not subjected to the additional translation induced by the swelling of the healthy discs overnight (Fig. 5.13).

As illustrated in Fig. 5.15, when standing with PR simulation (Case 1) was repeated using degenerated disc properties (Case 5), the mean disc pressure decreased at all levels except for L5/S1, where it increased. That is, with muscles included in the model, the effect of altered disc condition on the L1-L3 IDP was quantified as up to 19% lower values compared to the healthy disc simulation (Case 1). From a geometrical point of view, mid disc heights at the upper levels slightly increased in Case 5 (Table 5.8) following a tendency that was qualitatively similar to that of IDP results: predictions in Case 5 were lower than in Case 1. Nevertheless, the disc height values of the degenerated discs were closer to the initial heights than the ones of the healthy discs (Table 5.8). This was expected, since disc degeneration (grade 3) reduced the swelling capacity of these discs and therefore, despite the 8-hour simulated rest before standing, they were smaller compared to Case 1 and virtually less hydrated. Between L3-L5, healthy discs continued their height increasing tendency, while for the degenerated discs (grade 3, 4), the small mid height reduction from the initial height predicted (Table 5.8) might have been due to the damage accumulation at these levels. As such, the combination of caudal IDP increase (Fig. 5.15 left) and higher muscle activation captured by the model close to L4-L5 (Fig. 5.17) was suggested to act as the system's mechanism to overcome the altered disc mechanical role and reestablish the spine stability while in standing posture. Indeed, as reported in Table 5.7, muscles with longer fascicles covering several lumbar levels, such as the superficial MF and PS fascicles, were found to be more activated when degenerated discs were simulated.

Analysis of the IDP results in lying position (Fig. 5.16 left) showed that, without external loads, the discs with altered mechanical properties were not able to increase the IDP to the levels achieved with healthy discs. Moreover, considering degenerated disc behavior and total muscle absence, the disc pressure predicted at L4/L5 (grade 4) was 69% lower compared to its value for a healthy spine (0.14 MPa) (Fig. 5.16 right). That is, although the effect of MS on the IDP of healthy discs was null (Table 5.5), when muscle absence was combined with disc degeneration, the model captured a significant impact on the internal load development in the studied postures.

Explorations with the full L1-S1 FE model addressed several of the limitations discussed in Chapter 4, such as the design of more pragmatic thoracic BC, and the obvious need for the inclusion of upper level soft tissues. Actually, the multi-parameter analysis performed in standing and lying posture was extended to explore also the effect of altered disc material properties on load transfer. Yet, consideration of for example, realistic disc geometries, such as bulging or flattened discs, is expected to influence the biomechanical response predicted. Therefore, the results obtained further highlighted the principal objective of this thesis: the need for P-SP models that include as many of the mechanical and biological aspects of the spine possible to address the understanding of the apparently critical interplay between disc multiphysics and muscle function.

5.4.2 Patient-specific model

Unlike the generic model where symmetric bilateral contractions were predicted, fascicle strain and activation profiles in the P-SP model were mostly asymmetrical when standing was simulated (Table 5.9, Table 5.10). Increased fascicle shortening was calculated for the left side of most dorsal muscles, and the active force values were 31 and 20% higher than at the right side in standing with (Case 1) and without PR (Case 2), respectively. For the LTpTh, the unilateral contraction predicted at the upper levels (Fig. 5.19, Table 5.10) might reflect its role as an indirect flexor of the lumbar spine in agreement with previous studies (2.2.5.3.1). Still, analysis of the centroid motion in Fig. 5.28 A, C revealed that the general asymmetry of the fascicle response tended to reduce the load-induced lateral bending caused by the geometrical asymmetry of the patient osteoligamentous spine. Such role of the muscles had been previously suggested in the literature [323] and was further supported in the present study by the augmented lateral bend of the lumbar spine calculated when muscles were not considered (Fig. 5.28 A, Case 3). What is more, in the latter case an added increase of the IDP was predicted at L1/L2 - L2/L3 (Fig. 5.25). Since the calculated disc height reduction was very similar between Cases 1 and 3 (Fig. 5.30), stress analysis showed an increased NP expansion and compression of the lateral AF when muscles were not simulated. That is, loads were found to be transferred directly through the AF. Hence, the results allowed for the interpretation that muscles might help to have functional load transfers through the IVD and also to protect the AF.

With regard to the lumbar lordosis in standing position, results in Cases 1 and 3 showed a short dependance of the L1-S1 Cobb angle on muscle presence that resulted in a 0.1% reduction of the lordotic angle. In this model, two geometrical limitations should be taken into account for the interpretation of the obtained results: the restricted motion of the L5/S1 joint applied in lack of sacrum and/or pelvis joints, and the absence of the major trunk flexor group, i.e. the abdominal muscles. As such, any variation of the lumbar lordosis captured in upright standing was explored via the analysis of the L1/L2 and L2/L3 kinematics, and the action of the back muscles expected to act as posterior sagittal rotators. Indeed, comparisons of the sagittal ISR showed an alternating pattern of forward-backward bend among the upper two levels (Table 5.12), such behavior being probably the reason for a rather small change in the lordotic angle between Cases 1 and 3. A closer look on the force predictions of the spinal extensor muscles revealed that, on one hand, the highest loads were actually developed at L2/L3 and particularly by the MF (-2.4 N approximately) and ILpL fascicles (about -1 N). From a biomechanical viewpoint, since the line of action of the long MF fascicles lies behind the lordotic curve, such increased loads could justify a small accentuation of the lordotic angle. On the other hand, in absence of abdominal muscles, the calculated PS shortening and its compressive forces between L1-L3 (Fig. 5.18) could be interpreted as a limited but valuable representation of the opposing anterior sagittal rotation of the lumbar spine. Whether the lordotic angle and pelvic tilt are affected more by the action of muscles in groups (i.e. flexors-extensors) or their particular strength in separate is unclear [318]. Similarly, the existence of a correlation between the lumbar lordosis shape and back pain symptoms is also an ongoing debate ([324], [325], [326], [130]). Yet, with all limitations in mind as well as the restrictive fact of studying only one patient model, the predicted imbalance between trunk flexors and extensors captured in simulated standing could be considered as representative of the altered kinematics of a degenerated lumbar spine. Moreover, the prediction of an increased lumbar lordosis in the patient model compared to the healthy configuration was in line with the conclusions in [327].

In standing, disc pressure ranges in the patient model were generally higher than those predicted with the generic model with non-degenerated IVDs, and the calculated inter-level IDP variations were different (Table 5.5, 5.11). For instance, when PR was simulated (Cases 1, 3), the highest disc pressure for the generic model was predicted at L1/L2 (healthy), whereas in the patient model the peak was at L4/L5 (grade 4). In fact, between L3 and L4, the IDP in the P-SP spine was found to increase in either of these cases (Fig. 5.25). At the upper lumbar spine, the IDP predictions confirmed the suggestion that strong trunk muscles decrease the disc pressure in upright standing. At L4/L5, however, the IDP was slightly increased in the simulation with muscles (0.42 MPa) and was on the whole higher than at any other level. The tensile loads predicted in the PS fascicles attached to the L4/L5 disc rim and the L4 VB (Fig. 5.19), as well as the anteriorly displaced NP favored a forward flexion that would compromise the upright posture of the trunk. Assessment of the validity of such predictions for degenerated discs is delicate since the multi-parameter nature of back disorders does not permit for an accurate definition of the problem. Yet, in spite of the few direct measurements and the distinct clinical history of the volunteers, the model's results at L3/L4 were within the SD of the *corrected*[2] data in [176] measured in volunteers with LBP symptoms and sciatica. At L4/L5, the IDP prediction laid in the range[2] reported by [328] for volunteers with LBP and BW within 69-93 kg.

The predictions of overnight pressure increase confirmed the great impact of altered disc multiphysics on its strength and therefore its ability to sustain weight during the activities following. For instance, the pressure exerted on these discs after rest was 4-6 times smaller than in standing position (Table 5.11). Except for the L5/S1 IVD, the IDP increase at all remaining levels in the patient model was around 0.07 MPa, i.e. up to 54% lower al disc after a 7-hour rest, and it was in the range of pressures recorded by Sato et al. [198] in lying prone than the corresponding increase predicted in the generic model. Although comparisons with experimental data should be definitely made with caution, the average increase computed was half of the increase measured by Wilke et al. [195] in a normal discs with mild and moderate degeneration. At the lumbosacral level, however, the IDP increase in the IVD (grade 2) was 22% bigger than in the simulation with healthy properties. As described previously in this chapter, a higher $\Delta\pi$ was defined for the grade 2 disc (0.24 MPa) compared to a healthy one (0.15 MPa) as derived from the optimization study of Malandrino et al. [281]. Should such hypothesis is representative of a mildly degenerated IVD or a material artifact remains questionable. Based on the calculations performed though, the disc clearly benefited from the rest to virtually

---

[2] Nachemson retrospectively suggested a revision of the reported data in [176] and [328] claiming a possible overestimation in the recorder pressures related to the technology of the transducer used in the cited study. Corrected values were derived from [329].

hydrate, and after 8 hours the IDP increase was almost 0.20 MPa, i.e. very similar to the $\Delta\pi$ applied at the beginning of the simulation (0.24 MPa). Indeed, calculation of the ratios of the overnight pressure increase (Fig. 5.31) to the initial $\Delta\pi$ showed higher correlations in healthy (91-100%) than in the degenerated discs (77-86%). When comparisons were performed without MS, similar behavior was seen but the ratio values were generally smaller: 88-100% in healthy and 66-81% in degenerated. That is, even though direct evaluation of MS via the IDP increase results showed almost zero effect (Fig. 5.31), these correlations revealed that in the P-SP model overnight muscle action might have actually helped the IVD reestablish its pressure before additional external loads are applied.

In standing with PR, the internal load distribution in the patient model with healthy discs was generally altered in a similar way as in the generic model except for the levels where high degeneration was present. In particular, at L4/L5 (grade 4), the increased IDP predicted was constant independently of the disc material properties used (Fig. 5.32 left). Muscle activation per level, in contrast, was significantly raised when discs were defined as degenerated (Fig. 5.34). That is, because of the reduced bearing ability of the severely degenerated discs, trunk muscles adapted their action as to sustain the erect position of the trunk. In order to investigate also the effect of disc shape, comparisons between the patient and generic models with degenerated disc properties were made. The results revealed that the thinner L3/L4 (grade 3) increased the IDP in the patient model by 26%, while at L4/L5 where in addition the disc was flattened, the pressure increase was over 60% (Fig. 5.33). At the upper two IVDs with heights similar to those of the generic discs (Table 5.13), IDP differences were rather low. In other words, excluding the L5/S1 joint, the results proposed that the importance of disc geometry on the intradiscal pressure in the standing position was increased with the consideration of degenerated material properties from up to downwards.

An overview of the predictions of active and total muscle forces showed that the biomechanical behavior of the lumbar spine in upright standing can benefit from previous rest depending on both the functional and anatomical condition of the tissues (Fig. 5.35, 5.36). Specifically, the model of a healthy lumbar spine demonstrated that disc swelling helped strengthen the discs so when standing followed, less activation was needed to counterbalance the anterior external loads. The degenerated spine, in contrast, was more challenged to oppose the gravity loads due to both the altered biomechanics and the collapsed shaped of some of its discs. As such, higher load transfer was produced at the upper levels using the trunk muscles as to compensate the mechanical instabilities introduced by the L3/L4 IVDs and at last protect the L5/S1 joint that would otherwise be overloaded. Such functional interactions between the lumbar IVD multiphysics and the trunk muscle action captured by the models might be crucial for the understanding of the patterns in a complicated system both anatomically and mechanically.

Finally, the major muscle modeling limitations should be also outlined. The methodology proposed tried to address as much possible the personalization of the model by keeping the computational cost of the simulations at realistic levels. For instance, elegant constitutive formulations have been previously proposed for 3D models of skeletal muscles taking into consideration the fascicle curvature [258] or the time effects [261] for the stress and strain predictions. Nevertheless, such models include an increased number of material parameters (14 and 13 per muscle, respectively) that would be hard to control if applied to the simulation of the lumbar system. In this thesis, the limited number of five parameters of the model was calibrated against only one set of kinematical data collected in a hyperlordosis motion that implied shortening of all fascicles. Even though the fascicle strains calculated in standing position with the models were within the range of strain values used for the calibration, further investigation of the ranges of the active parameter is considered necessary. Whether the model as it stands is able to represent realistic muscle behavior under long-lasting loads remains also to be addressed. Furthermore, as aforementioned, all P-SP simulations were carried out for one patient model. As such, general conclusions on the role of geometry on the IVD-muscle interactions should involve explorations on a larger cohort using the methodology proposed and implemented in this thesis. At last, further explorations of the degenerated IVD parameters, such as through *in situ* characterization and *in vitro* tests, as well as the consideration of subject-specific ligament properties would contribute towards the full personalization of the models.

To sum up, the highlights of the results obtained in the simulations presented in this chapter are:

- Full L1-S1 FE MSL models of both a generic and P-SP geometries were developed using and both healthy and condition-dependent tissue material properties.
- Proper convergence in the simulations of standing and lying in both models demonstrated the robustness of the theoretical models used for the different passive and active tissues.
- Degenerated disc properties in the generic model resulted in up to 14 times higher active force predictions in standing with PR and suggested possible implications of the interplay between IVD multiphysics and muscle function in low back disorders.
- Asymmetric fascicle activation with increased shortening of the left side fascicles and a lateral bending of the trunk was captured in simulated standing in the P-SP model.
- Improved correlations of the IDP predictions using the P-SP model and degenerated disc properties with previous *in vivo* measurements greatly contributed towards the validation of the methodology proposed.

Chapter 6

General conclusion and remarks

The methodology developed in the present thesis allowed for the very first time an explicit and rational exploration of the interactions between muscle function and passive tissue biomechanics in the lumbar spine. To achieve this, a computational approach based on the continuum mechanics theory implemented in FE analyses was used. Through constitutive modeling, the basic mechanical properties of the muscle extracellular matrix were coupled with muscle fibers, modeled through a Hill-based theoretical model suitable for the simulation of relatively large systems (Chapter 3). For the IVD, solid and fluid phases were combined using poro-hyperelastic formulations for the matrix and additional fiber reinforcement for the AF and osmotic effects for the NP according to previous models ([302], [279]).

The proposed schemes were initially implemented for a 46-fascicle muscle network coupled to a generic L3-S1 osteo-ligamentous FE model of a healthy spine. The robust theoretical models used for the different passive and active tissues allowed proper model convergence with implicit FE solvers. In flexion, the simulations captured activation of the trunk muscles to support the spine against excessive bending. The IDP values calculated reproduced previous *in vivo* data showing the predictive ability of the methodology. Results without muscles revealed up to six times lower IDP values and ten times higher reaction moment at L3/L4. Such outcome was in agreement with previous models that concluded that simulating muscles affects the disc pressure, even though there is still no consensus on whether it is by decreasing

[310] or increasing its value [311]. Hence, further analyses were carried out exploring the effect of muscles on load transfers in other postures that involved compression of the lumbar spine. Simulation of standing confirmed that MS increased the IDP to balance the eccentrically distributed compressive loads that represented body weight, but results were underestimated compared to experimental data. When rest was simulated prior to standing, higher IDP were predicted in line with *in vivo* measurements reported in ([203], [202], [307]), which indirectly validated the method proposed. Moreover, different inter-level load transfers were computed with tensile loads that were progressively higher from L3/L4 and down. Actually, during simulated night rest, the disc pressure realistically built up and induced an increased activation of the muscle fascicles especially at L3/L4. This was a result of the cumulative effect of disc swelling from the L5/S1 to the L3/L4 IVD that increased the stretch of the upper fascicles. These simulated effects of previous rest suggested the existence of functional interactions between the IVD multiphysics and muscle activity.

To confirm such predicted interplay, efforts were directed towards the development of full LS MSL models with generic and P-SP geometries using both healthy and condition-specific disc properties. Predictions in standing for a generic 94-fascicle L1-S1 FE model with healthy IVD properties reproduced most of the patterns seen for the L3-S1 assembly, such as the posterior sagittal rotating action of the back muscles, or the decrease of the IDP when muscles were not simulated. Nonetheless, in standing without PR, the load distributions at the lower lumbar levels and the action mainly of the global muscles was different than in the L3-S1 model. For instance, the activation of the PS was larger when the whole lumbar spine was modeled and tensile loads were developed at all levels. Such action was favoring the flexion of the trunk between L3 and L5 since the PS fascicles at these levels were under shortening, whereas at the upper levels the fascicles were mainly opposing the motion. The IST results further highlighted the importance of previous disc swelling that reduced the activation needed to mechanically stabilize the lumbar spine. In particular, the increased activation predicted at the upper levels seemed to mechanically protect the lower levels that would otherwise bear extra loads.

Moving one step forward, the study of the influence of the IVD function was extended by simulating altered disc conditions combined with healthy disc geometries. Notably lower IDP results with degenerated disc properties along with up to tenfold higher active forces in standing with PR showed that the aforesaid relation between IVD multiphysics and muscle activity might have strong implications in low back disorders. Further coupling the 94-fascicle network with a P-SP FE model that represented an adult patient with LBP enhanced the understanding of the IVD-muscles relation under degenerated condition. In standing with PR, significantly higher IDP values were calculated at the levels with moderate and severe degeneration (L3/L4, L4/L5) compared to the results of the generic model and healthy *in vivo* measurements ([203], [202], [307]). Similar to what happened with the generic model geometry, the reduced swelling capacity of the discs was related to an overall increase of the muscle activation needed to balance the gravity loads that tended to flex the P-SP spine model. The predicted asymmetrical contraction of trunk muscles in the patient model in standing correlated with the EMG-driven estimations in neutral posture in [240], and a left lateral bending and important IST in the frontal plane were calculated. When the effects of MS and PR were analyzed together, an augmented ISR was predicted especially at L1/L2, along with reduced disc pressures. Similar to the generic model, disc condition was found to decrease the IDP values at the levels with mild degeneration in the P-SP model. However, at L4/L5 where severe degeneration was present, the IDP was barely affected. Comparisons with the IDP values predicted for the generic model with degenerated disc properties showed a clear impact of the disc geometry: the IDP in the flattened disc of the patient model at L4/L5 was more than 60% higher (Fig. 5.33). Importantly, whether the geometrical asymmetry of the osteoligamentous spine and/or the increased lumbar lordosis in the P-SP model could also affect the IDP in a severely degenerated disc (grade 4) needs further explorations in a larger number of patient models.

All in all, the approach proposed and the first results achieved in this thesis clearly paved the way to investigate the underexplored so far idea that muscle function and disc degeneration might influence each other. As such, it can eventually contribute to a deep revision of the LBP treatments and assessment thereof. The method was adopted to analyze for the first time the MSL LS and stands for a novel and computationally affordable approach for the advanced prediction of spinal loads using continuum mechanics theories. Considering the current SOTA of computational explorations (2.3.2), the present study achieved to address several limitations of the latest LS MSL models reported. For instance, thanks to the predictive ability of the constitutive formulations, muscle and intersegmental loads could be calculated under any deformation using an active model with a limited number of parameters that took into account the muscle mechanical characteristics and did not require the knowledge of kinematical data. In combination with the FE technology, this approach enabled the modeling of deformable IVDs and its multiphysics by considering factors such as altered disc geometry and degenerated material properties. Indeed, the challenge of a fully personalized model of the degenerated IVD has not been completely achieved since additional experimental (*in vitro* and *in situ*) and modeling explorations are required for better descriptions of the altered mechanical behavior. Still, the obtained outcomes allowed the first educated considerations about the interplay between muscle activity and IVD mechanical competence, highlighting possible serious consequences of muscle weakness along disc degeneration, and the importance of night rest on the LS internal and functional biomechanics, which had not been reported previously.

Explorations of a larger number of models with different LS geometries, disc degeneration profiles and diverse anthropometric and occupational data could allow for advanced classifications of patients based on internal biomechanics descriptors that might be of clinical interest. Moreover, the ability of the IVD and muscle models to be optimized using dynamic MRI [28], *in vitro* [281], or elastography techniques [115] opens the path for fully personalized analyses not only geometrically but also mechanically. An application could be for instance via the prototype computing platform developed in the framework of the EU-funded Project *My SPINE*. The platform performs simulations using P-SP models with the aim to quantify the tissue load distributions and help clinical decision on the most adequate treatment, invasive or not.

Bibliography

[1] Podniece, Z.: Work-related musculoskeletal disorders: Prevention report. Technical report, European Agency for Safety and Health at Work - Office for Official Publications of the European Communities, Luxembourg (2008)

[2] Ehrlich, G.: Low back pain. Bulletin of the World Health Organization **81**(9) (2003) 671–676

[3] Fujii, T., Matsudaira, K.: Prevalence of low back pain and factors associated with chronic disabling back pain in Japan. European Spine Journal **22**(2) (2013) 432–438

[4] Dunn, K.M., Croft, P.R.: Epidemiology and natural history of low back pain. Europa Medicophysica **40**(1) (2004) 9–13

[5] Carey, T.S., Evans, A.T., Lieberman, G., Kalsbeek, W.D., Jackman, A.M., Fryer, J.G., McNutt, R.A.: Acute severe low back pain. A population-based study of prevalence and care-seeking. Spine **21**(3) (1996) 339–44

[6] Juniper, M., Le, T.K., Mladsi, D.: The epidemiology, economic burden, and pharmacological treatment of chronic low back pain in France, Germany, Italy, Spain and the UK: a literature-based review. Expert opinion on pharmacotherapy **10**(16) (2009) 2581–2592

[7] Katz, J.N.: Lumbar disc disorders and low-back pain: socioeconomic factors and consequences. The Journal of bone and joint surgery. American volume **88**(Suppl 2) (2006) 21–24

[8] Malter, A.D., McNeney, B., Loeser, J.D., Deyo, R.A.: 5-year reoperation rates after different types of lumbar spine surgery. Spine **23**(7) (1998) 814–820

[9] Olmarker, K., Rydevik, B., Nordborg, C.: Autologous nucleus pulposus induces neurophysiologic and histologic changes in porcine cauda equina nerve roots. Spine **18**(11) (1993) 1425–1432

[10] Videman, T., Nurminen, M.: The occurrence of anular tears and their relation to lifetime back pain history: a cadaveric study using barium sulfate discography. Spine **29**(23) (2004) 2668–2676

[11] Nachemson, A.L.F.: The future of low back pain research. In Frymoyer, J., Gordon, S.L., eds.: New perspectives on low back pain, Illinois, American Academy of Orthopedic Surgeons Symposium (1989)

[12] Friberg, S., Hirsch, C.: Anatomical and clinical studies on lumbar disc degeneration. Acta Orthopaedica Scandinavica **19**(2) (1949) 222–242

[13] Freemont, A.J., Peacock, T.E., Goupille, P., Hoyland, J.A., O'Brien, J., Jayson, M.I.: Nerve ingrowth into diseased intervertebral disc in chronic back pain. Lancet **350** (1997) 178–181

[14] Stirling, A., Worthington, T., Rafiq, M., Lambert, P.A., Elliott, T.S.J.: Association between sciatica and Propionibacterium acnes. Lancet **357**(9273) (2001) 2024–2025

[15] Boden, S.D., McCowin, P.R., Davis, D.O., Dina, T.S., Mark, a.S., Wiesel, S.: Abnormal magnetic-resonance scans of the cervical spine in asymptomatic subjects. A prospective investigation. The Journal of bone and joint surgery. American volume **72**(8) (1990) 1178–1184

[16] Frymoyer, J.W., Newberg, A., Pope, M.H., Wilder, D.G., Clements, J., MacPherson, B.: Spine radiographs in patients with low-back pain. An epidemiological study in men. The Journal of bone and joint surgery. American volume **66**(7) (1984) 1048–1055

[17] Andersson, G.B.J., An, H.S., Oegema, T.R.J., Setton, L.A.: Intervertebral disc degeneration. The Journal of bone and joint surgery. American volume **88**(4) (2006) 895–899

[18] Battié, M.C., Videman, T., Kaprio, J., Gibbons, L.E., Gill, K., Manninen, H., Saarela, J., Peltonen, L.: The Twin Spine Study: contributions to a changing view of disc degeneration. The Spine Journal **9**(1) (2009) 47–59

[19] Frymoyer, J.W.: Lumbar disc disease: epidemiology. Instructional course lectures **41** (1992) 217–223

[20] Riihimäki, H.: Low-back pain, its origin and risk indicators. Scandinavian Journal of Work, Environment and Health **17**(2) (1991) 81–90

[21] Battié, M.C., Haynor, D.R., Fisher, L.D., Gill, K., Gibbons, L.E., Washington, S., Videman, T.: Similarities in degenerative findings on magnetic resonance images of the lumbar spines of identical twins. The Journal of bone and joint surgery. **77-A**(11) (1995) 1662–1670

[22] Hsieh, A.H., Yoon, S.T.: Update on the pathophysiology of degenerative disc disease and new developments in treatment strategies. Open Access Journal of Sports Medicine **1** (2010) 191–199

[23] Arjmand, N., Gagnon, D., Plamondon, A., Shirazi-Adl, A., Larivière, C.: A comparative study of two trunk biomechanical models under symmetric and asymmetric loadings. Journal of Biomechanics **43**(3) (2010) 485–491

[24] Gagnon, D., Arjmand, N., Plamondon, A., Shirazi-Adl, A., Larivière, C.: An improved multi-joint EMG-assisted optimization approach to estimate joint and muscle forces in a musculoskeletal model of the lumbar spine. Journal of biomechanics **44**(8) (may 2011) 1521–9

[25] Heydari, A., Nargol, A.V.F., Jones, A.P.C., Humphrey, A.R., Greenough, C.G.: EMG analysis of lumbar paraspinal muscles as a predictor of the risk of low-back pain. European Spine Journal **19**(7) (2010) 1145–1152

[26] Süüden, E., Ereline, J., Gapeyeva, H., Pääsuke, M.: Low back muscle fatigue during Sørensen endurance test in patients with chronic low back pain: relationship between electromyographic spectral compression and anthropometric characteristics. Electromyography and clinical neurophysiology **Apr-May 48**(3-4) (2008) 185–192

[27] Christophy, M., Faruk Senan, N.A., Lotz, J.C., O'Reilly, O.M.: A Musculoskeletal model for the lumbar spine. Biomechanics and Modeling in Mechanobiology **11**(1-2) (2012) 19–34

[28] Dao, T.T., Pouletaut, P., Charleux, F., Lazáry, Á., Eltes, P., Varga, P.P., Tho, M.C.H.B.: Estimation of Patient Specific Lumbar Spine Muscle Forces Using Multi-physical Musculoskeletal Model and Dynamic MRI. Knowledge and Systems Engineering **96-97** (2015) 3–18

[29] Drake, R.L., Vogl, A.W., Mitchell, A.W.M.: Gray's Anatomy for students. Churchill Livingstone (2004)

[30] Huelke, D.F.: An overview of anatomical considerations of infants and children in the adult world of automobile safety design. In: Annual Proceedings of the Association for the advancement of automotive medicine. Volume 42. (1998) 93–113

[31] Cramer, G.D.: General Characteristics of the Spine. In Cramer, G.D., Darby, S.A., eds.: Clinical Anatomy of the Spine, Spinal Cord, and Ans (Third Edition). Third edit edn. Elsevier Inc. (2014) 15–64

[32] Wood, K.B., Kos, P., Schendel, M., Persson, K.: Effect of patient position on the sagittal-plane profile of the thoracolumbar spine. Journal of Spinal Disorders **9**(2) (1996) 165–169.

[33] De Carvalho, D.E., Soave, D., Ross, K., Callaghan, J.P.: Lumbar Spine and Pelvic Posture Between Standing and Sitting: A Radiologic Investigation Including Reliability and Repeatability of the Lumbar Lordosis Measure. Journal of Manipulative and Physiological Therapeutics **33**(1) (2010) 48–55

[34] Black, K.M., McClure, P., Polansky, M.: The influence of different sitting positions on cervical and lumbar posture. Spine **21**(1) (1996) 65–70

[35] Katzman, W., Wanek, L., Shepherd, J.A., Sellmeyer, D.E.: Age-related hyperkyphosis: its causes, consequences, and management. Journal of orthopaedic and sports physical therapy **40**(6) (2010) 352–360

[36] Feltrin, G.P., Macchi, V., Saccavini, C., Tosi, E., Dus, C., Fassina, A., Parenti, A., De Caro, R.: Fractal analysis of lumbar vertebral cancellous bone architecture. Clinical anatomy (New York, N.Y.) **14**(6) (2001) 414–417

[37] Bogduk, N.: Clinical anatomy of the lumbar spine and sacrum. Fourth edn. Elsevier, Edinburgh (2005)

[38] Masharawi, Y., Salame, K., Mirovsky, Y., Peleg, S., Dar, G., Steinberg, N., Hershkovitz, I.: Vertebral body shape variation in the thoracic and lumbar spine: Characterization of its asymmetry and wedging. Clinical Anatomy **21**(1) (2008) 46–54

[39] Pal, G.P., Cosio, L., Routal, R.V.: Trajectory architecture of the trabecular bone between the body and the neural arch in human vertebrae. The Anatomical record **222**(4) (1988) 418–425

[40] Roberts, S., Menage, J., Urban, J.P.G.: Biochemical and structural properties of the cartilage end-plate and its relation to the intervertebral disc. Spine **14**(2) (1989) 166–174

[41] Nguyen, C., Poiraudeau, S., Rannou, F.: Vertebral subchondral bone. Osteoporosis International **23**(8 SUPPL) (2012) 857–860

[42] Grosland, N.M., Goel, V.K.: Vertebral endplate morphology follows bone remodeling principles. Spine **32** (2007) E667–673

[43] Wang, Y., Battié, M.C., Videman, T.: A morphological study of lumbar vertebral endplates: Radiographic, visual and digital measurements. European Spine Journal **21**(11) (2012) 2316–2323

[44] Davis, P.R.: Human lower lumbar vertebrae: some mechanical and osteological considerations. Journal of anatomy **95** (1961) 337–344

[45] Pal, G.P., Routal, R.V.: Transmission of weight through the lower thoracic and lumbar regions of the vertebral column in man. Journal of anatomy **152** (1987) 93–105

[46] Adams, M.a., Hutton, W.C.: The effect of posture on the role of the apophysial joints in resisting intervertebral compressive forces. The Journal of bone and joint surgery. British volume **62**(3) (1980) 358–362

[47] Horwitz, T., Smith, R.M.: An anatomical, pathological and roentgenological study of the intervertebral joints of the lumbar spine and of the sacroiliac joints. American journal of roentgenology **43** (1940) 173–186

[48] Jeffries, B.: Facet joint injections. Spine :State of the art reviews **2** (1988) 409–417

[49] Cramer, G.D.: The lumbar region. In Cramer, G.D., Darby, S.A., eds.: Clinical Anatomy of the Spine, Spinal Cord, and Ans (Third Edition). Third edit edn. Elsevier Inc., St. Louis, MO (2014) 246–311

[50] Huang, Y.C., Urban, J.P.G., Luk, K.D.K.: Intervertebral disc regeneration: do nutrients lead the way? Nature reviews. Rheumatology (2014) 1–6

[51] Kraemer, J., Kolditz, D., Gowin, R.: Water and electrolyte content of human intervertebral discs under variable load. Spine **10**(1) (1985) 69–71

[52] Martin, M.D., Boxell, C.M., Malone, D.G.: Pathophysiology of lumbar disc degeneration: a review of the literature. Neurosurg Focus **13**(2) (2002) E1

[53] Coventry, M.B.: Anatomy of the intervertebral disc. Clinical orthopaedics and related research **67** (1969) 9–15

[54] Hutton, W.C., Ganey, T.M., Elmer, W.A., Kozlowska, E., Ugbo, J.L., Doh, E.S., Whitesides, T.E.: Does long-term compressive loading on the intervertebral disc cause degeneration? Spine **25**(23) (2000) 2993–3004

[55] Iatridis, J.C., Wedenbaum, M., Setton, L.A., Mow, V.C.: Is the nucleus pulposus a solid or a fluid? Mechanical Behaviors of the nucleus pulposus of the human intervertebral disc. Spine **21**(May 1996) (1996) 1174–1184

[56] Alexander, L.A., Hancock, E., Agouris, I., Smith, F.W., MacSween, A.: The response of the nucleus pulposus of the lumbar intervertebral discs to functionally loaded positions. Spine **32**(14) (2007) 1508–1512

[57] Nachemson, a.L.F.: Electromyographic studies on the vertebral portion of the psoas muscle. Acta Orthopaedica Scandinavica **37** (1966) 177–190

[58] Botsford, D.J., Esses, S.I., Ogilvie-Harris, D.J.: In vivo diurnal variation in intervertebral disc volume and morphology. Spine **19**(8) (1994) 935–940

[59] Boos, N., Wallin, A., Aebi, M., Boesch, C.: A new magnetic resonanse imaging analysis method for the measurement of disc height variations. Spine **21**(5) (1996) 563–570

[60] Wilke, H.J., Neef, P., Caimi, M., Hoogland, T., Claes, L.E.: New in vivo measurements of pressures in the intervertebral disc in daily life. Spine **24**(8) (1999) 755–762

[61] LeBlanc, A.D., Schonfeld, E., Schneider, V.S., Evans, H.J., Taber, K.H.: The spine: changes in T2 relaxation times from disuse. Radiology **169**(1) (1988) 105–107

[62] Belavý, D.L., Armbrecht, G., Richardson, C.A., Felsenberg, D., Hides, J.A.: Muscle atrophy and changes in spinal morphology: is the lumbar spine vulnerable after prolonged bed-rest? Spine **36**(2) (2011) 137–145

[63] Neumann, D.A.: Kinesiology of the Musculoskeletal System: Foundations for Rehabilitation. Second edi edn. Mosby Elsevier (2010)

[64] Ellingson, A.M., Mehta, H., Polly Jr, D.W., Ellermann, J., Nuckley, D.J.: Disc degeneration assessed by quantitative T2* (T2 star) correlated with functional lumbar mechanics. Spine **38**(24) (2013) 612–625

[65] Eyre, D.R.: Biochemistry of the intervertebral disc. International review of connective tissue research **8** (1979) 227–291

[66] Ruiz, C., Noailly, J., Lacroix, D.: Material property discontinuities in intervertebral disc porohyperelastic finite element models generate numerical instabilities due to volumetric strain variations. Journal of the mechanical behavior of biomedical materials **26** (oct 2013) 1–10

[67] Issy, a.C., Castania, V., Castania, M., Salmon, C.E.G., Nogueira-Barbosa, M.H., Del Bel, E., Defino, H.L.a.: Experimental model of intervertebral disc degeneration by needle puncture in Wistar rats. Brazilian Journal of Medical and Biological Research **46**(3) (2013) 235–244

[68] Eyre, D.R.: Collagens of the disc. In Ghosh, P., ed.: The biology of the intervertebral disc. CRC Press, Boca Raton, FL (1988) 171–188

[69] Natarajan, R.N., Andersson, G.B.J.: A model to study the disc degeneration process. Spine **19** (1994) 259–265

[70] Tanaka, M., Nakahara, S., Inoue, H.: A pathologic study of discs in the elderly. Separation between the cartilaginous endplate and the vertebral body. Spine **18**(11) (1993) 1456–1462

[71] Fields, A.J., Rodriguez, D., Gary, K.N., Liebenberg, E.C., Lotz, J.C.: Influence of biochemical composition on endplate cartilage tensile properties in the human lumbar spine. Journal of Orthopaedic Research **32**(2) (2014) 245–252

[72] Malko, J.A., Hutton, W.C., Fajman, W.A.: An in vivo magnetic resonance imaging study of changes in the volume (and fluid content) of the lumbar intervertebral discs during a simulated diurnal load cycle. Spine **24**(10) (1999) 1015–1022

[73] Ayotte, D.C., Ito, K., Perren, S.M., Tepic, S.: Direction-dependent constriction flow in a poroelastic solid: the intervertebral disc valve. Journal of biomechanical engineering **122**(6) (2000) 587–593

[74] Edwards, W.T., Zheng, Y., Ferrara, L.A., Yuan, H.A.: Structural features and thickness of the vertebral cortex in the thoracolumbar spine. Spine **26**(2) (2001) 218–225

[75] Uhthoff, H.K.: Prenatal development of the iliolumbar ligament. Journal of Bone and Joint Surgery **75**(1) (1993) 93–95

[76] Luk, K.D.K., Leong, J.C.Y.: The iliolumbar ligament. Journal of Bone and Joint Surgery **68B** (1986) 197–200

[77] Hanson, P., Magnusson, S.P., Sorensen, H., Simonsen, E.B.: Differences in the iliolumbar ligament and the transverse process of the L5 vertebra in young white and black people. Acta anatomica **163**(4) (1998) 218–223

[78] Rucco, V., Basadonna, P.T., Gasparini, D.: Anatomy of the iliolumbar ligament: a review of its anatomy and a magnetic resonance study. American journal of physical medicine and rehabilitation **75**(6) (1996) 451–455

[79] Alderink, G.J.: The Sacroiliac Joint : Review of Anatomy , Mechanics , and Function. Journal of orthopaedic and sports physical therapy **13**(2) (1991) 71–84

[80] Aihara, T., Takahashi, K., Ono, Y., Moriya, H.: Does the Morphology of the Iliolumbar Ligament Affect Lumbosacral Disc Degeneration ? Spine **27**(14) (2002) 1499–1503

[81] Basadonna, P.T., Gasparini, D., Rucco, V.: Iliolumbar ligament insertions. In vivo anatomic study. Spine **21**(20) (1996) 2313–2316

[82] Noailly, J.: Model developments for in silico studies of the lumbar spine biomechanics. PhD thesis, Universitat Politècnica de Catalunya, Barcelona, Spain (2009)

[83] Cholewicki, J., Panjabi, M.M., Khachatryan, A.: Stabilizing function of trunk flexor-extensor muscles around a neutral spine posture. Spine **22**(19) (1997) 2207–2212

[84] Bakkum, B.W., Cramer, G.D.: Muscles That Influence the Spine. In: Clinical Anatomy of the Spine, Spinal Cord, and Ans (Third Edition). Third edit edn. Elsevier Inc. (2014) 98–134

[85] Huxley, H.E., Hanson, J.: Changes in the cross-striations of muscle during contraction and stretch and their structural interpretation. Nature **173**(4412) (1954) 973–976

[86] Huxley, A.F., Niedergerke, R.: Structural changes in muscle during contraction; interference microscoopy of living muscle fibres. Nature **173**(4412) (1954) 971–973

[87] Huxley, H.E.: The double array of filaments in cross-striated muscle. Journal of biophysical and biochemical cytology **3**(5) (1957) 631–673

[88] Huxley, H.E.: Electron microscope studies on the structure of natural and synthetic protein filaments from striated muscle. Journal of molecular biology **7** (1963) 281–308

[89] Alberts, B., Johnson, A., Lewis, J., Raff, M., Roberts, K., Walter, P.: The Cytoskeleton. In: Molecular Biology of the Cell. Fourth edn. Garland Science, New York (2002)

[90] Lorenz, T., Campello, M.: Biomechanics of skeletal muscle. In Nordin, M., Frankel, V.H., eds.: Basic biomechanics of the musculoskeletal system. Third edn. Lippincott Williams Wilkins (2001) 148–175

[91] Banker, B.Q.: Basic reaction of muscle. In Engel, A.G., Franzini-Armstrong, C., eds.: Myology. Second edn. McGraw-Hill Inc., New York (1994)

[92] Smerdu, V., Karsch-Mizrachi, I., Campione, M., Leinwand, L., Schiaffino, S.: Type IIx myosin heavy chain transcripts are expressed in type IIb fibers of human skeletal muscle. The American journal of physiology **267**(6 Pt 1) (1994) C1723–C1728

[93] Stone, M.H., Stone, M., Sands, W.A.: Neuromuscular physiology. In: Principles and practice of resistance training. Human Kinetics Publishers, Champaign, United States of America (2007) 384

[94] Loeb, G.E., Pratt, C.a., Chanaud, C.M., Richmond, F.J.: Distribution and innervation of short, interdigitated muscle fibers in parallel-fibered muscles of the cat hindlimb. Journal of morphology **191**(1) (1987) 1–15

[95] Ounjian, M., Roy, R.R., Eldred, E., Garfinkel, A., Payne, J.R., Armstrong, A., Toga, A.W., Edgerton, V.R.: Physiological and developmental implications of motor unit anatomy. Journal of neurobiology **22** (1991) 547–559

[96] Lieber, R.L., Fridén, J.: Functional and Clinical Significance. Muscle Nerve **23**(November) (2000) 1647–1666

[97] Alexander, R., Vernon, A.: The dimension of knee and ankle muscles and the forces they exert. Journal of human movement studies **1** (1975) 115–123

[98] Blix, M.: Die Lange und die Spannung des Muskels. Scandinavian Archives of Physiology **5** (1894) 149–206

[99] Gordon, a.M., Huxley, a.F., Julian, F.J.: The variation in isometric tension with sarcomere length in vertebrate muscle fibres. The Journal of physiology **184**(1) (may 1966) 170–92

[100] Rassier, D.E., MacIntosh, B.R., Herzog, W.: Length dependence of active force production in skeletal muscle. Journal of applied physiology (Bethesda, Md. : 1985) **86**(5) (may 1999) 1445–57

[101] Walker, S.M., Schrodt, G.R.: I segment lengths and thin filament periods in skeletal muscle fibers of the Rhesus monkey and the human. The Anatomical record **178**(1) (1974) 63–81

[102] Lieber, R.L., Loren, G.J., Fridén, J.: In vivo measurement of human wrist extensor muscle sarcomere length changes. Journal of neurophysiology **71**(3) (1994) 874–881

[103] Maganaris, C.N.: Force-length characteristics of in vivo human skeletal muscle. Acta Physiologica Scandinavica **172** (2001) 279–285

[104] Gollapudi, S.K., Lin, D.C.: Experimental determination of sarcomere force-length relationship in type-I human skeletal muscle fibers. Journal of Biomechanics **42**(13) (2009) 2011–2016

[105] ter Keurs, H.E., Iwazumi, T., Pollack, G.H.: The sarcomere length-tension relation in skeletal muscle. The Journal of general physiology **72**(4) (1978) 565–592

[106] Lieber, R.L., Bodine-Fowler, S.C.: Skeletal muscle mechanics: implications for rehabilitation. Physical therapy **73**(12) (1993) 844–856

[107] Horowits, R.: Passive force generation and titin isoforms in mammalian skeletal muscle. Biophysical journal **61**(February) (1992) 392–398

[108] Linke, W.a., Ivemeyer, M., Olivieri, N., Kolmerer, B., Rüegg, J.C., Labeit, S.: Towards a molecular understanding of the elasticity of titin. Journal of molecular biology **261**(1) (1996) 62–71

[109] Granzier, H., Helmes, M., Cazorla, O., McNabb, M., Labeit, D., Wu, Y., Yamasaki, R., Redkar, A., Kellermayer, M., Labeit, S., Trombitás, K.: Mechanical properties of titin isoforms. Advances in experimental medicine and biology **481** (2000) 283–300

[110] Magid, A., Law, D.J.: Myofibrils bear most of the resting tension in frog skeletal muscle. Science **230**(December) (1985) 1280–1281

[111] Soderberg, G.L.: Kinesiology: Application to pathological motion. Sixth edn. Lippincott Williams Wilkins, Baltimore (1986)

[112] Davis, J., Kaufman, K.R., Lieber, R.L.: Correlation between active and passive isometric force and intramuscular pressure in the isolated rabbit tibialis anterior muscle. Journal of Biomechanics **36**(4) (apr 2003) 505–512

[113] Rassier, D.E., Lee, E.J., Herzog, W.: Modulation of passive force in single skeletal muscle fibres. Biology letters **1**(3) (2005) 342–345

[114] Magnusson, S.P.: Passive properties of human skeletal muscle during stretch maneuvers. A review. Scandinavian journal of medicine science in sports **8**(2) (1998) 65–77

[115] Koo, T.K., Guo, J.Y., Cohen, J.H., Parker, K.J.: Relationship between shear elastic modulus and passive muscle force: An ex-vivo study. Journal of Biomechanics **46**(12) (2013) 2053–2059

[116] Fenn, W.O., Marsh, B.S.: Muscular force at different speeds of shortening. The Journal of physiology **85**(3) (1935) 277–297

[117] Hill, A.V.: The Heat of Shortening and the Dynamic Constants of Muscle. Proceedings of the Royal Society B: Biological Sciences **126**(843) (oct 1938) 136–195

[118] Hill, A.V.: First and last experiments in muscle mechanics. Cambridge University Press, London (1970)

[119] Katz, B.Y.B.: The relation between force and speed in muscular contraction. Journal of physiology **96** (1939) 45–64

[120] Herzog, W.: Force production in human skeletal muscle. In Nigg, B.M., Macintosh, B.R., Mester, J., eds.: Biomechanics and biology of movement. Human Kinetics Publishers (2000)

[121] Westing, S.H., Seger, J.Y., Thorstensson, A.: Effects of electrical stimulaton on eccentric and concentric torque-velocity relationships during knee extension in man. Acta Physiologica Scandinavica **140**(1) (1990) 17–22

[122] Josephson, R., Stokes, D.: The force-velocity properties of a crustacean muscle during lengthening. The Journal of experimental biology **202** (1999) 593–607

[123] Aagaard, P.: Entrenamiento excéntrico de fuerza : consecuencias en la marca deportiva y en la rehabilitación y prevención de lesiones. In: IX Jornadas sobre medicina y deporte de alto nivel, Madrid (2009)

[124] Chow, J.W., Darling, W.G.: The maximum shortening velocity of muscle should be scaled with activation. Journal of applied physiology (Bethesda, Md. : 1985) **86**(3) (1999) 1025–1031

[125] Buchanan, T.S., Lloyd, D.G., Manal, K., Besier, T.F.: Neuromusculoskeletal modeling: Estimation of muscle forces and joint moments and movements from measurements of neural command. Journal of applied biomechanics **20**(4) (2004) 367–395

[126] Clark, B.C., Manini, T.M., Thé, D.J., Doldo, N.a., Ploutz-Snyder, L.L.: Gender differences in skeletal muscle fatigability are related to contraction type and EMG spectral compression. Journal of applied physiology (Bethesda, Md. : 1985) **94**(6) (2003) 2263–2272

[127] McGill, S.M., Patt, N., Norman, R.W.: Measurement of the trunk musculature of active males using CT scan radiography: implications for force and moment

generating capacity about the L4/L5 joint. Journal of Biomechanics **21** (1988) 329–334

[128] Bogduk, N., Pearcy, M.J., Hadfield, G.: Anatomy and biomechanics of psoas major. Clinical Biomechanics **7**(2) (1992) 109–119

[129] Little, T.L., Mansoor, J.: Low back pain associated with internal snapping hip syndrome in a competitive cyclist. British journal of sports medicine **42**(4) (2008) 308–309; discussion 309

[130] Nourbakhsh, M.R., Arab, A.M.: Relationship between mechanical factors and incidence of low back pain. The Journal of orthopaedic and sports physical therapy **32**(9) (2002) 447–460

[131] Sajko, S., Stuber, K.: Psoas Major: a case report and review of its anatomy, biomechanics, and clinical implications. The Journal of the Canadian Chiropractic Association **53**(4) (dec 2009) 311–8

[132] Mallick, I.H., Thoufeeq, M.H., Rajendran, T.P.: Iliopsoas abscesses. Postgraduate medical journal **80** (2004) 459–462

[133] Skandalakis, J.E., Colburn, G.L., Weidman, T.A., Badalament, R.A., Parrott, T.S., Galloway, N.T.M., Scalijon, W.M.: Kidney and ureters. In Skandalakis, J.E., ed.: Skandalaki's surgical anatomy: The embryologic and anatomic basis of modern surgery. Paschalidis Medical Publications Ltd. (2004)

[134] Nachemson, a.L.F.: The Possible importance of the psoas muscle for stabilization of the lumbar spine. Acta Orthopaedica Scandinavica **39** (1968) 47–57

[135] de Groot, M., Pool-Goudzwaard, a.L., Spoor, C.W., Snijders, C.J.: The active straight leg raising test (ASLR) in pregnant women: Differences in muscle activity and force between patients and healthy subjects. Manual Therapy **13**(1) (2008) 68–74

[136] Santaguida, P.L., McGill, S.M.: The psoas major muscle: a three-dimensional geometric study. Journal of Biomechanics **28**(3) (1995) 339–345

[137] Basmajian, J.V.: Electromyography of iliopsoas. Anatomical Record **132** (1958) 127–132

[138] Woodburne, R.T., Burkel, W.E.: Essentials of human anatomy. Oxford University Press, New York (1988)

[139] Moore, K.L., Dalley, A.F.: Clinically orientated anatomy. Fifth edn. Lippincott Williams Wilkins, Baltimore (2006)

[140] Romanes, G.J.: Cunningham's textbook of anatomy. Twelvth edn. Oxford University Press, Toronto (1981)

[141] Hamilton, W.J.: Textbook of human anatomy. Second edn. Harper and Row, Baltimore (1972)

[142] Penning, L.: Psoas muscle and lumbar spine stability: A concept uniting existing controversies. Critical review and hypothesis. European Spine Journal **9**(6) (2000) 577–585

[143] Jemmett, R.S., Macdonald, D.a., Agur, A.M.R.: Anatomical relationships between selected segmental muscles of the lumbar spine in the context of multiplanar segmental motion: a preliminary investigation. Manual therapy **9**(4) (nov 2004) 203–10

[144] Andersson, E.A., Oddsson, L., Grundström, H., Thorstensson, A.: The role of the psoas and iliacus muscles for stability and movement of the lumbar spine, pelvis and hip. Scandinavian journal of medicine science in sports **5**(1) (1995) 10–16

[145] Hadjipavlou, A.G., Farfan, H.F., Simmons, J.W.: The functioning spine. In Farfan, H.F., Simmons, J.W., Hadjipavlou, A.G., eds.: The sciatic syndrome. Slack, Slack, Thorofare,NJ (1996) 41–73

[146] Andersson, E.a., Nilsson, J., Thorstensson, A.: Intramuscular EMG from the hip flexor muscles during human locomotion. Acta physiologica Scandinavica **161**(3) (1997) 361–370

[147] Keagy, R.D., Brumlik, J., Bergan, J.: Direct electromyography of the psoas major muscle in man. The Journal of bone and joint surgery. **48**(7) (1966) 1377–1382

[148] Dangaria, T.R., Naesh, O.: Changes in cross-sectional area of psoas major muscle in unilateral sciatica caused by disc herniation. Spine **23**(8) (1998) 928–931

[149] Barker, K.L., Shamley, D.R., Jackson, D.: Changes in the cross-sectional area of multifidus and psoas in patients with unilateral back pain. Spine **29**(22) (2004) E515–E519

[150] Hides, J.A., Belavý, D.L., Stanton, W., Wilson, S.J., Rittweger, J., Felsenberg, D., Richardson, C.A.: Magnetic resonance imaging assessment of trunk muscles during prolonged bed rest. Spine **32**(15) (2007) 1687–1692

[151] Macintosh, J.E., Bogduk, N.: The biomechanics of the lumbar multifidus. Clinical Biomechanics **1**(4) (1986) 205–213

[152] Valenica, F., Munro, R.: Morphology of the lumbar multifidus in man. Journal of anatomyJournal of anatomy **139** (1984) 196

[153] Shindo, H.: Anatomical study of the lumbar multifidus muscle and its innervation in human adults and fetuses. Nihon Ika Daigaku Zasshi. **62**(5) (1995) 439–446

[154] Lonnemann, M., Paris, S., Gorniak, G.: A morphological comparison of the human lumbar multifidus by chemical dissection. Journal of Manual and Manipulative Therapy **16**(4) (2008) E84–E92

[155] Lewin, T., Moffet, B., Viidik, A.: The morphology of the lumbar synovial intervertebral joints. Acta Morphologica Scandinavica **4** (1962) 299–319

[156] Paris, S.: Anatomy as related to function and pain. The orthopedic clinics of North America **14**(3) (1983) 475–489

[157] Porterfield, J., DeRosa, C.: Mechanical low back pain: Perspectives in functional anatomy. W.B. Saunders Co., Philadelphia (1991)

[158] De Foa, J.L., Forrest, W.J., Biedermann, H.J.: Muscle fibre direction of longissimus, iliocostalis and multifidus: landmark-derived reference lines. Journal of anatomy **163** (apr 1989) 243–7

[159] Biedermann, H.J., De Foa, J.L., Forrest, W.J.: Muscle fibre directions of iliocostalis and multifidus: male-female differences. Journal of anatomy **179** (1991) 163–167

[160] Hollinshead, W., Rosse, C.: Textbook of anatomy. Fifth edn. Lippincott Williams Wilkins, Baltimore (1997)

[161] Ward, S.R., Kim, C.W., Eng, C.M., Gottschalk, L.J., Tomiya, A., Garfin, S.R., Lieber, R.L.: Architectural analysis and intraoperative measurements demonstrate the unique design of the multifidus muscle for lumbar spine stability. The Journal of bone and joint surgery. American volume **91**(1) (jan 2009) 176–85

[162] Rosatelli, A.L., Ravichandiran, K., Agur, A.M.: Three-dimensional study of the musculotendinous architecture of lumbar multifidus and its functional implications. Clinical anatomy (New York, N.Y.) **21**(6) (sep 2008) 539–46

[163] Ng, J.K.F., Richardson, C.A., Parnianpour, M., Kippers, V.: EMG activity of trunk muscles and torque output during isometric axial rotation exertion: A comparison between back pain patients and matched controls. Journal of Orthopaedic Research **20**(1) (2002) 112–121

[164] Middleditch, A., Oliver, J.: Structure of the vertebral column. In: Functional anatomy of the spine. Second edn. Elsevier (2005) 47–51

[165] Vleeming, A., Van Wingerden, J.P., Stoeckart, R., Stijnen, T.: Load application to the sacrotuberous ligament; influences on sacroiliac joint mechanics. Clinical Biomechanics **4**(4) (1989) 204–209

[166] Bogduk, N.: A reappraisal of the anatomy of the human lumbar erector spinae. Journal of anatomy **131**(3) (oct 1980) 525–40

[167] Bustami, F.: A new description of the lumbar erector spinae in man. J Anatom **144** (1986) 81–91

[168] Macintosh, J.E., Bogduk, N.: 1987 Volvo award in basic science. The morphology of the lumbar erector spinae. Spine **12**(7) (1987) 658–668

[169] Daggfeldt, K., Huang, Q.M., Thorstensson, A.: The visible human anatomy of the lumbar erector spinae. Spine **25**(21) (nov 2000) 2719–25

[170] Macintosh, J.E., Bogduk, N.: The attachments of the lumbar erector spinae. Spine **16**(7) (1991) 783–792

[171] Arjmand, N., Shirazi-Adl, A.: Model and in vivo studies on human trunk load partitioning and stability in isometric forward flexions. Journal of biomechanics **39**(3) (jan 2006) 510–21

[172] Macintosh, J.E., Bogduk, N., Pearcy, M.J.: The effects of flexion on the geometry and actions of the lumbar erector spinae. Spine **18**(7) (1993) 884–893

[173] Jorgensen, M.J., Marras, W.S., Gupta, P., Waters, T.R.: Effect of torso flexion on the lumbar torso extensor muscle sagittal plane moment arms. Spine Journal **3**(5) (2003) 363–369

[174] Tveit, P., Daggfeldt, K., Hetland, S., Thorstensson, A.: Erector spinae lever arm length variations with changes in spinal curvature. Spine **19**(2) (1994) 199–204

[175] Carragee, E.J., Don, A.S., Hurwitz, E.L., Cuellar, J.M., Carrino, J.A., Herzog, R.: 2009 ISSLS Prize Winner: Does discography cause accelerated progression of degeneration changes in the lumbar disc: a ten-year matched cohort study. Spine **34**(21) (2009) 2338–2345

[176] Nachemson, A.L.F., Morris, J.: In Vivo Measurements of Intradiscal Pressure. The Journal of bone and joint surgery. American volume **46**(5) (1964) 1077–1092

[177] Nachemson, a.L.F.: The effect of forward leaning on lumbar intradiscal pressure. Acta Orthopaedica Scandinavica **35** (1965) 314–328

[178] El-Rich, M., Shirazi-Adl, A., Arjmand, N.: Muscle activity, internal loads, and stability of the human spine in standing postures: combined model and in vivo studies. Spine **29**(23) (dec 2004) 2633–42

[179] Bradl, I., Mörl, F., Scholle, H.C., Grassme, R., Müller, R., Grieshaber, R.: Back muscle activation pattern and spectrum in defined load situations. Pathophysiology : the official journal of the International Society for Pathophysiology / ISP **12**(4) (dec 2005) 275–80

[180] Dickx, N., Roseline, D., Cagnie, B., Deschepper, E., Verstraete, K., Danneels, L.: Magnetic Resonance Imaging and Electromyography to Measure Lumbar Back Muscle Activity. Spine **35**(17) (2010) 836–842

[181] Rohlmann, A., Graichen, F., Weber, U., Bergmann, G.: 2000 Volvo Award winner in biomechanical studies: Monitoring in vivo implant loads with a telemeterized internal spinal fixation device. Spine **25**(23) (2000) 2981–2986

[182] Rohlmann, A., Graichen, F., Bender, A., Kayser, R., Bergmann, G.: Loads on a telemeterized vertebral body replacement measured in three patients within the first postoperative month. Clinical Biomechanics **23**(2) (2008) 147–158

[183] Bogduk, N., Macintosh, J.E., Pearcy, M.J.: A universal model of the lumbar back muscles in the upright position. Spine **17**(8) (1992) 897–913

[184] McNeill, T., Warwick, D., Andersson, G.B.J., Schultz, A.: Trunk strength in attempted flexion, extension, and lateral bending in healthy subjects and patients with low-back disorders. Spine **5**(6) (1980) 529–538

[185] Arnold, E.M., Ward, S.R., Lieber, R.L., Delp, S.L.: A model of the lower limb for analysis of human movement. Annals of biomedical engineering **38**(2) (feb 2010) 269–79

[186] Powell, P.L., Roy, R.R., Kanim, P., Bello, M.a., Edgerton, V.R.: Predictability of skeletal muscle tension from architectural determinations in guinea pig hindlimbs. Journal of Applied Physiology **57**(6) (1984) 1715–1721

[187] Larivière, C., Gagnon, D., Gravel, D., Bertrand Arsenault, A., Dumas, J.P., Goyette, M., Loisel, P.: A triaxial dynamometer to monitor lateral bending

and axial rotation moments during static trunk extension efforts. Clinical Biomechanics **16**(1) (2001) 80–83

[188] Cohen, I., Rainville, J.: Aggressive exercise as treatment for chronic low back pain. Sports medicine **32**(1) (2002) 75–82

[189] Rainville, J., Sobel, J.B., Hartigan, C., Wright, A.: The effect of compensation involvement on the reporting of pain and disability by patients referred for rehabilitation of chronic low back pain. Spine **22**(17) (1997) 2016–2024

[190] Reid, S., Hazard, R.G., Fenwick, J.W.: Isokinetic trunk-strength deficits in people with and without low-back pain: a comparative study with consideration of effort. Journal of spinal disorders **4**(1) (1991) 68–72

[191] Mayer, J.M., Graves, J.E., Clark, B.C., Formikell, M., Ploutz-Snyder, L.L.: The use of magnetic resonance imaging to evaluate lumbar muscle activity during trunk extension exercise at varying intensities. Spine **30**(22) (2005) 2556–2563

[192] Dickx, N., Cagnie, B., Achten, E., Vandemaele, P., Parlevliet, T., Danneels, L.: Changes in lumbar muscle activity because of induced muscle pain evaluated by muscle functional magnetic resonance imaging. Spine **33**(26) (2008) E983–E989

[193] Nachemson, a.L.F.: The influence of spinal movements on the lumbar intradiscal pressure and on the tensile stresses in the annulus fibrosus. Acta Orthopaedica Scandinavica **33** (1963) 183–207

[194] Nachemson, A.L.F.: Towards a better understanding of low-back pain: a review of the mechanics of the lumbar disc. Rheumatology and rehabilitation **14**(3) (1975) 129–143

[195] Wilke, H.J., Neef, P., Hinz, B., Seidel, H., Claes, L.E.: Intradiscal pressure together with anthropometric data–a data set for the validation of models. Clinical biomechanics (Bristol, Avon) **16 Suppl 1**(1) (2001) S111–S126

[196] Althoff, I., Brinckmann, P., Frobin, W., Sandover, J., Burton, K.: An improved method of stature measurement for quantitative determination of spinal

loading. Application to sitting postures and whole body vibration. Spine **17**(6) (1992) 682–693

[197] Rohlmann, a., Bergmann, G., Graichen, F.: Loads on internal spinal fixators measured in different body positions. European spine journal **8**(5) (jan 1999) 354–9

[198] Sato, K., Kikuchi, S., Yonezawa, T.: In vivo intradiscal pressure measurement in healthy individuals and in patients with ongoing back problems. Spine **24**(23) (dec 1999) 2468–74

[199] Nachemson, a.L.F., Schultz, A., Berkson, M.H.: Mechanical properties of human lumbar spine motion segments. Influence of age, sex, disc level, and degeneration. Spine **4**(1) (1979) 1–8

[200] Schultz, A., Warwick, D., Berkson, M.H., Nachemson, a.L.F.: Mechanical properties of human lumbar spine motion segments - Part I: Response in flexion, extension, lateral bending and torsion. Journal of biomechanical engineering **101** (1979) 46–52

[201] Adams, M.a., McNally, D.S., Dolan, P.: 'Stress' distributions inside intervertebral discs. The effects of age and degeneration. The Journal of bone and joint surgery. British volume **78**(6) (1996) 965–972

[202] Andersson, G.B.J., Örtengren, R., Nachemson, a.L.F., Elfström, G.: Lumbar disc pressure and myoelectric back muscle activity during sitting. Scandinavian journal of rehabilitation medicine **6** (1974) 104–114

[203] Schultz, A., Andersson, G.B.J., Örtengren, R., Haderspeck, K., Nachemson, A.L.F.: Loads on the Lumbar Spine. Journal of Bone and Joint Surgery **64**(5) (1982)

[204] McNally, D.S., Adams, M.A.: Internal intervertebral disc mechanics as revealed by stress profilometry. Spine **17**(1) (1992) 66–73

[205] Adams, M.a., McMillan, D.W., Green, T.P., Dolan, P.: Sustained loading generates stress concentrations in lumbar intervertebral discs. (1996)

[206] Steffen, T., Baramki, H.G., Rubin, R., Antoniou, J., Aebi, M.: Lumbar intradiscal pressure measured in the anterior and posterolateral annular regions during asymmetrical loading. Clinical Biomechanics **13**(7) (1998) 495–505

[207] Wilke, H.J., Claes, L.E., Schmitt, H., Wolf, S.: A universal spine tester for in vitro experiments with muscle force simulation. European Spine Journal **3** (1994) 91–97

[208] Wilke, H.J., Wolf, S., Claes, L.E., Arandt, M., Wiesend, A.: Stability increase of the lumbar spine with different muscle groups. A biomechanical in vitro study. Spine **20**(2) (1995) 192–198

[209] Quint, U., Wilke, H.J., Shirazi-Adl, A., Parnianpour, M., Löer, F., Claes, L.E.: Importance of the intersegmental trunk muscles for the stability of the lumbar spine: a biomechanical study in vitro. Spine **23** (1998) 1937–1945

[210] Wilke, H.J., Rohlmann, A., Neller, S., Graichen, F., Claes, L.E., Bergmann, G.: ISSLS Prize Winner : A Novel Approach to Determine Trunk Muscle Forces During Flexion and Extension. Spine **28**(23) (2003) 2585–2593

[211] Panjabi, M.M.: Hybrid multidirectional test method to evaluate spinal adjacent-level effects. Clinical Biomechanics **22**(3) (2007) 257–265

[212] Rohlmann, A., Claes, L.E., Bergmannt, G., Graichen, F., Neef, P., Wilke, H.J.: Comparison of intradiscal pressures and spinal fixator loads for different body positions and exercises. Ergonomics **44**(8) (2001) 781–794

[213] Mulholland, R.C.: The myth of lumbar instability: The importance of abnormal loading as a cause of low back pain. European Spine Journal **17**(5) (2008) 619–625

[214] Brekelmans, W.a., Poort, H.W., Slooff, T.J.: A new method to analyse the mechanical behaviour of skeletal parts. Acta orthopaedica Scandinavica **43**(5) (1972) 301–317

[215] Stokes, I.A.F., Gardner-Morse, M.G.: Lumbar spine maximum efforts and muscle recruitment patterns predicted by a model with multijoint muscles and joints with stiffness. Journal of biomechanics **28**(2) (mar 1995) 173–86

[216] de Zee, M., Hansen, L., Wong, C., Rasmussen, J., Simonsen, E.B.: A generic detailed rigid-body lumbar spine model. Journal of biomechanics **40**(6) (jan 2007) 1219–27

[217] Han, K.S., Rohlmann, A., Zander, T., Taylor, W.R.: Lumbar spinal loads vary with body height and weight. Medical engineering physics **35**(7) (jul 2013) 969–77

[218] Hajihosseinali, M., Arjmand, N., Shirazi-Adl, A.: Effect of body weight on spinal loads in various activities: A personalized biomechanical modeling approach. Journal of Biomechanics **48**(2) (2015) 276–282

[219] Gardner-Morse, M.G., Stokes, I.A.F., Laible, J.P.: Role of muscles in lumbar spine stability in maximum extension efforts.pdf. Journal of Orthopaedic Research **13** (1995) 802–808

[220] Arjmand, N., Shirazi-Adl, A.: Biomechanics of changes in lumbar posture in static lifting. Spine **30**(23) (dec 2005) 2637–48

[221] Zander, T., Rohlmann, A., Calisse, J., Bergmann, G.: Estimation of muscle forces in the lumbar spine during upper-body inclination. Clinical biomechanics (Bristol, Avon) **16 Suppl 1**(1) (jan 2001) S73–80

[222] Shirazi-Adl, A., Sadouk, S., Parnianpour, M., Pop, D.: Muscle force evaluation and the role of posture in human lumbar spine under compression. European Spine Journal **11** (2002) 519–526

[223] Rohlmann, A., Bauer, L., Zander, T., Bergmann, G., Wilke, H.J.: Determination of trunk muscle forces for flexion and extension by using a validated finite element model of the lumbar spine and measured in vivo data. Journal of biomechanics **39**(6) (jan 2006) 981–9

[224] Rohlmann, a., Zander, T., Rao, M., Bergmann, G.: Realistic loading conditions for upper body bending. Journal of biomechanics **42**(7) (may 2009) 884–90

[225] Rohlmann, A., Zander, T., Rao, M., Bergmann, G.: Applying a follower load delivers realistic results for simulating standing. Journal of biomechanics **42**(10) (jul 2009) 1520–6

[226] Schmidt, H., Shirazi-Adl, A., Galbusera, F., Wilke, H.J.: Response analysis of the lumbar spine during regular daily activities–a finite element analysis. Journal of biomechanics **43**(10) (jul 2010) 1849–56

[227] Dreischarf, M., Zander, T., Bergmann, G., Rohlmann, A.: A non-optimized follower load path may cause considerable intervertebral rotations. Journal of biomechanics **43**(13) (sep 2010) 2625–8

[228] Noailly, J., Ambrosio, L., Tanner, K.E., Planell, J.a., Lacroix, D.: In silico evaluation of a new composite disc substitute with a L3-L5 lumbar spine finite element model. European Spine Journal (mar 2011)

[229] Thelen, D.G., Schultz, A., Ashton-Miller, J.A.: Co-contraction of lumbar muscles during the development of time-varying triaxial moments. Journal of Orthopaedic Research **13**(3) (1995) 390–398

[230] Arjmand, N., Shirazi-Adl, A.: Role of intra-abdominal pressure in the unloading and stabilization of the human spine during static lifting tasks. European spine journal : official publication of the European Spine Society, the European Spinal Deformity Society, and the European Section of the Cervical Spine Research Society **15**(8) (aug 2006) 1265–75

[231] Cholewicki, J., Juluru, K., McGill, S.M.: Intra-abdominal pressure mechanism for stabilizing the lumbar spine. Journal of Biomechanics **32**(1) (1999) 13–17

[232] Stokes, I.A.F., Gardner-Morse, M.G., Henry, S.M.: Abdominal muscle activation increases lumbar spinal stability: Analysis of contributions of different muscle groups. Clinical biomechanics (Bristol, Avon) **26**(8) (may 2011) 797–803

[233] Bean, J.C., Chaffin, D.B., Schultz, A.: Biomechanical model calculation of muscle contraction forces: a double linear programming method. Journal of biomechanics **21**(1) (jan 1988) 59–66

[234] Hughes, R.E., Chaffin, D.B., Lavender, S.a., Andersson, G.B.J.: Evaluation of muscle force prediction models of the lumbar trunk using surface electromyography. Journal of Orthopaedic Research **12**(5) (1994) 689–698

[235] McGill, S.M., Norman, R.W.: Partitioning of the L4-L5 dynamic moment into disc, ligamentous, and muscular components during lifting. Spine **11**(7) (1986) 666–678

[236] Granata, K.P., Marras, W.S.: An EMG-assisted model of trunk loading during free-dynamic lifting. Journal of Biomechanics **28**(11) (1995) 1309–1317

[237] Cholewicki, J., McGill, S.M., Norman, R.W.: Comparison of muscle forces and joint load from an optimization and EMG assisted lumbar spine model: towards development of a hybrid approach. Journal of biomechanics **28**(3) (mar 1995) 321–31

[238] Gagnon, D., Larivière, C., Loisel, P.: Comparative ability of EMG, optimization, and hybrid modelling approaches to predict trunk muscle forces and lumbar spine loading during dynamic sagittal plane lifting. Clinical biomechanics (Bristol, Avon) **16**(5) (jun 2001) 359–72

[239] Arjmand, N., Shirazi-Adl, A., Parnianpour, M.: Trunk biomechanical models based on equilibrium at a single-level violate equilibrium at other levels. European spine journal : official publication of the European Spine Society, the European Spinal Deformity Society, and the European Section of the Cervical Spine Research Society **16**(5) (may 2007) 701–9

[240] Arjmand, N., Gagnon, D., Plamondon, A., Shirazi-Adl, A., Larivière, C.: Comparison of trunk muscle forces and spinal loads estimated by two biomechanical models. Clinical biomechanics (Bristol, Avon) **24**(7) (aug 2009) 533–41

[241] Arjmand, N., Plamondon, A., Shirazi-Adl, A., Larivière, C., Parnianpour, M.: Predictive equations to estimate spinal loads in symmetric lifting tasks. Journal of Biomechanics **44**(1) (2011) 84–91

[242] Anderson, D.E., D'Agostino, J.M., Bruno, A.G., Manoharan, R.K., Bouxsein, M.L.: Regressions for estimating muscle parameters in the thoracic and lumbar trunk for use in musculoskeleta modeling. Journal of Biomechanics **45**(1) (2012) 66–75

[243] Delp, S.L., Anderson, F.C., Arnold, A.S., Loan, P., Habib, A., John, C.T., Guendelman, E., Thelen, D.G.: OpenSim: open-source software to create and analyze dynamic simulations of movement. IEEE transactions on bio-medical engineering **54**(11) (dec 2007) 1940–50

[244] Thelen, D.G.: Adjustment of muscle mechanics model parameters to simulate dynamic contractions in older adults. Journal of biomechanical engineering **125**(1) (2003) 70–77

[245] White III, A.A., Panjabi, M.M.: Clinical biomechanics of the spine. Second edn. Lippincott Williams Wilkins, Philadelphia (1990)

[246] Granata, K.P.: Response to "Static and dynamic stability of the spine". Journal of Biomechanics **39**(15) (2006) 2921–2922

[247] Han, K.S., Zander, T., Taylor, W.R., Rohlmann, A.: An enhanced and validated generic thoraco-lumbar spine model for prediction of muscle forces. Medical Engineering and Physics **34**(6) (2012) 709–716

[248] Hedenstierna, S.: 3D Finite Element Modeling of Cervical Musculature and its Effect on Neck Injury Prevention Royal Institute of Technology School of Technology and Health Division of Neuronic Engineering. PhD thesis, KTH Technology and Health (2008)

[249] Hedenstierna, S., Halldin, P.: How does a three-dimensional continuum muscle model affect the kinematics and muscle strains of a finite element neck model compared to a discrete muscle model in rear-end, frontal, and lateral impacts. Spine **33**(8) (apr 2008) E236–45

[250] Brolin, K., Halldin, P., Leijonhufvud, I.: The effect of muscle activation on neck response. Traffic injury prevention **6**(1) (2005) 67–76

[251] Meyer, G.a., McCulloch, a.D., Lieber, R.L.: A Nonlinear Model of Passive Muscle Viscosity. Journal of Biomechanical Engineering **133**(9) (2011) 091007

[252] Winters, J.M., Woo, S.L.Y.: Multiple muscle systems: Biomechanics and movement organization. First edn. Springer-Verlag New York Inc. (1990)

[253] Kojic, M., Mijailovic, S., Zdravkovic, N.: Modelling of muscle behaviour by the finite element method using Hill's three-element model. International Journal for Numerical and Analytical Methods in Engineering **43** (1998) 941–953

[254] Martins, J.a.C., Pires, E.B., Salvado, R., Dinis, P.B.: A numerical model of passive and active behavior of skeletal muscles. Computer Methods in Applied Mechanics and Engineering **151**(3-4) (jan 1998) 419–433

[255] Humphrey, J.D., Yin, F.C.: A new constitutive formulation for characterizing the mechanical behavior of soft tissues. Biophysical journal **52**(4) (oct 1987) 563–70

[256] Zajac, F.E.: Muscle and tendon: properties,model,scaling,and application to biomechanics and motor control. Critical reviews in biomedical engineering **17**(4) (1989) 359–410

[257] D'Aulignac, D., Martins, J.a.C., Pires, E.B., Mascarenhas, T., Jorge, R.M.N.: A shell finite element model of the pelvic floor muscles. Computer methods in biomechanics and biomedical engineering **8**(5) (oct 2005) 339–47

[258] Blemker, S.S., Pinsky, P.M., Delp, S.L.: A 3D model of muscle reveals the causes of nonuniform strains in the biceps brachii. Journal of Biomechanics **38**(4) (2005) 657–665

[259] Weiss, J.a., Maker, B., Govindjee, S.: Finite element implementation of incompressible,transversly isotropic hyperelasticity.pdf. Computer Methods in Applied Mechanics and Engineering **135** (1996) 107–128

[260] Criscione, J.C., Douglas, A.S., Hunter, W.C.: Physically based strain invariant set for materials exhibiting transversely isotropic behavior. Journal of the Mechanics and Physics of Solids **49** (apr 2001) 871–897

[261] Lu, Y.T., Beldie, L., Walker, B., Richmond, S., Middleton, J.: Parametric study of a Hill-type hyperelastic skeletal muscle model. Proceedings of the Institution of Mechanical Engineers, Part H: Journal of Engineering in Medicine **225**(5) (apr 2011) 437–447

[262] Tang, C.Y., Zhang, G., Tsui, C.P.: A 3D skeletal muscle model coupled with active contraction of muscle fibres and hyperelastic behaviour. Journal of biomechanics **42**(7) (may 2009) 865–72

[263] Fernandez, J.W., Buist, M.L., Nickerson, D.P., Hunter, P.J.: Modelling the passive and nerve activated response of the rectus femoris muscle to a flexion loading: a finite element framework. Medical engineering physics **27**(10) (dec 2005) 862–70

[264] Böl, M., Weikert, R., Weichert, C.: A coupled electromechanical model for the excitation-dependent contraction of skeletal muscle. Journal of the mechanical behavior of biomedical materials **4**(7) (oct 2011) 1299–310

[265] Shorten, P.R., O'Callaghan, P., Davidson, J.B., Soboleva, T.K.: A mathematical model of fatigue in skeletal muscle force contraction. Journal of muscle research and cell motility **28**(6) (jan 2007) 293–313

[266] Röhrle, O., Davidson, J.B., Pullan, A.J.: A physiologically based, multi-scale model of skeletal muscle structure and function. Frontiers in Physiology **3 SEP**(September) (2012) 1–14

[267] Mow, V.C., Lai, W.M., Armstrong, C.G.: Biphasic creep and stress relaxation of articular cartilage in compression? Theory and experiments. Journal of biomechanical engineering **102**(1) (1980) 73–84

[268] Biot, M.A.: General theory of three-dimensional consolidation. Journal of applied physics **12**(2) (1941) 155–164

[269] Simon, B.R.: Multiphase poroelastic finite element models for soft tissue structures. Appled mechanics reviews **45**(6) (1992) 191–218

[270] Huyghe, J.M., Janssen, J.D.: Quadriphasic mechanics of swelling incompressible porous media. International journal of engineering science **35**(8) (1997) 793–802

[271] Simon, B.R., Kaufmann, M.V., McAfee, M.A., Baldwin, A.L., Wilson, L.M.: Identification and determination of materia properties for porohypereastic analysis of large arteries. Journal of biomechanical engineering **120**(2) (1998) 188–194

[272] Holzapfel, G.A.: Nonlinear solid mechanics. A continuum approach for engineering. John Wiley Sons, Chichester (2000)

[273] Eberlein, R., Holzapfel, G.A., Schulze-Bauer, C.a.J.: An Anisotropic Model for Annulus Tissue and Enhanced Finite Element Analyses of Intact Lumbar Disc Bodies. Computer Methods in Biomechanics and Biomedical Engineering **4**(3) (2001) 209–229

[274] Gasser, T.C., Ogden, R.W., Holzapfel, G.A.: Hyperelastic modelling of arterial layers with distributed collagen fibre orientations. Journal of the Royal Society, Interface / the Royal Society **3**(6) (2006) 15–35

[275] Argoubi, M., Shirazi-Adl, A.: Poroelastic creep response analysis of a lumbar motion segment in compression. Journal of Biomechanics **29**(10) (1996) 1331–1339

[276] Schroeder, Y., Wilson, W., Huyghe, J.M., Baaijens, F.P.T.: Osmoviscoelastic finite element model of the intervertebral disc. European Spine Journal **15**(SUPPL. 3) (2006) 361–371

[277] Périé, D., Korda, D., Iatridis, J.C.: Confined compression experiments on bovine nucleus pulposus and annulus fibrosus: Sensitivity of the experiment in the determination of compressive modulus and hydraulic permeability. Journal of Biomechanics **38**(11) (2005) 2164–2171

[278] Schroeder, Y., Elliott, D.M., Wilson, W., Baaijens, F.P.T., Huyghe, J.M.: Experimental and model determination of human intervertebral disc osmoviscoelasticity. Journal of Orthopaedic Research **26**(8) (2008) 1141–1146

[279] Malandrino, A., Noailly, J., Lacroix, D.: The Effect of Sustained Compression on Oxygen Metabolic Transport in the Intervertebral Disc Decreases with Degenerative Changes. PLoS Computational Biology **7**(8) (aug 2011) e1002112

[280] Zhu, Q., Jackson, A.R., Gu, W.Y.: Cell viability in intervertebral disc under various nutritional and dynamic loading conditions: 3d Finite element analysis. Journal of Biomechanics **45**(16) (2012) 2769–2777

[281] Malandrino, A., Pozo, J.M., Castro-Mateos, I., Frangi, A.F., van Rijsbergen, M.M., Ito, K., Wilke, H.J., Dao, T.T., Ho Ba Tho, M.C., Noailly, J.: On the Relative Relevance of Subject-Specific Geometries and Degeneration-Specific Mechanical Properties for the Study of Cell Death in Human Intervertebral Disk Models. Frontiers in Bioengineering and Biotechnology **3**(February) (2015) 1–15

[282] Dormieux, L., Kondo, D., Ulm, F.J.: A micromechanical analysis of damage propagation in fluid-saturated cracked media. Comptes Rendus - Mecanique **334**(7) (2006) 440–446

[283] Laible, J.P., Pflaster, D.S., Krag, M., Simon, B.R., Haugh, L.D.: A poroelastic-swelling finite element model with application to the intervertebral disc. Spine **18**(5) (1993) 659–670

[284] Ferguson, S.J., Ito, K., Nolte, L.P.: Fluid flow and convective transport of solutes within the intervertebral disc. Journal of Biomechanics **37**(2) (2004) 213–221

[285] Stokes, I.A.F., Chegini, S., Ferguson, S.J., Gardner-morse, M.G., Iatridis, J.C., Laible, J.P.: Limitation of finite element analysis of poroelastic behavior of biological tissues undergoing rapid loading. Annals of biomedical engineering **38**(5) (2010) 1780–1788

[286] Chen, D.T., Zeltzer, D.: Pump It Up: Computer animation of a biomechanically model of muscle using the finite element method. Computer Graphics **26**(2) (1992) 89–98

[287] Ho Ba Tho, M.C., Dao, T.T., Bensamoun, S., Dakpe, S., Devauchelle, B., Rachik, M.: Subject Specific Modeling of the Muscle Activation: Application to the Facial Mimics. Knowledge and Systems Engineering **2** (2014) 423–433

[288] Weiss, J.a., Gardiner, J.C.: Computational modeling of ligament mechanics. Critical reviews in biomedical engineering **29**(4) (2001) 1–70

[289] Bouten, C.V.C., Breuls, R.G.M., Peeters, E.a.G., Oomens, C.W.J., Baaijens, F.P.T.: In vitro models to study compressive strain-induced muscle cell damage. Biorheology **40**(1-3) (jan 2003) 383–8

[290] Brooks, S.V., Zerba, E., Faulkner, J.a.: Injury to muscle fibres after single stretches of passive and maximally stimulated muscles in mice. The Journal of physiology **488 (Pt 2**(1995) (oct 1995) 459–69

[291] Lieber, R.L., Fridén, J.: Muscle damage is not a function of muscle force but active muscle strain. Journal of Applied Physiology **74**(2) (1985)

[292] Farfan, H.F.: Mechanical disorders of the low back. Lea Febiger, Philadelphia (1973)

[293] Weis-Fogh, T., Alexander, R.M.: The sustained power output from striated muscle. In Pedley, T.J., ed.: Scale effects in animal locomotion. Academic Press, London (1977) 511–525

[294] Ikai, M., Fukunaga, T.: Calculation of muscle strength per unit cross-sectional area of human muscle by means of ultrasonic measurement. Internationale Zeitschrift für Angewandte Physiologie Einschließlich Arbeitsphysiologie **26**(1) (1968) 26–32

[295] Hansen, L., de Zee, M., Rasmussen, J., Andersen, T.B., Wong, C., Simonsen, E.B.: Anatomy and biomechanics of the back muscles in the lumbar spine with reference to biomechanical modeling. Spine **31**(17) (aug 2006) 1888–99

[296] Vasavada, A., Li, S., Delp, S.L.: Influence of muscle morphometry and moment arms on the moment-generating capacity of human neck muscles. Spine **23**(4) (1998) 412–422

[297] Stokes, I.A.F., Gardner-Morse, M.: Lumbar spinal muscle activation synergies predicted by multi-criteria cost function. Journal of Biomechanics **34**(6) (2001) 733–740

[298] Ghiasi, M.S., Arjmand, N., Boroushaki, M.: Investigation of trunk muscle activities during lifting using a multi objective optimization based model and intelligent optimization algorithms. Medical Biological Engineering Computing **54**(2) (2015) 431–440

[299] Noailly, J., Wilke, H.J., Planell, J.A., Lacroix, D.: How does the geometry affect the internal biomechanics of a lumbar spine bi-segment finite element model? Consequences on the validation process. Journal of Biomechanics **40**(11) (jan 2007) 2414–25

[300] Panjabi, M.M., Greenstein, G., Duranceau, J., Nolte, L.P.: Three-dimensional quantitative morphology of lumbar spinal ligaments. Journal of Spinal Disorders **4**(1) (1991) 54–62

[301] Sánchez Egea, A.J., Valera, M., Parraga Quiroga, J.M., Proubasta, I., Noailly, J., Lacroix, D.: Impact of hip anatomical variations on the cartilage stress: A finite element analysis towards the biomechanical exploration of the factors that may explain primary hip arthritis in morphologically normal subjects. Clinical biomechanics (Bristol, Avon) **29**(4) (apr 2014) 444–50

[302] Malandrino, A., Planell, J.A., Lacroix, D.: Statistical factorial analysis on the poroelastic material properties sensitivity of the lumbar intervertebral disc under compression, flexion and axial rotation. Journal of biomechanics **42**(16) (dec 2009) 2780–8

[303] Johannessen, W., Elliott, D.M.: Effects of degeneration on the biphasic material properties of human nucleus pulposus in confined compression. Spine **30**(24) (dec 2005) E724–9

[304] Pearsall, D.J., Reid, J.G., Livingston, L.a.: Segmental inertial parameters of the human trunk as determined from computed tomography. Annals of biomedical engineering **24**(2) (1996) 198–210

[305] Vette, A.H., Yoshida, T., Thrasher, T.A., Masani, K., Popovic, M.R.: A complete, non-lumped, and verifiable set of upper body segment parameters for three-dimensional dynamic modeling. Medical engineering physics **33**(1) (jan 2011) 70–9

[306] Ivancic, P.C., Panjabi, M.M., Ito, S.: Cervical spine loads and intervertebral motions during whiplash. Traffic injury prevention **7**(4) (dec 2006) 389–99

[307] Takahashi, I., Kikuchi, S.i., Sato, K., Sato, N.: Mechanical load of the lumbar spine during forward bending motion of the trunk-a biomechanical study. Spine **31**(1) (2006) 18–23

[308] Malandrino, A., Noailly, J., Lacroix, D.: Regional annulus fibre orientations used as a tool for the calibration of lumbar intervertebral disc finite element models. Computer Methods in Biomechanics and Biomedical Engineering (January) (jan 2013) 37–41

[309] Heuer, F., Schmidt, H., Wilke, H.J.: The relation between intervertebral disc bulging and annular fiber associated strains for simple and complex loading. Journal of Biomechanics **41**(5) (2008) 1086–1094

[310] Wilke, H.J., Wolf, S., Lutz, E.C., Arandt, M., Wiesend, A.: Influence of varying muscle forces on lumbar intradiscal pressure: an in vitro study. Journal of biomechanics **29**(4) (1996) 549–555

[311] Goel, V.K., Kong, W., Han, J.S., Weinstein, J.N., Gilbertson, L.G.: A combined finite element and optimization investigation of lumbar spine mechanics with and without muscles. Spine **18**(11) (1979) 1531–1541

[312] Masi, A.T., Hannon, J.C.: Human resting muscle tone (HRMT): Narrative introduction and modern concepts. Journal of Bodywork and Movement Therapies **12**(4) (2008) 320–332

[313] Frobin, W., Brinckmann, P., Kramer, M., Hartwig, E.: Height of lumbar discs measured from radiographs compared with degeneration and height classified from MR images. European Radiology **11**(2) (2001) 263–269

[314] Hong, C.H., Park, J.S., Jung, K.J., Kim, W.J.: Measurement of the normal lumbar intervertebral disc space using magnetic resonance imaging. Asian spine journal **4**(1) (2010) 1–6

[315] Roberts, N., Gratin, C., Whitehouse, G.H.: MRI analysis of lumbar intervertebral disc height in young and older populations. Journal of Magnetic Resonance Imaging **7**(5) (1997) 880–886

[316] Pfirrmann, C.W., Metzdorf, A., Zanetti, M., Hodler, J., Boos, N.: Magnetic resonance classification of lumbar intervertebral disc degeneration. Spine **26**(17) (2001) 1873–1878

[317] Cobb, J.R.: Outline for the study of scoliosis. American Academy of Orthopaedic Surgeons Instr Course Lect **5** (1948) 261–275

[318] Been, E., Kalichman, L.: Lumbar lordosis. Spine Journal **14**(1) (2014) 87–97

[319] Damasceno, L.: Lumbar lordosis : A study of angle values and of vertebral bodies and intervertebral discs role. Acta Orthopaedica Bras **14**(4) (2006) 193–198

[320] Hong, J.Y., Suh, S.W., Modi, H.N., Hur, C.Y., Song, H.R., Park, J.H.: Reliability analysis for radiographic measures of lumbar lordosis in adult scoliosis: A case-control study comparing 6 methods. European Spine Journal **19**(9) (2010) 1551–1557

[321] Walker, M.L., Rothstein, J.M., Finucane, S.D., Lamb, R.L.: Relationships between lumbar lordosis, pelvic tilt, and abdominal muscle performance. Physical therapy **67**(4) (1987) 512–516

[322] Kim, M.S., Chung, S.W., Hwang, C., Al., E.: A radiographic analysis of sagittal spinal alignment for the standardization of standing lateral position. Journal of the Korean Orthopaedic Association **40** (2005) 861–7

[323] Kim, K., Kim, Y.H., Lee, S.: Investigation of optimal follower load path generated by trunk muscle coordination. Journal of biomechanics **44**(8) (may 2011) 1614–7

[324] Murrie, V.L., Dixon, A.K., Hollingworth, W., Wilson, H., Doyle, T.A.: Lumbar lordosis: study of patients with and without low back pain. Clinical anatomy (New York, N.Y.) **16**(2) (2003) 144–147

[325] Epstein, J.A., Epstein, B.S., Lavine, L.: Nerve Root Compression Associated With Narrowing of the Lumbar Spinal Canal. Journal of Neurology, Neurosurgery Physchiatry **25**(2) (1962) 165–176

[326] Tüzün, C., Yorulmaz, I., Cindas, A., Vatan, S.: Low back pain and posture. Clinical Rheumatology **18**(4) (1999) 308–312

[327] Christie, H.J., Kumar, S., Warren, S.A.: Postural aberrations in low back pain. Archives of Physical Medicine and Rehabilitation **76**(3) (1995) 218–224

[328] Nachemson, A.L.F., Elfström, G.: Intravital dynamic pressure measurements in lumbar discs. A study of common movements, maneuvers and exercises. Scandinavian journal of rehabilitation medicine **1**(1) (1970) 1–40

[329] Dreischarf, M., Shirazi-Adl, A., Arjmand, N., Rohlmann, A., Schmidt, H.: Estimation of loads on human lumbar spine: A review of in vivo and computational model studies. Journal of Biomechanics **49**(6) (2016) 833–845

Biosketch

Themis Toumanidou (August 12, 1986 - Veria, Greece) graduated as a Dipl-Ing in Mechanical Engineering from the University of Thessaly (UTH) in Volos, Greece, in 2009. During her undergraduate studies, she received three honors and two financial awards from the State Scholarship Foundation, the Deligeorgi Foundation and the Technical Chamber of Greece. In April 2011, she obtained her M.Sc. degree in the State-of-the-Art Design and Analysis Methods in Mechanics, Materials and Manufacturing from the same department. She developed her Master thesis on the biomechanical analysis of external fixators for patients with tibia deformations and fractures using computational methods in a multi-center collaboration between the Mechanics and Materials Lab of the UTH, and the University Hospital of Lárisa, Greece.

In May 2011, she moved to Barcelona where she started her Ph.D. studies in the Universitat Politècnica de Catalunya (UPC) and the Biomechanics and Mechanobiology research group of the Institute for Bioengineering of Catalonia (IBEC). Her Ph.D. thesis focuses on the numerical explorations of the healthy and degenerated lumbar spine musculoskeletal system and was supervised by Dr. Jérôme Noailly. Between 2013 and 2014, she was awarded with the Basic Sciences and 4th Best Work Prize from the Spanish Chapter of the European Society of Biomechanics, and the Best Flash Presentation Prize in the 6th IBEC Symposium on Bioengineering and Nanomedicine held in Barcelona. As part of her thesis, she spent 3 months in the Laboratoire Biomécanique et Bioingénierie of the Universitè de Technologie de Compiègne (UTC) in France working with Prof. Marie-Christine Ho Ba Tho on the personalization of a constitutive model of the back muscles using dynamic MRI and vertebrae kinematics data.

In February 2015, together with the whole team of the Biomechanics and Mechanobiology group, they joined the Simulation, Imaging and Modelling for Biomedical Systems (SIMBIOsys) group at the Universitat Pompeu Fabra (UPF). During her time in the UPF, she taught Musculoskeletal Modeling (3rd year), Biomaterials (2nd year), Biomedical Imaging Systems (2nd year), and Computational Techniques in Biomedicine (1st year) to Bachelor degree students in Biomedical Engineering. The results of her Ph.D. work have been scientifically reviewed and accepted in 15 conferences and symposia (eight international, seven national) for oral and poster presentations. She has one article published in a peer-reviewed journal and another one currently in preparation. Since May 2016, she is a scientific reviewer for the PLoS ONE journal.

Publications

Peer-reviewed journal articles and manuscripts

- **Toumanidou, T.** and Noailly, J.: Musculoskeletal modeling of the lumbar spine to explore functional interactions between back muscle loads and intervertebral disk multiphysics. Frontiers in Bioengineering and Biotechnology **3**(August):111 (2015) 1-13. doi: 10.3389/fbioe.2015.00111 3
- **Toumanidou, T.**, Dao, T.T., Pozo, J.M., Frangi, A.F., González Ballester, M.A., Ho Ba Tho, M.C., Noailly, J.: On the relative relevance of personalized musculoskeletal modeling for the prediction of internal loads in the healthy and degenerated lumbar spine. *In preparation*

Peer-reviewed conference contributions

Manuscripts:

- **Toumanidou, T.**, Fortuny, G., Lacroix, D., Noailly, J.: Constitutive modelling of the lumbar spine musculature. Proceedings of the 10th International symposium, Computer Methods in Biomechanics and Biomedical Engineering (CMMBE) (2012), 693-698 ARUP – ISBN: 978-0-9562121-5-3
- **Toumanidou, T.**, Fortuny, G., Lacroix, D., Noailly, J.: On the constitutive modelling of lumbar spine muscles. Proceedings of the 18th Congress of the European Society of Biomechanics (ESB). Journal of Biomechanics **45**(1) (2012), S609
- **Toumanidou, T.**, Noailly, J., Puigjaner, D., Fortuny, G.: A continuum model for the whole muscle. Proceedings of the 18th Congress of the European Society of Biomechanics (ESB). Journal of Biomechanics **45**(1) (2012), S484
- **Toumanidou, T.**, Fortuny, G., Lacroix, D., Noailly, J.: Assessment of a muscle constitutive model through the biomechanical analysis of a L3-L5 lumbar spine musculoskeletal model under upper-body inclination. Proceedings of the 11th International Symposium, Computer Methods in Biomechanics and Biomedical Engineering (CMMBE) (2013), 160-161 – ISBN: 978-0-615-79003-9

Abstracts:

- **Toumanidou, T.**, Fortuny, G., Lacroix, D., Noailly, J.: On the constitutive modelling of the lumbar spine musculature. 5th Symposium of the Institute for Bioengineering of Catalonia (IBEC) on Bioengineering and Nanomedicine, Barcelona, Spain, June 11, 2012.
- **Toumanidou, T.**, Fortuny, G., Lacroix, D., Noailly, J.: A novel active lumbar spine muscle model. 2nd VPH Conference on Integrative Approaches to Computational Biomedicine (VPH), London, United Kingdom, September 18-20, 2012 - Abstract 117.
- **Toumanidou, T.**, Fortuny, G., Lacroix, D., Noailly, J.: A Hill-type hyperelastic lumbar spine muscle model. II Reunión del Capitulo Español de la Sociedad Europea de Biomecánica, Sevilla, Spain, October 25, 2012 (CD-ROM).
- **Toumanidou, T.**, Fortuny, G., Noailly, J.: Lumbar muscle forces and spinal loads derived from external loading by using a muscle constitutive model. 6th Symposium of the Institute for Bioengineering of Catalonia (IBEC) on Bioengineering and Nanomedicine, Barcelona, Spain, May 8, 2013.
- **Toumanidou, T.**, Fortuny, G., Noailly, J.: On the patient-specific calibration of an active constitutive model for the lumbar muscles. 19th Congress of the European Society of Biomechanics (ESB), Patras, Greece, August, 25-28, 2013 - Abstract S38.5, 568.
- **Toumanidou, T.**, Noailly, J.: Explicit simulation of muscle activation in combination with intervertebral disc swelling reproduces in vivo intradiscal pressures in a L3-S1 lumbo-sacral spine model. III Reunión del Capitulo Español de la Sociedad Europea de Biomecánica, Barcelona, Spain, October 23-24, 2013 (CD-ROM).
- **Toumanidou, T.**, Noailly, J.:Simulating muscle activation in the lumbar spine while accounting for condition-dependent intervertebral disc multiphysics. 7th World Congress of Biomechanics (WCB) - 20th Congress of the European Society of Biomechanics (ESB), Boston, MA, United States, July 6-11, 2014 (Plenary talk)
- **Toumanidou, T.**, Noailly, J.: Active muscle modelling in combination with intervertebral disc swelling in a L3-S1 lumbar spine model captures the importance of night rest. 3rd VPH Conference on Integrative Approaches to Computational Biomedicine (VPH), Trondheim, Norway, September 9-12, 2014.

- **Toumanidou, T.**, Noailly, J.: The effect of disc degeneration in combination with muscle activity on the intradiscal pressures: a continuum approach using a L1-S1 patient-specific FE model for simulated standing. 7th Symposium of the Institute for Bioengineering of Catalonia (IBEC) on Bioengineering and Nanomedicine, Barcelona, Spain, September 29, 2014.

- **Toumanidou, T.**, Noailly, J.: Simulating the interaction between muscle activation and condition-dependent intervertebral disc multiphysics in patiens with low back pain. IV Reunión del Capitulo Español de la Sociedad Europea de Biomecánica, València, Spain, November 20-21, 2014 (CD-ROM).

- **Toumanidou, T.**, Noailly, J.: Simulating the interaction between muscle activation and condition-dependent intervertebral disc multiphysics in patiens with low back pain. XXXII Congreso Anual de la Sociedad Española de Ingeniería Biomédica (CASEIB), Barcelona, Spain, November 26-28, 2014 (CD-ROM).

- **Toumanidou, T.**, Dao, T.T., Ho Ba Tho, M.C., Noailly, J.: Exploring the interactions between muscle function and intervertebral disc multiphysics in the healthy and the degenerated lumbar spine. 12th World Congress on Computational Mechanics (WCCM XII) - 6th Asia-Pacific Congress on Computational Mechanics (APCOM VI), Seoul, Korea, July 20-25, 2016 - Paper 152365.

Acknowledgements

This piece of research was carried out during the last five years along with numerous experiences lived and many lessons learned. I feel grateful for every encounter and opportunity that favored my scientific growth and, in a personal level, unraveled a better and braver version of myself.

First of all, I would like to express my sincere gratitude to my supervisor, Dr. Jérôme Noailly, and to Prof. Damien Lacroix for replying to my repeated requests for an interview back in 2011. Thank you to Prof. Marie-Christine Ho Ba Tho and Dr. Tuan Dao for the fruitful collaboration and for receiving me at the Biomecànique et Biongenierie Lab of the UTC in Compiègne, France.

Jérôme, ¡he aprendido tanto de ti! Gracias por todos los consejos, los comentarios y las exigencias, las oportunidades y los desafíos. Gracias por enseñarnos a trabajar como un equipo. Por todas las experiencias y la presión, el ánimo y la motivación, pero sobre todo por el apoyo y la comprensión que has mostrado durante estos años. Espero que el resultado final te deje igual de contento que a mí. Merci pour tout, J!

I consider myself lucky to have worked within a group of good researchers, supportive colleagues and friends with whom I shared the stress of deadlines, the excitement of accepted papers, the fun of traveling for work, and the mixed feelings during our theses writing. Andrea, Andy, Carlos, Simone, gracias por todo IBECers! Aura, Diego, Joana y Sara P, ¡infinitas gracias además por todas las aventuras! Dr. Sánchez Ferrero, especial menció per a tu. Gràcies per seguir-me donant ànims tot i que no deixava de queixar-me, i gràcies per haver-me fet riure tant! À Sebastian J, Farah, Julia, Jessy, Nicole, Bassam et Felipe, merci les amis pour tous les bons moments chez l'UTC! Además, en nuestra nueva casa en la UPF, ha sido una suerte encontrar una oficina cálida, tanto por la cantidad de ordenadores como por el buen rollo de las personas. Gracias por la ayuda que he recibido durante la redacción de la tesis a todos y particularmente a Oualid, Cecilia y Rubén. A mi amigo David S, mil gracias por tu actitud positiva, la motivación y las infinitas conversaciones. I am especially grateful to Marco for all sources of inspiration he introduced me to, for giving me new perspectives, and for all the time dedicated to support and help me. ¡Gracias por recordarme siempre que uno se cae sólo si deja de pedalear!

Finally, I am thankful to my parents and grandparents who have been always proud of me even though they did not agree with my choices. To my sister, *Κικη*, and to Montse C, the two persons really aware of the emotional roller coaster this adventure has been for me, I am forever indebted and grateful to you.

Themis, 22 de septiembre 2016

TESI DOCTORAL / 2016